Virtual Flight Testing in a Wind Tunnel Using a Manoeuvre Rig

Thesis

By

PUNSARA D. B. NAVARATNA

Department of Aerospace Engineering
UNIVERSITY OF BRISTOL

A dissertation submitted to the University of Bristol in accordance with the requirements of the degree of DOCTOR OF PHILOSOPHY in the Faculty of Engineering.

NOVEMBER 2019

Word count: 66,000 (approx.)

Abstract

The manoeuvre rig is a novel dynamic wind tunnel rig developed at the University of Bristol. It is capable of five degrees-of-freedom for the aircraft model: roll, pitch, yaw, heave, and sway. This rig is unique relative to other dynamic test rigs due to the presence of an aerodynamic compensator at the rear, with four control surfaces capable of creating moments onto the rig.

The concept of the manoeuvre rig was created to achieve three main objectives: 1) to develop mathematical models using parameter estimation, 2) to study non-linear or unsteady aerodynamic phenomena, and 3) to physically simulate free-flight manoeuvres. The first two objectives have been explored previously and results have been published. This thesis will focus primarily on the third objective of true physical free-flight simulation on the manoeuvre rig. This aspect is initially explored computationally via simulations of the full non-linear mathematical model of the rig, with attention to the effects of kinematic constraints on the motion responses of the aircraft model. A concept to reduce these effects on the manoeuvre rig in order to better match a free-flying aircraft is presented, which is achieved by applying an external force using the rig's aerodynamic compensator. This is demonstrated experimentally including rig inertial, aerodynamic, and kinematic compensation via reaction force control, and results are presented. The limitations and capabilities of the rig and the compensation concept on this regard are covered. The thesis will cover the latest modifications to the manoeuvre rig with the implementation of a six-axis load cell which further extends the capabilities of the rig as an experimental testing platform. In addition, the thesis covers several new applications of the manoeuvre rig with the study of stall hysteresis and self-sustained oscillatory motion on an approximate subscale BAe Hawk model.

Progress has been made with regards to the novel concept of rig compensation for achieving true free-flying responses of an aircraft model on the manoeuvre rig. This work has also been successful in extending the overall capability of the manoeuvre rig as a wind tunnel testing platform for subscale aircraft models.

Dedication and acknowledgements

I would like to dedicate this work first and foremost to my family: my parents Amma and Appachchi, my sister Punsala, and Thiththa. I would never have come this far without them. I will forever cherish your endless love and support that you all have given me. I love you all!

I want to especially thank my sister for her infinite and unconditional support throughout this journey. Thank you so much for bearing my many requests to proofread my writing. I could not ask for a better sister, you're the best!

A very special thank you goes to my supervisors Prof. Lowenberg and Prof. Neild. I truly feel lucky to have been fortunate enough to have supervisors who were inspiring as well as unconditionally supportive and encouraging. Thank you for your support and invaluable advice, and for always guiding me in the right direction.

A special thank you to Prof. Mikhail Goman. Meetings with you have always been extremely useful in discovering and learning more about the rig you conceived and your research.

A special thank you to Sergio Araujo-Estrada and Matthew Zheng Gong. You have both been very helpful and insightful, giving my great advice about any problem I had (both in general and with the manoeuvre rig). Thank you for helping me familiarise myself with the manoeuvre rig and its codes. Sergio, the rate at which I learned things from you was much higher than if I had learned it all by myself!

I would like to thank Lee Winter and Russ Eyre for their support in the wind tunnel laboratory with the rig and Hawk model. Without their expertise, I would not have been able to produce the results I did.

Thank you B for all the laughs and fun moments throughout the years. You are an amazing friend!

And finally, I would like to sincerely thank the University of Bristol and the Alumni Association for giving me this opportunity to do a PhD, a scholarship, and for the unforgettable and exhilarating experience it has been. I am truly grateful.

AUTHOR'S DECLARATION

I declare that the work in this dissertation was carried out in accordance with the requirements of the University's Regulations and Code of Practice for Research Degree Programmes and that it has not been submitted for any other academic award. Except where indicated by specific reference in the text, the work is the candidate's own work. Work done in collaboration with, or with the assistance of, others, is indicated as such. Any views expressed in the dissertation are those of the author.

SIGNED: ..... DATE: .....

PUBLICATIONS

A conference and journal paper that have been published as a result of this work:

1. Navaratna, P. D. B., Lowenberg, M. H., Neild, S., and Zhang, X., "Physical simulation of free-flight in captive wind tunnel tests," Applied Aerodynamics Conference, Royal Aeronautical Society, Bristol, 2016.
2. Banneheka Navaratna, P., Lowenberg, M., and Neild, S., "Minimally-constrained flight simulation in a wind tunnel," Journal of Aircraft, 1 2019, doi:10.2514/1.C035199.

TABLE OF CONTENTS

Page

List of Tables **xiii**

List of Figures **xvii**

1 Introduction **5**

2 Literature review **7**

2.1 Introduction 7
2.2 Traditional experimental testing techniques 7
2.3 Dynamic scaling of test models 9
2.4 Multi-Degree-Of-Freedom wind tunnel test rigs 10
2.5 Manoeuvre simulation 11
2.6 The manoeuvre rig 14
2.6.1 Advantages of using the manoeuvre rig for free-flight simulation 16
2.6.2 Dynamic scaling on the manoeuvre rig 17
2.7 Aircraft loss-of-control 18
2.8 Research motivation and objectives 19
2.9 Thesis structure 22

3 Development of Equations of Motion **25**

3.1 Introduction 25
3.2 2D linear state-space mathematical model of the manoeuvre rig 26
3.3 Choice of coordinate axes 27
3.4 3D rigid-body mathematical model of the manoeuvre rig 28
3.5 Quaternions 31
3.6 Rig constraints equations 33
3.6.1 Relative position fixed constraint 34
3.6.2 Relative attitude fixed constraint 36
3.6.3 Ball and socket joint 37
3.6.4 Quaternion constraint 38

3.6.5 Additional constraints . . . 38
3.7 Combined constraint equations . . . 42
3.8 Aerodynamics mathematical model . . . 43
3.8.1 Linear aerodynamics model for the Hawk . . . 45
3.8.2 Aerodynamic model for the compensator . . . 45
3.8.3 Higher order aerodynamics model for the Hawk . . . 47
3.8.4 The HHIRM . . . 48
3.8.5 The A-4D model . . . 49
3.9 Friction model . . . 49
3.10 Servo models . . . 50
3.11 Implementation of the equations of motion . . . 51
3.12 Summary . . . 51

4 Investigations on Rig Kinematic Effects on Aircraft Model Dynamics 55
4.1 Introduction . . . 55
4.2 Longitudinal kinematic analysis using a simplified 2D model . . . 56
4.2.1 Simplified longitudinal equations of motion for the aircraft model . . . 56
4.2.2 Simplified longitudinal constraint reaction forces . . . 58
4.2.3 Response comparison . . . 59
4.2.4 Free-flight with controlled speed . . . 60
4.2.5 Compensation concept for the arc constraint in 2D . . . 64
4.3 3D analysis of kinematic constraints . . . 69
4.3.1 Mathematical model . . . 69
4.3.2 Response comparison . . . 71
4.3.3 Compensation concept for the spherical constraint in 3D . . . 76
4.3.4 Response comparison when applying $\mathbf{F_c}^*$ and $\mathbf{F_c}^{**}$ . . . 81
4.3.5 Effect of kinematic compensation on perceived aerodynamic coefficients . . . 90
4.4 Practical aspects of compensation . . . 93
4.5 Summary . . . 95

5 Load Cell Implementation 99
5.1 Introduction . . . 99
5.2 Estimation of load cell requirements . . . 99
5.3 Selected load cell: Mini45 . . . 108
5.4 Rig modifications . . . 109
5.5 Software implementation . . . 117
5.6 Rig mass, inertia and gimbal friction estimation . . . 119
5.7 Summary . . . 121

6 Applications of the manoeuvre rig **125**
6.1 Introduction . . . 125
6.2 Hawk static aerodynamic measurements . . . 125
6.2.1 Methodology . . . 126
6.2.2 Noise and filtering . . . 127
6.2.3 Results . . . 129
6.3 Hawk dynamic tests . . . 139
6.4 Investigation of Hawk Stall Hysteresis . . . 148
6.5 Investigation of 2DOF Roll and Yaw Oscillation . . . 153
6.6 Summary . . . 158

7 Rig Inertial, Aerodynamic and Kinematic Compensation **161**
7.1 Introduction . . . 161
7.2 Rig inertial and aerodynamic compensation . . . 162
7.2.1 Preliminary experimental results . . . 162
7.2.2 Experimental results using the load cell . . . 163
7.3 Kinematic compensation . . . 176
7.4 Summary . . . 182

8 Conclusion and Further Work **187**
8.1 Introduction . . . 187
8.2 Mathematical modelling of the manoeuvre rig . . . 187
8.3 Kinematic rig effects . . . 188
8.4 Load cell implementation and application . . . 189
8.5 Experimental compensation . . . 191
8.6 Other work . . . 193
8.6.1 Manoeuvre rig operation safety . . . 193
8.6.2 Update to electronics . . . 194

References **195**

Appendix A Quaternion transformation matrices **203**

Appendix B Subscale A-4D aircraft model properties **205**

Appendix C Hawk CFD data **207**

Appendix D Compensator and Hawk control surface model parameters **211**

Appendix E Manoeuvre rig body properties **215**

Appendix F Rig compensator aerodynamic coefficients **217**

Appendix G Algebraic loops **219**

Appendix H Mini45 Drawing **221**

H.1 Drawing of the ATI Mini45 load cell 222

H.2 Drawing of the load cell wireless transmitter 223

List of Tables

Table **Page**

2.1 Similitude parameter comparison between the full-scale Hawk aircraft and 1/16 scale Hawk model 19

3.1 Simple friction model coefficients for Equation 3.118 50
3.2 Static continuously differentiable friction model coefficients for Equation 3.119 50
3.3 Mathematical model usage throughout this thesis 54

4.1 Root-mean-square error of the arc constrained compensated responses relative to the unconstrained aircraft at constant ground speed 69
4.2 Short-period mode: root mean square error relative to unconstrained aircraft model with constant thrust 83
4.3 Short-period mode: root mean square error relative to unconstrained aircraft model with controlled thrust for constant ground speed 84
4.4 Dutch roll mode: root mean square error relative to unconstrained aircraft model with constant thrust 85
4.5 Dutch roll mode: root mean square error relative to unconstrained aircraft model with controlled thrust for constant ground speed 86
4.6 Spiral mode: root mean square error relative to unconstrained aircraft model with constant thrust 87
4.7 Spiral mode: root mean square error relative to unconstrained aircraft model with controlled thrust for constant ground speed 88
4.8 Roll subsidence mode: root mean square error relative to unconstrained aircraft model with constant thrust 89
4.9 Roll subsidence mode: root mean square error relative to unconstrained aircraft model with controlled thrust for constant ground speed 90
4.10 Estimating longitudinal aerodynamic coefficients from short-period response (0 to 6 seconds) 92
4.11 Estimating lateral-directional aerodynamic coefficients from Dutch roll response (0 to 6 seconds) 93

4.12 RMS comparison between the spherically constrained aircraft model (without thrust) responses with delayed $\mathbf{F}_\mathbf{c}^*$ relative to the unconstrained response with constant thrust (0 to 6 seconds) 95

5.1 T-tail model maximum and minimum dynamic loads (wind axes) at 40 m/s wind speed 104
5.2 Aircraft model (subscript m) and rig arm (subscript a) attitudes considered for load cell load simulation (approximate limitations of the manoeuvre rig) 104
5.3 Maximum and minimum load cell reaction loads (body axes) at 40 m/s wind speed with rig arm fixed 105
5.4 Maximum rig arm rotation rates 105
5.5 Maximum and minimum load cell reaction loads (body axes) at 40 m/s wind speed with the rig free to move 106
5.6 Load cell required capacities for the lower position (318.3 mm below aircraft model) . 106
5.7 Load cell required capacities for the upper position (88.3 mm below aircraft model) . 107
5.8 Load cell required resolution decided by the change in loads due a change in α of 0.5° at a wind speed of 20 m/s (Hawk) 107
5.9 Load cell required resolution decided by the change in loads due a change in β of 0.5° at a wind speed of 20 m/s (Hawk) 107
5.10 Load cell capacities, resolutions and accuracy data 109
5.11 Estimated non-dimensional load coefficient uncertainties 110
5.12 Estimated properties of the whole updated manoeuvre rig (excluding the aircraft model)123

6.1 Summary of the experimentally measured, computationally predicted and parameter estimated static Hawk aerodynamic coefficients (at zero attitude and control surface deflection angles) 141
6.2 Estimated Hawk dynamic aerodynamic derivatives and centre of gravity location relative to the aircraft rotation point (body axes) 150

7.1 Gains calculated using the Ziegler-Nichols method 174

B.1 A-4D model aircraft reference dimensions, mass and inertia properties 205
B.2 A-4D aircraft non-dimensional aerodynamic stability derivatives at Mach 0.4 206
B.3 Comparison between the A-4D aerodynamic coefficients and Hawk model's experimentally measured values 206

C.1 Aerodynamic data for the BAe Hawk model 207
C.2 Hawk aerodynamic derivatives for Equations 3.114-3.116 by performing a surface fit on data points given in Table C.1 208

D.1 Estimated parameters for the control surface actuation model shown in Figure 3.11 . 211

E.1 Manoeuvre rig body properties used for simulation 215

F.1 Rig compensator pitching moment parameters (at $\theta_c = 0$) 217
F.2 Rig compensator yawing moment parameters 217
F.3 Rig compensator rolling moment parameters 218

List of Figures

Figure **Page**

2.1 2-DOF model developed at the University of Manchester capable of motion in model roll and pitch [1] . . . 10
2.2 2-DOF rig developed at the University of Cambridge capable of motion in model roll and yaw [2] . . . 10
2.3 3-DOF rig developed at the University of Bristol capable of motion in model roll, pitch, and yaw [3] . . . 11
2.4 4-DOF rig developed at Cranfield University capable of motion in model roll, pitch, yaw, and heave [4] . . . 11
2.5 The AirStar dynamically scalled UAV testbed [5] . . . 12
2.6 Free-flying wind tunnel model of a Blended Wing Body aircraft [6] . . . 12
2.7 The 6-DOF Model Positioning Mechanism [7] . . . 13
2.8 The 3-DOF Dynamic Plunge-Pitch-Roll rig [8] . . . 13
2.9 The Georgia Tech. 3-DOF traverse rig [9] . . . 13
2.10 The manoeuvre rig . . . 15
2.11 Regions of loss-of-control relative to an aircraft's normal operating flight envelope [5] 20

3.1 The manoeuvre rig bodies and their c.g. positions . . . 28
3.2 Reaction force in a polar and Cartesian coordinate systems . . . 29
3.3 The manoeuvre rig bodies and constraints . . . 32
3.4 Gimbal lock caused by coincident axes of rotation . . . 33
3.5 Relative position fixed constraint . . . 36
3.6 Spherical and planar kinematic constraints . . . 40
3.7 Spherical coordinates . . . 41
3.8 Manoeuvre rig body position vectors . . . 43
3.9 Dynamic lift overshoot modelled by HHIRM . . . 48
3.10 Planform views of the Hawk model and A-4D aircraft . . . 49
3.11 Servo model block diagram . . . 51
3.12 Simulink® model outline . . . 52
3.13 Simulink® Animations Viewer for the manoeuvre rig . . . 53

4.1 Reference axes and external forces . . . 57
4.2 Response to an elevator doublet input . . . 61
4.3 Response to an elevator wavelet input . . . 62
4.4 Aircraft response with controlled speed . . . 65
4.5 Reaction forces applied on the aircraft by an arc constraint . . . 66
4.6 Responses including $F_c{}^*$ compensation . . . 68
4.7 Short-period and phugoid mode responses . . . 73
4.8 Dutch roll mode responses . . . 75
4.9 Spiral mode responses . . . 77
4.10 Roll subsidence mode responses . . . 78
4.11 Spherical constraint forces . . . 81
4.12 Short-period mode responses with and without compensation . . . 83
4.13 Dutch roll mode responses with and without compensation . . . 85
4.14 Spiral mode responses with and without compensation . . . 87
4.15 Roll subsidence mode responses with and without compensation . . . 89
4.16 Short-period mode responses with a Morlet wavelet . . . 92
4.17 Dutch roll mode responses with a Morlet wavelet . . . 93
4.18 Simplified block diagram of the simulation . . . 95
4.19 Short-period response with $\mathbf{F_c^*}$ compensation including transmission delay . . . 96
4.20 Effects of friction on the short-period response with kinematic compensation . . . 97

5.1 T-tail model pitch frequency sweep response at 40 m/s wind speed (elevator input of 0.5 to 3.0 Hz) . . . 102
5.2 T-tail model yaw frequency sweep response at 40 m/s wind speed (rudder input of 0.5 to 3.0 Hz) . . . 103
5.3 ATI Mini45 load cell . . . 109
5.4 Modification to the gimbal yaw shaft . . . 111
5.5 Load cell lower attachment . . . 112
5.6 Load cell upper attachment . . . 112
5.7 Rig arm hole reinforcement . . . 113
5.8 Load cell wireless transmitter attachment . . . 114
5.9 Overview of rig modifications for load cell installation . . . 115
5.10 Exploded view of the modified assembly . . . 116
5.11 Load cell system incorporated into the manoeuvre rig . . . 117
5.12 Updated aircraft model gimbal . . . 118
5.13 Updated manoeuvre rig Graphical User Interface . . . 119
5.14 Load cell typical packet clock offset and delay . . . 120
5.15 Rig roll forced oscillation by hand for mass, inertia and friction parameter estimation 122
5.16 Rig pitch forced oscillation by hand for mass, inertia and friction parameter estimation 123

5.17 Rig yaw forced oscillation by hand for mass, inertia and friction parameter estimation 124

6.1 Feedback control used to suppress the Hawk's limit cycle oscillations 127
6.2 Frequency spectrum of the measured forces by the load cell 128
6.3 Frequency spectrum of the measured moments by the load cell 129
6.4 Static Hawk rudder ramp at zero attitude angles and at a wind speed of 30 m/s 130
6.5 Static Hawk aileron control effectiveness at wind speeds of 20 m/s and 30 m/s 132
6.6 Static Hawk elevator control effectiveness at a wind speed of 30 m/s 133
6.7 Static Hawk rudder control effectiveness at a wind speed of 30 m/s 134
6.8 Static Hawk pitch aerodynamic stiffness measured at wind speeds of 20 m/s and 30 m/s135
6.9 Static Hawk yaw aerodynamic stiffness measured at a wind speed of 30 m/s 136
6.10 Static Hawk measured lift, drag and side force coefficient change due to elevator deflection at a wind speed of 30 m/s 137
6.11 Quasi-static measured force coefficients at a wind speed of 30 m/s 138
6.12 Change in angle of attack due to elevator deflection at a wind speed of 30 m/s and zero angle of sideslip 139
6.13 Hawk roll asymmetry observed in the measured rolling and yawing moment coefficients during the quasi-static pitch sweep test case at a wind speed of 30 m/s and zero angle of sideslip 140
6.14 Self-induced oscillation in aircraft heave as the aircraft pitch rate feedback gain is reduced 142
6.15 Amplitude, frequency and phase difference variation of the angle of attack and pitch angle as a function of pitch rate feedback gain (k_q) 143
6.16 Amplitude, frequency and phase difference variation of the rate of change of angle of attack and pitch rate as a function of pitch rate feedback gain (k_q) 144
6.17 Hawk longitudinal 2-DOF aircraft pitch and rig pitch forced oscillation test for the estimation of dynamic derivatives 145
6.18 Amplitude, frequency and phase difference variation of the angle of attack and pitch angle as a function of compensator elevator input frequency 146
6.19 Amplitude, frequency and phase difference variation of the rate of change angle of attack and pitch rate as a function of compensator elevator input frequency 147
6.20 Comparison between measured friction and friction modelled by Equation 3.119 . . . 148
6.21 Comparison between measured and simulated 2-DOF Hawk pitch and rig pitch test for parameter estimation 149
6.22 Limit cycle oscillation suppression on the Hawk model using the controller defined in Equation 6.6 with $K_{q_m} = 0.15$ 151
6.23 Stall hysteresis observed on the Hawk aircraft model 154
6.24 Schematic of the stall hysteresis observed on the Hawk aircraft model 155
6.25 Self-induced oscillations in aircraft model roll and yaw on the manoeuvre rig 159

7.1 Preliminary feedback controller for rig inertia and aerodynamic compensation 163
7.2 Preliminary experimental and computational simulation comparison for rig inertial and aerodynamic compensation 164
7.3 Open loop aircraft response to a damped doublet elevator input 166
7.4 Aircraft response to a damped doublet elevator input with proportional feedback for rig inertial and aerodynamic compensation 167
7.5 Effect of second on low pass Butterworth filter cut-off frequency on compensation response 169
7.6 Delay caused by a second order low pass Butterworth filter 170
7.7 Frequency content of the measured tangential reaction force (R) 171
7.8 Aircraft response to a damped doublet elevator input with proportional and derivative feedback for rig inertial and aerodynamic compensation 172
7.9 Aircraft response to a damped doublet elevator input with proportional and integral feedback for rig inertial and aerodynamic compensation 173
7.10 The feedforward and feedback controller used for rig compensation 174
7.11 Tangential reaction force responses to sine wave aircraft elevator input with rig feedforward compensation gains K_{FF} of (a) 0, (b) -0.5, (c) -1, (d) -1.5, (e) -2, (f) -2.5, (g) 3, and (h) -3.5 175
7.12 Change in the amplitude of aircraft's angle of attack due to compensator feedforward amplitude 176
7.13 Responses to aircraft elevator sine wave input with rig compensation controller having feedforward and feedback proportional gains K_P of (a) 0, (b) 1, (c) 2, (d) 3, (e) 4, and (f) 5177
7.14 Responses to aircraft elevator sine wave input with rig compensation controller having feedforward and (a) PI feedback, and (b) PID feedback 178
7.15 Responses to aircraft elevator damped doublet input with feedforward and feedback control for rig inertia and aerodynamic compensation (zero reaction force demand) . . 179
7.16 Experimental kinematic compensation for the Hawk model by demanding a tangential reaction force of $\mathbf{F}_\mathbf{c}^*$ 183
7.17 Simulated ideal kinematic compensation for the Hawk model 184

8.1 Possible method to measure drag created by the link connecting the load cell to the aircraft model 191
8.2 Possible method to measure aerodynamic interference caused by the link and aircraft cut-out 191

C.1 Surface plot for the Hawk model lift 208
C.2 Surface plot for the Hawk model drag 209
C.3 Surface plot for the Hawk model pitching moment 209

D.1 Compensator control surface actuation responses 212

D.2 Hawk control surface actuation responses 213

E.1 Drawing of the different load cell positions considered for the manoeuvre rig 216

NOMENCLATURE

Roman Symbols

$\bar{q}$	Dynamic pressure
$\ddot{\boldsymbol{q}}$	Linear and rotational accelerations vector
$\ddot{\boldsymbol{R}}$	Vector of linear accelerations
$\overline{\boldsymbol{F}}_{\boldsymbol{\theta}}$	Vector of external moments
$\boldsymbol{C}(\boldsymbol{q}, t)$	Vector of constraint equations
$\boldsymbol{Q}_C$	Vector created as a result of differentiating the constraint equation twice with respect to time
$\boldsymbol{Q}_E$	Combined external forces and moments vector
$\boldsymbol{R}$	Global position vector of a body
$\boldsymbol{v}$	Axis of rotation vector
$\boldsymbol{Q}_{\boldsymbol{R}}$	Vector of external forces
$\ddot{x}$, $\ddot{y}$, $\ddot{z}$	Inertial axes linear accelerations
$\dot{\overline{p}}$, $\dot{\overline{q}}$, $\dot{\overline{r}}$	Body axes rotational accelerations
$\mathbf{F}_{\mathbf{c}}^{*}$	Tangential reaction force required for kinematic compensation
$\mathbf{F}_{\mathbf{c}}^{**}$	Tangential reaction force required for kinematic compensation and artificial thrust
$\overline{\boldsymbol{u}}$	Position vector of a body in the body axes frame of reference
$\overline{G}$	Quaternion transformation matrix
$\overline{I}_{ab}$	Aircraft inertia about axis ab
$\overline{m}$	Mass of a component
$\overline{M}_x$, $\overline{M}_y$, $\overline{M}_z$	Body axes moments

A Transformation matrix

a Speed of sound

AR Aspect ratio

b Reference wing span

c Reference chord length

C_D Non-dimensional coefficient of drag

C_L Non-dimensional coefficient of lift

C_l, C_m, C_n Non-dimensional coefficients of rolling, pitching and yawing moments

C_q Constraint Jacobian matrix

C_Y Non-dimensional coefficient of side force

e Oswald's efficiency factor

F_x, F_y, F_z Inertial axes forces

g Gravitational acceleration

I_i Identity matrix of size i

I_{xx}, I_{yy}, I_{zz} Moments of inertia about the x, y and z axes

K Controller gain

L Lift

l, m, n Rolling, pitching and yawing moment

M Mass and inertia tensor matrix

M_{fr} Friction moment

m_{RR} Mass matrix

n_z z acceleration as a factor of g

p,q,r Roll, pitch and yaw rotation rates respectively

Q_e External loads vector

Q_v Quadratic velocity vector

r Spherical/rig arm radius

S Reference surface area

T Thrust force

t Time

u, v, w Velocity perturbations in the x, y, and z directions respectively

V_0 Wind velocity

x, y, z Cartesian coordinates/translation perturbations

$x_{c.g.}$ x distance of the centre of gravity from the arm's rotation point

$z_{c.g.}$ z distance of the centre of gravity from the arm's rotation point

$\overline{I}_{\theta\theta}$ Inertia tensor matrix

Greek Symbols

α Angle of attack

β Angle of sideslip

$\ddot{\boldsymbol{\theta}}$ Vector of rotational accelerations

$\boldsymbol{\lambda}$ Lagrange multiplier

$\boldsymbol{\omega}$ Rotational velocity vector

$\overline{\boldsymbol{\omega}}$ Aircraft body axes rotational velocity vector

$\boldsymbol{\theta_q}$ Quaternions vector representing rotation

δ_a, δ_e, δ_r Aileron, elevator and rudder deflections

γ Flight path angle

γ Rotation angle

ϕ^i, θ^i, ψ^i Roll, pitch and yaw Euler attitude angles

ρ Air density

θ_s, ϕ_s Spherical coordinates: inclination and azimuth angles

CHAPTER 1

INTRODUCTION

The prediction of aerodynamic characteristics, stability, and flying qualities are essential to the design of an aircraft; these predictions allow manufacturers to make informed decisions during the early stages of the design process. The data gathered are also used for the design and development of aircraft control laws, as well as for the study of aircraft loss-of-control and recovery. Many methods exist to measure these properties, ranging from full-scale aircraft testing to subscale model testing in wind tunnels. Computational Fluid Dynamics methods also exist and widely used to complement experimental data. Each testing technique has its own advantages and drawbacks. Testing of full-scale aircraft would provide the most accurate of data, however, the expenses associated with such testing are relatively the largest, and generally occur towards the end of an aircraft's design process. Wind tunnel testing techniques have proved to be a more cost-effective alternative when it comes to the gathering of the same kind of data. With dynamic scaling of wind tunnel aircraft models, it is possible to extrapolate findings to the full-scale aircraft in order to make meaningful comparisons. Another advantage of wind tunnel testing is the much higher repeatability of experiments due to the controllability of testing conditions.

Conventional static and dynamic wind tunnel testing have been a staple technique for the measurements of aerodynamic characteristics. Unconventional types of dynamic rigs have been developed throughout the world that are capable of motion in a variety of degrees-of-freedom (DOF). The novel manoeuvre rig developed at the University of Bristol is one such rig. The rig places the aircraft model at the front end of an arm. Two rotation gimbals (one for the arm and another for the aircraft model) provides a total of five degrees-of-freedom for the aircraft model: roll, pitch, yaw, heave, and sway. The rig and aircraft model are outfitted with a multitude of sensors capable of measuring attitudes, rates, and accelerations. This rig is unique in the sense

that it has an aerodynamic compensator attached to the rear of the rig which can be used to impart moments onto it. As a result, the compensator can be used to drive motion of the aircraft similar to conventional dynamic tests, or to compensate for rig effects.

The concept of the manoeuvre rig was created with two main end goals in mind. First, the rig will have the capability of performing large amplitude dynamic tests, and second, it will also have the capacity to perform free-flight manoeuvres within the wind tunnel. The former has successfully been achieved through the work done by Pattinson and Araujo-Estrada [10, 11]. Investigations of the later idea have been initiated by Araujo-Estrada by demonstrating multi-DOF motion of a subscale Hawk model on the manoeuvre rig. Suggested requirements for performing free-flying manoeuvres were also stated; these highlight the importance of understanding and negating the effects the rig has on the motion of the aircraft model.

The work presented in this thesis aims to further extend the investigations into performing free-flight manoeuvres on the rig. Extensive studies of the effects applied by the kinematic constraint created by the manoeuvre rig are performed using computational simulations. A concept to compensate for these effects are presented. Experimental demonstrations of free-flight responses of a subscale BAe Hawk model in the longitudinal sense will also be performed. Furthermore, additional new capabilities of the manoeuvre rig as a result of the implementation of a load cell are also presented. The results of this work have demonstrated the viability of the manoeuvre rig as a very capable, all-round testing platform for the gathering of aerodynamic data of aircraft models and performing free-flight manoeuvres.

The next chapter will present a survey of the literature base in relation to experimental aircraft testing techniques.

CHAPTER 2

LITERATURE REVIEW

2.1 Introduction

This chapter presents the survey of the literature on the various experimental tools and techniques available today for the study of aircraft aerodynamics and mechanics. Special interest is given to techniques used to perform or simulate free-flight manoeuvres within a wind tunnel.

Section 2.2 presents a summary of conventional experimental testing techniques used for the collection of aerodynamic data. Section 2.3 covers the importance of dynamic scaling of wind tunnel models in order to make meaningful comparisons between the subscale wind tunnel model data and that of full scale aircraft. Section 2.4 gives an overview of current multi-degree-of-freedom rigs used for aerodynamic testing. Section 2.5 presents the current research for simulating aircraft manoeuvres within a wind tunnel. Section 2.6 summarises the current state of the manoeuvre rig developed at the University of Bristol. This is followed by Section 2.7 which gives a brief introduction to aircraft loss-of-control research. Finally, the motivation behind the work here and main objectives are presented in Section 2.8.

2.2 Traditional experimental testing techniques

Wind tunnel and free-flight testing of sub-scaled models have been used for many decades to study their aerodynamics and motion characteristics, as well as to extend that knowledge onto the full-scale of aircraft. Together with Computational Fluid Dynamics (CFD), these investigations help ensure the predictability of the aircraft behaviour and hence its safety. Furthermore, it increases the efficiency and effectiveness of the aircraft's designed mission before full-scale flight tests.

Wind tunnel tests can be divided into two categories: static and dynamic tests. Static tests are the simpler of the two; this involves placing a model (which can range from aerofoil sections to sub-scale aircraft models) in an oncoming air stream inside a wind tunnel and measuring the aerodynamic forces and moments with the use of a load measuring device. Dynamic tests, on the other hand, cover a broader range of test types which traditionally include captive wind tunnel tests, 1-DOF wind tunnel tests, free-flying wind tunnel tests and atmospheric free-flying tests [6].

Captive wind tunnel tests include rotary balance and forced oscillation type tests. Note that in these types of tests, the model motion is driven by some mechanism. Rotary balance tests are used to measure an aircraft's damping derivatives, as well as predicting and modelling spins for simulations [6, 12–14]. The rotary balance rig can also be used to perform high angle of attack manoeuvres such as velocity vector roll [15]. Forced oscillation tests can be used to measure damping and stiffness derivatives by oscillating the model in various motions (such as sine waves or frequency sweeps) and measuring the resulting aerodynamic loads [15–18].

1-DOF wind tunnel testing uses a rig capable of either free or forced oscillations about a specific axis such as the free-to-roll [19] and free-to-pitch rigs [20]. Free oscillation techniques are primarily used to test unsteady and nonlinear aerodynamic effects [6] as well as to estimate dynamic stability derivatives by measuring the motion responses of models.

Free-flying wind tunnel tests can be further divided into free-flying tests, free-spin tests, free-fall and free-tumble tests [6]. Free-flying tests are essentially powered remote controlled model aircraft (dynamically scaled) fitted with control surface actuators and fitted with telemetry to gather air and motion data. This can be used to assess flying qualities and the effectiveness of control laws while using hardware and software-in-the-loop systems [6, 21, 22]. Free-spin, free-fall, and free-tumble tests are carried out in vertical wind tunnels to assess attitude motions, trajectories, and recovery procedures as the aircraft enters regions of the flight envelope where loss of control occurs [6, 22].

Lastly, there are atmospheric free-flying tests which include model drop tests (done using a helicopter) and using Unmanned Aerial Vehicles (UAV), which can be both remotely piloted or autonomously controlled [6]. These types of tests are essentially conducted to gain more reliable information prior to running full-scale flight tests which are inherently costly and involve high risk.

For all wind tunnel tests, except for free-flying tests, aerodynamic interference with the model support system and tunnel boundary are of concern and is commonly given priority when designing test rigs [22]. Corrections for tunnel blockage also need to be applied. In general for all subscale aircraft models, meeting all scaling criteria required for full-scale aircraft comparison is often challenging.

All these testing techniques are used to gather aerodynamic data either through direct load measurement or system identification from measurements of motion for the modelling of aircraft aerodynamics. They can then be used for a multitude of purposes such as aircraft design,

assessment of handling qualities, and control law development.

2.3 Dynamic scaling of test models

Atmospheric free-flight and wind tunnel tests of sub-scale aircraft are conducted to gain knowledge on the aerodynamic characteristics and motion behaviour of the full-scale aircraft. In order for this to be done, similitude requirements exist and must be achieved between the sub-scale and full-scale aircraft in order to extrapolate the understanding gained from sub-scale tests and predict the behaviour of full-scale aircraft.

These similitude requirements are in the form of scaling parameters that must be the same for both the full-scale and reduced scaled aircraft. These scaling parameters are derived by dimensional analysis of forces and moments [23] and can be categorised for static and dynamic type tests. For static wind tunnel tests, the similitude parameters used are Reynolds number, Mach number, control surface deflections, and aircraft attitude relative to the wind (α, β). For dynamic tests, the similitude parameters used in addition to those used in static tests are reduced angular velocity, Strouhal number (reduced oscillation frequency), reduced linear acceleration, reduced angular acceleration, Froude number, relative density, relative mass moments of inertia, and reduced-time parameter. Several similitude parameters also exist which are used for aeroelasticity similarity, but these are not conventionally used for flight dynamics/aerodynamic testing; both the sub-scale and full-scale aircraft are considered as rigid bodies.

For both static and dynamic testing, it is very difficult, if not impossible, to simultaneously satisfy all similitude parameters mentioned above. Instead, certain parameters are prioritised for matching to full scale based on the type of test conducted and the aerodynamic characteristics that are of interest for a given specific case [6]. For example, in low speed static tests, the Mach number is not important and the effects of Reynolds number may also be ignored if the flow separating location is fixed on the lifting surface on both the sub-scale and full-scale aircraft. When compressibility effects are of concern, then Mach number similarity is given priority. Similarly, for subscale free-flight dynamic tests, it is difficult to accurately scale the inertia together with the mass requirement. Instead, the inertia ratios are matched such that the inertial coupling between axes are captured. However, the rotational velocity due to this coupling is still not representative of the full-scale aircraft. By convention, for free-flight testing, the main similarity parameters used are the Froude number, relative density factor, and relative mass moment of inertia. For specific dynamic wind tunnel tests such as 1-DOF free oscillation tests, inertial coupling similarity is inherently not required. In fact, the single axis rotational inertial scaling can also be neglected and full-scale motion can still be accurately predicted [6].

For regions of the flight envelope where the aerodynamics are linear, mismatch in similarity parameters may be tolerated and still give acceptable predictions for the full-scale aircraft. However, in regions where the aerodynamics become highly nonlinear (flow separations), the

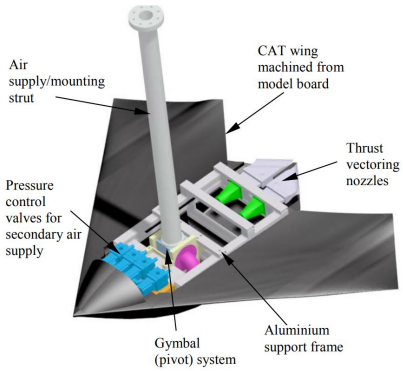

FIGURE 2.1. 2-DOF model developed at the University of Manchester capable of motion in roll and pitch [1].

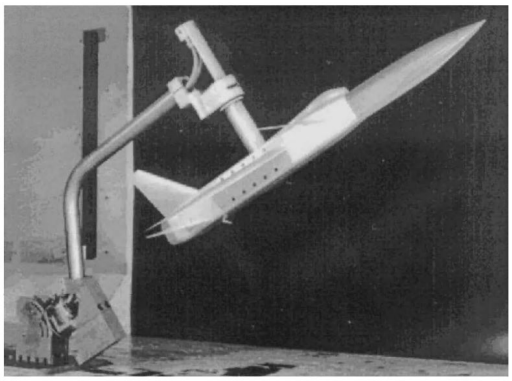

FIGURE 2.2. 2-DOF model developed at the University of Cambridge capable of motion in roll and yaw [2].

full-scale prediction uncertainty is high and is still a problem for experimental testing methods [6].

2.4 Multi-Degree-Of-Freedom wind tunnel test rigs

Bulding upon the free-oscillation 1-DOF test rigs, many rigs have been designed and constructed to allow motion in multiple degrees of freedom. For example, the 2-DOF model developed at the University of Manchester is capable of rotation in roll and pitch (see Figure 2.1), which has been used for studying flow control systems [1]. Another example is the rig designed at the University of Cambridge capable of rotation in roll and yaw (see Figure 2.2) which has been used for control law development [2]. 3-DOF rigs have also been conceived capable of roll, pitch, and yaw motions, and have been used, for example, the rig created at the University of Bristol for parameter estimation of static and dynamic stability derivatives for a model aircraft (see Figure 2.3) [3].

One issue with estimating the stability derivatives using any of the above rigs is that it is impossible to separate some derivatives, for example, the pitch damping derivatives: C_{M_q} and $C_{M_{\dot{\alpha}}}$ due to the lack of translational motion. As a result, rigs such as the 4-DOF rig created at Cranfield University are designed to also facilitate heave motion (see Figure 2.4) [4].

Pendulum type rigs have also been developed capable of up to 5-DOF motion where the additional translation motions are approximate sway and fore-aft motions [24, 25]. This technique has been successful in estimating the longitudinal stability and control derivatives for a test model [25] and studying unsteady aerodynamic phenomena such as limit cycles [26, 27]. This rig was modified to also include heave motion (to give full 6-DOF capability), but was unsuccessful due to significant frictional effects [10]. This lead to the conception of a novel 5-DOF rig at the University of Bristol called the “manoeuvre rig”. More detail on this rig is presented in Section

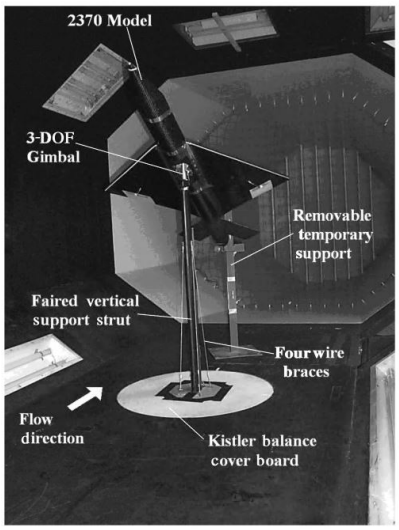

FIGURE 2.3. 3-DOF rig developed at the University of Bristol capable of motion in model roll, pitch, and yaw [3].

FIGURE 2.4. 4-DOF rig developed at Cranfield University capable of motion in model roll, pitch, yaw, and heave [4].

2.6. Both the pendulum rig and the manoeuvre rig concepts at the University of Bristol was conceived by Prof. Mikhail Goman, and further work was conducted in collaboration with him.

Rigs capable of full 6-DOFs also exist such as the Stewart platform rigs [28] or the Model Positioning Mechanism (MPM) (see Figure 2.7), which are based on the parallel kinematic concept [7]. However, these rigs typically have a limited working space, reduced stiffness at some locations of the workspace in a certain direction, and the rig itself can be large in size. The MPM is able to simulate realistic flight manoeuvres. Multi-DOF rigs used to perform virtual flight tests are discussed in Section 2.5.

2.5 Manoeuvre simulation

Apart from full-scale aircraft flight tests, remotely controlled subscale models are used to perform free-flight manoeuvres to assess handling qualities and response characteristics that otherwise cannot be obtained from conventional static and dynamic wind tunnel tests. Models are manufactured to either be flown in the atmosphere or within the wind tunnel. One such example of an aircraft model designed for atmospheric flight is the AirStar project developed at NASA Langley Research Center [5]. The AirStar model is a dynamically scaled generic airliner unmanned aircraft equipped with telemetry for remote control capability and instrumentation for taking measurements (see Figure 2.5). Unlike many subscale free flight models, it is powered and therefore flies to and from a runway - rather than being of the drop-model type. It has been

FIGURE 2.5. The AirStar dynamically scalled UAV testbed [30].

FIGURE 2.6. Free-flying wind tunnel model of a Blended Wing Body aircraft [6].

used for the development of control laws and for the research of aircraft loss-of-control. Research on aircraft loss-of-control is presented in Section 2.7.

Subscale aircraft models are also designed for unconstrained flight within a wind tunnel. An example is the free-flying model testing carried out at NASA Langley Research Center (see Figure 2.6) [6, 29]. Such models generally require a large wind tunnel to perform manoeuvres with several pilots to control it. Their thrust is usually produced by pressurised air passed through a tether. Good representation of full-scale manoeuvres can be obtained using this technique, and has been used for the assessment of stability, controllability and flying qualities.

Apart from unconstrained subscale free-flying models, unconventional rigs have been developed with the goal of performing realistic flight manoeuvres. The following are examples of such rigs.

The Model Positioning Mechanism (MPM) is a 6-DOF wind tunnel test rig developed at the German-Dutch Wind Tunnels (see Figure 2.7) [7, 31, 32]. The rig consists of six struts that can be controlled individually using six linear motors. It is capable of producing accelerations up to 2.5g, and has accuracy in attitude of 0.005°. The maximum possible angle of attack attained on this rig is 30°, but this can be higher depending on the mounting position of the aircraft model. This rig has successfully performed dynamic oscillatory tests in roll, pitch, and yaw, and has the capability of performing realistic manoeuvres such as Dutch roll and a 2g pull up manoeuvre. Note that the motion of the model in the wind tunnel is not exactly "free"; the virtual simulations are performed by first starting at trim conditions, with the forces and moments due to control surface deflections then measured. These loads are then used to calculate freestream conditions such as angle of attack and sideslip using real-time flight-mechanics

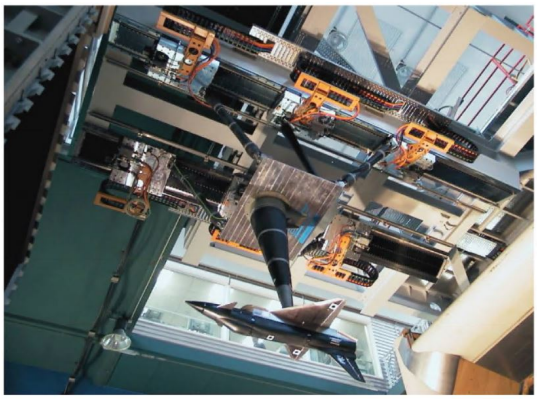

FIGURE 2.7. The 6-DOF Model Positioning Mechanism [7].

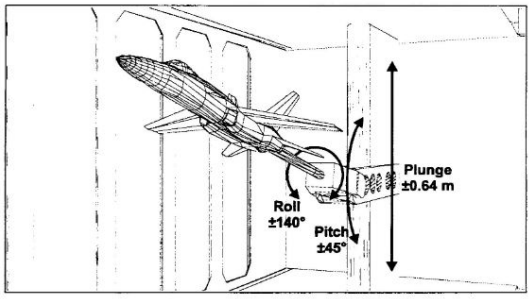

FIGURE 2.8. The 3-DOF Dynamic Plunge-Pitch-Roll rig [8].

FIGURE 2.9. The Georgia Tech. 3-DOF traverse rig [9].

calculations and then move the physical model to match those states. This process repeats in a continuous loop. Therefore, the model's physical motion may not match true flight; its motion is calculated virtually through the computational simulation. Another rig that performs similar pre-programmed manoeuvres is the 3-DOF Dynamic Plunge-Pitch-Roll (DyPPiR) rig developed at the Virginia Polytechnic Institute and State University (see Figure 2.8) [8]. Again, the trajectory of the aircraft is pre-calculated and forced using actuators, and the resulting aerodynamic loads measured which are used to recompute its trajectory. The DyPPiR rig is capable of pitch motion in a $\pm 45^{\circ}$ range, roll motion in a $\pm 140^{\circ}$ range, and plunge ± 0.64 m range. This technique is also knows as captive trajectory testing or Virtual Flight Testing (VFT) which has been used for weapons testing and the assessment of flight characteristics [33–39]. Some publications also refer to this technique as "hardware-in-the-loop simulations", where the trajectory of the aircraft is predicted experimentally [22, 40, 41].

A 3-DOF traverse rig has been developed at the Georgia Institute of Technology (see Figure 2.9) [9, 42]. The three available DOFs are bank, heave, and pitch. As a result, the rig allows

for the "true" physical simulation for the longitudinal dynamics of an aircraft model, unlike the MPM system which calculates the aircraft trajectory virtually. Force and moment sensors are used in feedback control to actively alter the aircraft properties such as weight, inertia and translation friction, thus altering the dynamics characteristics of the aircraft model. The loads are transferred onto the model using linear actuators and springs. This rig has been used for the study of flow control techniques using an aerofoil model [43–45].

2.6 The manoeuvre rig

The manoeuvre rig is a novel 5-DOF wind tunnel test rig developed at the University of Bristol, and has been in continuous development ever since its conception in 2010 [10]. An overview of the rig is shown in Figure 2.10. The manoeuvre rig is capable of a maximum of 5-DOFs for the aircraft: roll, pitch, yaw, approximate heave, and approximate sway. The latter two motions are provided by the pitch and yaw motions of the rig's arm. In fact, the rig has a total of six degrees of freedom provided by two 3-DOF gimbals, one for the arm and the other for the aircraft. The additional freedom is a redundant arm roll motion. This effectively decouples the rig and aircraft roll dynamics. Most motion freedoms of the rig can be locked to perform tests with lower DOFs [46, 47].

The rear of the rig is fitted with an aerodynamic compensator. It has four wings in a cruciform configuration, each with a control surface that can be commanded individually (driven by four servo actuators). This can be used to create forced rig motions or to attempt to compensate rig effects on the aircraft model response.

The rig is currently equipped with potentiometers to measure the attitude of the arm, encoders to measure the aircraft's attitude relative to the arm, and an Inertial Measurement Unit (IMU) to measure the aircraft's body axes accelerations and rotational velocities. The aircraft model currently being used (an approximation to a BAe System's Hawk, at 1/16th scale) contains 5 servo actuators for each of its control surfaces. All servos have been modified to allow control surface positions to be measured from the inbuilt potentiometers.

All servo commands and measurements taken are transferred (at 244 Hz) using a WiFi system to a remote computer station. This computer controls the rig using a GUI developed in Python together with Matlab and Simulink for fast prototyping of controllers.

A rig very similar to the manoeuvre rig has also been constructed in IIT Kanpur in India and has also been used for the identification of aircraft derivatives [48].

Compared to traditional techniques, the manoeuvre rig is capable of estimating stability and control derivatives of an aircraft using parameter estimation techniques. However, prior to this PhD there was no guarantee on the accuracy of these estimates as no direct measurement of aerodynamic loads has been done, nor any comparisons with free-flight data. The manoeuvre rig has the added benefit that it may perform free as well as forced motions using its aerodynamic

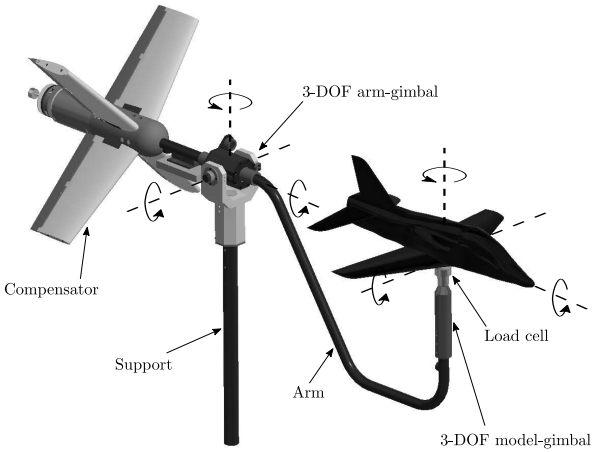

FIGURE 2.10. The manoeuvre rig.

compensator.

Next, the research that was conducted on the manoeuvre rig before the start of this PhD is outlined. The manoeuvre rig was originally developed with two key motivations in mind: the first being that it would be capable of allowing large amplitude dynamic tests similar to actual free-flying tests, and the second being that it could be used as a platform for developing and prototyping control laws. The subscale BAe Hawk model has been the main subject for testing since the inception of the manoeuvre rig. This model has exhibited an unsteady longitudinal limit cycle oscillation in pitch, which has been investigated in References [49, 50]. The tests were carried out in a quasi-static sense where the Hawk model was free only in pitch and a slow ramp elevator input was given to sweep the aircraft in pitch. This aircraft pitch oscillation is also present when the model is free to heave as well (by unlocking the rig in pitch).

The cause of the limit cycle has been suggested to be related to dynamic stall on the wings, however the actual cause is still uncertain. Flow visualization experiments (China clay, tufts and smoke) done in Reference [51] showed possible interaction of the wing wake with the tailplane affecting pitch damping. Asymmetry between the wings was also observed. The left wing of the Hawk model is in fact longer that the right due to manufacturing errors, since the model was handmade. Reference [47] further extends the investigation of the limit cycle and discovered that it also has a lateral-directional component coupling into oscillations in aircraft roll and yaw.

A more recent study done with the same equipment in Reference [52] further investigated the asymmetry by observing the onset of Hawk model's roll and yaw motion. The research also discovered static hysteresis at stall on the Hawk model once the limit cycle is stabilised, which was theorised to be linked with the observed asymmetry. The experiments were carried out in a similar quasi-static sense, where a slow ramp elevator input is given to the Hawk model with the manoeuvre rig free to move in pitch and aircraft model free to move in roll, pitch, and yaw made possible by its 3DOF aircraft gimbal. As the manoeuvre rig did not then have the capability

of directly measuring lift, instead the normal force was estimated from its relationship with the rig's pitch angle, since the aircraft forces are in balance with the forces created by the rig's aerodynamic compensator. It has been suggested that since the aircraft model has freedom in heave due to the pitching motion of the rig, the motion and aerodynamics of the model may be more relatable to that of an actual free-flying aircraft model. As the aircraft model on the rig is effectively "floating", it is also more isolated from vibrations caused by a rigid support structure which may affect sensitive or fragile flow mechanisms such as air flow separation and reattachment. Note that all these studies were solely based on the motion the aircraft model and fitting mathematical models onto those responses. No direct aerodynamic force or moment measurements of the Hawk model had been carried out on the rig.

The manoeuvre rig has also been used for system identification studies, as presented in References [11, 53]. The stability and control derivatives of the Hawk model, as well as the inertial and aerodynamic properties of the rig itself, were estimated by fitting free and forced motion responses onto a mathematical model using techniques such as Equation Error Method and Output Error Method. Note that by the nature of the mathematical model used, the coefficients of drag could not be estimated; this is due to the modelling approach, which considers the total moment created about the rig's centre of rotation, contributed by the rig's compensator and the aircraft model. It was assumed that for small rig attitude angles the moment contribution by drag is negligible relative to the moment due to lift, due to a small moment arm. The validity of this assumption was not investigated.

Due to approximate translational motions being possible on the manoeuvre rig, it has the capability to differentiate between aerodynamic derivatives such as C_{M_q} and $C_{M_{\dot{\alpha}}}$. This has been attempted in Reference [53]. Note that the previously mentioned modified pendulum rig [10] attempted translation motion by making the model translate vertically along a cable; this was unsuccessful however due to friction.

Rig roll compensation has also been successfully implemented, where the aim was to use the aerodynamic compensator to follow a commanded aircraft roll rate such that the aircraft's gimbal physical limits are not reached [11, 54]. Since the aircraft gimbal has it's own roll DOF, the roll inertia of the rig is decoupled from that of the aircraft model. The capability of the manoeuvre rig system in aiding the design of aircraft control laws was also demonstrated by designing an aircraft controller to achieve a steady roll rate. A maximum continuous roll rate of about $330°/s$ was achieved for the Hawk model, limited by the rate at which the compensator can roll the arm.

2.6.1 Advantages of using the manoeuvre rig for free-flight simulation

With regards to using the manoeuvre rig in performing free-flight responses, there are several advantages in comparison with an actual free-flying model. The first is that the manoeuvre rig requires a much smaller wind tunnel working section to operate such as the 7'x5' tunnel at the University of Bristol, whereas a free-flying wind tunnel model needs a much larger working

section to accommodate for possible large model translations, such as the 22'x14' tunnel at NASA Langley Research Center. UAV type free-flying models of course require an airfield in order to perform tests, such as the AirSTAR Project [5]. Performing tests in a smaller wind tunnel with the manoeuvre rig also implies lower operating costs. UAV type models also require much more extensive sensors, telemetry, and supporting equipment which are also expensive.

Secondly, the aircraft model used on the manoeuvre rig does not need to produce thrust since the constraint provided by the rig's arm applies a component of thrust as a reaction force. As a result, the testing of subscale aircraft models used in conventional wind tunnel testing which generally do not produce thrust is also possible on the manoeuvre rig.

Thirdly, the rig can be used to modify the effective weight of the aircraft model by applying a roughly constant vertical force acting through the aircraft's centre of gravity using the rig's compensator. This has the benefit of relieving the model manufacturing target weight requirement in order to achieve Froude similitude.

Fourthly, it is possible to use the manoeuvre rig to modify initial conditions of the aircraft model. For a free-flying model, the model response always has to start at trim conditions whereas on the manoeuvre rig, the model control surface deflections can be set to any off-trim point but still held at the centre of the wind tunnel (or some other desirable position) within the wind tunnel before it is "released".

In addition, the manoeuvre rig offers other testing capabilities such as forced oscillation tests which cannot be performed using a free-flying model. This makes the manoeuvre rig a much more versatile testing platform for model aircraft.

2.6.2 Dynamic scaling on the manoeuvre rig

Section 2.3 described the various similitude parameters available to make meaningful comparisons with the subscale aircraft model and the full-scale aircraft. As mentioned before, it is nearly impossible to match all similitude parameters. For static tests, the main scaling parameters of interest are the Reynolds number and Mach number. They can be expressed as:

$$\text{Reynolds number} = \frac{\text{Inertial force}}{\text{Viscous force}} = \frac{\rho V_0^2 c^2}{\mu V_0 c} = \frac{\rho V_0 c}{\mu} \tag{2.1}$$

$$\text{Mach number} = \frac{\text{Inertial force}}{\text{Pressure force}} = \left(\frac{\rho V_0^2 c^2}{\rho a^2 c^2}\right)^{1/2} = \frac{V_0}{a} \tag{2.2}$$

A match in these parameters are required for a similar airflow field around the model, which will result in the match in force and moment coefficients between the subscale and full-scale aircraft. However, it is difficult to match these parameters. Differences in Reynolds number may be tolerated if the aerodynamics are linear and the separation point is known and fixed on the surface of the model using boundary layer trips/wires or rough grit. A correction to the skin

friction drag coefficient can also be applied which is also affected mainly by Reynolds number [55]. Since the manoeuvre rig is limited to low speed testing, compressibility effects cannot be replicated.

Dynamic similarity ensures that the motion of the subscale model can be compared with the full-scale aircraft. This includes their attitudes, velocities, and accelerations. To achieve this, two additional parameters are required to be matched: Froude number and mass ratio. They are expressed as:

$$\text{Froude number} = \frac{\text{Inertial force}}{\text{Weight}} = \frac{\overline{m}V_0^2/c}{\overline{m}g} = \frac{V_0^2}{gc} \tag{2.3}$$

$$\text{Mass ratio} = \frac{\text{Inertial force}}{\text{Aerodynamic force}} = \frac{\overline{m}V_0^2/c}{\rho V_0^2 c^2} = \frac{\overline{m}}{\rho c^3} \tag{2.4}$$

The concept of mass ratio is the same for mass distribution and aerodynamic moments resulting a moment of inertia similitude requirement. in Table 2.1 compares the similitude parameters between the full-scale Hawk aircraft and the subscale model currently being used on the manoeuvre rig (at mean sea level conditions). Note that the full-scale mean aerodynamic chord was estimated from the subscale model, and the mass of the fullscale aircraft was obtained from Reference [56] (HS 1182 A variant was chosen as an example). A full-scale airspeed of $80m/s$ was chosen by Reference [10] as the flight condition based on Froude number scaling with a wind tunnel speed of $20m/s$. The current Hawk model being used on the manoeuvre rig is not dynamically scaled and is not representative of the actual Hawk aircraft. The comparison assumes the full-scale and subscale aircraft are geometrically identical, however, there are manufacturing defects on the subscale model (uneven wings) which will affect similarity. The subscale Hawk model itself is built from model aircraft plans and the exact differences relative to its true geometry are unknown. The manoeuvre rig has the advantage of being able to modify the effective mass of the aircraft model (using the rig's compensator), thus having the ability of achieving a match in mass ratio even with an incorrect aircraft model mass. For example, for the current Hawk model's mass of $1.97kg$, applying a constant upward reaction force of $7.87N$ will reduce the mass ratio to 326, thereby matching the full-scale aircraft. However, this correction does not affect the mass distribution and therefore the inertia of the aircraft model will be unchanged.

2.7 Aircraft loss-of-control

Aircraft loss-of-control (LOC) is defined qualitatively by Wilborn and Foster [57] as motion which is "outside the normal operating flight envelope; not predictably altered by pilot control; characterized by nonlinear effects, such as kinematic/inertial coupling, disproportionately large responses to small static variables, or oscillatory/divergent behaviour; likely to result in high

TABLE 2.1. Similitude parameter comparison between the full-scale Hawk aircraft and 1/16 scale Hawk model (at sea level).

	Full-scale Hawk aircraft	**Current subscale Hawk model**
Mean aerodynamic chord (m)	2.29	0.143
Mass (kg)	4795	1.97
Speed (m/s)	80	20
Reynolds number	1.25×10^7	2×10^5
Mach number	0.23	0.087
Froude number	285	285
Mass ratio	326	550

angular rates and displacements; characterised by the inability to maintain heading, altitude, and wings-level flight". LOC situations such as stall and spins are a major cause of aviation fatalities, as recovery from LOC is difficult. As a result, many studies have been conducted in an attempt to understand these aircraft behaviours and flight regimes. Figure 2.11 shows regions of the flight envolope at which LOC occurs. Methods of study include the use of subscale radio controlled models equipped with telemetry to measure air data, attitude and rotation rates, spin tunnel tests, rotary balance tests, and flight tests [58]. Flight tests inherently involve high risk and costs. Comparisons of sub-scale radio controlled model tests with full-scale aircraft have shown good agreement (effects of geometry changes, response to control, and recovery procedures) with the exception of Reynolds number effects [58]. UAV test platforms have been created such as the National Aeronautics and Space Administration's (NASA) Airborne Subscale Transport Aircraft Research (AirSTAR) project specifically with the goal of reducing accident rates caused by LOC [5].

The Simulation of Upset Recovery in Aviation (SUPRA) is another project investigating upset and upset recovery methods [59, 60]. Their aim has been to develop a wide-envelope airliner model by gathering data from wind tunnel testing combined with CFD methods.

2.8 Research motivation and objectives

The free-flying responses of an aircraft model are used for the measurement of stability derivatives, control law design and evaluation, assessment of flying qualities and performance, and for research into loss-of-control recovery [22]. When it comes to obtaining data regarding aircraft manoeuvres through wind tunnel testing, three methods exist: using unconstrained free-flying models, using Virtual Flight Testing (VFT) techniques, and through the use of a captive rig compensation method, as presented in Section 2.5.

The testing of free-flying models have been performed extensively at facilities such as at NASA Langley Research Center where good representation of full-scale manoeuvres were obtained [6, 29]. This type of testing generally requires a large section wind tunnel to accommodate

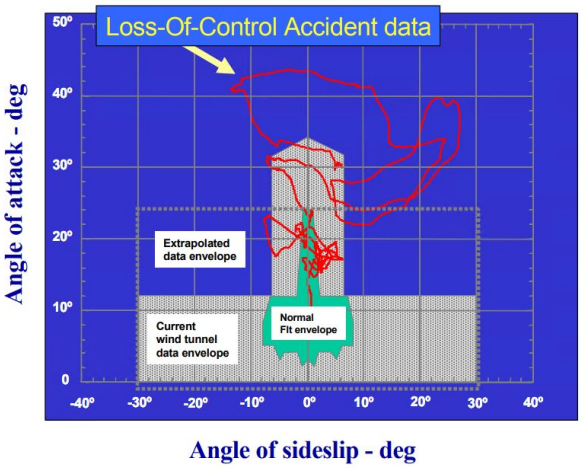

FIGURE 2.11. Regions of loss-of-control relative to an aircraft's normal operating flight envelope [5].

the model's motion. Accurate closed-loop control is required in order to perform the desired manoeuvres due to the high rates of motion. If the model is flown manually, multiple pilots are required to split the workload due to the same reason.

VFT techniques have also been largely used to simulate aircraft manoeuvre responses and trajectories. Although VFT is used to obtain free motion of the aircraft, most rigs produce these responses via digital calculations (hence the term "virtual"), and are not true physical responses. In indirect simulations, the model motion is forced such that flow conditions in the wind tunnel match that of the virtual simulation. The measured loads in the wind tunnel drive the digital simulation response which in turn drives the motion of the physical model. Direct simulations of the motion also exist where the model has full freedom to rotate (using low friction gas bearings, for example [61]), but its translation is fixed which is recreated digitally using force measurements [34]. As a result, there can be uncertainty as to whether the responses are truly representative of actual free motion. Differences between VFT and true free-flight due to the lack of translation capability of VFT were identified in Reference [62].

A rig capable of simulating true free-flying manoeuvres in the longitudinal sense exists [9]. This rig uses real-time feedback control to cancel the effects of the rig and even alter the model's dynamic characteristics. However, this rig is limited to longitudinal responses and only results for an aerofoil section model have been published to date.

As described in Section 2.6, the manoeuvre rig developed at the University of Bristol has previously been used for the identification of aerodynamic derivatives through 1-DOF and coupled multi-DOF rig motions, study of linear, nonlinear and unsteady aerodynamic phenomena, and the prototyping of control laws. With regards to the physical simulation of true free-flying motion, which was one of the goals for the rig on its conception, so far this has only been accomplished in roll with all other DOFs fixed [11, 54]. This was made possible by the modification of the aircraft

gimbal to also include aircraft roll, thus decoupling the rig's roll inertia from that of the aircraft model. The rig's compensator was then used to make the rig follow the aircraft's motion in roll, allowing for continuous motion. Note that when using a rig of this type, the aircraft model does not need to have the capability of producing its own thrust, therefore conventional models can be used for testing.

The work presented here aims to further extend the manoeuvre rig's overall capability as a testing platform for aircraft models, with particular focus on the novel concept of true physical simulation of free-flight motion in multiple degrees of freedom within a wind tunnel using the manoeuvre rig. Note that the terms "virtual" and "physical" flight testing will be used interchangeably in this work and will mean performing true free-flight responses on the manoeuvre rig. In achieving this goal, the manoeuvre rig can prove itself to be a viable alternative to free-flying wind tunnel model testing, or serve as a valuable intermediate stage, for the investigations into aircraft stability, controllability, and upset behaviour as well as aid in control law development. This work will focus on mitigating the effects the rig has the aircraft model's motion: mainly inertial, aerodynamic, and kinematic. It will be demonstrated that this can be achieved by controlling the reaction forces applied by the rig onto the aircraft (measured by a load cell that will be installed as part of this work) using the rig's aerodynamic compensator. The limitations of the rig in performing this task needs to be identified and what this entails for physical response simulation understood. These identified limitations can then be used to further improve the rig to meet its goals. The manoeuvre rig's physical flight simulation capability can then potentially be used for the study of upset conditions related to loss-of-control by simulating the onset conditions. With the implementation of a load cell on the manoeuvre rig, it will be seen that is also possible to perform conventional static and dynamic tests since the aerodynamic loads will be measured directly. The aerodynamic derivatives estimated in previous work via parameter estimation techniques can then be validated.

In support of the above aim for extending the capabilities of the manoeuvre rig, the objectives for this work are summarised as follows:

1. Development of the full nonlinear rigid-body equations of motion for the coupled rig/aircraft-model dynamics.

2. Identify the influence of kinematic effects of the rig on the aircraft model responses.

3. Implementation of a load cell

    a) Define load cell requirements.

    b) Rig physical modifications to accommodate the load cell.

    c) Software integration of the load cell with the current system.

    d) Re-estimation of rig mass and inertial properties.

4. Demonstration of the rig's new capability of performing conventional static and dynamic tests.

5. Additional applications of the manoeuvre rig in investigating stall hysteresis, and a new method for generating self-excited oscillations in aircraft roll and yaw.

6. Practical demonstration of rig inertial, aerodynamic and kinematic compensation for physical flight simulation.

2.9 Thesis structure

The structure of the thesis in describing the objectives defined in Section 2.8 is as follows.

Chapter 3 fulfills Objective 1. It initially presents a linear mathematical model for the manoeuvre rig, followed by the derivation of the full 3D nonlinear rigid-body model using differential and algebraic equations in the Newton-Euler form. The Lagrange multiplier method is used to mathematically describe constraints that arise from coupling the manoeuvre rig components together. Imaginary constraints are also defined and used to study the effects of kinematic constraints in Chapter 4. Various models used to define the aerodynamics of the rig and aircraft models are then presented. Models used to represent gimbal friction and servo actuator dynamics are also described.

Chapter 4 investigates Objective 2 where the nonlinear mathematical models described in Chapter 3 are used to study the effects of various kinematic constraints. Following this study, a concept for reducing the effect of a spherical constraint is presented by controlling the tangential reaction force applied by the rig. This concept requires the measurement of the reaction force between the aircraft model and rig, which requires a load cell.

Chapter 5 achieves Objective 3. It covers the process of implementing a load cell onto the manoeuvre rig which includes the estimation of the load cell requirements, selection of a load cell, modifications required to accommodate it, software integration, and rig inertia re-estimation. The equations of motion created in Chapter 3 are used to simulate the loads experienced by the load cell. Finite Element Analysis is performed when designing the attachment components. The inertia of the rig is estimated in a new way, using measurements from the load cell.

Chapter 6 achieves Objective 4 and 5. In this section, static and dynamic aerodynamic derivatives are measured with the newly implemented load cell. Measurement noise is also analysed. Following this, stall hysteresis, previously observed on the Hawk model, is investigated and additional insights are drawn using the load cell measured data. A method for producing self-induced oscillations in aircraft model combined roll and yaw is also presented and validated.

Chapter 7 achieves Objective 6 where the rig inertial and aerodynamic compensation as well as the kinematic compensation concept described in Chapter 4 are implemented and assessed. Several controllers are tested including simple proportional feedback control to PID feedback with

feedforward control. The results in terms of how well each controller performed are presented, along with discussions of their shortcomings and potential improvements.

Chapter 8 concludes this work by summarising the main findings. Suggestion for further improvements, areas of interest for investigation, and recommendations for future work are also presented.

CHAPTER 3

DEVELOPMENT OF EQUATIONS OF MOTION

3.1 Introduction

This chapter presents the development of the two sets of equations of motion for the manoeuvre rig which will be used for computational simulations. The first mathematical model is a linear longitudinal model. The second mathematical model consists of the nonlinear equations in the differential-algebraic form describing the rigid-body mechanics [63]. Within these equations, the aircraft model, the link between the load cell and the aircraft, the load cell, the rig arm, and the aerodynamic compensator are treated as five separate bodies so that modifications made to any component of the rig can be applied to the equations easily for each body. Each body is connected to each other via constraint equations which will also be discussed in this chapter. This method allows for the extraction of the reaction loads between components which has not been possible in previous models of the rig. The reaction loads between the aircraft model and the rig play a key role in the kinematic compensation concept derived in Chapter 4 and in the estimation of load cell requirements in Chapter 5. These constraints may also be applied to a single body alone, which is useful when investigating the kinematic effects the rig applies onto the aircraft model, as discussed in Chapter 4. External forces and moments such as aerodynamic loads are modelled separately and applied as point loads acting through the body's centre of gravity. This model was developed with the intent to define the reaction force between the manoeuvre rig and the aircraft model. This reaction force is used to investigate the influences the manoeuvre rig has on the motion of the aircraft model. The results of this study and the development of a compensation concept is presented in Chapter 4.

3.2 2D linear state-space mathematical model of the manoeuvre rig

This section presents a linear state-space model created for the manoeuvre rig in the longitudinal sense. It is used during the early stages of PhD to investigate rig inertia and aerodynamic effects on the aircraft model and to derive compensation feedback in order to negate these effects using the rig's compensator. This compensation was tested in preliminary experiments and is detailed in Chapter 4.

This modelling approach considers all forces and moments acting on a body are lumped together and act through their respective centres of gravity for simplicity. The actual points through which the lift act cannot be distinguished since the mathematical model cannot separate the moments caused by lift and the aerodynamic pitching moment itself. The mass of the rig includes both the masses of the compensator and the rig arm. This model is linearised about the equilibrium point when the rig's arm is horizontal and is only valid for small angle deviations since small angle approximations are made. This model also assumes the effects of the aircraft's centre of gravity offset from its gimbal rotation point are negligible. The model is created by deriving the rotational accelerations about the aircraft's and the rig arm rotation points. A diagram labelled with the main dimensions is shown in Figure 3.1. The subscripts 'r', 'c' and 'm' correspond to rig, compensator and aircraft model respectively. The aircraft model's pitching acceleration equation can be derived in terms of aircraft model pitch angle (θ_m) and rig arm pitch angle (θ_r) as

$$I_{yy_m}\ddot{\theta}_m = m_m \tag{3.1}$$

where I_{yy_m} is the aircraft model's pitching moment of inertia, θ_m the aircraft's pitch angle and m is the pitching moment. The equation for m can be obtained from Equations 3.100 and 3.107, where

$$\alpha_m = \theta_m - \frac{x_{c.g._a}\dot{\theta}_r}{V_0} \tag{3.2}$$

$$q_m = \dot{\theta}_m. \tag{3.3}$$

Similarly, the rotational acceleration about the arm's rotation point is derived as

$$\left(I_{yy_r} + \overline{m}_m {x_{c.g._m}}^2\right)\ddot{\theta}_r = x_{c.g._m}L_m - x_{c.g._c}L_c + z_{c.g._r}\overline{m}_r g\theta_r \tag{3.4}$$

where $\overline{m}$ is the mass, $x_{c.g.}$ is the x distance of the centre of gravity from the arm's rotation point, $z_{c.g.}$ is the z distance of the centre of gravity from the arm's rotation point, and L is the lift. The definition of L_m can be obtained from Equations 3.100 and 3.105 and the definition of L_c from Equations 3.100 and 3.108 where

$$\alpha_c = \theta_r \tag{3.5}$$

$$q_c = \dot{\theta}_r. \tag{3.6}$$

The $z_{c.g._r}\overline{m}_r g\theta_r$ term in Equation 3.4 is caused by the horizontal motion of the rig's centre of gravity due to its vertical offset from the arm's rotation point. Additionally, the vertical acceleration of the aircraft model as multiple of g (n_z) can be included in the output vector

$$n_z = \frac{x_{c.g._m}}{g}\ddot{\theta}_r \tag{3.7}$$

The equations derived above can now be written in the conventional state space form where $\dot{\boldsymbol{x}} = A\boldsymbol{x} + B\boldsymbol{u}$ is shown in Equation 3.8, and $\boldsymbol{y} = C\boldsymbol{x} + D\boldsymbol{u}$ is shown in Equation 3.9. The properties of the rig and aircraft used in this model were obtained previously using parameter estimation techniques [46, 53]. The mass and inertial properties of the each body, as well as their centre of gravity positions can be found in Appendix E. The aerodynamic coefficients for the Hawk model found using various techniques is presented in Tables 6.1 and 6.2. The aerodynamic coefficients for the compensator are presented in Appendix F.

$$\begin{pmatrix} \dot{\theta}_m \\ \ddot{\theta}_m \\ \dot{\theta}_r \\ \ddot{\theta}_r \end{pmatrix} = \begin{bmatrix} 0 & 1 & 0 & 0 \\ \frac{\bar{q}S_m c_m C_{m_{am}}}{I_{yy_m}} & \frac{\bar{q}S_m {c_m}^2 C_{m_{qm}}}{2V_0 I_{yy_m}} & 0 & -\frac{\bar{q}S_m c_m C_{m_{am}} x_{c.g.m}}{V_0 I_{yy_m}} \\ 0 & 0 & 0 & 1 \\ \frac{\bar{q}S_m x_{c.g.m} C_{L_{am}}}{I_{yy_r}+\bar{m}_m {x_{c.g.m}}^2} & \frac{\bar{q}S_m x_{c.g.m} C_{L_{qm}} c_m}{2V_0(I_{yy_r}+\bar{m}_m {x_{c.g.m}}^2)} & -\frac{\bar{q}S_c x_{c.g.c} C_{L_{ac}} - \bar{m}_r g z_{c.g.r}}{I_{yy_r}+\bar{m}_m {x_{c.g.m}}^2} & -\frac{\bar{q}S_m x_{c.g.m} {}^2 C_{L_{am}}}{V_0(I_{yy_r}+\bar{m}_m {x_{c.g.m}}^2)} - \frac{\bar{q}S_c x_{c.g.c} C_{L_{qc}} c_c}{2V_0(I_{yy_r}+\bar{m}_m {x_{c.g.m}}^2)} \end{bmatrix} \begin{pmatrix} \theta_m \\ \dot{\theta}_m \\ \theta_r \\ \dot{\theta}_r \end{pmatrix} + \begin{bmatrix} 0 & 0 \\ \frac{\bar{q}S_m c_m C_{m_{\delta_{em}}}}{I_{yy_m}} & 0 \\ 0 & 0 \\ \frac{\bar{q}S_m x_{c.g.m} C_{L_{\delta_{em}}}}{I_{yy_r}+\bar{m}_m {x_{c.g.m}}^2} & -\frac{\bar{q}S_c x_{c.g.c} C_{L_{\delta_{ec}}}}{I_{yy_r}+\bar{m}_m {x_{c.g.m}}^2} \end{bmatrix} \begin{pmatrix} \delta_{e_m} \\ \delta_{e_c} \end{pmatrix} \tag{3.8}$$

$$\begin{pmatrix} \dot{\theta}_m \\ \ddot{\theta}_m \\ \dot{\theta}_r \\ \ddot{\theta}_r \\ \alpha_m \\ n_z \end{pmatrix} = \begin{bmatrix} 1 & 0 & 0 & 0 \\ 0 & 1 & 0 & 0 \\ 0 & 0 & 1 & 0 \\ 0 & 0 & 0 & 1 \\ 1 & 0 & 0 & -x_{c.g._m}/V_0 \\ \frac{\bar{q}S_m x_{c.g.m} C_{L_{am}}}{I_{yy_r}+\bar{m}_m {x_{c.g.m}}^2}\frac{x_{c.g.m}}{g} & \frac{\bar{q}S_m x_{c.g.m} C_{L_{qm}} c_m}{2V_0(I_{yy_r}+\bar{m}_m {x_{c.g.m}}^2)}\frac{x_{c.g.m}}{g} & -\frac{\bar{q}S_c x_{c.g.c} C_{L_{ac}} - \bar{m}_r g z_{c.g.r}}{I_{yy_r}+\bar{m}_m {x_{c.g.m}}^2}\frac{x_{c.g.m}}{g} & -\frac{\bar{q}S_m x_{c.g.m} {}^2 C_{L_{am}}}{V_0(I_{yy_r}+\bar{m}_m {x_{c.g.m}}^2)}\frac{x_{c.g.m}}{g} - \frac{\bar{q}S_c x_{c.g.c} C_{L_{qc}} c_c}{2V_0(I_{yy_r}+\bar{m}_m {x_{c.g.m}}^2)}\frac{x_{c.g.m}}{g} \end{bmatrix} \begin{pmatrix} \theta_m \\ \dot{\theta}_m \\ \theta_r \\ \dot{\theta}_r \end{pmatrix} + \begin{bmatrix} 0 & 0 \\ 0 & 0 \\ 0 & 0 \\ 0 & 0 \\ 0 & 0 \\ \frac{\bar{q}S_m x_{c.g.m} C_{L_{\delta_{em}}}}{I_{yy_r}+\bar{m}_m {x_{c.g.m}}^2}\frac{x_{c.g.m}}{g} & -\frac{\bar{q}S_c x_{c.g.c} C_{L_{\delta_{ec}}}}{I_{yy_r}+\bar{m}_m {x_{c.g.m}}^2}\frac{x_{c.g.m}}{g} \end{bmatrix} \begin{pmatrix} \delta_{e_m} \\ \delta_{e_c} \end{pmatrix} \tag{3.9}$$

3.3 Choice of coordinate axes

Before deriving the nonlinear equations of motion in the next section, a coordinate system has to be chosen first. The chosen coordinate system plays a key role in calculating the reaction forces applied on the aircraft model, due to the rig's kinematic constraints imposed through its arm. The

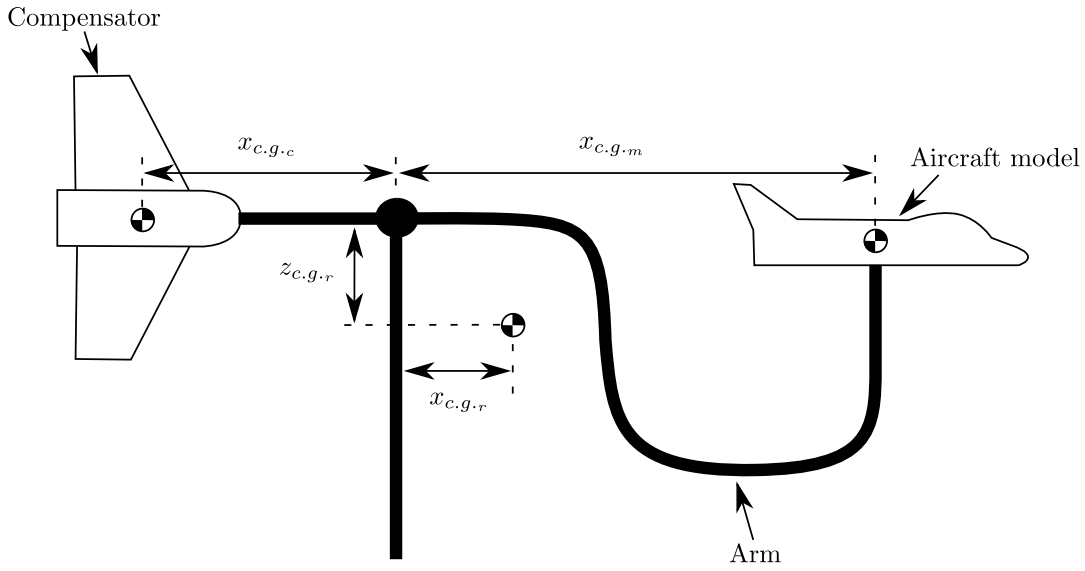

FIGURE 3.1. The manoeuvre rig bodies and their c.g. positions

reaction forces will be considered further when deriving the inertial and kinematic compensation concept in Chapter 4.

The significance of the choice of coordinates can be demonstrated using a simple frictionless pendulum example. The position, velocity, acceleration of a pendulum mass, including the external loads acting on the body, can be described using polar or Cartesian coordinates. The Lagrange method of deriving the equations of motion uses the concept of virtual work. If polar coordinates are used, the reaction force (in the case of a pendulum, the centripetal force) always acts in the radial direction. As a result, the work (displacement times the component of the force in that direction) done by the reaction force is always zero because the displacement is always tangential (see Figure 3.2(a)). The reaction force therefore does not appear in the final equations.

On the other hand, if a Cartesian coordinate system is used, there will be a component of the reaction force in both x and y directions (see Figure 3.2(b)). Multiplying these components with the displacement in both directions results in the work done by the reaction force in each coordinate direction. As a result, the reaction force will appear in the final equations. One major aim of this work is to develop a method to control this reaction force. In the ideal case for the manoeuvre rig, for instance, if the reaction forces acting on the aircraft model should reduce to zero, the dynamics will mimic that of a free-flying model. Because the manoeuvre rig can also be conceptualised as a horizontal pendulum, the above principles can be applied here.

3.4 3D rigid-body mathematical model of the manoeuvre rig

This section presents the derivation of the full nonlinear rigid-body equations of motion for the manoeuvre rig. The equations are described using differential and algebraic equations in

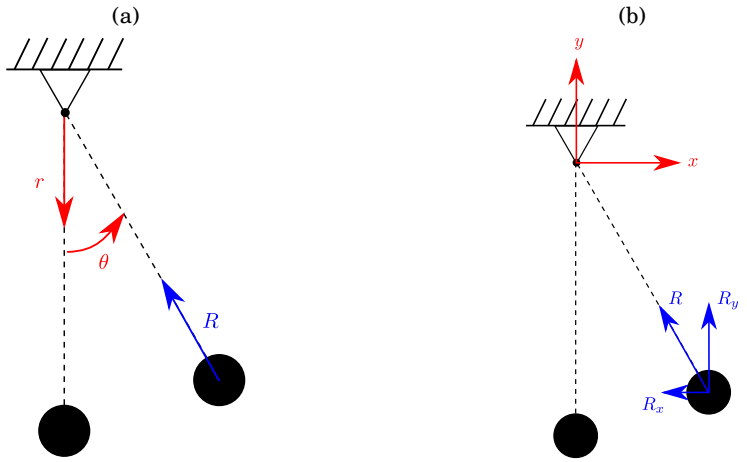

FIGURE 3.2. Reaction force in (a) polar and (b) Cartesian coordinate systems.

the Newton-Euler form which is extended for multi-body systems. The method uses Lagrange multipliers ($\boldsymbol{\lambda}$) to simultaneously solve the equations for individual body dynamics together with constraint equations. The development of the constraint equations are presented in Section 3.6. The techniques used here are described in Ref. [63]. For a system of bodies, once the kinetic energy, virtual work and kinetic constraints equations have been established, the Lagrange's equation or Hamilton's principle can be used to create the equations of motion for each body i in the form

$$M^i \ddot{\boldsymbol{q}}^i + {C_q}^T \boldsymbol{\lambda} = {Q_e}^i + {Q_v}^i. \tag{3.10}$$

In the above equation, M^i is the mass and inertial tensor matrix for individual bodies, $\boldsymbol{q}^i$ is the vector of generalised coordinates, C_q is the constraint Jacobian matrix, $\boldsymbol{\lambda}$ is the vector of Lagrange multipliers, ${Q_e}^i$ is the vector of externally applied loads, and ${Q_v}^i$ is a quadratic velocity vector term created when forming the Lagrange equation of motion from the kinetic energy equation. This ${Q_v}^i$ term is created as a result of differentiating the kinematic equation with respect to time and each coordinate and does not represent a physical force. The generalised coordinates used here are Cartesian coordinates to represent position and Euler angles to represent attitude. Hence, for each body i, the generalised coordinates are

$$\boldsymbol{q}^i_{(6\times1)} = \begin{bmatrix} \boldsymbol{R}^i \\ \boldsymbol{\theta}^i \end{bmatrix} \tag{3.11}$$

where

$$\boldsymbol{R}^i = \begin{bmatrix} x^i \\ y^i \\ z^i \end{bmatrix}, \boldsymbol{\theta}^i = \begin{bmatrix} \phi^i \\ \theta^i \\ \psi^i \end{bmatrix}. \tag{3.12}$$

The kinematic constraint equations for a single or multiple bodies can be written in the form

$$\boldsymbol{C}(\boldsymbol{q},t)=0 \tag{3.13}$$

where $\boldsymbol{C}$ is a vector of linearly independent algebraic constraint equations and t is time. Equations 3.10 and 3.13 can be solved simultaneously by first differentiating the constraint equation (3.13) twice with respect to time to form the differential equation:

$$\frac{\partial \boldsymbol{C}}{\partial q}\ddot{\boldsymbol{q}}=-\frac{\partial^2 \boldsymbol{C}}{\partial t\partial t}-\frac{\partial}{\partial \boldsymbol{q}}\left(\frac{\partial \boldsymbol{C}}{\partial \boldsymbol{q}}\dot{\boldsymbol{q}}\right)\dot{\boldsymbol{q}}-2\frac{\partial^2 \boldsymbol{C}}{\partial t\partial \boldsymbol{q}}\dot{\boldsymbol{q}} \tag{3.14}$$

which is in the form

$$C_q\ddot{\boldsymbol{q}}=\boldsymbol{Q_C} \tag{3.15}$$

where

$$C_q=\frac{\partial \boldsymbol{C}}{\partial \boldsymbol{q}} \tag{3.16}$$

and

$$\boldsymbol{Q_C}=-\frac{\partial^2 \boldsymbol{C}}{\partial t\partial t}-\frac{\partial}{\partial \boldsymbol{q}}\left(\frac{\partial \boldsymbol{C}}{\partial \boldsymbol{q}}\dot{\boldsymbol{q}}\right)\dot{\boldsymbol{q}}-2\frac{\partial^2 \boldsymbol{C}}{\partial t\partial \boldsymbol{q}}\dot{\boldsymbol{q}} \tag{3.17}$$

Note that an example derivation of the constraint equation (Equation 3.15) is given in Section 3.6.1. Equations 3.10 and 3.15 can be combined into matrix form to create the equations of motion for an arbitrary system of bodies. This can be written as

$$\begin{bmatrix} M_{(6n\times 6n)} & {C_q}^T_{(6n\times nc)} \\ C_{q_{(nc\times 6n)}} & 0_{(nc\times nc)} \end{bmatrix}\begin{bmatrix} \ddot{\boldsymbol{q}}_{(6n\times 1)} \\ \boldsymbol{\lambda}_{(nc\times 1)} \end{bmatrix}=\begin{bmatrix} \boldsymbol{Q_E}_{(6n\times 1)} \\ \boldsymbol{Q_C}_{(nc\times 1)} \end{bmatrix}. \tag{3.18}$$

where $\boldsymbol{Q_E}=Q_e+Q_v$ to simplify the equation. In Equation (3.18), M is the combined mass and inertial tensor matrix for all bodies of the system (where the body axis origin coincides with its centre of mass). C_q and $\boldsymbol{Q_C}$ are derived by differentiating each constraint equation twice with respect to time (see Section 3.6). Note that $\boldsymbol{Q_C}$ is created as a result of the procedure of solving the dynamic equations and does not represent a physical force. The subscripts n and nc in Equation (3.18) represent the number of bodies and constraint equations used respectively. The ${C_q}^T\boldsymbol{\lambda}$ term is effectively the total reaction load acting on each body. This is useful for simulating the possible loads that will be measured by the load cell. In more detail, we can write

$$M_{(6n\times 6n)}=\begin{bmatrix} M^1 & 0 & \cdots & 0 \\ 0 & M^2 & \cdots & 0 \\ \vdots & \vdots & \ddots & 0 \\ 0 & 0 & 0 & M^n \end{bmatrix},\ddot{\boldsymbol{q}}_{(6n\times 1)}=\begin{bmatrix} \ddot{\boldsymbol{q}}^1 \\ \ddot{\boldsymbol{q}}^2 \\ \vdots \\ \ddot{\boldsymbol{q}}^n \end{bmatrix},\boldsymbol{Q_E}_{(6n\times 1)}=\begin{bmatrix} \boldsymbol{Q_E^1} \\ \boldsymbol{Q_E^2} \\ \vdots \\ \boldsymbol{Q_E^n} \end{bmatrix}, \tag{3.19}$$

$$M^i=\begin{bmatrix} {m_{RR}}^i & 0_3 \\ 0_3 & {\overline{I}_{\theta\theta}}^i \end{bmatrix},{m_{RR}}^i=\begin{bmatrix} m^i & 0 & 0 \\ 0 & m^i & 0 \\ 0 & 0 & m^i \end{bmatrix},{\overline{I}_{\theta\theta}}^i=\begin{bmatrix} {\overline{I}_{xx}}^i & -{\overline{I}_{xy}}^i & -{\overline{I}_{xz}}^i \\ -{\overline{I}_{yx}}^i & {\overline{I}_{yy}}^i & -{\overline{I}_{yz}}^i \\ -{\overline{I}_{zx}}^i & -{\overline{I}_{zy}}^i & {\overline{I}_{zz}}^i \end{bmatrix}, \tag{3.20}$$

$$\ddot{\boldsymbol{q}}^{i}_{(6\times1)} = \begin{bmatrix} \ddot{\boldsymbol{R}}^{i} \\ \ddot{\boldsymbol{\theta}}^{i} \end{bmatrix}, \ddot{\boldsymbol{R}}^{i} = \begin{bmatrix} \ddot{x}^{i} \\ \ddot{y}^{i} \\ \ddot{z}^{i} \end{bmatrix}, \ddot{\boldsymbol{\theta}}^{i} = \begin{bmatrix} \dot{\overline{p}}^{i} \\ \dot{\overline{q}}^{i} \\ \dot{\overline{r}}^{i} \end{bmatrix}, \tag{3.21}$$

$$\boldsymbol{Q_E}^{i} = \begin{bmatrix} \boldsymbol{Q_R}^{i} \\ \overline{\boldsymbol{F}}_{\boldsymbol{\theta}}{}^{i} - \overline{\boldsymbol{\omega}}^{i} \times \overline{I}_{\theta\theta}{}^{i} \overline{\boldsymbol{\omega}}^{i} \end{bmatrix}, \boldsymbol{Q_R}^{i} = \begin{bmatrix} {F_x}^{i} \\ {F_y}^{i} \\ {F_z}^{i} \end{bmatrix}, \overline{\boldsymbol{F}}_{\boldsymbol{\theta}}{}^{i} = \begin{bmatrix} \overline{M}_x{}^{i} \\ \overline{M}_y{}^{i} \\ \overline{M}_z{}^{i} \end{bmatrix}, \overline{\boldsymbol{\omega}}^{i} = \begin{bmatrix} \overline{p}^{i} \\ \overline{q}^{i} \\ \overline{r}^{i} \end{bmatrix}. \tag{3.22}$$

Here $\boldsymbol{Q_R}^{i}$ and $\boldsymbol{F_\theta}^{i}$ are the force and moment vectors respectively. $\boldsymbol{\omega}^{i}$ is the body rotational velocity vector. The bar above a symbol represents the quantity in the local body frame of reference. Note that if the body axes origin does not coincide with the body's centre of gravity then ${m_{RR}}^{i}$ will have off diagonal terms to account for the inertial coupling between the translation and rotation of the body. The above equations can be expanded to recreate the conventional form of the translational and rotational nonlinear single rigid-body equations of motion for an aircraft. Here, a Cartesian coordinate system is used along with quaternions to represent rotations.

The set of equations shown above are solved in Matlab Simulink using the Runge-Kutta solver ode45 and its implementation is discussed in Section 3.11. Appendix E shows the values used for the mass, inertia and position vector for each body.

For the manoeuvre rig, a total of five bodies are used: the aircraft model, the link between the aircraft model and the load cell, the load cell itself, the rig's arm, as well as the aerodynamic compensator, as shown in Figure 3.3. They will be denoted by superscript m, l, lc, a and c respectively in the equations of motion. The rig's arm and the compensator could also be modelled as a single body since they are rigidly attached to one another; however, they are modelled separately here for future convenience as any physical changes made to them can be applied individually into the mathematical model. Modelling the load cell separately allows for the measured loads to be simulated using the reaction loads term ${C_q}^{T}\boldsymbol{\lambda}$.

3.5 Quaternions

Euler transformation describes rotations using a series of three orthogonal rotations, where the axes of rotation moves along as well as in sequence. However, gimbal lock can occur when using Euler transformations which is when two rotation axes become coincident, for example, for an aircraft where the conventional rotation sequence is yaw (ψ), pitch (θ), roll (ϕ), when the aircraft is at 90° pitch, the roll and yaw rotation axes become coincident (see Figure 3.4). Therefore the roll and yaw angles cannot be distinguished individually. Quaternion transformations describe rotation as a unit vector and a single rotation about that vector, thus effectively avoiding gimbal lock. However, these extreme attitudes will most likely not be reached in the manoeuvre rig, but nevertheless, quaternions are preferred since it is a more computationally efficient method to represent rotations. A disadvantage of using quaternions is that physical visualisation becomes

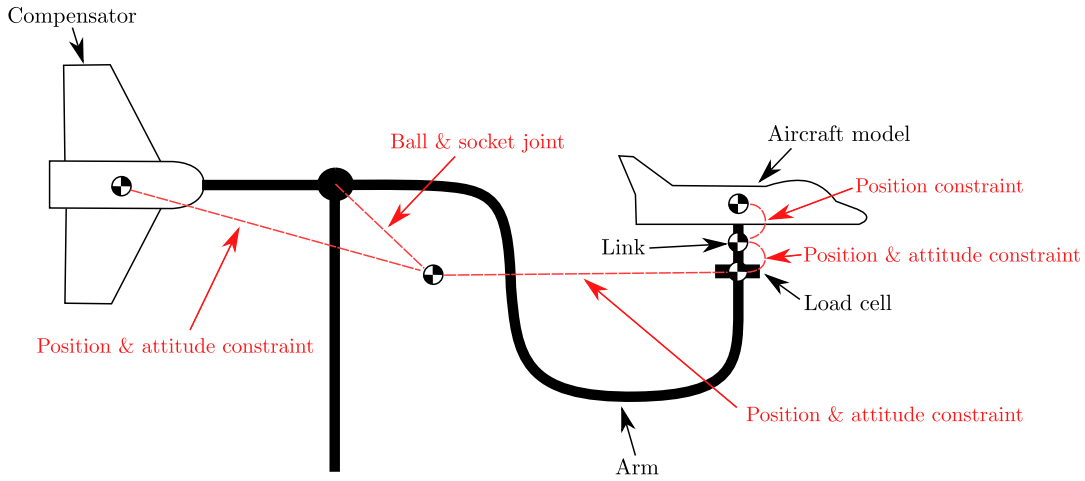

FIGURE 3.3. The manoeuvre rig bodies and constraints

difficult since one cannot immediately picture a body's attitude given the quaternion parameters. The quaternion parameters are defined as

$$\boldsymbol{\theta_q} = \begin{bmatrix} \theta_{q0} \\ \theta_{q1} \\ \theta_{q2} \\ \theta_{q3} \end{bmatrix}, \tag{3.23}$$

where

$$\theta_{q0} = \cos\frac{\gamma}{2}, \tag{3.24}$$

$$\theta_{q1} = v_1 \sin\frac{\gamma}{2}, \tag{3.25}$$

$$\theta_{q2} = v_2 \sin\frac{\gamma}{2}, \tag{3.26}$$

$$\theta_{q3} = v_3 \sin\frac{\gamma}{2}. \tag{3.27}$$

The vector $\boldsymbol{v} = [\ v_1 \quad v_2 \quad v_3\ ]^T$ is the axis of rotation and γ is the rotation angle. The use of quaternions requires the following changes to be made to Equations 3.20 to 3.22:

$$\ddot{\boldsymbol{q}}^i_{(7\times1)} = \begin{bmatrix} \ddot{\boldsymbol{R}}^i \\ \ddot{\boldsymbol{\theta}}^i_{\boldsymbol{q}} \end{bmatrix}, \tag{3.28}$$

$$\boldsymbol{M}^i_{(7\times7)} = \begin{bmatrix} m_{RR}{}^i & 0_{3,4} \\ 0_{4,3} & \overline{G}^{iT}\overline{I}_{\theta\theta}{}^i\overline{G}^i \end{bmatrix}, \boldsymbol{Q_E}^i_{(7\times1)} = \begin{bmatrix} \boldsymbol{Q_R}{}^i \\ \overline{G}^{iT}\left(\overline{\boldsymbol{F}}_{\boldsymbol{\theta}}{}^i - \overline{\boldsymbol{\omega}}^i \times \overline{I}_{\theta\theta}{}^i\overline{\boldsymbol{\omega}}^i\right) \end{bmatrix}, \overline{\boldsymbol{\omega}}^i_{(3\times1)} = \overline{G}^i\dot{\overline{\boldsymbol{\theta}}}^i_{\boldsymbol{q}}, \tag{3.29}$$

where $\overline{G}^i$ is a quaternion transformation matrix (see Appendix A). When only a single body is examined the superscript i is removed for the purpose of clarity. The quaternion Euler parameters

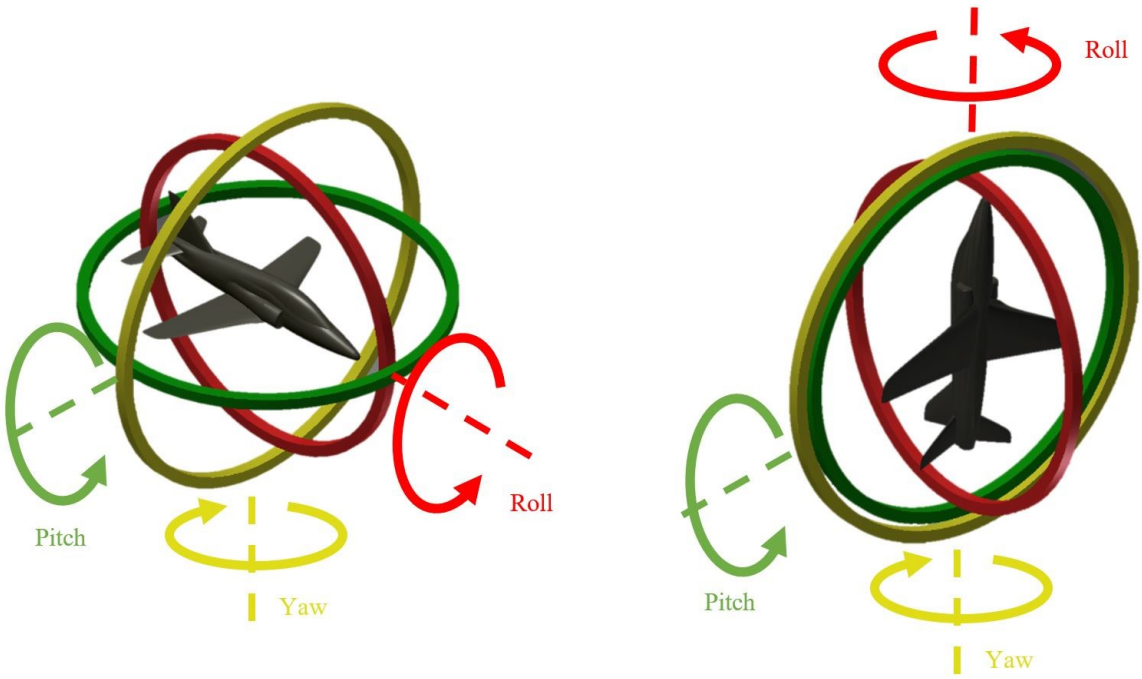

FIGURE 3.4. Gimbal lock caused by coincident axes of rotation.

are not independent and must satisfy the unit norm condition:

$$\boldsymbol{\theta_q}^{i\,T}\boldsymbol{\theta_q}^{i} = 1. \tag{3.30}$$

3.6 Rig constraints equations

The individual components of the rig (aircraft model, link, load cell, arm and compensator) are essentially connected to each other via specific types of constraints:

1. The aircraft model is attached to the load cell link via a pure **position constraint**. This ensures that the aircraft is free to rotate but keeps the relative position of the aircraft model to the arm fixed.

2. The load cell link is attached to the load cell itself with a **position constraint** as well as an **attitude constraint**. This ensures the position and attitude of the link remains constant relative to the rig.

3. The load cell is attached to the rig's arm again with a **position constraint** and an **attitude constraint** due to the same reason as above.

4. The rig's arm is held via a **ball and socket joint** to ensure its centre of gravity is at a fixed distance to the arm's rotation point and its attitude revolves around this point.

5. The compensator is attached to the arm again with a **position constraint** and an **attitude constraint**.

These constraints are depicted in Figure 3.3. The constraints stated above are described mathematically in the following subsections in order to derive the C_q and $\boldsymbol{Q_C}$ terms for Equation 3.18.

3.6.1 Relative position fixed constraint

This constraint ensures the relative position of two bodies remain constant within the local body axes of the first body. The constraint can be described in general for two bodies (denoted by subscripts a and b) as

$$\boldsymbol{R}_a = \boldsymbol{R}_b + A_b \overline{\boldsymbol{u}}_{ab} \tag{3.31}$$

where $\boldsymbol{R}$ is the global position vector of a body, A is the transformation matrix which transforms a vector from the body axes onto the global axes, and $\overline{\boldsymbol{u}}_{ab}$ is the position vector of body a relative to body b in the body frame of reference of body b. This is visualized in Figure 3.5. Note that $\boldsymbol{u}_{ab} = A_b \overline{\boldsymbol{u}}_{ab}$. The above equation can be written in the same form as Equation 3.13 to give

$$\boldsymbol{R}_a - \boldsymbol{R}_b - A_b \overline{\boldsymbol{u}}_{ab} = 0. \tag{3.32}$$

Following the same procedure as explained earlier, the above equation can be differentiated twice with respect to time to obtain the constraint equation in the form as Equation 3.15. Differentiating once gives

$$\dot{\boldsymbol{R}}_a - \dot{\boldsymbol{R}}_b - \dot{A}_b \overline{\boldsymbol{u}}_{ab} - A_b \dot{\overline{\boldsymbol{u}}}_{ab} = 0 \tag{3.33}$$

$$\dot{\boldsymbol{R}}_a - \dot{\boldsymbol{R}}_b - (\boldsymbol{\omega_b} \times A_b \overline{\boldsymbol{u}}_{ab}) - A_b \dot{\overline{\boldsymbol{u}}}_{ab} = 0 \tag{3.34}$$

where $\boldsymbol{\omega}$ is the rotational velocity vector. Taking the time derivative again gives

$$\ddot{\boldsymbol{R}}_a - \ddot{\boldsymbol{R}}_b - A_b \ddot{\overline{\boldsymbol{u}}}_{ab} - 2(\boldsymbol{\omega}_b \times \dot{\boldsymbol{u}}_{ab}) - (\dot{\boldsymbol{\omega}}_b \times \boldsymbol{u}_{ab}) - \boldsymbol{\omega}_b \times (\boldsymbol{\omega}_b \times \boldsymbol{u}_{ab}) = 0 \tag{3.35}$$

or

$$\ddot{\boldsymbol{R}}_a - \ddot{\boldsymbol{R}}_b - A_b \ddot{\overline{\boldsymbol{u}}}_{ab} - 2(\boldsymbol{\omega}_b \times A_b \dot{\overline{\boldsymbol{u}}}_{ab}) - (\dot{\boldsymbol{\omega}}_b \times A_b \overline{\boldsymbol{u}}_{ab}) - \boldsymbol{\omega}_b \times (\boldsymbol{\omega}_b \times A_b \overline{\boldsymbol{u}}_{ab}) = 0 \tag{3.36}$$

or equivalently,

$$\ddot{\boldsymbol{R}}_a - \ddot{\boldsymbol{R}}_b - A_b \ddot{\overline{\boldsymbol{u}}}_{ab} - A_b \left[2(\overline{\boldsymbol{\omega}}_b \times \dot{\overline{\boldsymbol{u}}}_{ab})\right] - A_b \left[\dot{\overline{\boldsymbol{\omega}}}_b \times \overline{\boldsymbol{u}}_{ab}\right] - A_b \left[\overline{\boldsymbol{\omega}}_b \times (\overline{\boldsymbol{\omega}}_b \times \overline{\boldsymbol{u}}_{ab})\right] = 0 \tag{3.37}$$

where the terms with a bar represent the local quantities relative to their body axes. Assuming the link is rigid ($\overline{\boldsymbol{u}}$ is constant), the velocity and acceleration of the body in the local body frame of

reference will be zero ($\dot{\overline{\boldsymbol{u}}} = \ddot{\overline{\boldsymbol{u}}} = 0$), i.e. there will be no Coriolis or linear acceleration, which leaves just the tangential and centripetal/normal acceleration terms. This reduces the equation to

$$\ddot{\boldsymbol{R}}_a - \ddot{\boldsymbol{R}}_b - (\dot{\boldsymbol{\omega}}_b \times A_b \overline{\boldsymbol{u}}_{ab}) - \boldsymbol{\omega}_b \times (\boldsymbol{\omega}_b \times A_b \overline{\boldsymbol{u}}_{ab}) = 0 \tag{3.38}$$

or,

$$\ddot{\boldsymbol{R}}_a - \ddot{\boldsymbol{R}}_b - A_b \left[\dot{\overline{\boldsymbol{\omega}}}_b \times \overline{\boldsymbol{u}}_{ab}\right] - A_b \left[\overline{\boldsymbol{\omega}}_b \times (\overline{\boldsymbol{\omega}}_b \times \overline{\boldsymbol{u}}_{ab})\right] = 0. \tag{3.39}$$

This clearly shows that the effect of this constraint will manifest in the body's equations of motion as additional tangential and normal accelerations. The C_q and $\boldsymbol{Q_C}$ terms can be found by separating the acceleration terms from Equation 3.38 as shown below:

$$\ddot{\boldsymbol{R}}_a - \ddot{\boldsymbol{R}}_b - (\dot{\boldsymbol{\omega}}_b \times A_b \overline{\boldsymbol{u}}_{ab}) = \boldsymbol{\omega}_b \times (\boldsymbol{\omega}_b \times A_b \overline{\boldsymbol{u}}_{ab}) \tag{3.40}$$

$$\ddot{\boldsymbol{R}}_a - \ddot{\boldsymbol{R}}_b + \widetilde{(A_b \overline{\boldsymbol{u}}_{ab})} \dot{\boldsymbol{\omega}}_b = \boldsymbol{\omega}_b \times (\boldsymbol{\omega}_b \times A_b \overline{\boldsymbol{u}}_{ab}) \tag{3.41}$$

where $\widetilde{(A_b \overline{\boldsymbol{u}}_{ab})}$ is the 3×3 skew symmetric (antisymmetric) matrix of the 3×1 vector $A_b \overline{\boldsymbol{u}}_{ab}$ defined as

$$\widetilde{(A_b \overline{\boldsymbol{u}}_{ab})} = \begin{bmatrix} 0 & -A_b \overline{\boldsymbol{u}}_{ab}(3) & A_b \overline{\boldsymbol{u}}_{ab}(2) \\ A_b \overline{\boldsymbol{u}}_{ab}(3) & 0 & -A_b \overline{\boldsymbol{u}}_{ab}(1) \\ -A_b \overline{\boldsymbol{u}}_{ab}(2) & A_b \overline{\boldsymbol{u}}_{ab}(1) & 0 \end{bmatrix}. \tag{3.42}$$

Equation 3.41 can be written in matrix form:

$$\begin{bmatrix} I_3 & -I_3 & \widetilde{(A_b \overline{\boldsymbol{u}}_{ab})} \end{bmatrix} \begin{bmatrix} \ddot{\boldsymbol{R}}_a \\ \ddot{\boldsymbol{R}}_b \\ \dot{\boldsymbol{\omega}}_b \end{bmatrix} = \boldsymbol{\omega}_b \times (\boldsymbol{\omega}_b \times A_b \overline{\boldsymbol{u}}_{ab}) \tag{3.43}$$

where I_3 is a 3×3 identity matrix. The above equation in the same form as Equation 3.15 and the C_q and $\boldsymbol{Q_C}$ terms can be described as

$$C_q = \begin{bmatrix} I_3 & -I_3 & \widetilde{(A_b \overline{\boldsymbol{u}}_{ab})} \end{bmatrix} \tag{3.44}$$

$$\boldsymbol{Q_C} = \boldsymbol{\omega}_b \times (\boldsymbol{\omega}_b \times A_b \overline{\boldsymbol{u}}_{ab}). \tag{3.45}$$

If quaternions are used then Equation 3.43 becomes

$$\begin{bmatrix} I_3 & -I_3 & 2\widetilde{(A_b \overline{\boldsymbol{u}}_{ab})} E_b \end{bmatrix} \begin{bmatrix} \ddot{\boldsymbol{R}}_a \\ \ddot{\boldsymbol{R}}_b \\ \ddot{\boldsymbol{\theta}}_{q_b} \end{bmatrix} = \boldsymbol{\omega}_b \times (\boldsymbol{\omega}_b \times A_b \overline{\boldsymbol{u}}_{ab}) \tag{3.46}$$

and

$$C_q = \begin{bmatrix} I_3 & -I_3 & 2\widetilde{(A_b \overline{\boldsymbol{u}}_{ab})} E_b \end{bmatrix} \tag{3.47}$$

$$\boldsymbol{Q_C} = \boldsymbol{\omega}_b \times (\boldsymbol{\omega}_b \times A_b \overline{\boldsymbol{u}}_{ab}). \tag{3.48}$$

where the following definitions apply:

$$\boldsymbol{\omega} = 2E\dot{\boldsymbol{\theta}}_q \tag{3.49}$$

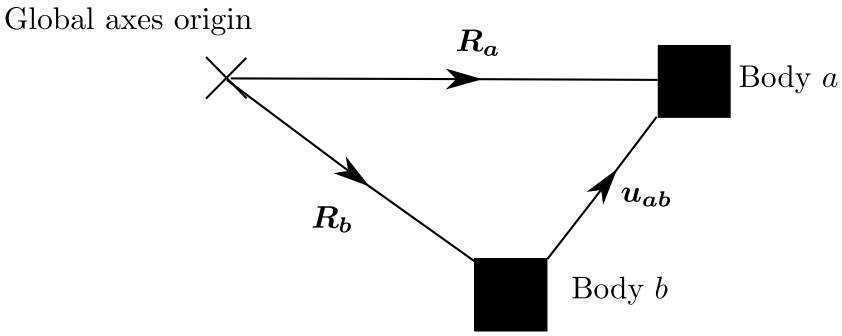

FIGURE 3.5. Relative position fixed constraint

$$\dot{\boldsymbol{\omega}} = 2E\ddot{\boldsymbol{\theta}}_q. \tag{3.50}$$

The definition for matrix E can be found in Appendix A. As stated before, this constraint is used to attach the aircraft onto the load cell link, the load cell link onto the load cell itself, the load cell onto the arm, and the compensator onto the arm.

3.6.2 Relative attitude fixed constraint

In addition to the previous constraint, the attitude fixed constraint can be used to rigidly attach one body to another. This is described with the following equation:

$$\begin{bmatrix} \phi_a - \phi_b \\ \theta_a - \theta_b \\ \psi_a - \psi_b \end{bmatrix} = \begin{bmatrix} 0 \\ 0 \\ 0 \end{bmatrix} \tag{3.51}$$

where ϕ, θ and ψ are the Euler attitude angles. The same procedure as the previous constraint can be applied here (differentiating twice with respect to time) to find the C_q and $\boldsymbol{Q_C}$ terms:

$$\begin{bmatrix} I_3 & -I_3 \end{bmatrix} \begin{bmatrix} \dot{\boldsymbol{\omega}}_a \\ \dot{\boldsymbol{\omega}}_b \end{bmatrix} = \begin{bmatrix} 0 \\ 0 \\ 0 \end{bmatrix} \tag{3.52}$$

where

$$C_q = \begin{bmatrix} I_3 & -I_3 \end{bmatrix} \tag{3.53}$$

$$\boldsymbol{Q_C} = \begin{bmatrix} 0 \\ 0 \\ 0 \end{bmatrix}. \tag{3.54}$$

If quaternions are used, the above equations become

$$\begin{bmatrix} I_4 & -I_4 \end{bmatrix} \begin{bmatrix} \ddot{\boldsymbol{\theta}}_{qa} \\ \ddot{\boldsymbol{\theta}}_{qb} \end{bmatrix} = \begin{bmatrix} 0 \\ 0 \\ 0 \\ 0 \end{bmatrix} \tag{3.55}$$

where I_4 is a 4 × 4 identity matrix and

$$C_q = \begin{bmatrix} I_4 & -I_4 \end{bmatrix} \tag{3.56}$$

$$\boldsymbol{Q_C} = \begin{bmatrix} 0 \\ 0 \\ 0 \\ 0 \end{bmatrix}. \tag{3.57}$$

This constraint together with the relative position fixed constraint is used to rigidly attach the load cell link to the load cell, the load cell to the rig arm, and the compensator to the rig arm. This constraint may also be used for cases when the aircraft needs to be fully fixed onto the rig and not be allowed to rotate (aircraft gimbal locked in all axes), such as in conventional static wind tunnel testing.

3.6.3 Ball and socket joint

This constraint is used to describe the motion of the rig arm which is essentially a body revolving around a point. Mathematically this constraint is similar to the relative position fixed constraint and can be described as

$$\boldsymbol{R}_a = A_a \overline{\boldsymbol{u}}_a \tag{3.58}$$

where $\boldsymbol{R}_a$ is the position vector of the body centre of gravity in the global frame of reference, A_a is the transformation matrix and $\overline{\boldsymbol{u}}_a$ is the position vector of the body centre of gravity from the global axes origin in the body frame of reference. Taking the time derivative twice with respect time creates the following equation:

$$\begin{bmatrix} I_3 & \widetilde{(A_a \overline{\boldsymbol{u}}_a)} \end{bmatrix} \begin{bmatrix} \ddot{\boldsymbol{R}}_a \\ \dot{\boldsymbol{\omega}}_a \end{bmatrix} = \boldsymbol{\omega}_a \times (\boldsymbol{\omega}_a \times A_a \overline{\boldsymbol{u}}_a) \tag{3.59}$$

Therefore,

$$C_q = \begin{bmatrix} I_3 & \widetilde{(A_a \overline{\boldsymbol{u}}_a)} \end{bmatrix} \tag{3.60}$$

$$\boldsymbol{Q_C} = \boldsymbol{\omega}_a \times (\boldsymbol{\omega}_a \times A_a \overline{\boldsymbol{u}}_a). \tag{3.61}$$

If quaternions are used then Equation 3.59 becomes

$$\begin{bmatrix} I_3 & 2\widetilde{(A_a \overline{\boldsymbol{u}}_a)} E_a \end{bmatrix} \begin{bmatrix} \ddot{\boldsymbol{R}}_a \\ \ddot{\boldsymbol{\theta}}_{qa} \end{bmatrix} = \boldsymbol{\omega}_a \times (\boldsymbol{\omega}_a \times A_a \overline{\boldsymbol{u}}_a) \tag{3.62}$$

and

$$C_q = \begin{bmatrix} I_3 & 2\widetilde{(A_a \overline{\boldsymbol{u}}_a)} E_a \end{bmatrix} \tag{3.63}$$

$$\boldsymbol{Q_C} = \boldsymbol{\omega}_a \times (\boldsymbol{\omega}_a \times A_a \overline{\boldsymbol{u}}_a). \tag{3.64}$$

3.6.4 Quaternion constraint

As stated earlier, if quaternion Euler parameters are used then the unit norm condition must be satisfied. Expanding Equation 3.30 gives

$$\theta_{q0}{}^2 + \theta_{q1}{}^2 + \theta_{q2}{}^2 + \theta_{q3}{}^2 = 1. \tag{3.65}$$

Differentiating the above equation twice with respect to time gives the equation below in matrix form:

$$\begin{bmatrix} \theta_{q0} & \theta_{q1} & \theta_{q2} & \theta_{q3} \end{bmatrix} \ddot{\boldsymbol{\theta}}_q = -(\dot{\theta}_{q0}^2 + \dot{\theta}_{q1}^2 + \dot{\theta}_{q2}^2 + \dot{\theta}_{q3}^2). \tag{3.66}$$

Therefore,

$$C_q = \begin{bmatrix} \theta_{q0} & \theta_{q1} & \theta_{q2} & \theta_{q3} \end{bmatrix} \tag{3.67}$$

$$\boldsymbol{Q_C} = -(\dot{\theta}_{q0}^2 + \dot{\theta}_{q1}^2 + \dot{\theta}_{q2}^2 + \dot{\theta}_{q3}^2). \tag{3.68}$$

3.6.5 Additional constraints

These constraints may be used in addition to the constraints described previously for special cases for the rig, such as when the arm is fully locked to not rotate, or to study the difference between planar and spherical constraints and how they affect the dynamic motion of an aircraft model (this is studied in Chapter 4).

3.6.5.1 Attitude fixed constraint

This constraint can be used to fix a body at a constant attitude, such as at zero attitude angles. For example, such a constraint can be applied onto the rig arm to effectively lock it. In order to lock the aircraft's attitude to the rig, the relative attitude fixed constraint shown in Section 3.6.2 should be used instead. The equation below describes the attitude fixed constraint for zero attitude angles:

$$\begin{bmatrix} \phi \\ \theta \\ \psi \end{bmatrix} = \begin{bmatrix} 0 \\ 0 \\ 0 \end{bmatrix}. \tag{3.69}$$

Taking the time derivative twice gives the constraint equation in matrix form and the respective C_q and $\boldsymbol{Q_C}$ terms as shown below:

$$\begin{bmatrix} I_3 \end{bmatrix} \dot{\boldsymbol{\omega}} = \begin{bmatrix} 0 \\ 0 \\ 0 \end{bmatrix} \tag{3.70}$$

where

$$C_q = \begin{bmatrix} I_3 \end{bmatrix} \tag{3.71}$$

$$\boldsymbol{Q_C} = \begin{bmatrix} 0 \\ 0 \\ 0 \end{bmatrix}. \tag{3.72}$$

If quaternions are used, the above equations become

$$\begin{bmatrix} I_4 \end{bmatrix} \ddot{\boldsymbol{\theta}}_q = \begin{bmatrix} 0 \\ 0 \\ 0 \\ 0 \end{bmatrix} \tag{3.73}$$

where

$$C_q = \begin{bmatrix} I_4 \end{bmatrix} \tag{3.74}$$

$$\boldsymbol{Q_C} = \begin{bmatrix} 0 \\ 0 \\ 0 \\ 0 \end{bmatrix}. \tag{3.75}$$

3.6.5.2 Spherical constraint

A spherical constraint is a kinematic constraint that only allows motion with a constant radius about a point without any constraint on the body's attitude. This constraint can be expressed by the equation below:

$$\sqrt{(x+r)^2 + y^2 + z^2} = r \tag{3.76}$$

where r is the radius of the sphere, as shown in Figure 3.6(a). Note that the origin of the inertial axes is placed at the initial position of the aircraft's centre of gravity, at the forward most point on the sphere. Differentiating the above equation twice with respect to time gives

$$\begin{bmatrix} (x+r) & y & z \end{bmatrix} \ddot{\boldsymbol{R}} = -\dot{x}^2 - \dot{y}^2 - \dot{z}^2 \tag{3.77}$$

where

$$C_q = \begin{bmatrix} (x+r) & y & z \end{bmatrix} \tag{3.78}$$

$$\boldsymbol{Q_C} = -\dot{x}^2 - \dot{y}^2 - \dot{z}^2. \tag{3.79}$$

3.6.5.3 Planar constraint

The planar constraint can be thought of as a special case of the spherical constraint where the sphere radius is infinite (see Figure 3.6(b)). The constraint equations can be derived using a spherical coordinate system, as shown in Figure 3.7. Note that the origin of the inertial axis is

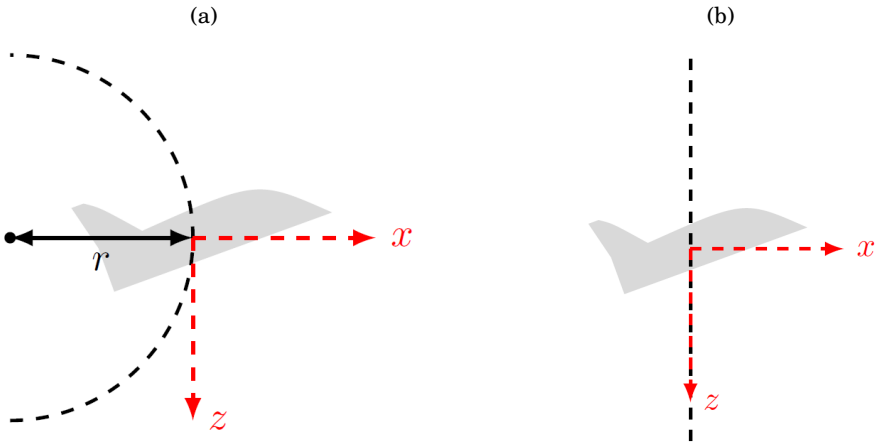

FIGURE 3.6. Physical kinematic constraints: (a) spherical constraint and (b) planar constraint.

again placed at the initial position of the aircraft's centre of gravity, at the front of the sphere. The Cartesian coordinates in terms of the inclination (θ_s) and azimuth (ϕ_s) angles are

$$x = r\sin\theta_s\cos\phi_s - r, \tag{3.80}$$

$$y = r\sin\theta_s\sin\phi_s, \tag{3.81}$$

$$z = r\cos\theta_s. \tag{3.82}$$

For an arbitrary y and z coordinate, the x coordinate on the sphere in terms of y and z is

$$x = r\sin\left[\arccos\left(\frac{z}{r}\right)\right]\cos\left[\arcsin\left(\frac{y}{r\sin\left[\arccos\left(\frac{z}{r}\right)\right]}\right)\right] - r, \tag{3.83}$$

since

$$\lim_{r\to\infty}\sin\left[\arccos\left(\frac{z}{r}\right)\right] = 1, \tag{3.84}$$

$$\lim_{r\to\infty}\cos\left[\arcsin\left(\frac{y}{r}\right)\right] = 1. \tag{3.85}$$

Therefore, we can write

$$\lim_{r\to\infty} x = 0, \tag{3.86}$$

and so the expression describing the planar constraint is:

$$x = 0. \tag{3.87}$$

Similar to the spherical constraint derivation, Equation (3.87) is differentiated twice with respect to time to give

$$\begin{bmatrix} 1 & 0 & 0 \end{bmatrix}\ddot{\boldsymbol{R}} = 0. \tag{3.88}$$

Hence, the C_q Jacobian matrix and $\boldsymbol{Q_C}$ vector are

$$C_q = \begin{bmatrix} 1 & 0 & 0 \end{bmatrix} \tag{3.89}$$

$$\boldsymbol{Q_C} = 0. \tag{3.90}$$

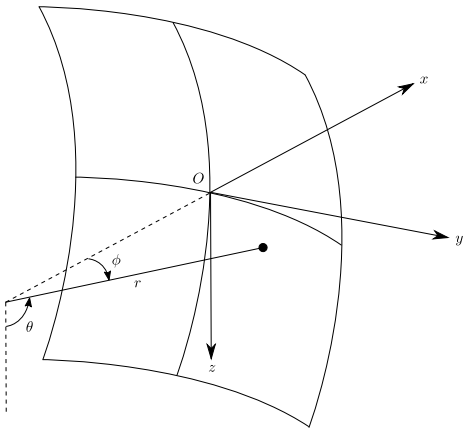

FIGURE 3.7. Spherical coordinates.

3.6.5.4 Position fixed constraint

This constraint prevents translation of the body but allows rotations and is described by the three equations below:

$$x = 0 \tag{3.91}$$

$$y = 0 \tag{3.92}$$

$$z = 0 \tag{3.93}$$

Therefore, differentiating twice with respect to time give the following constraints equations in matrix form:

$$\begin{bmatrix} 1 & 0 & 0 \\ 0 & 1 & 0 \\ 0 & 0 & 1 \end{bmatrix} \ddot{\boldsymbol{R}} = \begin{bmatrix} 0 \\ 0 \\ 0 \end{bmatrix}. \tag{3.94}$$

Hence, the C_q Jacobian matrix and $\boldsymbol{Q_C}$ vector are

$$C_q = \begin{bmatrix} 1 & 0 & 0 \\ 0 & 1 & 0 \\ 0 & 0 & 1 \end{bmatrix} \tag{3.95}$$

$$\boldsymbol{Q_C} = \begin{bmatrix} 0 \\ 0 \\ 0 \end{bmatrix}. \tag{3.96}$$

3.7 Combined constraint equations

The previously developed constraint equations can be combined to create the C_q Jacobian matrix and the $\boldsymbol{Q_C}$ vector required by Equation 3.18, as shown in Equations 3.97 and 3.98 respectively. The acceleration vector is shown in Equation 3.99. The superscripts m, l, lc, a and c represent the aircraft model, the link between the aircraft model and the load cell, the load cell itself, the rig's arm, and the compensator respectively. $\overline{\boldsymbol{u}}^m$ is the position vector of the aircraft model relative to the load cell link in the link's body axes, $\overline{\boldsymbol{u}}^l$ is the position vector of the load cell link relative to the load cell in the load cell body axes, $\overline{\boldsymbol{u}}^{lc}$ is the position vector of the load cell relative to the rig arm in the rig arm's body axes, $\overline{\boldsymbol{u}}^a$ is the position vector of the rig's arm relative to the arm's rotation point in the arm's body axes, and $\overline{\boldsymbol{u}}^c$ is the position vector of the compensator relative to the arm's rotation point in arm body axes. Note that these position vectors are for each body's centre of gravity. Figure 3.8 shows these position vectors. Appendix E shows the values used for the mass, inertia and position vector for each body.

$$C_q = \begin{bmatrix}
0_{3,3} & 0_{3,4} & I_3 & 2(\widetilde{A^a\overline{\boldsymbol{u}}^a})E^a & 0_{3,3} & 0_{3,4} & 0_{3,3} & 0_{3,4} & 0_{3,3} & 0_{3,4} \\
0_{3,3} & 0_{3,4} & 0_{3,3} & 0_{3,4} & 0_{3,3} & \boldsymbol{\theta}_{\boldsymbol{q}}^{m\,T} & 0_{3,3} & 0_{3,4} & 0_{3,3} & 0_{3,4} \\
I_3 & 0_{3,4} & 0_{3,3} & 2(\widetilde{A^a\overline{\boldsymbol{u}}^c})E^a & 0_{3,3} & 0_{3,4} & 0_{3,3} & 0_{3,4} & 0_{3,3} & 0_{3,4} \\
0_{4,3} & I_4 & 0_{4,3} & -I_4 & 0_{4,3} & 0_{4,4} & 0_{4,3} & 0_{4,4} & 0_{4,3} & 0 \\
0_{3,3} & 0_{3,4} & -I_3 & 2(\widetilde{A^a\overline{\boldsymbol{u}}^{lc}})E^a & 0_{3,3} & 0_{3,4} & I_3 & 0_{3,4} & 0_{3,3} & 0_{3,4} \\
0_{4,3} & 0_{4,4} & 0_{4,3} & I_4 & 0_{4,3} & 0_{4,4} & 0_{4,3} & -I_4 & 0_{4,3} & 0_{4,4} \\
0_{3,3} & 0_{3,4} & 0_{3,3} & 0_{3,4} & 0_{3,3} & 0_{3,4} & -I_3 & 2(\widetilde{A^{lc}\overline{\boldsymbol{u}}^l})E^{lc} & I_3 & 0_{3,4} \\
0_{4,3} & 0_{4,4} & 0_{4,3} & 0_{4,4} & 0_{4,3} & 0_{4,4} & 0_{4,3} & I_4 & 0_{4,3} & -I_4 \\
0_{3,3} & 0_{3,4} & 0_{3,3} & 0_{3,4} & I_3 & 0_{3,4} & 0_{3,3} & 0_{3,4} & -I_3 & 2(\widetilde{A^l\overline{\boldsymbol{u}}^m})E^l \\
0_{3,3} & 0_{3,4} & 0_{3,3} & \boldsymbol{\theta}_{\boldsymbol{q}}^{a\,T} & 0_{3,3} & 0_{3,4} & 0_{3,3} & 0_{3,4} & 0_{3,3} & 0_{3,4}
\end{bmatrix} \tag{3.97}$$

$$\boldsymbol{Q_C} = \begin{bmatrix}
\boldsymbol{\omega}^a \times (\boldsymbol{\omega}^a \times A^a\overline{\boldsymbol{u}}^a) \\
-(\dot{\theta}_{q0}^{m^2} + \dot{\theta}_{q1}^{m^2} + \dot{\theta}_{q2}^{m^2} + \dot{\theta}_{q3}^{m^2}) \\
\boldsymbol{\omega}^a \times (\boldsymbol{\omega}^a \times A^a\overline{\boldsymbol{u}}^c) \\
0_{4,1} \\
\boldsymbol{\omega}^a \times (\boldsymbol{\omega}^a \times A^a\overline{\boldsymbol{u}}^{lc}) \\
0_{4,1} \\
\boldsymbol{\omega}^{lc} \times (\boldsymbol{\omega}^{lc} \times A^{lc}\overline{\boldsymbol{u}}^l) \\
0_{4,1} \\
\boldsymbol{\omega}^l \times (\boldsymbol{\omega}^l \times A^l\overline{\boldsymbol{u}}^m) \\
-(\dot{\theta}_{q0}^{a^2} + \dot{\theta}_{q1}^{a^2} + \dot{\theta}_{q2}^{a^2} + \dot{\theta}_{q3}^{a^2})
\end{bmatrix} \tag{3.98}$$

$$\ddot{\boldsymbol{q}} = \begin{bmatrix} \ddot{\boldsymbol{R}}^c \\ \ddot{\boldsymbol{\theta}}^c \\ \ddot{\boldsymbol{R}}^a \\ \ddot{\boldsymbol{\theta}}^a \\ \ddot{\boldsymbol{R}}^m \\ \ddot{\boldsymbol{\theta}}^m \\ \ddot{\boldsymbol{R}}^{lc} \\ \ddot{\boldsymbol{\theta}}^{lc} \\ \ddot{\boldsymbol{R}}^l \\ \ddot{\boldsymbol{\theta}}^l \end{bmatrix} \tag{3.99}$$

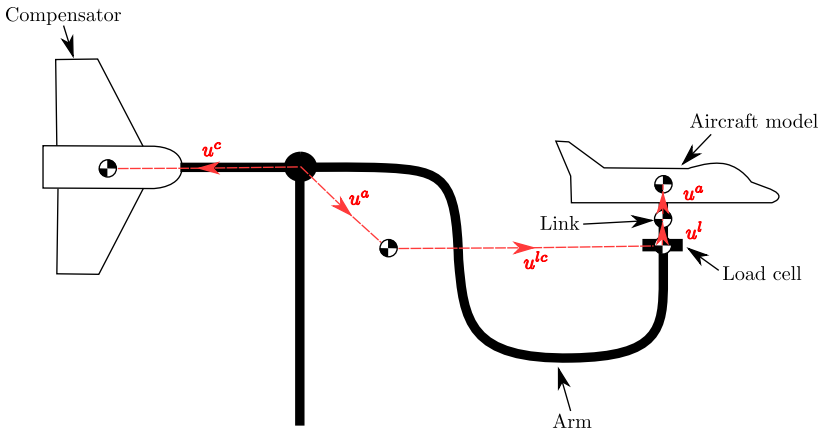

FIGURE 3.8. Manoeuvre rig body position vectors.

3.8 Aerodynamics mathematical model

This section describes the various aerodynamic models used with the simulation of the manoeuvre rig. Initial studies of the rig were done using a simple linear longitudinal aerodynamic model for the Hawk (Section 3.8.1) which was created from previous parameter estimation studies [11]. This model was used for the preliminary investigations into inertial and aerodynamic compensation of the rig presented in Section 7.2.1. A higher order polynomial model (Section 3.8.3) derived from CFD results acquired by collaborating with Nanjing University of Aeronautics & Astronautics was then created, which showed a good match with the linear model of the Hawk. The HHIRM aerodynamics model (Section 3.8.4) scaled to match the size of an airliner model being designed for testing on the manoeuvre rig was used to estimate load cell capacity requirements presented in Chapter 5. The aerodynamic model for the rig's compensator was also created by previous parameter estimation studies (Section 3.8.2). These various models for the Hawk will be compared with experimentally measured data using the load cell fitted onto

the manoeuvre rig (see Chapter 6). A linear aerodynamic model for an A-4D aircraft (Section 3.8.5) was used for the investigations into the effects of kinematic constraints on the motion of aircraft models which are presented in Chapter 4. The A-4D model was chosen since it is freely available for publication purposes and has features similar to the Hawk model. For all models, the aerodynamic forces and moments for both the aircraft model and compensator can be defined by

$$\begin{aligned} L &= \overline{q}SC_L, \\ Y &= \overline{q}SC_Y, \\ D &= \overline{q}SC_D, \\ l &= \overline{q}SbC_l, \\ m &= \overline{q}ScC_m, \\ n &= \overline{q}SbC_n, \end{aligned} \tag{3.100}$$

$$\overline{q} = \frac{1}{2}\rho V_0^2 \tag{3.101}$$

where L is the lift force, Y is the side force, D is the drag force, l, the rolling moment, m is the pitching moment, n is the yawing moment, $\overline{q}$ is the dynamic pressure, ρ is the air density, V_0 is the total wind speed, S is the reference wing area, b is the reference wing span, c is the reference chord, and C_x is the non-dimensional coefficient for load x . Note that the forces above are in the wind axes and the moments are in the body axes. Before these loads are inserted into the Equations 3.22, the forces needs to be transformed into the inertial/global axes. First they must be transformed onto the body axes by rotating through the angle of attack (α) and angle of sideslip (β). This can be achieved by calculating the transformation matrix (A) as shown in Appendix A by replacing the conventional rotation Euler angles with

$$\begin{aligned} \phi &= 0, \\ \theta &= \alpha, \\ \psi &= -\beta, \end{aligned} \tag{3.102}$$

where the definitions for α and β are

$$\begin{aligned} \alpha &= \tan^{-1}\left(\frac{V_z}{V_x}\right), \\ \beta &= \sin^{-1}\left(\frac{V_y}{V_0}\right), \\ V_0 &= \sqrt{V_x^2 + V_y^2 + V_z^2}. \end{aligned} \tag{3.103}$$

In the above equation V_x, V_y and V_z are the components of the total velocity in each direction of the body axes. Therefore, the forces in the body axes are

$$\boldsymbol{F}_{body} = A^T \boldsymbol{F}_{wind}. \tag{3.104}$$

Now the forces can be transformed again into the inertial axes with the known attitude angles of the body using the same method as above and inserted into Equations 3.22. The

following sections will describe the types of models used when calculating the non-dimensional load coefficients in Equation 3.100.

3.8.1 Linear aerodynamics model for the Hawk

A conventional linear longitudinal model was initially used for the Hawk for early studies of the rig dynamics. This model is expected to only be accurate in small angles about zero angle of attack (approximately in the range of $\pm 10^{\circ}$) when the air flow around the aircraft model is attached and well behaved. The coefficients for this model were obtained from preliminary parameter estimation studies done by a visiting researcher Z. Gong from the Nanjing University of Aeronautics and Astronautics. Since the model is linear, it is not capable of capturing any non-linear or time-dependent effects of the Hawk such as hysteresis or limit cycle oscillations. The equations for the model are shown below

$$C_{L_m} = C_{L_{0_m}} + C_{L_{\alpha_m}} \alpha_m + C_{L_{\delta_{e_m}}} \delta_{e_m} + C_{L_{q_m}} \frac{c}{2V_0} q_m \tag{3.105}$$

$$C_{D_m} = 0 \tag{3.106}$$

$$C_{m_m} = C_{m_{0_m}} + C_{m_{\alpha_m}} \alpha_m + C_{m_{\delta_{e_m}}} \delta_{e_m} + C_{m_{q_m}} \frac{c}{2V_0} q_m \tag{3.107}$$

where α_m is the angle of attack of the aircraft, δ_{e_m} is the aircraft elevator deflection, and q_m is the aircraft pitch rate. The values of each coefficient are shown in Chapter 6 in Tables 6.1 and 6.2 and Reference [11]. Note that this is an extremely simplified model and a better model must be created using the experimentally measured loads (shown in Chapter 6).

Note that this model was estimated by modelling the total moment about the arm gimbal. As a result, the lift and drag forces for the aircraft could not be estimated separately since they both contribute to the moment about the arm gimbal. The drag was assumed zero as the moment contribution by drag is small for small arm pitch angles. Therefore since the drag force would practically be a value above zero, it is expected that the lift force is overestimated by this model for positive arm pitch and underestimated for negative arm pitch angles (assuming the aircraft is producing positive lift). The induced component of the drag force could have been modelled since is it proportional to the lift force, however it would still be an underestimate of the total drag force.

3.8.2 Aerodynamic model for the compensator

The longitudinal model used for the compensator was

$$C_{L_c} = C_{L_{\alpha_c}} \alpha_c + C_{L_{\delta_{e_c}}} \delta_{e_c} + C_{L_{q_c}} \frac{b}{2V_0} q_c \tag{3.108}$$

$$C_{D_c} = 0 \tag{3.109}$$

$$C_{m_c} = 0 \tag{3.110}$$

where α_c is the angle of attack of the compensator, δ_{e_c} is the compensator elevator deflection, and q_c is the compensator/rig pitch rate. Note that since the compensator has four control surfaces, δ_{e_c} is the deflection of all of these surface equally where a positive δ_{e_c} is trailing edge down.

The coefficients for this model were obtained from preliminary parameter estimation studies done by the visiting researcher Z. Gong from the Nanjing University of Aeronautics and Astronautics. The value of each coefficient is shown in Appendix F. Similar to the linear aircraft model, the lift and drag forces cannot be estimated separately since they both contribute to the moment about the arm gimbal. Drag is assumed zero here as its moment contribution is small for small angles of the arm. The pitching moment of the compensator also could not be distinguished since it does not have a pitch freedom of its own. As a result, although this model may estimate the total moment created by the compensator about the arm gimbal to sufficient accuracy at small angles, it can be expected that the magnitude of the lift force generated by the compensator to be overestimated by this model since it has hidden contributions from the drag and pitching moment.

The lateral-directional model for the compensator is as follows. The side-force and yawing moments are similar to longitudinal model:

$$C_{Y_c} = C_{Y_{\beta_c}}\beta_c + C_{Y_{\delta_{r_c}}}\delta_{r_c} + C_{Y_{r_c}}\frac{b}{2V_0}r_c \tag{3.111}$$

$$C_{n_c} = 0 \tag{3.112}$$

where β_c is the angle of sideslip of the compensator, δ_{r_c} is the compensator rudder deflection, and r_c is the compensator/rig yaw rate. Note that since the compensator has four control surfaces, δ_{r_c} is the deflection of all of these surface equally where a positive δ_{r_c} is trailing edge left.

A nonlinear model for the rolling coefficient was used to include the aerodynamic effects of the rig support strut on the compensator. This model uses Fourier functions to fit experimentally obtained data [11]. The function can be written as

$$\begin{aligned}
C_{l_c} = {} & C_{l_c 0} + C_{l_{\phi_{c1}}}\cos(\phi_c k) + C_{l_{\phi_{c2}}}\sin(\phi_c k) \\
& + C_{l_{\phi_{c3}}}\cos(2\phi_c k) + C_{l_{\phi_{c4}}}\sin(2\phi_c k) \\
& + C_{l_{\phi_{c5}}}\cos(3\phi_c k) + C_{l_{\phi_{c6}}}\sin(3\phi_c k) \\
& + C_{l_{\phi_{c7}}}\cos(4\phi_c k) + C_{l_{\phi_{c8}}}\sin(4\phi_c k) \\
& + C_{l_{\delta_{a_{c11}}}}\tanh(C_{l_{\delta_{a_{c12}}}}\delta_{a_{c1}} - C_{l_{\delta_{a_{c13}}}}) + C_{l_{\delta_{a_{c14}}}} \\
& + C_{l_{\delta_{a_{c21}}}}\tanh(C_{l_{\delta_{a_{c22}}}}\delta_{a_{c2}} - C_{l_{\delta_{a_{c23}}}}) + C_{l_{\delta_{a_{c24}}}} \\
& + C_{l_{\delta_{a_{c31}}}}\tanh(C_{l_{\delta_{a_{c32}}}}\delta_{a_{c3}} - C_{l_{\delta_{a_{c33}}}}) + C_{l_{\delta_{a_{34}}}} \\
& + C_{l_{\delta_{a_{c41}}}}\tanh(C_{l_{\delta_{a_{c42}}}}\delta_{a_{c4}} - C_{l_{\delta_{a_{c43}}}}) + C_{l_{\delta_{a_{44}}}} \\
& + C_{l_{p_c}}\frac{b}{2V_0}p_c
\end{aligned} \tag{3.113}$$

where $C_{l_{c0-8}}$, k and $C_{l_{\delta_{a_{ci1-4}}}}$ are estimated constants, $\delta_{a_{ci}}$ is the aileron deflection and p_c is the compensator/rig roll rate where i represents each control surface of the compensator. This model also takes into account the drop-off in control surface power at higher deflection angles which occurs due to flow separation. All compensator coefficients are shown in Appendix F.

3.8.3 Higher order aerodynamics model for the Hawk

This higher order model for the Hawk was also used for early studies of the rig dynamics which uses aerodynamic coefficients estimated for discrete conditions using Computational Fluid Dynamics from Nanjing University of Aeronautics and Astronautics (see Appendix C). A digital half-model surface geometry of the Hawk was created by 3D scanning the model, therefore predicted aerodynamics is symmetric. The specific details of the computation method such as mesh generation, turbulence model and boundary conditions are unknown. The results are for a very small range of angle of attack of $-5°$ to $5°$. The data points were used to perform a surface fit (least squares method) on a third order Taylor series polynomial to capture the slight nonlinearity in a continuous function.

In the longitudinal sense, the lift coefficient (C_L) and pitching moment coefficient (C_m) can be assumed to be dependent on the four parameters: angle of attack (α), elevator deflection (δ_e), pitch rate (q), and acceleration in the body z-direction ($\dot{w}$ or $\dot{\alpha}$). The relationship between the aerodynamic coefficients and the two parameters q and w are assumed to be linear and their derivatives are estimated empirically [10, 64]. Similarly, the drag coefficient is assumed to be a function of α and δ_e only (their q and $\dot{w}$ drag derivatives are assumed to be negligible). The aerodynamic models used for lift, drag, and moment coefficients are as follows (numerical values and graphical illustrations are presented in Appendix C):

$$\begin{aligned} C_L = {} & C_{L_0} + (\alpha C_{L_\alpha} + \delta_e C_{L_{\delta_e}}) \\ & + (\alpha\delta_e C_{L_{\alpha\delta_e}} + \frac{1}{2}\alpha^2 C_{L_{\alpha\alpha}} + \frac{1}{2}\delta_e^2 C_{L_{\delta_e\delta_e}}) \\ & + (\frac{1}{3}\alpha\delta_e^2 C_{L_{\alpha\delta_e\delta_e}} + \frac{1}{3}\alpha^2\delta_e C_{L_{\alpha\alpha\delta_e}} + \frac{1}{6}\alpha^3 C_{L_{\alpha\alpha\alpha}} + \frac{1}{6}\delta_e^3 C_{L_{\delta_e\delta_e\delta_e}}) \\ & + q\frac{c}{V_0} C_{L_q} + \dot{w}\frac{c}{{V_0}^2} C_{L_{\dot{w}}} \end{aligned} \tag{3.114}$$

$$\begin{aligned} C_D = {} & C_{D_0} + (\alpha C_{D_\alpha} + \delta_e C_{D_{\delta_e}}) \\ & + (\alpha\delta_e C_{D_{\alpha\delta_e}} + \frac{1}{2}\alpha^2 C_{D_{\alpha\alpha}} + \frac{1}{2}\delta_e^2 C_{D_{\delta_e\delta_e}}) \\ & + (\frac{1}{3}\alpha\delta_e^2 C_{D_{\alpha\delta_e\delta_e}} + \frac{1}{3}\alpha^2\delta_e C_{D_{\alpha\alpha\delta_e}} + \frac{1}{6}\alpha^3 C_{D_{\alpha\alpha\alpha}} + \frac{1}{6}\delta_e^3 C_{D_{\delta_e\delta_e\delta_e}}) \end{aligned} \tag{3.115}$$

$$\begin{aligned} C_m = {} & C_{m_0} + (\alpha C_{m_\alpha} + \delta_e C_{m_{\delta_e}}) \\ & + (\alpha\delta_e C_{m_{\alpha\delta_e}} + \frac{1}{2}\alpha^2 C_{m_{\alpha\alpha}} + \frac{1}{2}\delta_e^2 C_{m_{\delta_e\delta_e}}) \\ & + (\frac{1}{3}\alpha\delta_e^2 C_{m_{\alpha\delta_e\delta_e}} + \frac{1}{3}\alpha^2\delta_e C_{m_{\alpha\alpha\delta_e}} + \frac{1}{6}\alpha^3 C_{m_{\alpha\alpha\alpha}} + \frac{1}{6}\delta_e^3 C_{m_{\delta_e\delta_e\delta_e}}) \\ & + q\frac{c}{V_0} C_{m_q} + \dot{w}\frac{c}{{V_0}^2} C_{m_{\dot{w}}} \end{aligned} \tag{3.116}$$

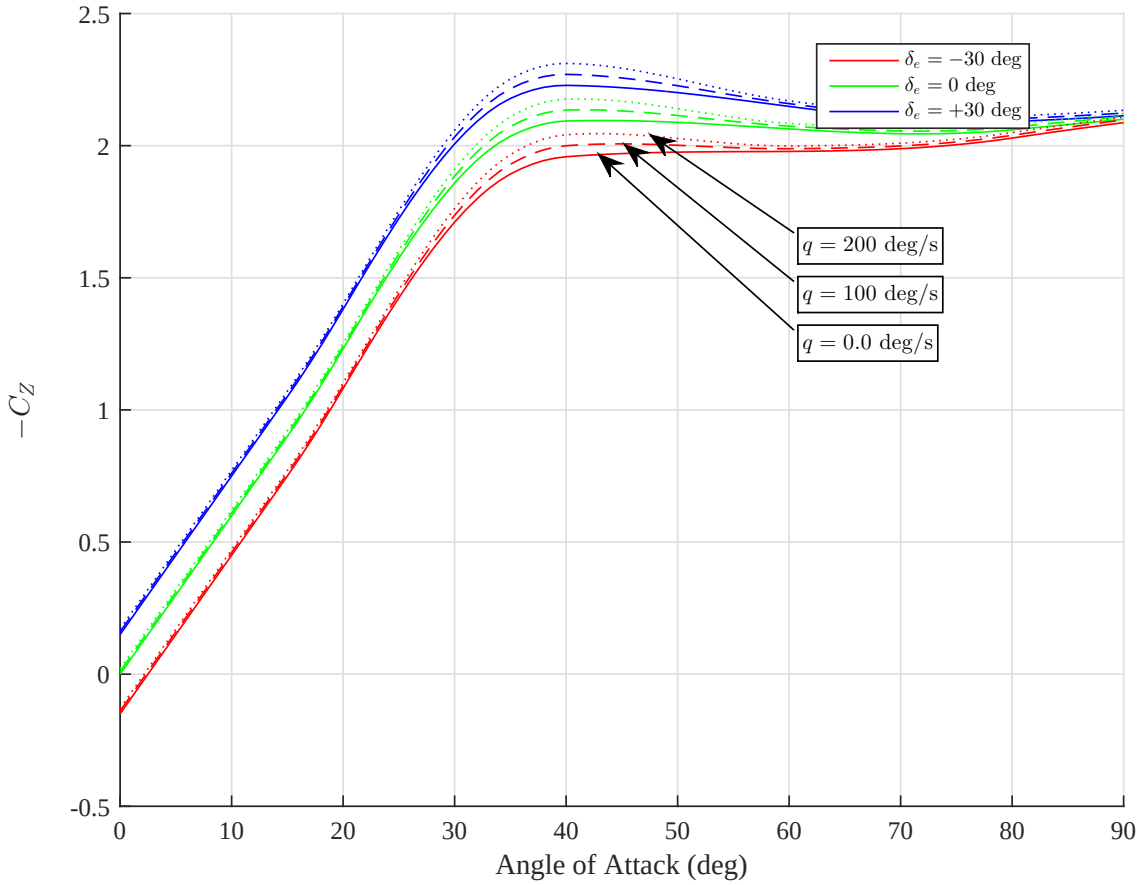

FIGURE 3.9. Dynamic lift overshoot modelled by HHIRM.

3.8.4 The HHIRM

The Hypothetical High Incidence Research Model (HHIRM [65]) scaled to match the size of a T-tail airliner model to be built for testing on the same rig was mainly used for acquiring load cell capacity requirements (in Chapter 5). This is a more complete aerodynamic model which include both the longitudinal and lateral directional aerodynamics models as well as dynamic phenomena such as lift overshoot and dynamic stalls, which would otherwise not be captured by a simple linear model. Dynamic lift overshoot can be thought to be mainly dependent on the pitch rate of the aircraft, angle of attack, and elevator deflection. The maximum lift can be expected to be observed when the aircraft pitch rate and elevator deflection are at their highest. This is shown in Figure 3.9 where the maximum lift occurs at an angle of attack of 40°. This model is valid for low speed conditions ($Mach < 0.4$).

The HHIRM is an asymmetric aerodynamic model, therefore for a symmetric manoeuvre, for example, using symmetric elevator deflections will lead to significant lateral-directional dynamics once large angles of attack are reached. This was simulated on Simulink and unstable behaviour was observed. In order to simulate high load case scenarios without the aircraft going unstable

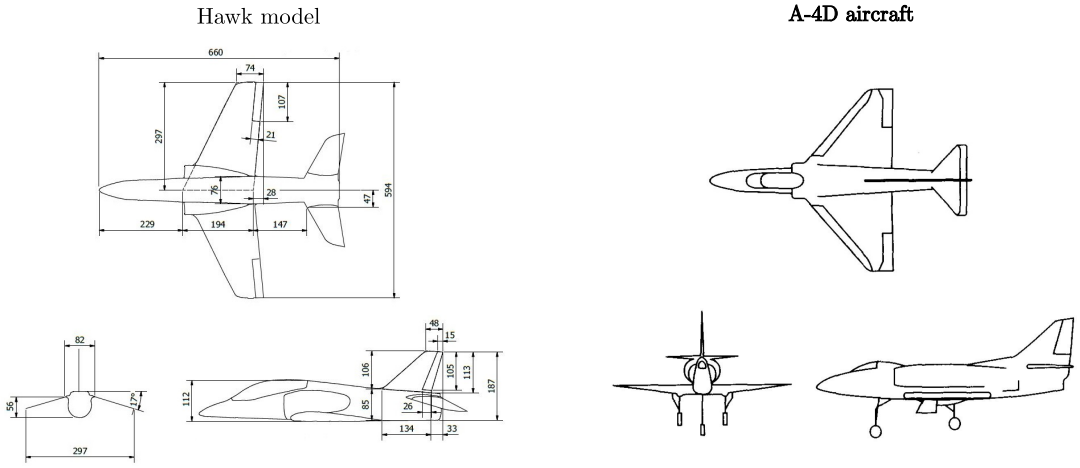

FIGURE 3.10. Planform views of the Hawk model and A-4D aircraft.

the HHIRM was made symmetric. This was done by setting lateral-directional aerodynamic moments to zero, for example for a pure pitching motion, the rolling and yawing moments were set to zero. Note that it was not necessary to set lateral-directional forces to zero because the simulation constrained the aircraft's c.g. to a fixed point.

3.8.5 The A-4D model

The aerodynamic model for the A-4D fighter aircraft (at sea level and Mach 0.4) [66] scaled to the Hawk model was primarily used to investigate the kinematic effects of the manoeuvre rig on the aircraft model dynamics. This study is presented in Chapter 4. The longitudinal and lateral directional models consist of conventional first order linear stability derivatives as shown below:

$$\begin{gathered} C_L = C_{L_0} + C_{L_\alpha}\alpha + C_{L_{\dot\alpha}}\frac{c}{2V}\dot\alpha + C_{L_{\delta_e}}\delta_e, \quad C_D = C_{D_0} + C_{D_\alpha}\alpha, \quad C_Y = C_{Y_\beta}\beta + C_{Y_{\delta_r}}\delta_r, \\ C_l = C_{l_\beta}\beta + C_{l_p}\frac{b}{2V}p + C_{l_r}\frac{b}{2V}r + C_{l_{\delta_a}}\delta_a + C_{l_{\delta_r}}\delta_r, \\ C_m = C_{m_\alpha}\alpha + C_{m_{\dot\alpha}}\frac{c}{2V}\dot\alpha + C_{m_q}\frac{c}{2V}q + C_{m_{\delta_e}}\delta_e, \\ C_n = C_{n_\beta}\beta + C_{n_p}\frac{b}{2V}p + C_{n_r}\frac{b}{2V}r + C_{n_{\delta_a}}\delta_a + C_{n_{\delta_r}}\delta_r. \end{gathered} \tag{3.117}$$

The numerical values for the aerodynamic derivatives and the scaled model properties are shown in Appendix B. Figure 3.10 shows the planform comparison between the Hawk model and the A-4D aircraft.

3.9 Friction model

Two friction models have been used with the manoeuvre rig simulation. The first is a simplified variation of the friction model developed in reference [10] and is described below. For the

longitudinal motion of the rig, the model used was

$$M^i_{fr} = \text{sign}\left(\dot{\theta}^i\right) k^i_1 + k^i_2 \dot{\theta}^i, \tag{3.118}$$

where M^i_{fr} is the friction moment in each gimbal i (in Nm), $\dot{\theta}^i$ is the rotation rate (in rad/s) and k^i_{1-2} are estimated constants. The values of the constants are given in Table 3.1. The more recent second model is developed in reference [11] by performing parameter estimation on free oscillation experiments for each degree of freedom of the rig. The friction model is written as

$$M^i_{fr} = k^i_3 \dot{\theta}^i + k^i_4 \tanh\left(k^i_5 \dot{\theta}^i\right) \tag{3.119}$$

where k^i_{3-5} are estimated constants and $\dot{\theta}^i$ is the rotation rate. The values for the rig arm gimbal have been re-estimated for this work using forced oscillation in all degrees of freedom and are shown in Table 3.2. This estimation process is described in Section 5.6. The values shown for the aircraft model gimbal are those estimated in reference [11]. With the addition of the load cell, it is possible to directly measure the friction moment in the aircraft model gimbal pitch and roll axes. Note that the rotation rates for the aircraft model gimbal are relative to the rig arm. Friction is inserted into the equations of motion as an external moment.

TABLE 3.1. Simple friction model coefficients for Equation 3.118.

	Rig arm gimbal	**Aircraft model gimbal**
k^i_1	0.0309	0.000977
k^i_2	0.00410	0.000394

TABLE 3.2. Static continuously differentiable friction model coefficients for Equation 3.119.

i	**Rig arm gimbal**			**Aircraft model gimbal**	
	ϕ_a	θ_a	ψ_a	ϕ_m	θ_m
k^i_3	40.43×10^{-3}	1.379×10^{-3}	802.1×10^{-3}	12.98×10^{-3}	35.97×10^{-3}
k^i_4	2.291×10^{-3}	12.62×10^{-3}	388.5×10^{-3}	4.09×10^{-3}	0.24×10^{-3}
k^i_5	3.483×10^3	7.783	72.10	406.3	112×10^3

3.10 Servo models

This section describes the model used to represent the control surface actuation in the manoeuvre rig compensator as well as in the Hawk aircraft. The model is defined as the transfer function:

$$\frac{\delta(s)}{\delta^c(s)} = \frac{K_1 K_2}{s^2 + K_2 s + K_1 K_2} \tag{3.120}$$

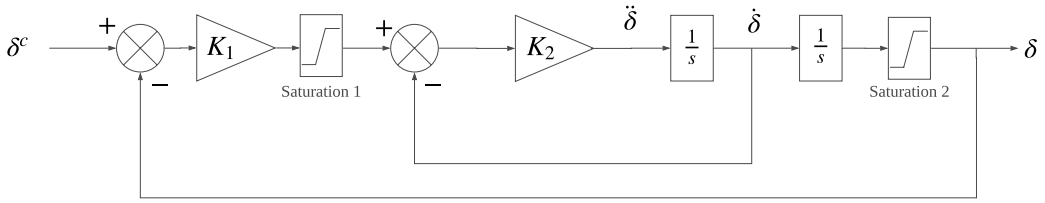

FIGURE 3.11. Servo model block diagram.

where δ^c is the commanded control surface deflection, δ is the actual response, K_1 and K_2 are estimated constants. The block diagram used for this model is presented in Figure 3.11. The values for the estimated constants and saturations are presented in Appendix D.

3.11 Implementation of the equations of motion

This section details the implementation of the equations of motion described in the previous sections of this Chapter in Matlab®/Simulink®. The main body of the equations are placed inside of a Matlab® function with the input being the states and velocity vectors ($\boldsymbol{q}$ and $\dot{\boldsymbol{q}}$ respectively), and the output being the acceleration vector ($\ddot{\boldsymbol{q}}$). The output acceleration vector is integrated twice to produce the states vector. The states and velocity vectors are looped back into the main function. Initial conditions are set at each integrator block. Algebraic loops are avoided with the use of initial condition blocks (further explained in Appendix G). The block diagram outline of the Simulink® model is shown in Figure 3.12. Various solvers and time step sizes were studied and the ode45 Runge-Kutta solver with a fixed time step of 0.001 seconds was chosen to be sufficiently accurate. The Simulink® 3D Animation Viewer was used to animate the simulated responses for visual aid, as shown in Figure 3.13. In the animation, each body is placed individually with its position and rotation angles. As such, it proved to be a useful tool to visually validate the equations and motion as well as the constraint equations.

3.12 Summary

This chapter details the various mathematical models derived and used during the course of the PhD. First a preliminary linear state-space longitudinal model for the manoeuvre rig was presented. A more complete mathematical model for the rig is required in order to capture the necessary coupled dynamics. The next section described the reasoning for the chosen coordinate system of the complete model. This was followed by the derivation of the complete nonlinear rigid-body mathematical model for the manoeuvre rig which covers both longitudinal and lateral-directional dynamics. This model requires constraint equations, which were described in the next

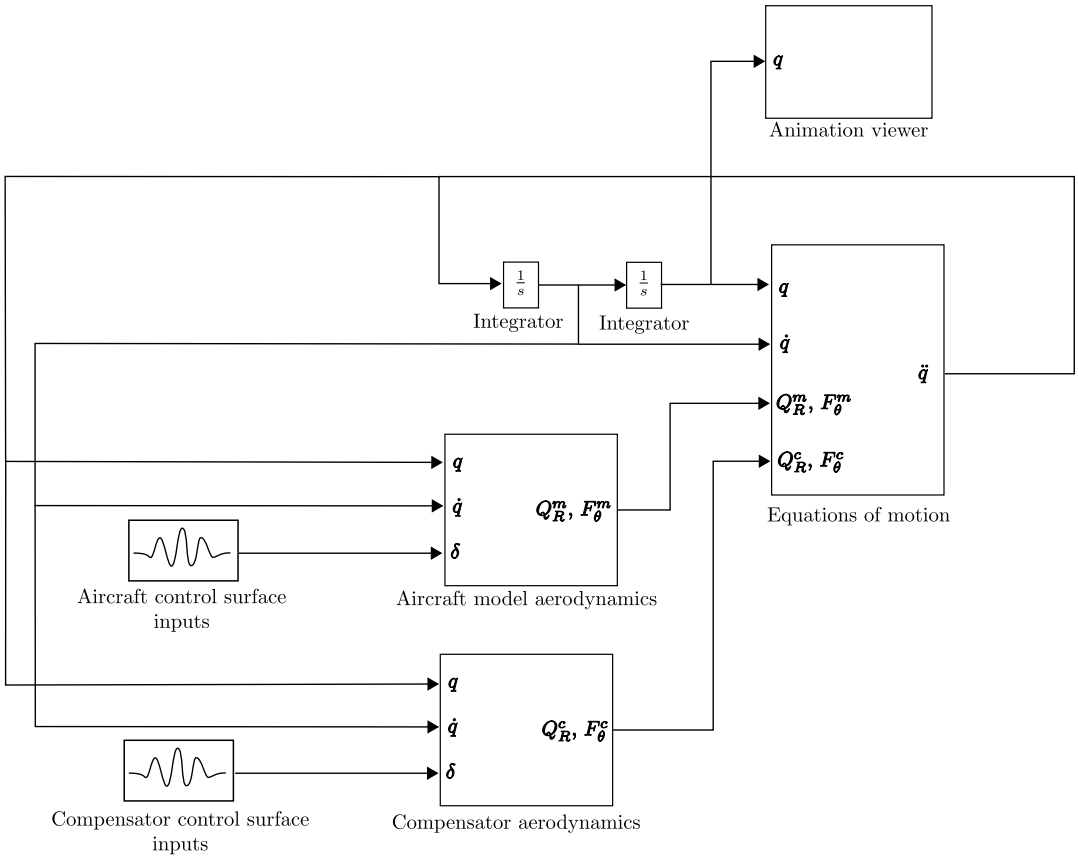

FIGURE 3.12. Simulink® model outline.

section. The advantages of using quaternions to represent rotations were described next. This was followed by the definitions of the various aerodynamic models used during the course of the PhD. This was followed by sections describing the models used to represent friction and control surface actuation. Finally, the implementation of the equations in Matlab®/Simulink® was described in the last section. Individual mathematical models will be referred to in the relevant sections in forthcoming chapters when they are used. Table 3.3 shows where each of the models derived in this Chapter was used. The numerical values of coefficients are shown in the appendices.

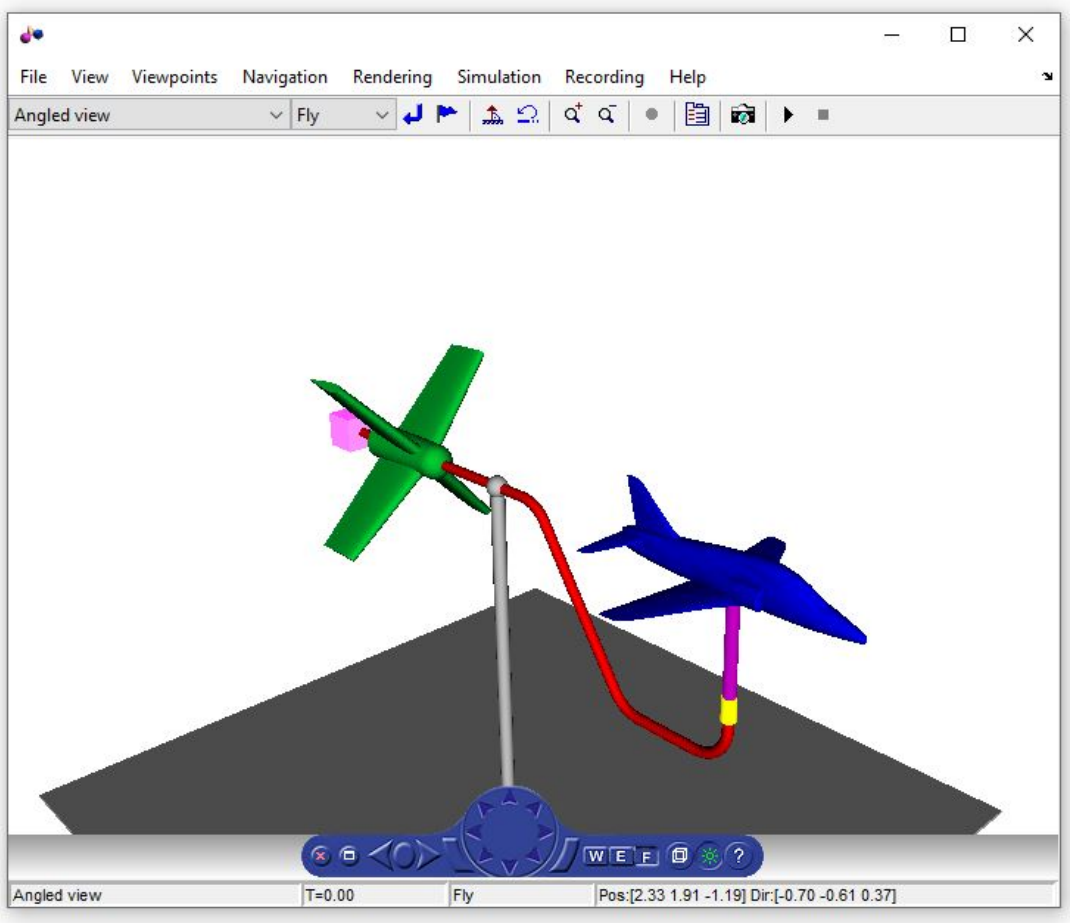

FIGURE 3.13. Simulink® Animations Viewer for the manoeuvre rig.

TABLE 3.3. Mathematical model usage throughout this thesis.

Mathematical model	**Section where the model is used**
3.2 2D linear state-space mathematical model	**7.2.1** Preliminary experimental results
3.4 3D rigid-body mathematical model of the manoeuvre rig **3.6** Rig constraints equations	**4.3** 3D analysis of kinematic constraints **5.2** Estimation of load cell requirements **5.6** Rig mass, inertia and gimbal friction estimation **6.3** Hawk dynamic tests **7.3** Kinematic compensation
3.8.1 Linear aerodynamics model for the Hawk	**4.2** Longitudinal kinematic analysis using a simplified 2D model **7.2.1** Preliminary experimental results
3.8.2 Aerodynamic model for the compensator	**5.2** Estimation of load cell requirements **7.2.1** Preliminary experimental results
3.8.3 Higher order aerodynamics model for the Hawk	**6.2** Hawk static aerodynamic measurements
3.8.4 The HHIRM	**5.2** Estimation of load cell requirements
3.8.5 The A-4D model	**4.3** 3D analysis of kinematic constraints
3.9 Friction model	**4.4** Practical aspects of compensation **5.6** Rig mass, inertia and gimbal friction estimation
3.10 Servo models	**5.2** Estimation of load cell requirements **7.2.1** Preliminary experimental results

CHAPTER 4

INVESTIGATIONS ON RIG KINEMATIC EFFECTS ON AIRCRAFT MODEL DYNAMICS

4.1 Introduction

An objective of the manoeuvre rig concept is to physically simulate free flight in order to study the behaviour of aircraft models such as at the edge of the flight envelope (upset regions) and for model identification purposes [10]. This chapter presents the investigations carried out on the kinematic effects of the manoeuvre rig on the overall dynamic behaviour of the aircraft model. In this chapter, these investigations are carried out computationally by simulating the mathematical models described in Sections 3.4 and 3.6.5. Experimental findings are presented in Chapter 7. The manoeuvre rig is currently still a novel concept and this study is important in order to identify its capabilities and limitations, and how it affects the dynamics of the aircraft model. Specifically the effects that are considered here centre around the kinematic constraint the rig applies onto the aircraft model.

The aerodynamic forces produced by the aircraft model induce a rotation of the manoeuvre rig's arm rather than a translation of the model centre of gravity. Aerodynamic and inertial loads created by the rig will also contribute to the rig-induced kinematics. The resulting change in motion affects the change in aerodynamic loads, which is in turn again coupled to the aircraft response.

The investigation starts by first comparing in 2D the differences in response between a free-flying/unconstrained aircraft model and a model constrained to fly on a line and on an arc. A compensation concept is derived with the aim of reducing these kinematic effects created by the arc constraint in order to better match the response of a free-flying aircraft model. The assessment of the kinematic effects are then extended to 3D in the following section for a plane

and spherical constraints, which are the 3D equivalent of the line and arc constraints respectively. The compensation concept is then re-derived in 3D. The responses are compared using several methods: time history plots, trajectory plots, root mean square errors and perceived changes to the aerodynamic coefficients of the aircraft model. Note that in this chapter, aerodynamic and inertial effects of the manoeuvre rig are assumed to have been ideally compensated for by an perfectly controlled compensator, hence the observed changes are purely due to the imposed kinematic constraints. This is done by not including the rig itself in the mathematical model and constraining the aircraft in each degree-of-freedom (DOF) using the equations described in section 3.6.5. Aerodynamic and inertial coupling of the rig itself are studied in Chapter 7. Practical consequences such as communication delays and compensator control surface actuation lags will also be considered here.

4.2 Longitudinal kinematic analysis using a simplified 2D model

Dynamic testing rigs have certain DOFs allowing the model aircraft to either heave, sway, pitch, roll, or yaw, or any combination of DOFs depending on the type of rig. This allows for the physical simulation of a free-flying model aircraft, to an extent. However, these DOFs also impose kinematic constraints on the motion of the model aircraft, which can cause its response to be different to that of an unconstrained free-flying aircraft. Compared to a free-flying model aircraft, the response of a constrained model aircraft will vary depending on the type of kinematic constraint applied. For example, the manoeuvre rig applies a constraint via its arm such that the aircraft model is made to always follow an arc in the longitudinal sense, or a surface of a sphere when including lateral-directional motion as the arm rotates about its gimbal.

In this section, two kinematic constraints will be investigated and compared to a free-flying model aircraft (both in the longitudinal sense): a vertical line constraint and an arc constraint (as in the current manoeuvre rig). The case of the vertical line constraint will be equivalent to the arc constraint with an infinite radius as shown in Section 3.6.5.3. All comparisons here are done by numerical simulation of the subscale Hawk model using Matlab Simulink. The wind tunnel air flow speed is $30m/s$ and air density is $1.225kg/m^3$.

4.2.1 Simplified longitudinal equations of motion for the aircraft model

A basic nonlinear mathematical model of the aircraft is created here for initial analysis. It models the motion of the aircraft in the xz plane and pitch rotation about the y axes which is assumed to be coincident with the aircraft model's centre of gravity. All external aerodynamic loads, thrust, and reaction forces act through the centre of gravity. Note that thrust is assumed to act in the body axes x direction, and act through the centre of gravity. The wind tunnel freestream direction is horizontal (as in a standard wind tunnel). The variables used to describe the aircraft's motion

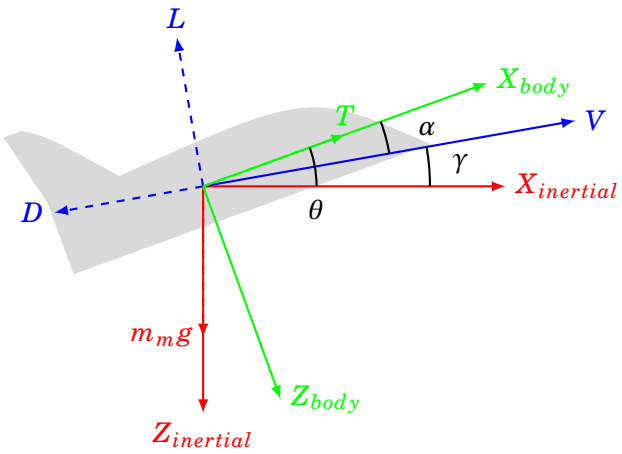

FIGURE 4.1. Reference axes and external forces.

are x, z, and θ. x and z represent the aircraft's forward and downward perturbations, respectively, relative to the inertial frame. θ is the pitch angle relative to the horizontal. Their respective velocities are $\dot{x}$, $\dot{z}$, and q. Their respective accelerations are $\ddot{x}$, $\ddot{z}$, and $\dot{q}$.

The wind velocity in the aircraft's body axis is given by

$$u_{wind} = (\dot{x} + V_0)\cos\theta - \dot{z}\sin\theta \tag{4.1}$$

$$w_{wind} = (\dot{x} + V_0)\sin\theta + \dot{z}\cos\theta \tag{4.2}$$

where V_0 is the velocity of the free stream wind. The angle of attack is

$$\alpha = \tan^{-1}\left(\frac{w_{wind}}{u_{wind}}\right) \tag{4.3}$$

The aerodynamic forces, thrust and weight now need to be resolved into the inertial axis which gives the external forces acting on the aircraft (see Figure 4.1). Any reaction forces present due to kinematic constraints will be added to the external forces, giving the total forces in the inertial frame (see Section 4.2.2).

The forces in the body axis (excluding the weight) are given by

$$X_{body} = T - D\cos\alpha + L\sin\alpha \tag{4.4}$$

$$Z_{body} = -D\sin\alpha - L\cos\alpha \tag{4.5}$$

Therefore, the total external forces in the inertial axis are

$$X_{inertial} = X_{body}\cos\theta + Z_{body}\sin\theta \tag{4.6}$$

$$Z_{inertial} = m_m g - X_{body}\cos\theta + Z_{body}\sin\theta \tag{4.7}$$

If kinematic constraints are present, their reaction forces are added:

$$X_{total} = X_{inertial} + X_{reaction} \tag{4.8}$$

$$Z_{total} = Z_{inertial} + Z_{reaction} \tag{4.9}$$

The aircraft's acceleration can then be found by

$$\ddot{x} = \frac{X_{total}}{m_m} \tag{4.10}$$

$$\ddot{z} = \frac{Z_{total}}{m_m} \tag{4.11}$$

$$\dot{q} = \frac{m}{I_{yy}} \tag{4.12}$$

The above differential equations can now be integrated to solve for the motion variables x, z and θ.

The linear aerodynamic model for the Hawk presented in Section 3.8.1 is used here but with the addition of a simple model for the induced drag instead of assuming drag to be negligible, as shown below. Note that profile drag (C_{D_0}) is neglected since this parameter has not been measured or estimated at this stage. As a result, the total drag modelled here is underestimated.

$$L = \frac{1}{2}\rho V^2 S C_{L_m} \tag{4.13}$$

$$D = \frac{1}{2}\rho V^2 S C_{D_m} \tag{4.14}$$

$$m = \frac{1}{2}\rho V^2 S c C_{m_m} \tag{4.15}$$

where

$$C_{L_m} = C_{L_{0_m}} + C_{L_{\alpha_m}}\alpha_m + C_{L_{\delta_{e_m}}}\delta_{e_m} + C_{L_{q_m}}\frac{c}{2V_0}q_m \tag{4.16}$$

$$C_{D_m} = \frac{{C_{L_m}}^2}{\pi A R e} \tag{4.17}$$

$$C_{m_m} = C_{m_{0_m}} + C_{m_{\alpha_m}}\alpha_m + C_{m_{\delta_{e_m}}}\delta_{e_m} + C_{m_{q_m}}\frac{c}{2V_0}q_m \tag{4.18}$$

$$V = \sqrt{(\dot{x} + V_0)^2 + \dot{z}^2}\,. \tag{4.19}$$

$AR = b^2/S$ is the model's wing aspect ratio (has a value of 4.15 for the Hawk) and e is the Oswald efficiency coefficient (its value is assumed to be one).

4.2.2 Simplified longitudinal constraint reaction forces

Kinematic constraints apply an additional external reaction force on the aircraft. The constraints investigated here are (see Figure 3.6):

1. Vertical line constraint

2. Arc constraint of radius $0.8m$

Note that here all inertial or aerodynamic effects of the rig are assumed to be ideally compensated for, hence the reaction forces are purely due to the kinematic constraints. Also the friction created by the aircraft gimbal is assumed to be negligible. The 3D equivalent constraint of the vertical line is the planar constraint derived in Section 3.6.5.3 and the 3D equivalent of the arc constraint is the spherical constraint derived in Section 3.6.5.2.

4.2.2.1 Vertical line constraint

When the aircraft is constrained on a vertical line, the total external forces will be reduced to only the forces in the vertical direction, i.e. $X_{total} = 0$. Therefore using equation 4.8:

$$X_{reaction} = -X_{inertial} \tag{4.20}$$

$$Z_{reaction} = 0 \tag{4.21}$$

4.2.2.2 Arc constraint

The reaction force due to an arc constraint acts purely in the radial direction. This radial reaction force consists of two components, both of which will contribute to the total tangential and radial (centripetal) parts of the aircraft's acceleration required for nonuniform circular motion. The first component (acting radially inwards) ensures that the total inertial force always acts in the tangential direction (this is responsible for changing speed along the circular path):

$$R_{radial_1} = X_{inertial}\cos\theta_r - Z_{inertial}\sin\theta_r \tag{4.22}$$

where $\theta_r = \tan^{-1}(-z/x)$. The second is the centripetal force (this is responsible for maintaining the circular path):

$$R_{radial_2} = mr\omega^2 \tag{4.23}$$

where $\omega = \sqrt{\dot{x}^2 + \dot{z}^2}/r$ and $r = 0.8m$. Therefore the reaction forces in the inertial frame are

$$X_{reaction} = -\left(R_{radial_1} + R_{radial_2}\right)\cos\theta_r \tag{4.24}$$

$$Z_{reaction} = \left(R_{radial_1} + R_{radial_2}\right)\sin\theta_r \tag{4.25}$$

4.2.3 Response comparison

This section presents and compares the aircraft responses for the free-flying/unconstrained case, line constrained, and arc constrained aircraft. Since most aircraft models produced for wind tunnel testing do not have the ability to produce thrust (such as the Hawk model) the constrained responses without thrust are also presented. Thrust is always included for the unconstrained aircraft responses. In the cases where thrust is included, it is held constant at the initial trim

value. The responses for a doublet elevator input are shown in Figure 4.2 and the responses for a Morlet wavelet elevator input are shown in Figure 4.3. Both these inputs are used to mainly excite the short-period modes of the Hawk model (which is about 0.8 Hz). The Morlet wavelet (defined as a zero mean oscillation) is scaled to have a centre frequency of 0.8 Hz.

Both figures show that the beginning of the short period pitch and heave response is not adversely affected by the presence of constraints. However, the long period motion is seen to be severely affected. The long period (phugoid) mode is caused by the aircraft's oscillation in forward velocity (u) which couples with aircraft pitch (θ) and height (z). Both the line and arc constraints obstruct this variation in u thus influencing the long period response. Section 4.2.4 investigates aircraft response with variable thrust to maintain a constant wind speed and ground speed.

An additional arc constrained response for the case where $X_{inertial}$ (Equation 4.6) is set to zero is also shown. Comparing with the line constrained response, any difference in motion is caused solely by motion in the x direction because of the circular path. It can be seen that this motion has a negligible effect on the pitch response but creates a slight deviation in the heave (z) response because $X_{inertial}$ is small.

Excluding thrust results in negligible change to the line constrained response. However, the arc constrained response is adversely affected. Excluding thrust increases the overall force in the negative x direction increasing the magnitude of $X_{inertial}$ (due to the aircraft's drag). This creates a destabilizing moment about the centre of the circular path which is large enough to make the aircraft swing around the full path. This is also the reason for the additional deviation, while including thrust, from the line constrained response caused due to a non-zero $X_{inertial}$. Knowledge of the x reaction force could be used to counteract this moment by using the compensator in the manoeuvre rig, which is investigated further in Section 4.2.5.

4.2.4 Free-flight with controlled speed

It has been shown that kinematic constraints impose velocity restrictions affecting the overall response of the aircraft. For comparison, the aircraft response with controlled speed will be investigated. This is achieved by ideally varying the thrust in order to maintain a desired speed. The previously shown unconstrained response has a constant thrust acting on the aircraft required for initial trim. This meant that any changes to its velocity was due to variations in lift, drag, and pitching moment only.

The two aircraft speeds will be explored: constant air speed and constant ground speed. The thrust required to achieve these speeds are shown below.

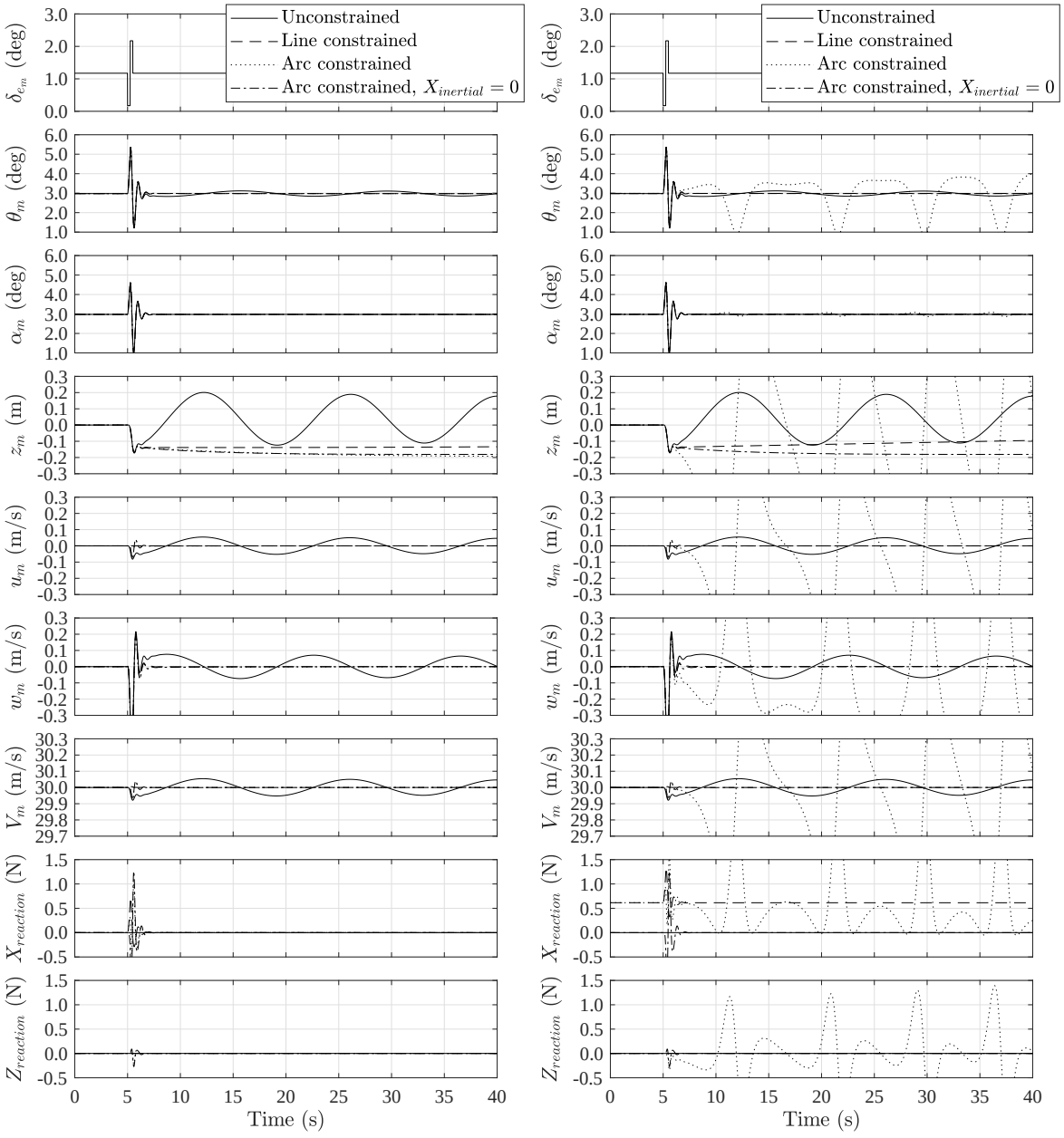

(a) Including constrained aircraft constant thrust

(b) Excluding constrained aircraft constant thrust

FIGURE 4.2. Response to an elevator doublet input.

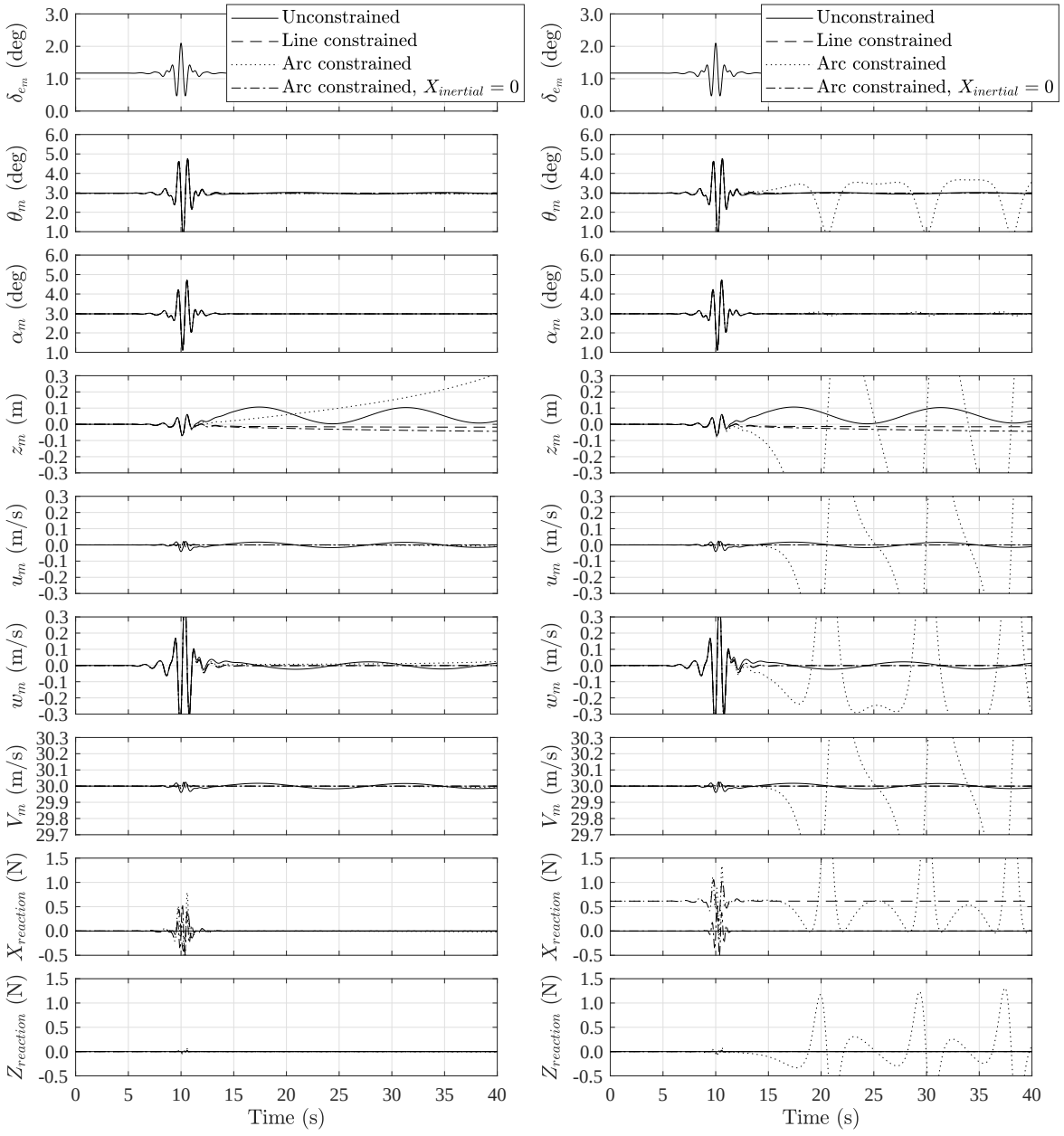

(a) Including constrained aircraft constant thrust

(b) Excluding constrained aircraft constant thrust

FIGURE 4.3. Response to an elevator wavelet input.

4.2.4.1 Constant airspeed

In order to keep the velocity in the wind axis constant, the forces in the wind axes x direction must be zero (for zero acceleration). Using Figure 4.1, the thrust required is

$$T = \frac{D + m_m g \sin\gamma}{\cos\alpha} \tag{4.26}$$

where $\gamma = \theta - \alpha$ is the flight path angle.

4.2.4.2 Constant ground speed

Similar to thrust required for constant airspeed, in order to keep the velocity in the inertial axes constant, the forces in the inertial axes x direction must be zero. Hence the thrust required is

$$T = \frac{D\cos\gamma + L\sin\gamma}{\cos\theta} \tag{4.27}$$

where $\gamma = \theta - \alpha$ is the flight path angle.

4.2.4.3 Response comparison

Figure 4.4 shows the speed controlled responses along with the line constrained responses for the cases with and without thrust. For comparison, the previous unconstrained response is also shown where the thrust is constant at the initial trim value. Note that for the case of the line constrained with thrust, the thrust is held at a constant value. The difference between the line constrained cases with and without thrust is caused by slightly different initial trim conditions and a component of thrust in the vertical direction. It can be seen that pitch responses for all cases are nearly identical. However, both unconstrained speed controlled responses drift upwards and show divergence in heave, and the unconstrained constant thrust (no speed control) response shows the phugoid mode. The divergence in the unconstrained speed controlled aircraft is due to an additional component of thrust present in the z direction compared to the line constrained aircraft without thrust, since the line constraint is artificially providing the x component of thrust. This component of thrust in the z direction changes as the requirement of thrust in the aircraft's body axes changes in order to keep the total force in the x direction zero and maintain the constant ground speed. This additional z component of thrust may be provided by the rig itself to an extent, for example by using the compensator on the manoeuvre rig. It should be noted that the divergent response in heave would indicate a required time limit for experiments to avoid the physical limits of the test rig.

The case of the line constrained aircraft is similar to the case of the aircraft flying at constant ground speed since both have purely vertical heave motions. When examining the difference between the line constrained reaction forces (without thrust) and unconstrained thrust for constant ground speed, this additional z component can be identified. From Equations 4.4, 4.5,

4.6, 4.20, and 4.21, the reaction forces in the inertial axes imposed by the line constraint (without thrust) are

$$X_{reaction} = D\cos\alpha\cos\theta - L\sin\alpha\cos\theta + D\sin\alpha\sin\theta + L\cos\alpha\sin\theta \quad (4.28)$$

$$Z_{reaction} = 0 \quad (4.29)$$

and the components of thrust required for constant ground speed in the inertial axes are

$$T_x = D\cos\gamma + L\sin\gamma \quad (4.30)$$

$$T_z = -\left(D\cos\gamma + L\sin\gamma\right)\tan\theta \quad (4.31)$$

Since $\gamma = \theta - \alpha$, trigonometric identities can be used to prove that Equations 4.28 and 4.30 are identical. Hence the difference in response is due to the additional vertical thrust component shown in Equation 4.31: adding this component of thrust as an external force onto the line constrained aircraft will make the heave response match with the unconstrained aircraft at constant ground speed exactly. This component can be artificially induced to an extent by creating a moment via the manoeuvre rig's compensator. This compensation would only be valid for small heave motions since the manoeuvre rig's arm is an arc constraint.

4.2.5 Compensation concept for the arc constraint in 2D

The previous section showed that it is possible to simulate a free-flying aircraft at constant ground speed on a line constrained rig. This section will study the same concept on an arc constraint such as on the manoeuvre rig. The manoeuvre rig is equipped with an aerodynamic compensator capable of inducing aerodynamic moments on the rig. This means that the rig is capable of only applying tangential forces on the aircraft model. The effects of the arc constraint applied by the manoeuvre rig on the overall aircraft response is presented here. A compensation concept to reduce the kinematic effects is also derived which can also artificially induce the effects of thrust discussed in Section 4.2.4.3 by applying a tangential external compensation force ($F_c{}^*$) which can be created by the manoeuvre rig's compensator.

Initially, it will be assumed that all inertial and aerodynamic properties of the manoeuvre rig are ideally compensated for by an ideally responsive compensator. Aircraft model gimbal friction is also assumed to be negligible. Figure 4.5 shows the radial reaction forces (solid green arrows) created by the arc constraint converting the external forces (dashed red arrows) acting on the aircraft into tangential forces (solid blue arrows). Note that this image is not to scale and the magnitudes of the forces are not representative; its purpose is purely for illustration and to aid in the derivation of the required tangential compensator force. The subscript in denotes that the external forces are in the inertial frame of reference.

For the case of the line constraint, it should be noted that the total force in the inertial axes x direction was zero. Hence, X_{in} does not have any influence on the aircraft response. This concept will be used with the arc constraint to reduce the effect of this kinematic constraint

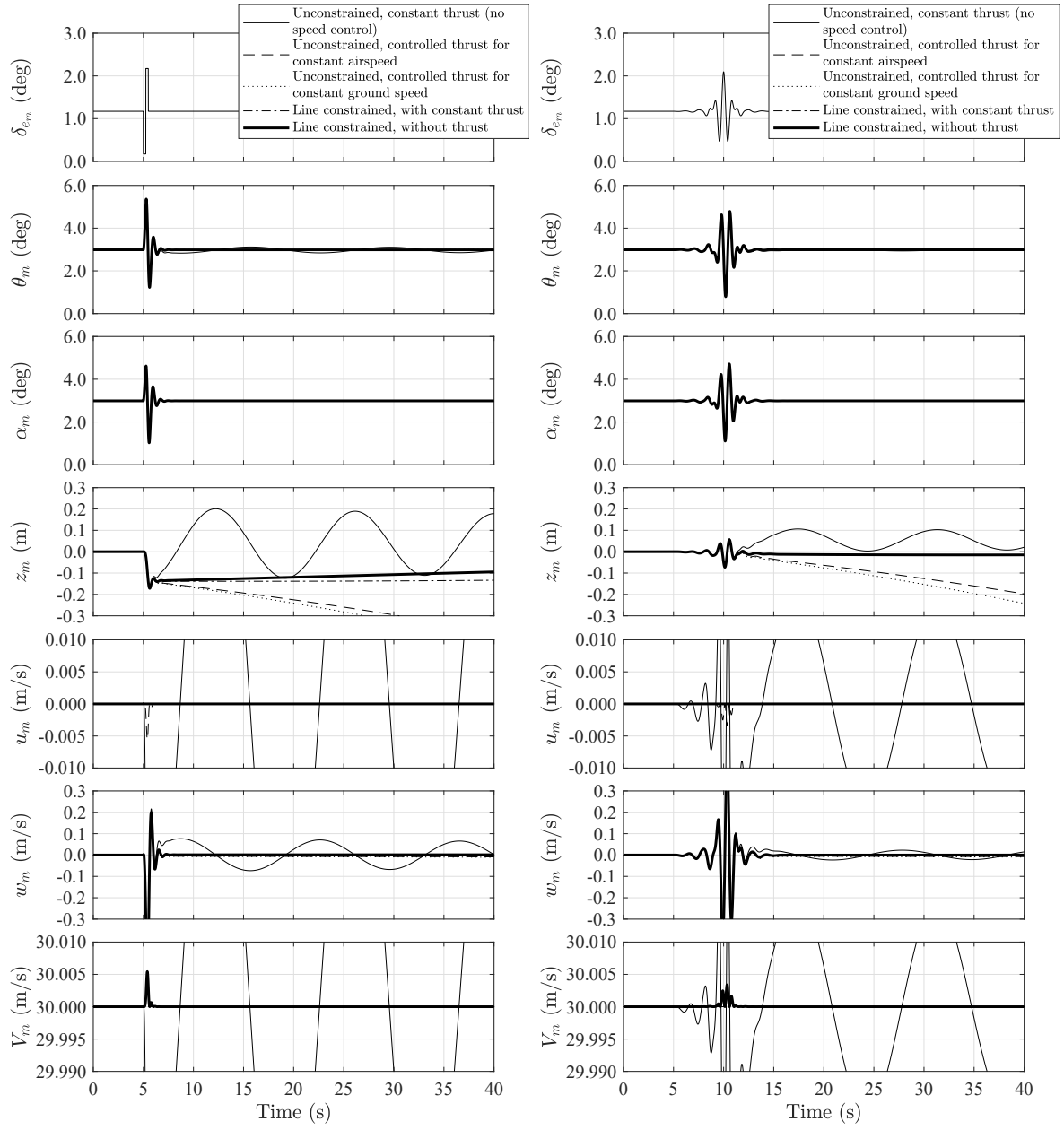

(a) Doublet response

(b) Wavelet response

FIGURE 4.4. Aircraft response with controlled speed.

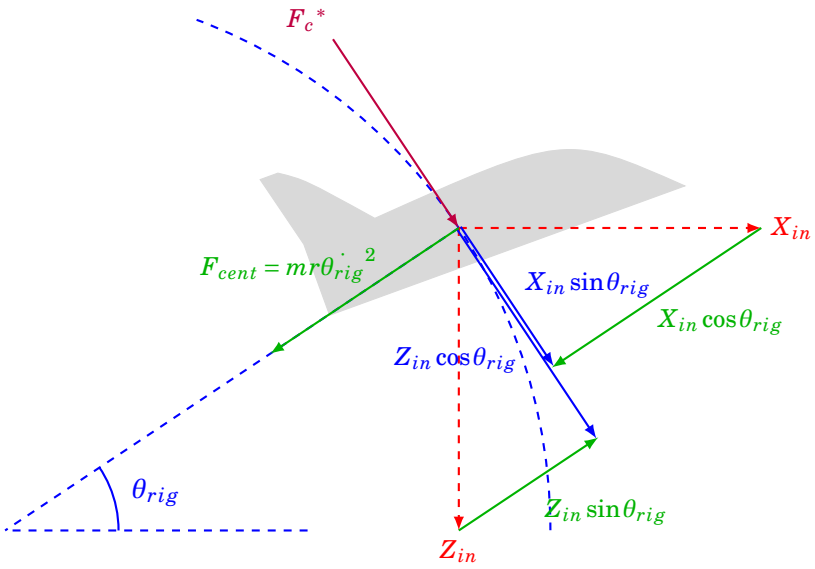

FIGURE 4.5. Reaction forces applied on the aircraft by an arc constraint.

by cancelling the tangential component of X_{in} using the compensator force $F_c{}^*$. Therefore the required external compensation force is

$$F_c{}^* = -X_{in}\sin\theta_a \tag{4.32}$$

where θ_a is the rig arm's pitch angle (which is the same as θ_{rig} in Figure 4.5). From Figure 4.5, the following radial (R_r) and tangential (R_t) resultant forces acting on the aircraft can be derived.

$$R_r = -X_{in}\cos\theta_a + Z_{in}\sin\theta_a - m_m r\dot{\theta}_a^2 \tag{4.33}$$

$$R_t = X_{in}\sin\theta_a + Z_{in}\cos\theta_a + F_c{}^* = -m_m r\ddot{\theta}_a \tag{4.34}$$

where m_m is the mass of the aircraft model, and r is the arc radius. R_r is positive radially outwards. If a load cell is attached between the aircraft and the arm, the only measurable component of the resultant force is R_r as a reaction force. Note that the tangential reaction force will ideally be zero since it is still assumed that the inertial and aerodynamic forces of the rig are compensated for. Assuming θ_a, $\dot{\theta}_a$, and $\ddot{\theta}_a$ are known quantities, equations 4.33 and 4.34 can be solved simultaneously to give the following equation for $F_c{}^*$ in terms of known/measured quantities.

$$F_c{}^* = R_r\tan\theta_a + m_m r\ddot{\theta}_a\tan^2\theta_a + m_m r\dot{\theta}_a^2\tan\theta_a \tag{4.35}$$

Previously it was noted that the vertical component of thrust has an effect on the aircraft's response (see Section 4.2.4.3). This component can now be artificially introduced using $F_c{}^*$ for

aircraft models that do not produce thrust. As stated before, for the aircraft to have a constant ground speed, the total external force in the inertial axes x must be zero. Therefore, the thrust required by the aircraft must be:

$$T = -\frac{X_{in}}{\cos\theta_m} \tag{4.36}$$

assuming T acts along the body axes x direction and X_{in} is the component of the aerodynamic force in the inertial axes x direction. The vertical component of T is therefore:

$$T_Z = X_{in}\tan\theta_m \tag{4.37}$$

and the tangential component is

$$T_{Z_{tan}} = X_{in}\tan\theta_m\cos\theta_a \tag{4.38}$$

The new ${F_c}^*$ becomes the combination of equations 4.32 and 4.38.

$${F_c}^{**} = -X_{in}\sin\theta_a + X_{in}\tan\theta_m\cos\theta_a \tag{4.39}$$

Solving equations 4.33 and 4.34 simultaneously again with the new ${F_c}^{**}$ above (as opposed to F_c^*) gives the following equation for ${F_c}^{**}$ in term of known quantities.

$${F_c}^{**} = \left(R_r + m_m r\ddot{\theta}_a\tan\theta_a + m_m r\dot{\theta}_a^2\right)\frac{(\sin\theta_a - \tan\theta_m\cos\theta_a)}{(\cos\theta_a + \tan\theta_m\sin\theta_a)} \tag{4.40}$$

Figure 4.6 shows the response comparisons between the unconstrained aircraft at constant ground speed with the cases of the arc constrained aircraft with no feedback, with arc constraint feedback (tangential X_{in} compensation, Equation 4.35), and including both arc constraint feedback and induced artificial thrust (Equation 4.40).

By observing the responses, it is clear that compensating for the tangential component of X_{in} essentially negates the destabilizing moment (about the arm pivot) created mostly by drag due to the absence of thrust. Furthermore, artificially inducing the vertical component of the thrust gives a better match to the unconstrained aircraft response at constant ground speed.

The compensated responses shown in Figure 4.6 are quantitatively compared against the unconstrained response (at constant ground speed) using root-mean-square error in Table 4.1. The deviation is calculated for the first 20 seconds of the time history which roughly contains the short period response. Note that the long period motion cannot be compared due to the significant influence of the kinematic constraints on the aircraft's long period response.

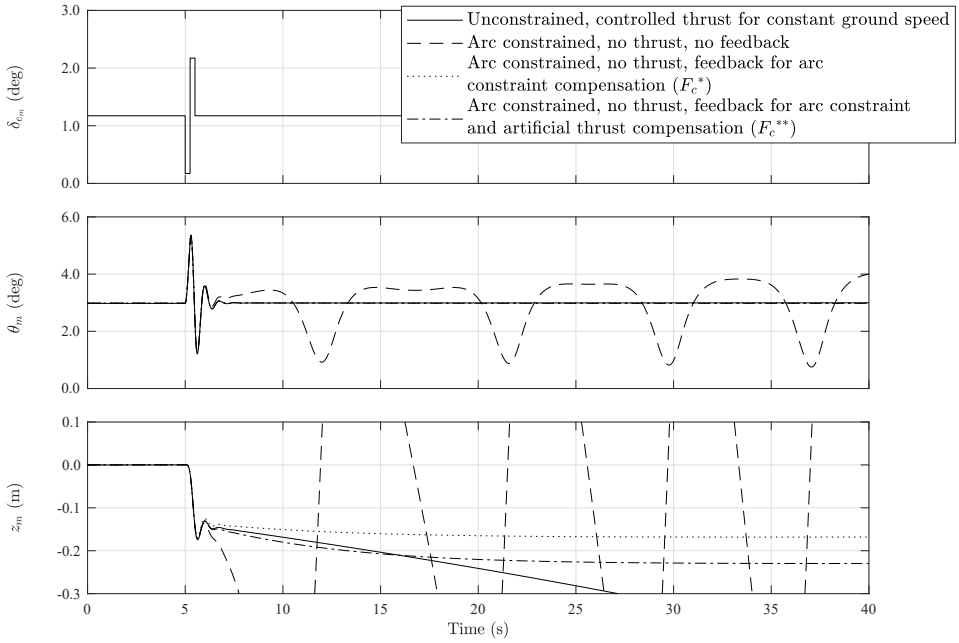

(a) Doublet response

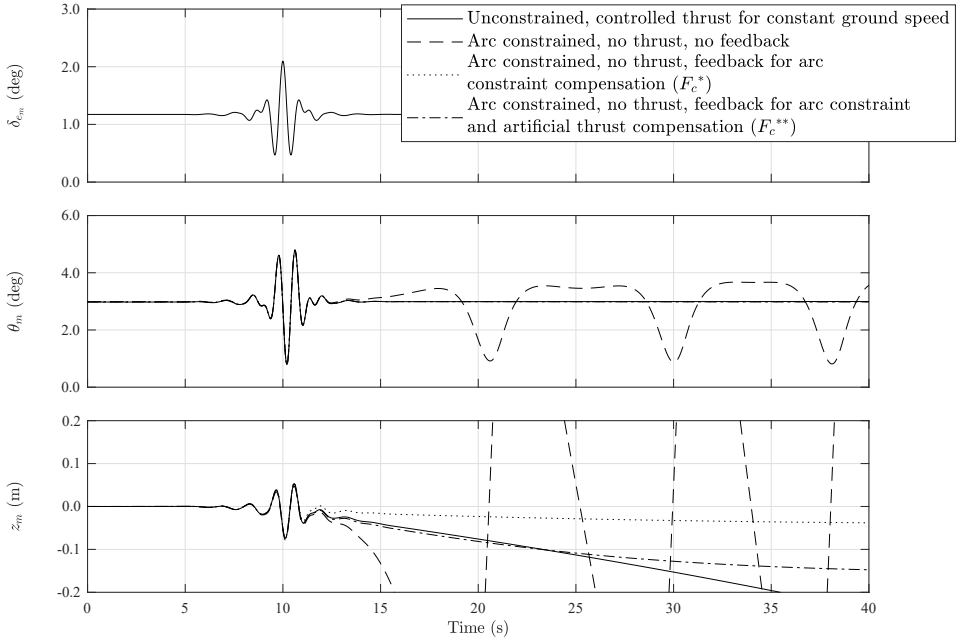

(b) Wavelet response

FIGURE 4.6. Responses including $F_c{}^*$ compensation.

TABLE 4.1. Root-mean-square error of the arc constrained compensated responses relative to the unconstrained aircraft at constant ground speed.

Feedback	Wavelet		Doublet	
	θ_{acm} (deg)	z (m)	θ_{acm} (deg)	z (m)
No feedback	0.2129	0.2408	0.5743	0.4154
Arc constraint feedback ($F_c{}^*$)	0.0082	0.0206	0.0076	0.0341
Arc constraint and artificial thrust feedback ($F_c{}^{**}$)	0.0015	0.0035	0.0067	0.0080

4.3 3D analysis of kinematic constraints

This section uses the 3D nonlinear equations of motion derived in Section 3.4 to analyse the kinematic effects imposed by a plane and spherical constraint, which are equivalent to the line and arc constraints respectively in 2D, as discussed in the Section 4.2. The derivation of the 3D constraints considered in this section is presented in Section 3.6.5.

This assessment is done using a different approach where the five longitudinal and lateral-directional dynamic modes of an aircraft are used to compare the kinematic effects. The aircraft model used in the analysis here is a scaled A-4D aircraft (whose dynamics feature conventional modes of motion) and its properties are shown in Appendix B. The longitudinal modes analysed are the short-period and phugoid modes, and the lateral-directional modes are Dutch roll, spiral, and roll subsidence. Each mode is excited individually using specific control surface inputs and the constrained motion is compared to that of a free-flying aircraft. Note that aerodynamic and inertial effects of the rig are still assumed to be ideally compensated for by an ideally responsive compensator. Aircraft gimbal friction is also assumed to be negligible. These effects will be considered in chapter 7. The study presented here has been published in Reference [67, 68].

4.3.1 Mathematical model

Since the aerodynamic and inertial effects of the rig are assumed to be compensated, the rig itself may be removed from the equations of motion. This reduces the 3D rig-body equations of motion for a single body only: the aircraft model. From Equations 3.19-3.22 and 3.23-3.29,

$$M_{(7\times7)} = \begin{bmatrix} m_{RRm} & 0_{3,4} \\ 0_{4,3} & \overline{G}_m{}^T \overline{I}_{\theta\theta m} \overline{G}_m \end{bmatrix}, \tag{4.41}$$

$$m_{RRm} = \begin{bmatrix} m_m & 0 & 0 \\ 0 & m_m & 0 \\ 0 & 0 & m_m \end{bmatrix}, \overline{I}_{\theta\theta m} = \begin{bmatrix} \overline{I}_{xxm} & -\overline{I}_{xy_m} & -\overline{I}_{xzm} \\ -\overline{I}_{yx_m} & \overline{I}_{yy_m} & -\overline{I}_{yz_m} \\ -\overline{I}_{zxm} & -\overline{I}_{zy_m} & \overline{I}_{zzm} \end{bmatrix}, \tag{4.42}$$

$$\ddot{\boldsymbol{q}}_{m_{(7\times1)}} = \begin{bmatrix} \ddot{\boldsymbol{R}}_m \\ \ddot{\overline{\boldsymbol{\theta}}}_{\boldsymbol{q}_m} \end{bmatrix}, \ddot{\boldsymbol{R}}_m = \begin{bmatrix} \ddot{x}_m \\ \ddot{y}_m \\ \ddot{z}_m \end{bmatrix}, \ddot{\overline{\boldsymbol{\theta}}}_{\boldsymbol{q}_m} = \begin{bmatrix} \theta_{q0_m} \\ \theta_{q1_m} \\ \theta_{q2_m} \\ \theta_{q3_m} \end{bmatrix}, \tag{4.43}$$

$$\boldsymbol{Q}_{\boldsymbol{E}(7\times1)} = \begin{bmatrix} \boldsymbol{Q}_{\boldsymbol{R}m} \\ \overline{G}_m{}^T \left(\overline{\boldsymbol{F}}_{\boldsymbol{\theta}m} - \overline{\boldsymbol{\omega}}_m \times \overline{I}_{\theta\theta m} \overline{\boldsymbol{\omega}}_m \right) \end{bmatrix}, \boldsymbol{Q}_{\boldsymbol{R}m} = \begin{bmatrix} F_{xm} \\ F_{ym} \\ F_{zm} \end{bmatrix}, \overline{\boldsymbol{F}}_{\boldsymbol{\theta}m} = \begin{bmatrix} \overline{M}_{xm} \\ \overline{M}_{ym} \\ \overline{M}_{zm} \end{bmatrix}, \tag{4.44}$$

$$\overline{\boldsymbol{\omega}}_{m_{(3\times1)}} = \overline{G}_m \dot{\overline{\boldsymbol{\theta}}}_{\boldsymbol{q}_m}, \tag{4.45}$$

where the subscript m represents the aircraft model. The transformation matrix $\overline{G}$ is defined in Appendix A. The aircraft model simulated is the A-4D aircraft model scaled roughly to match the dimensions, mass and inertial properties of the Hawk model [66]. The properties and coefficients used for this model are shown in Appendix B. The aerodynamics model used is detailed in Section 3.8.5. The equations of motion are solved as described in Section 3.11. The simulation is for a wind tunnel air flow speed of $30m/s$ and air density of $1.225kg/m^3$.

In total, five constrained responses are compared to that of the unconstrained aircraft: spherical constraints with three radii of $0.6m$, $0.8m$ and $1.0m$, a planar constraint perpendicular to the wind tunnel airflow, and finally a position fixed constraint which allows only aircraft model rotation. The type of constraint used will determine the constraint Jacobian matrix C_q and $\boldsymbol{Q_C}$ vector. Note that since quaternions are used, the unit norm condition described in Section 3.6.4 is present for all constrained and unconstrained cases.

The spherical constraint is described in Section 3.6.5.2. Combining Equation 3.77 with the quaternion constraint Equation 3.66 creates the combined constraints equations:

$$\begin{bmatrix} (x_m + r) & y_m & z_m & 0 & 0 & 0 & 0 \\ 0 & 0 & 0 & \theta_{q0_m} & \theta_{q1_m} & \theta_{q2_m} & \theta_{q3_m} \end{bmatrix} \begin{bmatrix} \ddot{\boldsymbol{R}}_m \\ \ddot{\boldsymbol{\theta}}_{q_m} \end{bmatrix} = \begin{bmatrix} -\dot{x}_m^2 - \dot{y}_m^2 - \dot{z}_m^2 \\ -(\dot{\theta}_{q0_m}^2 + \dot{\theta}_{q1_m}^2 + \dot{\theta}_{q2_m}^2 + \dot{\theta}_{q3_m}^2) \end{bmatrix} \tag{4.46}$$

where

$$C_q = \begin{bmatrix} (x_m + r) & y_m & z_m & 0 & 0 & 0 & 0 \\ 0 & 0 & 0 & \theta_{q0_m} & \theta_{q1_m} & \theta_{q2_m} & \theta_{q3_m} \end{bmatrix}, \tag{4.47}$$

$$\boldsymbol{Q_C} = \begin{bmatrix} -\dot{x}_m^2 - \dot{y}_m^2 - \dot{z}_m^2 \\ -(\dot{\theta}_{q0_m}^2 + \dot{\theta}_{q1_m}^2 + \dot{\theta}_{q2_m}^2 + \dot{\theta}_{q3_m}^2) \end{bmatrix}. \tag{4.48}$$

The planar constraint is described in Section 3.6.5.3. Similarly, combining Equation 3.88 with the quaternion constraint Equation 3.66 creates the combined C_q and $\boldsymbol{Q_C}$:

$$\begin{bmatrix} 1 & 0 & 0 & 0 & 0 & 0 & 0 \\ 0 & 0 & 0 & \theta_{q0_m} & \theta_{q1_m} & \theta_{q2_m} & \theta_{q3_m} \end{bmatrix} \begin{bmatrix} \ddot{\boldsymbol{R}}_m \\ \ddot{\boldsymbol{\theta}}_{q_m} \end{bmatrix} = \begin{bmatrix} 0 \\ -(\dot{\theta}_{q0_m}^2 + \dot{\theta}_{q1_m}^2 + \dot{\theta}_{q2_m}^2 + \dot{\theta}_{q3_m}^2) \end{bmatrix} \tag{4.49}$$

where

$$C_q = \begin{bmatrix} 1 & 0 & 0 & 0 & 0 & 0 & 0 \\ 0 & 0 & 0 & \theta_{q0_m} & \theta_{q1_m} & \theta_{q2_m} & \theta_{q3_m} \end{bmatrix}, \tag{4.50}$$

$$\boldsymbol{Q_C} = \begin{bmatrix} 0 \\ -(\dot{\theta}^2_{q0_m} + \dot{\theta}^2_{q1_m} + \dot{\theta}^2_{q2_m} + \dot{\theta}^2_{q3_m}) \end{bmatrix}. \tag{4.51}$$

The position fixed constraint is described in Section 3.6.5.4. Again, combining Equation 3.94 with the quaternion constraint Equation 3.66 creates the combined C_q and $\boldsymbol{Q_C}$:

$$\begin{bmatrix} 1 & 0 & 0 & 0 & 0 & 0 & 0 \\ 0 & 1 & 0 & 0 & 0 & 0 & 0 \\ 0 & 0 & 1 & 0 & 0 & 0 & 0 \\ 0 & 0 & 0 & \theta_{q0_m} & \theta_{q1_m} & \theta_{q2_m} & \theta_{q3_m} \end{bmatrix} \begin{bmatrix} \ddot{\boldsymbol{R}}_m \\ \ddot{\boldsymbol{\theta}}_{q_m} \end{bmatrix} = \begin{bmatrix} 0 \\ 0 \\ 0 \\ -(\dot{\theta}^2_{q0_m} + \dot{\theta}^2_{q1_m} + \dot{\theta}^2_{q2_m} + \dot{\theta}^2_{q3_m}) \end{bmatrix} \tag{4.52}$$

where

$$C_q = \begin{bmatrix} 1 & 0 & 0 & 0 & 0 & 0 & 0 \\ 0 & 1 & 0 & 0 & 0 & 0 & 0 \\ 0 & 0 & 1 & 0 & 0 & 0 & 0 \\ 0 & 0 & 0 & \theta_{q0_m} & \theta_{q1_m} & \theta_{q2_m} & \theta_{q3_m} \end{bmatrix}, \tag{4.53}$$

$$\boldsymbol{Q_C} = \begin{bmatrix} 0 \\ 0 \\ 0 \\ -(\dot{\theta}^2_{q0_m} + \dot{\theta}^2_{q1_m} + \dot{\theta}^2_{q2_m} + \dot{\theta}^2_{q3_m}) \end{bmatrix}. \tag{4.54}$$

Equation 3.18 can now be formed and solved to produce the aircraft responses.

4.3.2 Response comparison

This section compares the constrained responses of each aircraft mode with the unconstrained aircraft model. The two longitudinal modes simulated are the short-period and phugoid modes and the three lateral-directional modes are the Dutch roll, spiral, and roll subsidence modes. Each mode is excited with specific control surface commands [64]. As stated previously, the experimental rig inertia and aerodynamic effects are assumed to be compensated for ideally, therefore the study here considers purely the kinematic effects. Rig inertia and aerodynamics effects will be considered in Section 4.4. For all cases here the aircraft has a constant thrust set to the initial trim value. An additional unconstrained aircraft case where the thrust is varied to achieve a constant ground speed is compared, which was shown in Section 4.2.4 to be the best response that can be achieved by a planar constrained aircraft, or a spherically constrained aircraft with an infinite radius. The derivation of the thrust required for constant ground speed in 2D was shown in Section 4.2.4.2. The same can be derived in 3D. For zero acceleration in the inertial axes x direction, the total force in that direction must be zero, which can be written as

$$X_{in} + T_{inertial} \cdot \begin{bmatrix} 1 \\ 0 \\ 0 \end{bmatrix} = 0 \tag{4.55}$$

where X_{in} is the total aerodynamic force in the inertial axes x direction and $T_{inertial}$ is the thrust vector also in the inertial axes. $T_{inertial}$ can be written in terms of the thrust in the aircraft's body axes as

$$T_{inertial} = A_m T_{body} \tag{4.56}$$

where A_m is the 3×3 transformation matrix. Assuming the aircraft thrust acts along the body x axis only then $T_{body} = \begin{bmatrix} T & 0 & 0 \end{bmatrix}^T$. Equation 4.55 can now be solved for T:

$$T = \frac{-X_{in}}{A_{m_{1,1}}} \tag{4.57}$$

which is the thrust requirement for a constant ground speed.

Initially, all constrained cases have a constant thrust equal to the thrust required for the unconstrained case. All initial trim conditions are the same for all cases. This ensures that any differences in motion are purely caused by the kinematic constraints. Note that it is not necessary for the constrained aircraft to produce its own thrust but this can be beneficial. Conventional wind tunnel aircraft models usually do not produce thrust. The cases without thrust will follow the initial analysis. Each case is compared using time histories of the relevant variables associated with each mode and trajectory plots [69]. The five constrained cases compared against the unconstrained case with constant thrust are:

1. Spherical constraint of radius $0.6m$
2. Spherical constraint of radius $0.8m$ (as in the manoeuvre rig)
3. Spherical constraint of radius $1.0m$
4. Planar constraint (equivalent to a spherical constraint with infinite radius)
5. Position fixed constraint (allowing for only aircraft rotation)

The variety of spherical radii considered will allow for the observation of the sensitivity of the response to the radius.

Figure 4.7 shows the constrained short-period and phugoid responses along with the unconstrained aircraft mode. The modes are excited by an impulse command to the aircraft elevator. The short-period mode is a damped oscillation in pitch initiated by a disturbance to the pitch equilibrium with negligible change to the forward velocity whereas the phugoid is a lightly damped oscillation in aircraft forward velocity, pitch, and heave [64]. The variables associated with these modes are the aircraft pitch rate (q), angle of attack (α), and heave (z) which are plotted as time histories. For better visualisation, the trajectories for each constraint type are also presented. Note that the aircraft rotation angles in the trajectory plots have been magnified for clearer visualisation as the rotation perturbations are of small magnitude.

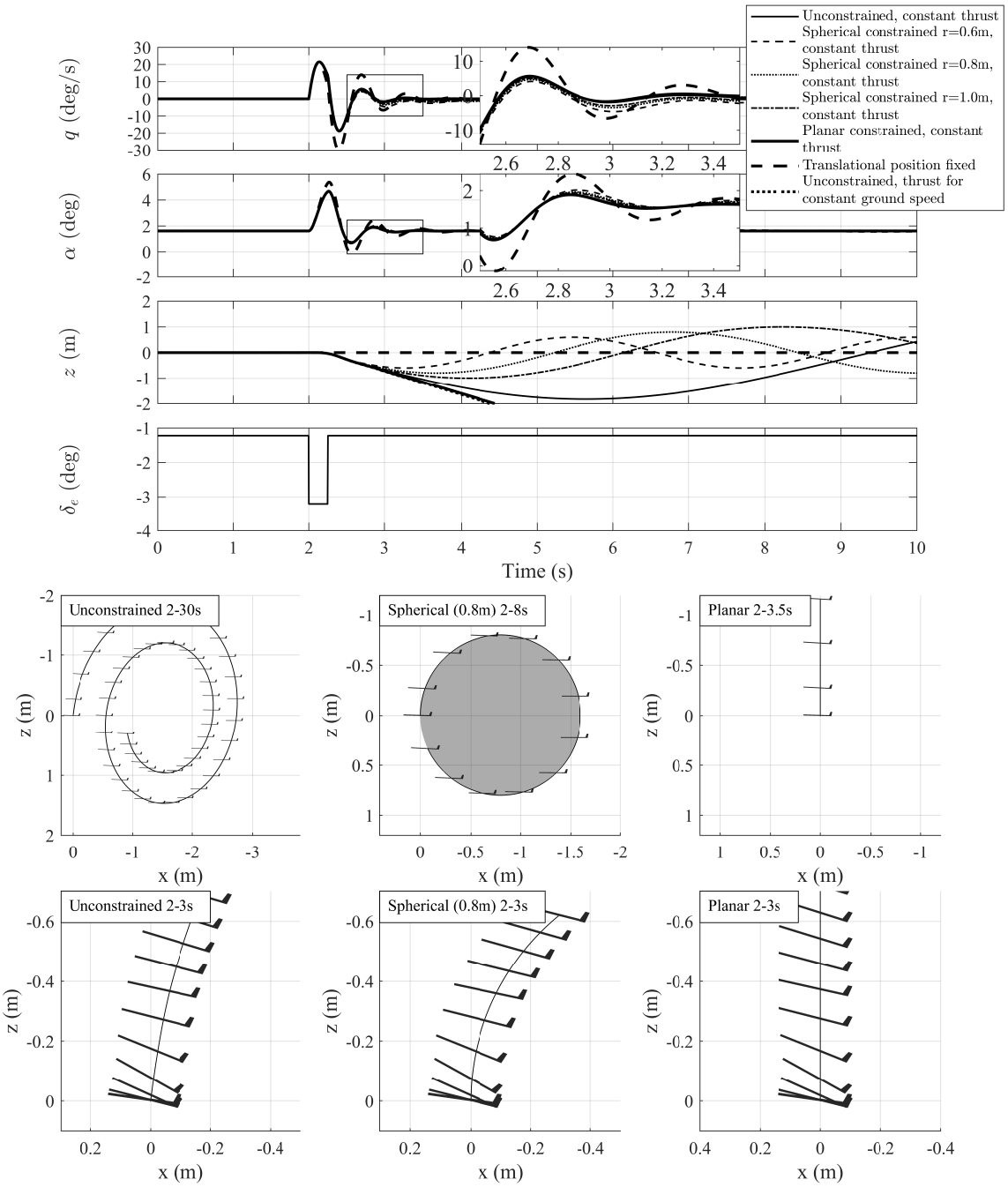

FIGURE 4.7. Short-period and phugoid mode responses.

As expected, the unconstrained aircraft exhibits both the damped short-period and phugoid modes. Note that the time histories are plotted up to a time of 10 seconds only where the regions of interest showing the differences between constraints for the short-period are most visible, and as a result they do not show the phugiod mode fully, which can be seen from the trajectory plot shown for a time frame of 30 seconds. Observing the constrained responses, the true phugoid motion is not replicated. The heave motion of the phugoid mode onset initiated by the elevator input matches well for all cases up to about one second after the input begins. After the three second mark clear differences in the constrained heave responses can be observed where the planar constraint shows the best match with the unconstrained case followed by the spherical constrained cases where the match decreases as the constraint radius decreases. In general the difference is due to the constraints restricting the aircraft velocity changes required for the phugoid mode to be observed. Both the spherical and planar responses show a divergence in heave where the spherically constrained aircraft continuously rotates around the sphere. The spherical constraint would have shown the best initial match if its radius matched the initial radius of the phugoid arc trajectory, which may be impractical as this may require a very long rig arm and would also depend of the aircraft being tested and the manoeuvre. For the A-4D aircraft longitudinal mode being simulated here, the best constraint radius would be about $2.0m$ to accurately simulate the onset of the phugoid mode. Since the ideal match is dependant on the aircraft and the simulated manoeuvre, it would be practical to compensate the spherically constrained aircraft response to attempt to match a planar constrained response which is equivalent to an aircraft flying at a constant ground speed as discussed in Section 4.2.4.3. When comparing the unconstrained response having thrust for constant ground speed with the planar response having constant thrust, the differences are very small. As explained in Section 4.2.4.3, if the additional vertical component of thrust for constant ground speed is present in the planar constrained case then their responses would be identical. Lastly the fixed position model response shows the largest difference. This is due to the effect that the lack of heave motion has on the angle of attack. When observing the short-period mode it follows the same trend where the best match observed is for the planar constraint followed by the spherical constraint with the match with the unconstrained aircraft response at constant ground speed decreasing as the radius decreases.

Figure 4.8 shows the constrained Dutch roll responses along with the unconstrained aircraft mode. The modes are excited by a doublet to the aircraft rudder. The Dutch roll mode is a damped oscillation in yaw coupled with roll [64]. The time histories of the aircraft yaw rate (r), roll rate (p), angle of attack (α), and angle of sideslip (β) are shown. Apart from the yaw rate of the position fixed response, all constrained motions match the unconstrained motion well. Although the differences when comparing the constrained responses are small, the trend remains: the planar constrained response still gives the best match with the unconstrained aircraft at constant ground speed, followed by the spherical constraint where the match improves as the radius

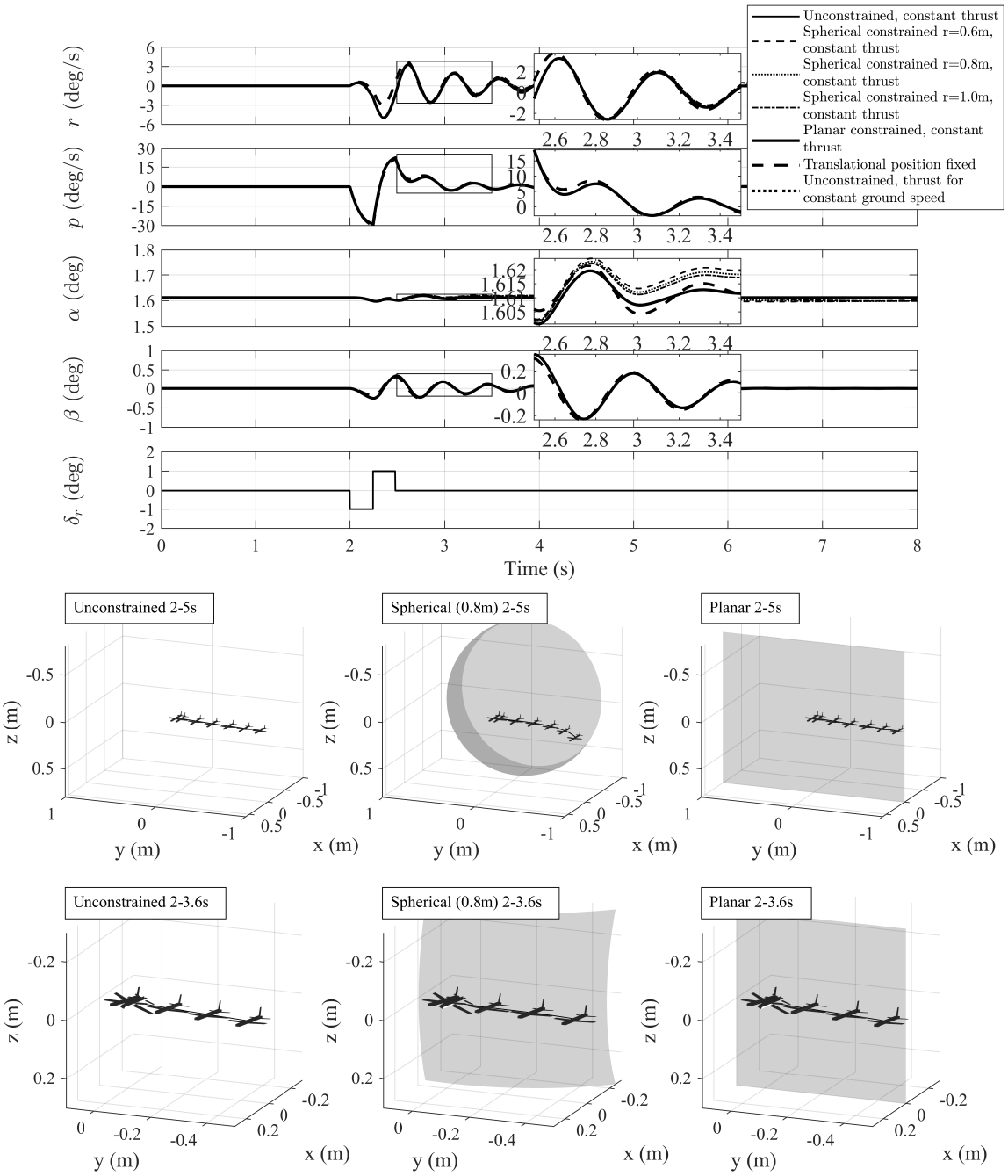

FIGURE 4.8. Dutch roll mode responses.

increases, and finally the position fixed constraint.

Figure 4.9 shows the constrained spiral mode responses along with the unconstrained aircraft mode. This motion is excited by a step input to the rudder. The spiral mode is a nonoscillatory mode involving coupled motion in roll, yaw, and sideslip [64]. The stability of the long term motion is determined by the dihedral effect and the fin effect. The motion is stable if the dihedral effect is greater or unstable if the fin effect is greater [64]. For the A-4D aircraft used in this simulation the spiral mode is stable. The time histories of the aircraft roll angle (ϕ), angle of attack (α), angle of sideslip (β), total velocity (V), and heave (z) are shown. Note that it is only possible to simulate the *onset* of the spiral mode due to the large motions associated with this mode which cannot be physically simulated while constrained or within the confines of a wind tunnel. Similarly to the Dutch roll mode, apart from the fixed position response, the constrained responses match the unconstrained well up to 2.75 seconds, after which the velocity restrictions produced by the constraints dominate the response. When inspected closer, it can be seen that again the planar constrained response still gives the best match with the unconstrained aircraft at constant ground speed, followed by the spherical constrained response where a larger radius gives a better match. The position fixed response is an oddity as its response seems to give a better match with the unconstrained aircraft past 2.75 seconds for angle of attack, sideslip and total velocity.

Figure 4.10 shows the constrained roll subsidence responses along with the unconstrained aircraft mode. The roll subsidence mode is also a nonoscillatory mode, consisting of pure roll [64]. This motion is excited by a square pulse to the aileron. The time histories of the aircraft roll rate (p), roll angle (ϕ), angle of attack (α), and angle of sideslip (β) are shown. Since the lateral response of this mode is rapid, the effects of the physical constraints become apparent past 3 seconds. Before 3 seconds, the constrained responses match well with the unconstrained in general with the position fixed response showing the most significant difference.

4.3.3 Compensation concept for the spherical constraint in 3D

This section extends the spherical constraint kinematic compensation presented in Section 4.2.5 to 3D. To restate the concept, it was previously noted that when analysing the line/planar constraint the total force in the inertial axes x direction was zero, hence the total force created by the aircraft model in the x direction (X_{in}, see Figure 4.5) does not have any influence on the aircraft response. If the aircraft model creates thrust then the magnitude of X_{in} is small, however if thrust is not present then X_{in} is large and dominated by drag. When analysing the arc/spherical constraint, X_{in} does influence the motion by creation of a moment about the arc/sphere radius, which however can be compensated for by externally applying a moment to cancel it. On the manoeuvre rig this compensation moment can be applied using the aerodynamic compensator at the rear of the rig. This compensation moment is equivalent to a compensation force ($\mathbf{F_c}^*$) applied on the aircraft centre of gravity tangentially to the arc/spherical constraint. Note that all inertial

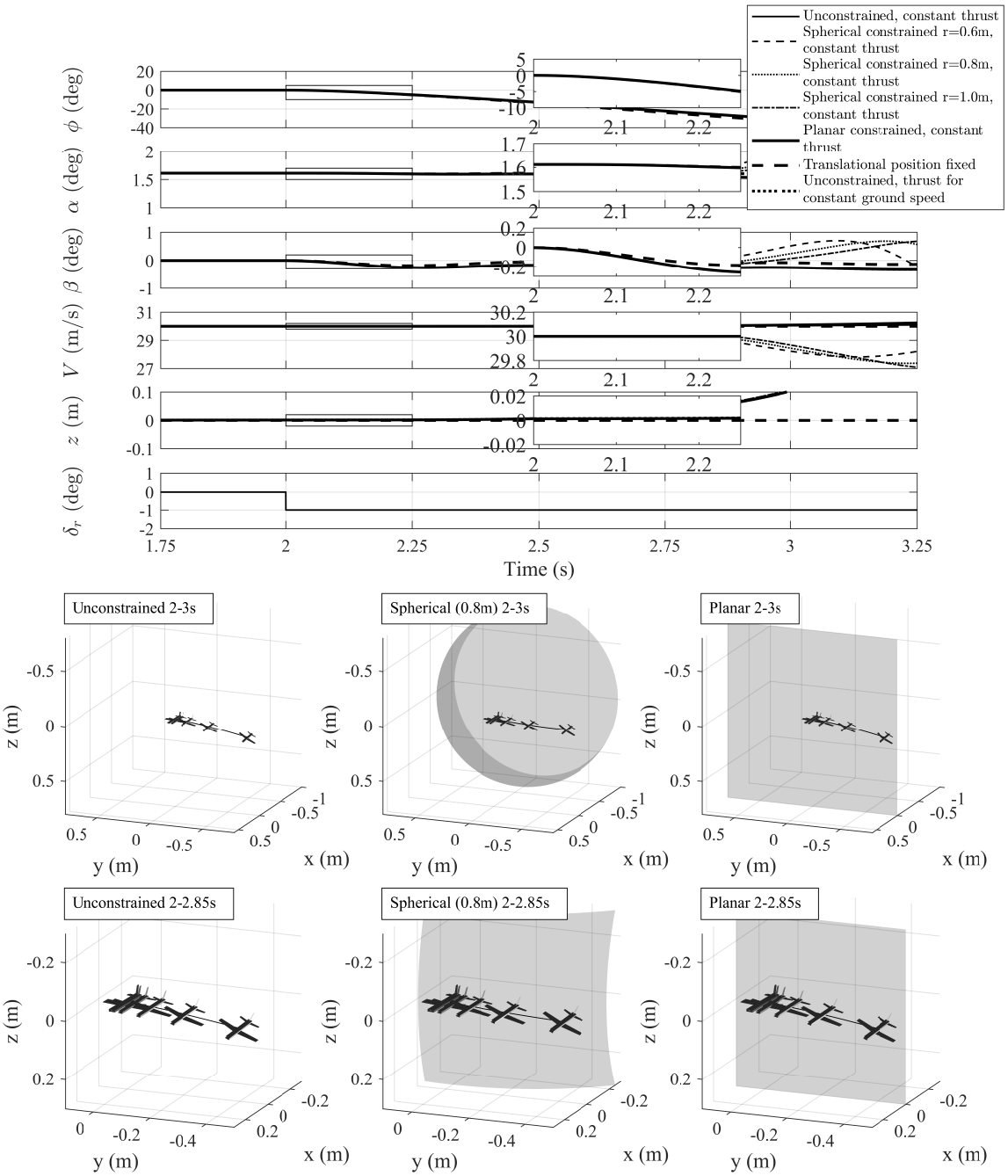

FIGURE 4.9. Spiral mode responses.

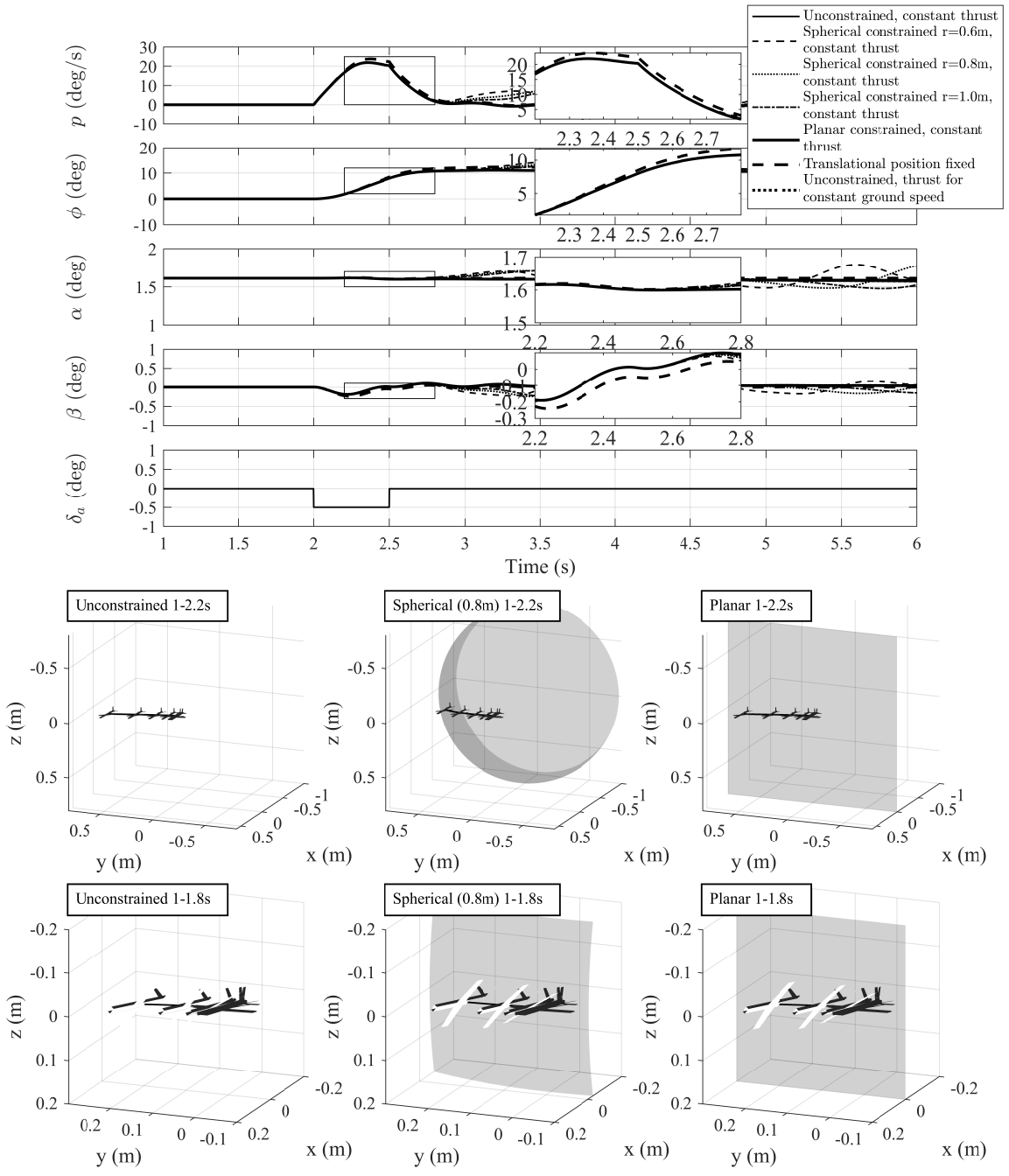

FIGURE 4.10. Roll subsidence mode responses.

and aerodynamic properties of the rig itself are still assumed to be ideally compensated for by an ideally responsive compensator. Therefore, $\mathbf{F_c}^*$ is the negative of the tangential component of X_{in}:

$$\mathbf{F_c}^* = -\mathbf{X_{in_{tan}}}, \tag{4.58}$$

$$\mathbf{X_{in_{tan}}} = \begin{pmatrix} X_{in} \\ 0 \\ 0 \end{pmatrix} - \mathbf{X_{in_{rad}}}, \tag{4.59}$$

$$\mathbf{X_{in_{rad}}} = \left(\begin{pmatrix} X_{in} \\ 0 \\ 0 \end{pmatrix} \cdot \hat{\mathbf{p}} \right) \hat{\mathbf{p}} \tag{4.60}$$

where $\mathbf{X_{in_{rad}}}$ and $\mathbf{X_{in_{tan}}}$ are the radial and tangential components of X_{in} respectively and $\hat{\mathbf{p}}$ is the normalised position vector of the aircraft relative to the centre of the sphere with respect to the inertial axis system. Figure 4.11 shows a diagram depicting these forces, where the forces in boxes are matched by the reaction force created by the spherical constraint. This reaction force can be measured by a load cell. The aerodynamic forces in the inertial axes are expressed as

$$\begin{pmatrix} X_{in} \\ Y_{in} \\ Z_{in} \end{pmatrix} = -R_{rad}\hat{\mathbf{p}} + m\mathbf{a_{cen}} + m\mathbf{a_{tan}} - \mathbf{F_c}^* \tag{4.61}$$

where

$$\mathbf{a_{cen}} = -r\omega^2\hat{\mathbf{p}}, \tag{4.62}$$

$$\mathbf{a_{tan}} = \mathbf{a} - \mathbf{a_{cen}}. \tag{4.63}$$

Here $\mathbf{a}$ is the total acceleration vector of the aircraft in the inertial axes. $\mathbf{a_{cen}}$ and $\mathbf{a_{tan}}$ are the centripetal and tangential accelerations respectively also in inertial axes frame of reference. m is the mass of the model aircraft, r is the sphere radius and ω is the angular velocity of the aircraft about the sphere. Note that all radial components are positive in the outward direction. $\mathbf{F_c}^*$ in Equation 4.61 cancels $\mathbf{X_{in_{tan}}}$, therefore X_{in} will only have a radial component. As a result, X_{in} and $\mathbf{X_{in_{rad}}}$ can be calculated by

$$X_{in} = \frac{\left\| \mathbf{X_{in_{rad}}} \right\|}{\begin{pmatrix} 1 \\ 0 \\ 0 \end{pmatrix} \cdot \hat{\mathbf{p}}}, \tag{4.64}$$

$$\left\| \mathbf{X_{in_{rad}}} \right\| = -\left\{ R_{rad}\hat{\mathbf{p}} + \left[\left(Y_{in} \begin{pmatrix} 0 \\ 1 \\ 0 \end{pmatrix} + Z_{in} \begin{pmatrix} 0 \\ 0 \\ 1 \end{pmatrix} \right) \cdot \hat{\mathbf{p}} \right] \hat{\mathbf{p}} - m\mathbf{a_{cen}} \right\} \cdot \hat{\mathbf{p}}, \tag{4.65}$$

Note that in the ideal case the tangential reaction force will be zero if the inertia of the experimental rig is fully compensated for. Y_{in} and Z_{in} are the resultant aerodynamic and inertial forces in the y and z directions respectively. Y_{in} and Z_{in} can be found by first calculating the projected total aerodynamic and inertial force onto the yz plane:

$$\mathbf{F_{yz}} = \frac{\|\mathbf{F_{tan}}\|}{\hat{\mathbf{v}}_\mathbf{p} \cdot \hat{\mathbf{F}}_\mathbf{tan}} \hat{\mathbf{v}}_\mathbf{p}, \tag{4.66}$$

$$\mathbf{v_p} = (\hat{\mathbf{p}} \times \mathbf{F_{tan}}) \times \begin{pmatrix} 1 \\ 0 \\ 0 \end{pmatrix}, \tag{4.67}$$

where $\hat{\mathbf{v}}_\mathbf{p}$ is a vector in line with the yz plane and $\mathbf{F_{tan}}$, and $\mathbf{F_{tan}}$ is

$$\mathbf{F_{tan}} = m\mathbf{a_{tan}} \tag{4.68}$$

Y_{in} and Z_{in} can be expressed as

$$Y_{in} = \mathbf{F_{yz}} \cdot \begin{pmatrix} 0 \\ 1 \\ 0 \end{pmatrix}, \; Z_{in} = \mathbf{F_{yz}} \cdot \begin{pmatrix} 0 \\ 0 \\ 1 \end{pmatrix}. \tag{4.69}$$

Equations 4.59 to 4.69 can be substituted back into Equation 4.58 to calculate the required kinematic compensation force vector $\mathbf{F_c}^*$.

The artificial thrust component (expressed in Equation 4.38 in 2D) can also be introduced. The thrust required from constant ground speed shown in Equation 4.57 projected on the yz plane is

$$\mathbf{T_{YZ}} = \begin{bmatrix} 0 & 0 & 0 \\ 0 & 1 & 0 \\ 0 & 0 & 1 \end{bmatrix} \left(A_m \begin{bmatrix} T \\ 0 \\ 0 \end{bmatrix} \right) \tag{4.70}$$

The tangential component of $\mathbf{T_{YZ}}$ is

$$\mathbf{T_{YZ_{tan}}} = \left(\mathbf{T_{YZ}} \cdot \hat{\mathbf{l}}_\mathbf{tan}\right) \hat{\mathbf{l}}_\mathbf{tan} \tag{4.71}$$

$$\mathbf{l_{tan}} = (\hat{\mathbf{p}} \times \mathbf{T_{YZ}}) \times \hat{\mathbf{p}} \tag{4.72}$$

where $\hat{\mathbf{l}}_\mathbf{tan}$ is a line tangential to the spherical constraint and in line with $\mathbf{T_{YZ}}$. Therefore, combining the kinematic compensation and artificial thrust, Equation 4.58 for the external compensation force can be rewritten as

$$\mathbf{F_c}^{**} = -\mathbf{X_{tan}} + \mathbf{T_{YZ_{tan}}}. \tag{4.73}$$

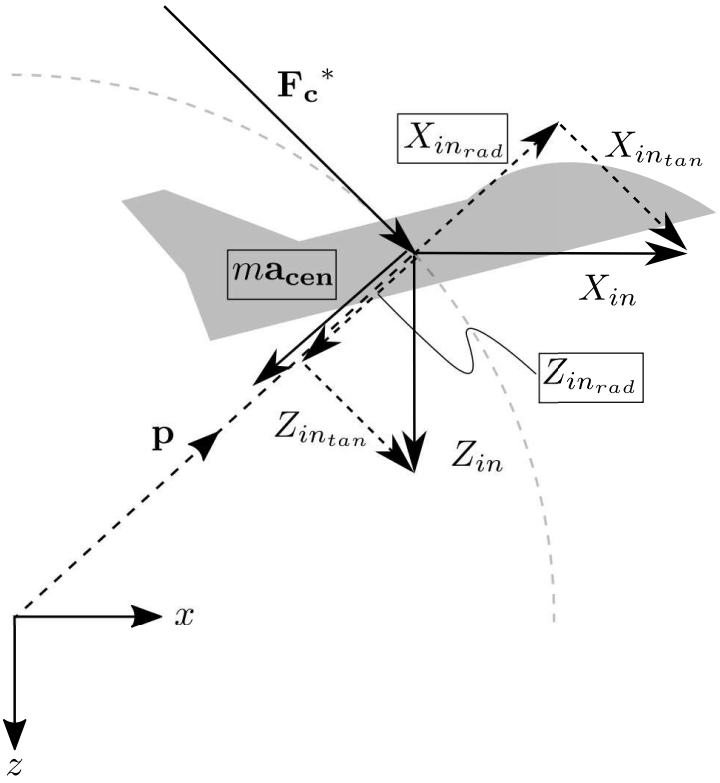

FIGURE 4.11. Spherical constraint forces.

4.3.4 Response comparison when applying $\mathbf{F_c}^*$ and $\mathbf{F_c}^{**}$

This section compares the changes to the mode responses as the tangential external compensation force $\mathbf{F_c}^*$ (compensation without artificial thrust) and $\mathbf{F_c}^{**}$ (compensation with artificial thrust) are applied onto the spherically constrained aircraft. The change to the compensated responses are measured quantitatively using root mean square errors of the motion variables. This is followed by a study investigating the effects on the perceived changes to the aircraft's aerodynamic coefficients estimated from the recorded motion as a means of evaluating the magnitude of the constraint effects on the aircraft model motions, and as a measure of the extent to which the application of $\mathbf{F_c}^*$ and $\mathbf{F_c}^{**}$ improves them. The parameter estimating technique used is the equation error method [70].

Three cases for the spherically constrained aircraft are simulated: no compensation, $\mathbf{F_c}^*$ compensation, and $\mathbf{F_c}^{**}$ compensation. All constrained aircraft are assumed to have no thrust producing capability, as in most wind tunnel aircraft models. The lack of thrust in the constrained aircraft setup exacerbates the effect of the total aerodynamic force in the X direction making the aircraft unstable while spherically constrained. The lack of thrust results in an increase in magnitude of X_{in} due to drag, akin to an inverted pendulum.

These constrained cases are compared to two unconstrained cases: a free-flying aircraft with

constant thrust, and a free-flying aircraft with controlled thrust for constant ground speed (akin to a planar constrained aircraft). These comparisons are repeated for each mode initiated by their respective aircraft control surface inputs. The spherical constraint radius is $0.8m$ and the onset wind speed is $30m/s$. In the case where $\mathbf{F_c}^*$ or $\mathbf{F_c}^{**}$ is not used, we assume perfect compensation for the inertial and aerodynamic forces of the rig for all cases as in the previous section.

Figure 4.12 shows the comparison graph for the short-period and phugoid modes. The time history plots are shown for the pitch rate (q), angle of attack (α), z translation, elevator input (δ_e), and the magnitude of the compensation force ($|\mathbf{F_c}|$). It can be observed that the spherically constrained response with $\mathbf{F_c}^*$ initially follows the response without compensation, however the divergent behaviour that is present without $\mathbf{F_c}^*$ is suppressed when $\mathbf{F_c}^*$ is introduced, improving its match with the unconstrained responses. Applying $\mathbf{F_c}^{**}$ compensation further improves this match.

These differences can be more clearly observed from the root mean square errors shown in Table 4.2, which shows the errors relative to the unconstrained aircraft with constant thrust, and in Table 4.3 which shows the errors relative to the unconstrained aircraft with controlled thrust for constant ground speed. A lower error value indicates a better match where zero would be a perfect match. It can be seen that a significant reduction in error, of up to 80%, can be obtained with the use of compensation . Note that when $\mathbf{F_c}^*$ compensation is used the initial trim states of the aircraft is different from the cases with thrust or with $\mathbf{F_c}^{**}$ which results in a larger initial perceived error when comparing the responses with the unconstrained cases. $\mathbf{F_c}^*$ compensation improves the match in response especially in the longer term since it cancels the divergent behaviour caused by drag. $\mathbf{F_c}^{**}$ compensation improves the initial match mainly due to the match in initial trim states and also further improves the overall match in most states, although to a lower extent. The reason for the match of some states getting worse with $\mathbf{F_c}^{**}$ compensation is associated with the hard limitation of the spherical constraint affecting the trajectory/velocity and therefore the forces and moments acting on the aircraft model. This is confirmed by applying an input of smaller magnitude which results in smaller translation of the aircraft and better response improvement by $\mathbf{F_c}^{**}$ compensation.

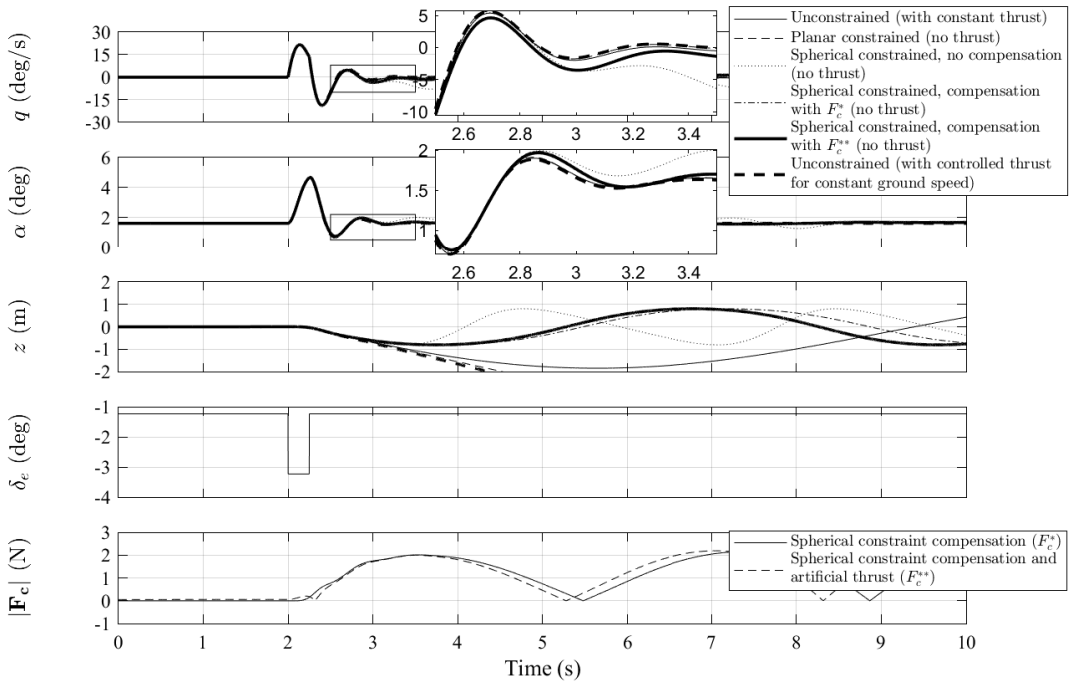

FIGURE 4.12. Short-period mode responses with and without compensation.

TABLE 4.2. Short-period mode: root mean square error relative to unconstrained aircraft model with constant thrust.

Compensation		**Time frame**			
		2.0s to 2.5s	2.0s to 3.0s	2.0s to 3.5s	2.0s to 4.0s
	None	0.0367	0.362	2.02	3.59
q (deg/s)	F_c^*	0.236 (544%)	0.622 (71.8%)	0.756 (-62.6%)	0.733 (-79.6%)
	F_c^{**}	0.127 (246%)	0.661 (82.5%)	0.835 (-58.7%)	0.835 (-76.7%)
	None	0.0204	0.0554	0.135	0.166
α (deg)	F_c^*	0.0361 (76.7%)	0.0537 (-3.08%)	0.0509 (-62.1%)	0.0483 (-70.8%)
	F_c^{**}	0.02 (-2.17%)	0.0415 (-25.1%)	0.0395 (-70.7%)	0.037 (-77.7%)
	None	0.000545	0.00681	0.0794	0.373
z (m)	F_c^*	0.00237 (334%)	0.0311 (356%)	0.111 (40.4%)	0.238 (-36.3%)
	F_c^{**}	0.000549 (0.71%)	0.0227 (233%)	0.102 (28.5%)	0.235 (-37.1%)

TABLE 4.3. Short-period mode: root mean square error relative to unconstrained aircraft model with controlled thrust for constant ground speed.

Compensation		**Time frame**			
		2.0s to 2.5s	2.0s to 3.0s	2.0s to 3.5s	2.0s to 4.0s
q (deg/s)	None	0.172	0.525	2.29	3.93
	F_c^*	0.378 (120%)	0.847 (61.2%)	1.06 (-53.6%)	1.1 (-72.2%)
	F_c^{**}	0.258 (50.1%)	0.875 (66.6%)	1.14 (-50.3%)	1.2 (-69.5%)
α (deg)	None	0.0347	0.0678	0.146	0.179
	F_c^*	0.0521 (49.9%)	0.0671 (-1.06%)	0.065 (-55.6%)	0.0635 (-64.4%)
	F_c^{**}	0.0329 (-5.27%)	0.0535 (-21.1%)	0.0522 (-64.3%)	0.051 (-71.5%)
z (m)	None	0.0029	0.0243	0.13	0.483
	F_c^*	0.00473 (62.9%)	0.0487 (100%)	0.164 (26.1%)	0.351 (-27.3%)
	F_c^{**}	0.00232 (-20.3%)	0.0401 (64.7%)	0.154 (18.6%)	0.348 (-27.9%)

Figure 4.13 shows the comparison graph for the Dutch roll mode. The time history plots are shown for the yaw rate (r), roll rate (p) angle of attack (α), angle of sideslip (β), rudder input (δ_r), and the magnitude of the compensation force ($|\mathbf{F_c}|$). Similar to the previous longitudinal modes, it can be seen that $\mathbf{F_c}^*$ suppresses the divergent behaviour caused by drag, giving a closer match to the unconstrained responses. Including the effects of artificial thrust by $\mathbf{F_c}^{**}$ further improves this match. Tables 4.4 and 4.5 shows the root mean square errors of the states relative to the unconstrained aircraft with constant thrust and with controlled thrust for constant ground speed, respectively. Again, the same trends as the longitudinal modes are seen. Compensation can improve the error in states by more that 80%. $\mathbf{F_c}^*$ improves the match for all states with $\mathbf{F_c}^{**}$ further improving it.

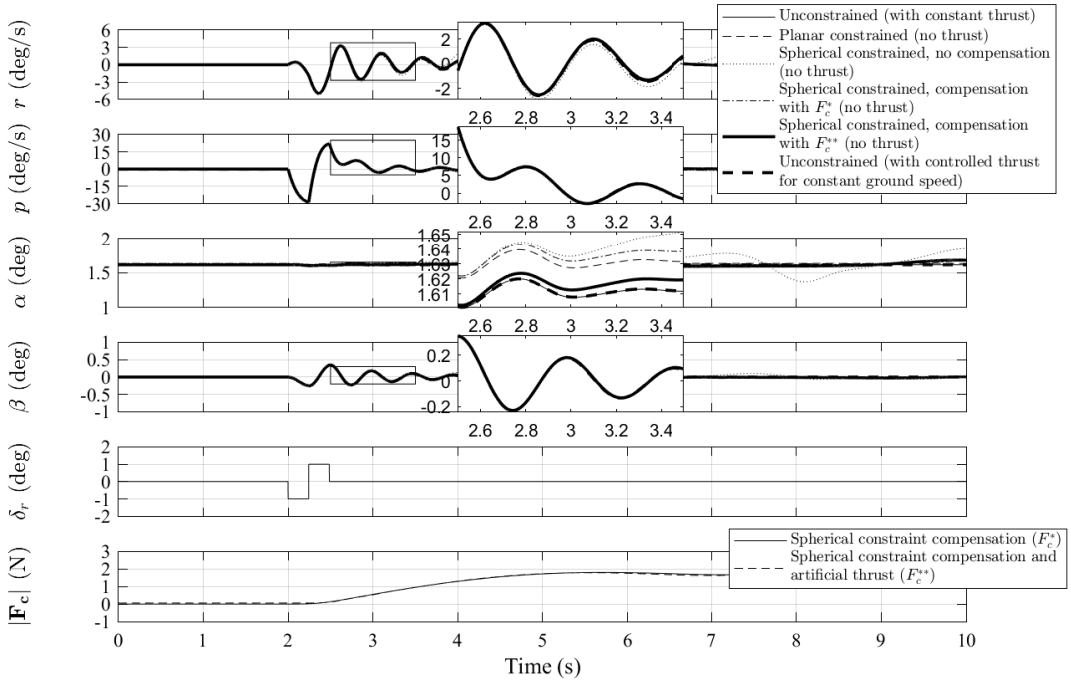

FIGURE 4.13. Dutch roll mode responses with and without compensation.

TABLE 4.4. Dutch roll mode: root mean square error relative to unconstrained aircraft model with constant thrust.

Compensation		**Time frame**			
		2.0s to 2.5s	2.0s to 3.0s	2.0s to 3.5s	2.0s to 4.0s
	None	0.027	0.17	0.262	0.386
r (deg/s)	F_c^*	0.0144 (-46.6%)	0.0449 (-73.6%)	0.0796 (-69.6%)	0.118 (-69.5%)
	F_c^{**}	0.000644 (-97.6%)	0.0325 (-80.9%)	0.0701 (-73.3%)	0.115 (-70.2%)
	None	0.0247	0.131	0.129	0.4
p (deg/s)	F_c^*	0.0261 (5.58%)	0.0407 (-69%)	0.0562 (-56.5%)	0.0741 (-81.5%)
	F_c^{**}	0.00554 (-77.6%)	0.0257 (-80.5%)	0.0477 (-63%)	0.0695 (-82.6%)
	None	0.0197	0.022	0.0264	0.0324
α (deg)	F_c^*	0.0197 (0.297%)	0.0213 (-3.26%)	0.0228 (-13.6%)	0.0241 (-25.7%)
	F_c^{**}	0.00036 (-98.2%)	0.00249 (-88.7%)	0.00421 (-84%)	0.00571 (-82.4%)
	None	0.00101	0.00482	0.00564	0.0184
β (deg)	F_c^*	0.00144 (42.9%)	0.00192 (-60.1%)	0.00288 (-49%)	0.00397 (-78.4%)
	F_c^{**}	0.000165 (-83.6%)	0.000997 (-79.3%)	0.00226 (-59.9%)	0.00362 (-80.4%)

TABLE 4.5. Dutch roll mode: root mean square error relative to unconstrained aircraft model with controlled thrust for constant ground speed.

Compensation		**Time frame**			
		2.0s to 2.5s	2.0s to 3.0s	2.0s to 3.5s	2.0s to 4.0s
r (deg/s)	None	0.027	0.17	0.262	0.386
	F_c^*	0.0145 (-46.4%)	0.0449 (-73.5%)	0.0795 (-69.6%)	0.118 (-69.6%)
	F_c^{**}	0.000694 (-97.4%)	0.0325 (-80.8%)	0.07 (-73.3%)	0.115 (-70.2%)
p (deg/s)	None	0.0249	0.131	0.129	0.4
	F_c^*	0.026 (4.35%)	0.0405 (-69.1%)	0.0558 (-56.7%)	0.0734 (-81.6%)
	F_c^{**}	0.00535 (-78.5%)	0.0255 (-80.6%)	0.0472 (-63.4%)	0.0688 (-82.8%)
α (deg)	None	0.0197	0.022	0.0263	0.0323
	F_c^*	0.0197 (0.297%)	0.0213 (-3.26%)	0.0227 (-13.6%)	0.0239 (-25.8%)
	F_c^{**}	0.000351 (-98.2%)	0.00244 (-88.9%)	0.0041 (-84.4%)	0.00556 (-82.8%)
β (deg)	None	0.00101	0.00482	0.00563	0.0184
	F_c^*	0.00145 (43.7%)	0.00192 (-60.1%)	0.00286 (-49.2%)	0.00394 (-78.6%)
	F_c^{**}	0.000167 (-83.4%)	0.000992 (-79.4%)	0.00224 (-60.2%)	0.00358 (-80.5%)

Figure 4.14 shows the time history plots for the spiral mode and how the applied compensation changes the response. The states shown are the roll angle (ϕ), angle of attack (α), angle of sideslip (β), total velocity (V), z translation, rudder input (δ_r), and the magnitude of the compensation force ($|\mathbf{F_c}|$). The improvements to the response can be more clearly seen from the root mean square errors shown in Tables 4.6 and 4.7, which show the errors relative to an unconstrained aircraft with constant thrust and with controlled thrust for constant ground speed, respectively. The aircraft departs from the initial position quickly in response to the input which results in the effects of the hard limitations of the spherical constraint being shown early. This is evident by the worsening of the match in β by about 2.75s and onwards. The other states show improvement in match as a result of compensation. This further shows that kinematic compensation on the spherical constraint will show improvement in responses with smaller magnitudes of translation from the initial position, or for the early stages of the motion for quicker responses.

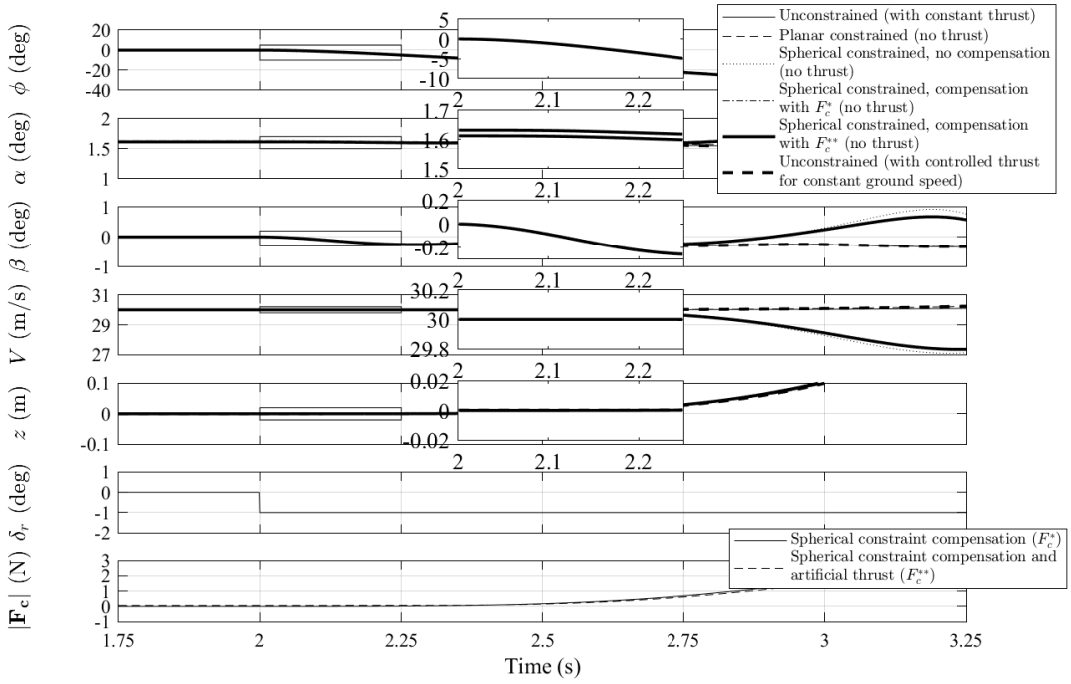

FIGURE 4.14. Spiral mode responses with and without compensation.

TABLE 4.6. Spiral mode: root mean square error relative to unconstrained aircraft model with constant thrust.

Compensation		**Time frame** 2.0s to 2.25s	2.0s to 2.5s	2.0s to 2.75s
ϕ (deg)	None	0.000607	0.00576	0.0165
	F_c^*	0.000483 (-20.5%)	0.00204 (-64.6%)	0.0116 (-29.5%)
	F_c^{**}	4.13e-05 (-93.2%)	0.000249 (-95.7%)	0.00928 (-43.8%)
α (deg)	None	0.0195	0.0197	0.025
	F_c^*	0.0195 (0.0411%)	0.0199 (1.01%)	0.0264 (5.77%)
	F_c^{**}	1.88e-05 (-99.9%)	0.00061 (-96.9%)	0.0104 (-58.2%)
β (deg)	None	0.000708	0.0017	0.00932
	F_c^*	0.000478 (-32.5%)	0.00103 (-39.5%)	0.0149 (59.8%)
	F_c^{**}	4.58e-06 (-99.4%)	0.000407 (-76.1%)	0.0146 (56.5%)
V (m/s)	None	0.000458	0.011	0.113
	F_c^*	0.000457 (-0.267%)	0.0107 (-2.56%)	0.107 (-5.89%)
	F_c^{**}	0.000456 (-0.437%)	0.0107 (-2.53%)	0.107 (-5.27%)
z (m)	None	7.83e-05	0.000128	0.000684
	F_c^*	9.69e-05 (23.8%)	0.00014 (8.95%)	0.000518 (-24.3%)
	F_c^{**}	0.000254 (225%)	0.000304 (137%)	0.000673 (-1.64%)

TABLE 4.7. Spiral mode: root mean square error relative to unconstrained aircraft model with controlled thrust for constant ground speed.

Compensation		**Time frame** 2.0s to 2.25s	2.0s to 2.5s	2.0s to 2.75s
	None	0.000577	0.00567	0.0165
ϕ (deg)	F_c^*	0.000452 (-21.6%)	0.00195 (-65.6%)	0.0115 (-30.6%)
	F_c^{**}	7.87e-06 (-98.6%)	0.000157 (-97.2%)	0.00914 (-44.8%)
	None	0.0195	0.0197	0.0252
α (deg)	F_c^*	0.0195 (0.0411%)	0.0199 (1.01%)	0.0267 (5.75%)
	F_c^{**}	7.88e-06 (-100%)	0.00063 (-96.8%)	0.0107 (-57.4%)
	None	0.000709	0.0017	0.00926
β (deg)	F_c^*	0.000479 (-32.5%)	0.00103 (-39.7%)	0.0148 (60.1%)
	F_c^{**}	4.96e-06 (-99.3%)	0.000404 (-76.3%)	0.0145 (56.8%)
	None	0.000219	0.0111	0.117
V (m/s)	F_c^*	0.000217 (-0.67%)	0.0108 (-2.54%)	0.11 (-5.7%)
	F_c^{**}	0.000216 (-1.09%)	0.0108 (-2.5%)	0.111 (-5.1%)
	None	6.54e-05	5.96e-05	0.000573
z (m)	F_c^*	4.68e-05 (-28.4%)	4.21e-05 (-29.5%)	0.0004 (-30.2%)
	F_c^{**}	0.000111 (69.7%)	0.000132 (122%)	0.000522 (-8.83%)

Figure 4.15 shows the time history plots for the roll subsidence mode and the effects of compensation. The states shown are the roll rate (p), roll angle (ϕ), angle of attack (α), angle of sideslip (β), aileron input (δ_a), and the magnitude of the compensation force ($|\mathbf{F_c}|$). The root mean square errors presented in Tables 4.8 and 4.9 show the errors relative to an unconstrained aircraft with constant thrust and with controlled thrust for constant ground speed, respectively. Similar to the spiral mode, the quickness in lateral departure results in the effects of the spherical kinematic constraint manifesting in states such as β as the aircraft is forced to follow the trajectory of the arc. However, improvements in other states are clear.

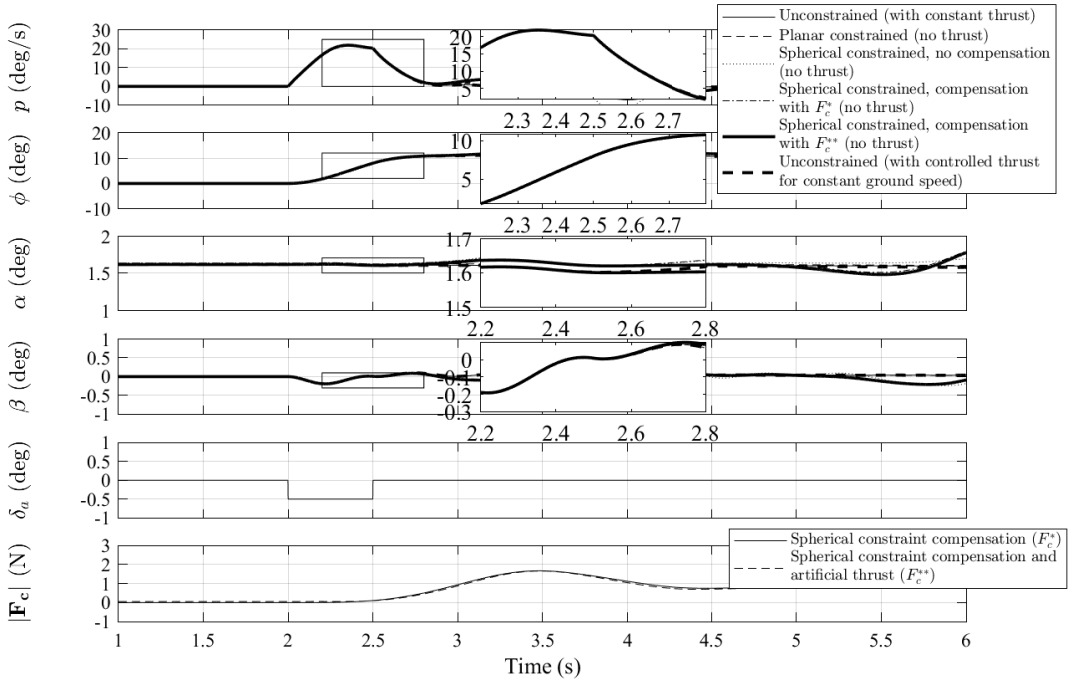

FIGURE 4.15. Roll subsidence mode responses with and without compensation.

TABLE 4.8. Roll subsidence mode: root mean square error relative to unconstrained aircraft model with constant thrust.

Compensation		**Time frame** 2.0s to 2.25s	2.0s to 2.5s	2.0s to 2.75s
p (deg/s)	None	0.0012	0.0249	0.0563
	F_c^*	0.00207 (72.1%)	0.00428 (-82.8%)	0.0651 (15.7%)
	F_c^{**}	6e-05 (-95%)	0.000429 (-98.3%)	0.0548 (-2.62%)
ϕ (deg)	None	4.87e-05	0.00154	0.0109
	F_c^*	6.99e-05 (43.4%)	0.000812 (-47.2%)	0.00546 (-49.7%)
	F_c^{**}	6.77e-06 (-86.1%)	6.26e-05 (-95.9%)	0.00364 (-66.5%)
α (deg)	None	0.0195	0.0195	0.0207
	F_c^*	0.0195 (0.0148%)	0.0196 (0.477%)	0.0211 (2.24%)
	F_c^{**}	7.29e-06 (-100%)	0.000213 (-98.9%)	0.00284 (-86.3%)
β (deg)	None	4.25e-05	0.00143	0.00217
	F_c^*	0.000132 (210%)	0.000188 (-86.8%)	0.00378 (74.5%)
	F_c^{**}	2.88e-06 (-93.2%)	8.8e-05 (-93.8%)	0.00329 (51.6%)

TABLE 4.9. Roll subsidence mode: root mean square error relative to unconstrained aircraft model with controlled thrust for constant ground speed.

Compensation		**Time frame** 2.0s to 2.25s	2.0s to 2.5s	2.0s to 2.75s
	None	0.00123	0.025	0.0563
p (deg/s)	F_c^*	0.00213 (72.8%)	0.00432 (-82.7%)	0.0652 (15.8%)
	F_c^{**}	6.02e-05 (-95.1%)	0.000411 (-98.4%)	0.0549 (-2.53%)
	None	4.82e-05	0.00152	0.0109
ϕ (deg)	F_c^*	7.49e-05 (55.5%)	0.000835 (-45.2%)	0.00547 (-49.6%)
	F_c^{**}	5.51e-06 (-88.6%)	4.3e-05 (-97.2%)	0.00365 (-66.4%)
	None	0.0195	0.0196	0.0208
α (deg)	F_c^*	0.0195 (0.0148%)	0.0197 (0.477%)	0.0212 (2.24%)
	F_c^{**}	2.4e-06 (-100%)	0.000235 (-98.8%)	0.00295 (-85.8%)
	None	4.29e-05	0.00143	0.00217
β (deg)	F_c^*	0.000132 (208%)	0.000187 (-87%)	0.00378 (73.6%)
	F_c^{**}	3.39e-06 (-92.1%)	8.6e-05 (-94%)	0.00328 (50.8%)

4.3.5 Effect of kinematic compensation on perceived aerodynamic coefficients

This section uses a different approach to study the effects kinematic compensation have on the aircraft by estimating the aerodynamic coefficients from its simulated motion and comparing them to the values used in the simulation model itself. Note that with the implementation of the load cell on the manoeuvre rig it is now possible to conduct conventional static and dynamic forced oscillation experiments to measure these aerodynamic coefficients directly rather than estimating them via motion responses. Regardless, the parameter estimation method is used here to give insight as to how the kinematic constraints and compensation change the perceived value of the aerodynamic coefficients.

The estimation technique used here is the equation error method as it is the simplest method and the responses do not contain noise. The suitability of this method is demonstrated by re-identifying the known aerodynamic coefficients from the motion of the unconstrained aircraft model [70]. The model used for the estimation assumes the aircraft model is unconstrained and produces constant thrust. All mass and inertial properties are assumed to be known. As an example, the system of equations to be solved for the longitudinal case is:

$$\begin{bmatrix} 1 & \alpha & \frac{c}{2V}\dot{\alpha} & \delta_e \\ \vdots & \vdots & \vdots & \vdots \\ 1 & \alpha_n & \frac{c}{2V_n}\dot{\alpha}_n & \delta_{e_n} \end{bmatrix} \begin{bmatrix} C_{L_0} \\ C_{L_\alpha} \\ C_{L_{\dot{\alpha}}} \\ C_{L_{\delta_e}} \end{bmatrix} = \begin{bmatrix} C_L \\ \vdots \\ C_{L_n} \end{bmatrix} \tag{4.74}$$

where the subscript n represents the total number of measurements taken. Taking the pseudo-inverse of the left hand side matrix and multiplying it with the right side vector results in the least-square estimation of the coefficients vector. The total forces and moments are calculated using the measured translation and rotation accelerations together with the aircraft mass and moments of inertia.

The states that are to be excited are largely dependant on the input signal used. Conventionally, signals such as the 3-2-1-1 signal are used for parameter estimation to sufficiently excite all states of the aircraft. The Morlet wavelet signal is used here since it produces smaller translations which were shown to be beneficial for the constrained response accuracy and also sufficiently excites most of the aircraft states. Two responses are used to estimate the longitudinal and lateral derivatives. Each of the responses are excited by a Morlet wavelet input to the elevator and rudder respectively. The central frequencies for each wavelet are 1.67 Hz and 2.00 Hz which correspond to the short-period and Dutch roll frequencies, determined using a Fast Fourier Transform of their responses.

Four constrained aircraft cases are presented here: a planar constrained aircraft, a spherically constrained aircraft with no compensation, a spherical constrained aircraft with kinematic compensation ($\mathbf{F_c}^*$), and a spherical constrained aircraft with kinematic compensation and artificial thrust ($\mathbf{F_c}^{**}$). Note that all these constrained aircraft do not produce any thrust. Figures 4.16 and 4.17 show the wavelet responses for the short-period and Dutch roll modes respectively. Tables 4.10 and 4.11 show the parameter estimation results for the longitudinal and lateral-directional derivatives respectively for each case. As previously mentioned, the derivatives of the unconstrained case are re-estimated first to demonstrate the accuracy of the estimation technique. The parameters were estimated to within 1% error showing the suitability of the technique and input signal used. Note a percentage error of zero means a perfect match.

It can be seen that all translation related coefficients (C_L and C_Y) are improved by kinematic compensation ($\mathbf{F_c}^*$) and further improved with the addition of artificial thrust ($\mathbf{F_c}^{**}$), similar to the results seen in the previous section. The exception is the estimation of the drag derivatives which show similar magnitudes of error for all constrained cases. This is caused by the lack of motion in the direction of drag which is an inherent limitation for all the constraints studied here. Another oddity is the error in the estimation of $C_{L_{\dot{\alpha}}}$ which is caused by insufficient excitation to the $\dot{\alpha}$ state and has a relatively small contribution to the total lift coefficient. Further investigations may be carried out, such as experimenting with various input signals to give better $\dot{\alpha}$ excitation and with different parameter estimation techniques; these are not done here as it is beyond the scope of this study. However, estimation of the $\dot{\alpha}$ derivatives for the Hawk model found using forced dynamic testing on the manoevure rig is presented in Chapter 6. The moment coefficients are estimated accurately given that the excitation of the relevant state is large enough. Compensation show negligible improvements to these coefficients. This indicates that compensation may not be required if rotation responses are of importance only. These results

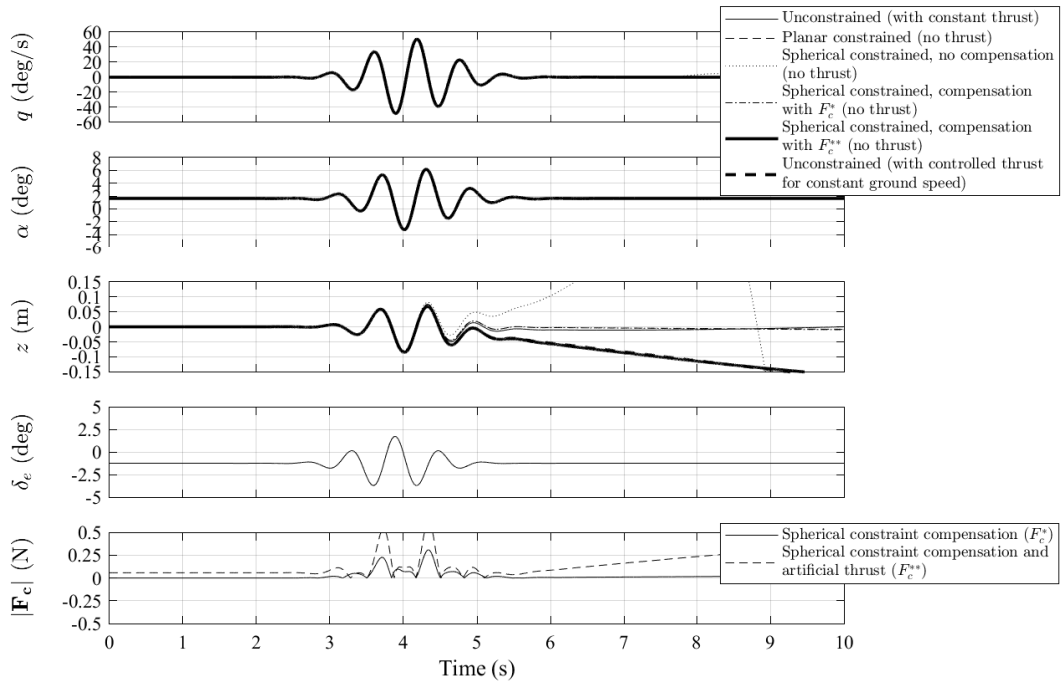

FIGURE 4.16. Short-period mode responses with a Morlet wavelet.

have been published in References [67, 68].

TABLE 4.10. Estimating longitudinal aerodynamic coefficients from short-period response (0 to 6 seconds).

Aerodynamic coefficients	**Simulation model value**	**Unconstrained (with constant thrust) estimate**	**Planar (no thrust) estimate**	**Spherical $0.8m$ (no thrust) estimate**		
				No compensation	With $\mathbf{F_c}^*$	With $\mathbf{F_c}^{**}$
C_{L_0}	0.28	0.28 (0%)	0.28 (0%)	0.282 (0.714%)	0.28 (0%)	0.28 (0%)
C_{L_α}	3.45	3.45 (0%)	3.41 (-1.16%)	3.37 (-2.32%)	3.4 (-1.45%)	3.44 (-0.29%)
$C_{L_{\dot{\alpha}}}$	0.72	0.726 (0.833%)	1.04 (44.4%)	2.05 (185%)	0.914 (26.9%)	0.488 (-32.2%)
$C_{L_{\delta_e}}$	0.36	0.36 (0%)	0.36 (0%)	0.425 (18.1%)	0.357 (-0.833%)	0.357 (-0.833%)
C_{D_0}	0.03	0.03 (0%)	0.0383 (27.7%)	0.0392 (30.7%)	0.0382 (27.3%)	0.0375 (25%)
C_{D_α}	0.3	0.3 (0%)	0.00422 (-98.6%)	-0.0127 (-104%)	0.00832 (-97.2%)	0.0303 (-89.9%)
C_{M_α}	-0.38	-0.38 (0%)	-0.38 (0%)	-0.38 (0%)	-0.38 (0%)	-0.38 (0%)
$C_{M_{\dot{\alpha}}}$	-1.1	-1.1 (0%)	-1.1 (0%)	-1.1 (0%)	-1.1 (0%)	-1.1 (0%)
C_{M_q}	-3.6	-3.6 (0%)	-3.6 (0%)	-3.6 (0%)	-3.6 (0%)	-3.6 (0%)
$C_{M_{\delta_e}}$	-0.5	-0.501 (0.2%)	-0.501 (0.2%)	-0.501 (0.2%)	-0.501 (0.2%)	-0.501 (0.2%)

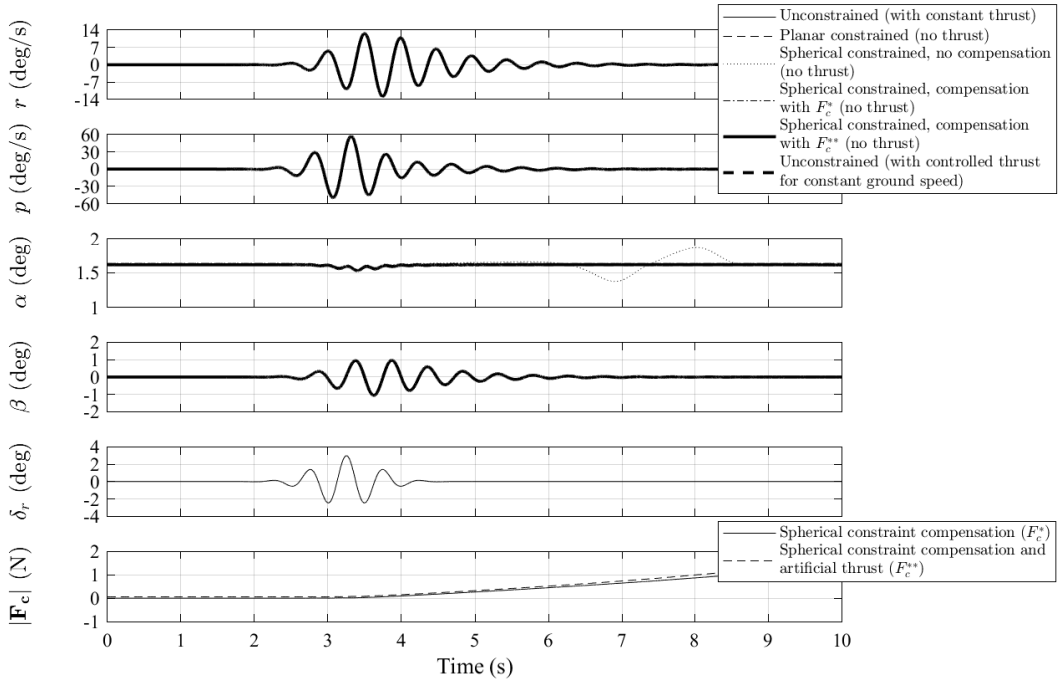

FIGURE 4.17. Dutch roll mode responses with a Morlet wavelet.

TABLE 4.11. Estimating lateral-directional aerodynamic coefficients from Dutch roll response (0 to 6 seconds).

Aerodynamic coefficients	**Simulation model value**	**Unconstrained (with constant thrust) estimate**	**Planar (no thrust) estimate**	**Spherical $0.8m$ (no thrust) estimate**		
				No compensation	With $\mathbf{F_c}^*$	With $\mathbf{F_c}^{**}$
C_{Y_β}	-0.98	-0.98 (0%)	-0.94 (-4.08%)	-0.937 (-4.39%)	-0.94 (-4.08%)	-0.979 (-0.102%)
$C_{Y_{\delta_r}}$	0.17	0.17 (0%)	0.17 (0%)	0.173 (1.76%)	0.17 (0%)	0.17 (0%)
C_{l_β}	-0.12	-0.127 (5.83%)	-0.127 (5.83%)	-0.127 (5.83%)	-0.127 (5.83%)	-0.127 (5.83%)
C_{l_p}	-0.26	-0.26 (0%)	-0.26 (0%)	-0.26 (0%)	-0.26 (0%)	-0.26 (0%)
C_{l_r}	0.14	0.15 (7.14%)	0.15 (7.14%)	0.15 (7.14%)	0.15 (7.14%)	0.15 (7.14%)
$C_{l_{\delta_r}}$	0.105	0.106 (0.952%)	0.106 (0.952%)	0.106 (0.952%)	0.106 (0.952%)	0.106 (0.952%)
C_{n_β}	0.25	0.247 (-1.2%)	0.247 (-1.2%)	0.247 (-1.2%)	0.247 (-1.2%)	0.247 (-1.2%)
C_{n_p}	0.022	0.0151 (-31.4%)	0.015 (-31.8%)	0.015 (-31.8%)	0.015 (-31.8%)	0.0151 (-31.4%)
C_{n_r}	-0.35	-0.345 (-1.43%)	-0.345 (-1.43%)	-0.345 (-1.43%)	-0.345 (-1.43%)	-0.345 (-1.43%)
$C_{n_{\delta_r}}$	-0.032	-0.0291 (-9.06%)	-0.0291 (-9.06%)	-0.0291 (-9.06%)	-0.0291 (-9.06%)	-0.0291 (-9.06%)

4.4 Practical aspects of compensation

When considering the extent of compensation, kinematic compensation alone ($\mathbf{F_c}^*$) gives a good match with the unconstrained aircraft with constant thrust, whereas trying to simulate an unconstrained aircraft at constant ground speed with the additional artificial thrust component ($\mathbf{F_c}^{**}$) causes the aircraft to deviate, as can be seen in Figure 4.16. Practically simulating the

unconstrained aircraft at constant ground speed would be limited since the motion will cause the rig's arm to reach it's physical stops. Since $\mathbf{F_c}^{**}$ only show minor improvements to the response match and perceived aerodynamic coefficients as shown in the previous sections, $\mathbf{F_c}^{*}$ alone may be sufficient especially for longer responses.

In all the previous analyses done in this chapter it was assumed that all aerodynamic and inertial effects of the manoeuvre rig have been compensated for. This means that there was no additional tangential reaction force acting on the aircraft model during its motion as a result of an ideal compensator control surface controller cancelling the aerodynamic and inertial forces of the rig itself. In addition, this controller was assumed to be able to ideally apply the kinematic compensatory force ($\mathbf{F_c}^{*}$ / $\mathbf{F_c}^{**}$) onto the aircraft model as a tangential reaction force. The ability of the compensator to achieve these objectives is largely dependant on the effectiveness of the compensator and its control surfaces, and the design of the controller. Assuming the aerodynamics of the compensator are linear, mass and inertial properties of the rig are known exactly, aerodynamic interference between the aircraft model and the downstream compensator are negligible, and the compensator control surfaces are ideally responsive, then an ideal controller may be calculated. However, when considering practical implementation, these conditions are very difficult to achieve especially when lag from control surface actuation and delay from data transmission are present. In addition, filters used to process noise will introduce additional lag. In this section the effect of delay when applying the kinematic compensation force is studied. Chapter 7 contains details on the practical implementation of the compensation derived here including controller design where the viability of this concept is analysed. On the manoeuvre rig, the compensator control surface actuation lag and data transmission delay are about 100 and 4 milliseconds respectively [54].

In the study here a range of delays from 0 to 250 milliseconds is applied to the compensation force for the short-period mode, as shown in Figure 4.18. Note that it is still assumed that the rig inertial and aerodynamic tangential reaction force component is ideally compensated for by an ideal controller and so the rig itself is not simulated, only the spherical kinematic constraint. Figure 4.19 shows a comparison for the short-period mode responses with a range of delays. The same wavelet input used in the previous section is adopted. In general the match with the unconstrained motion degrades as the delay increases especially for heave. Table 4.12 shows the root mean square errors of each delay case relative to the unconstrained aircraft with constant thrust. It can be seen that with regards to the pitch rate and angle of attack states, a delay of about 150 milliseconds is equivalent to the response with no compensation. Therefore improvements to the response can be obtained if the total delay is less than 150 milliseconds. The exception is the heave response since the error remains lower than without compensation even with a delay of 250 milliseconds. The trend can be seen for the Dutch roll mode as well although the motion degrades to a lesser extent.

Figure 4.20 shows the effect on the compensated response when aircraft gimbal friction

TABLE 4.12. RMS comparison between the spherically constrained aircraft model (without thrust) responses with delayed $\mathbf{F}_\mathbf{c}^*$ relative to the unconstrained response with constant thrust (0 to 6 seconds).

	0 ms delay	50 ms delay	100 ms delay	150 ms delay	200 ms delay	250 ms delay	No $\mathbf{F}_\mathbf{c}^*$
q (deg/s)	0.116	0.135	0.169	0.202	0.229	0.246	0.198
α (deg)	0.0218	0.0229	0.0247	0.0266	0.0281	0.0289	0.0265
z (m)	0.00344	0.00430	0.00524	0.00628	0.00740	0.00858	0.0312

(defined by Equation 3.119) is added. Friction is introduced as an external moment in the equations of motion. Two observations can be made: the first being the reduction in initial amplitudes of the pitch rate (q), angle of attack (α), and heave (z) responses, and the second being the divergence in heave in the long term response compared to the case without friction. These differences cannot by compensated by the manoeuvre rig since it does not have the capability of applying external moments onto the aircraft, only a tangential reaction force. However, the friction in the arm gimbal can be compensated for by the tangential reaction force. Therefore, it is important to reduce aircraft gimbal friction as much as possible in order to retain a close match in response with the unconstrained aircraft model.

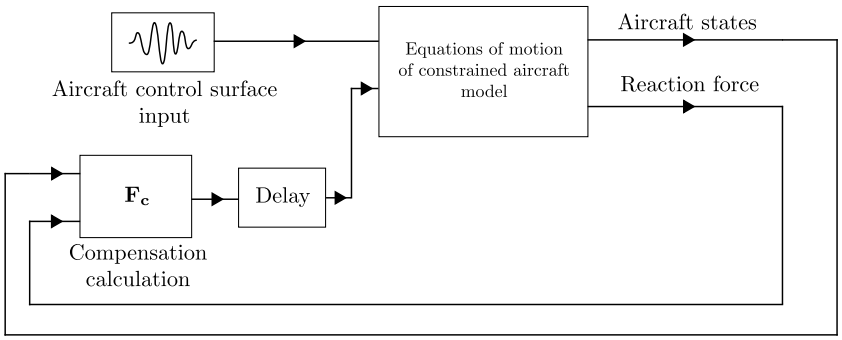

FIGURE 4.18. Simplified block diagram of the simulation.

4.5 Summary

This chapter has explored the effects the kinematic constraints (applied by the rig) have on the motion of an aircraft motion with special attention to the spherical constraint similar to the manoeuvre rig. It was shown that an aircraft with constant thrust constrained onto a plane is almost equivalent to an unconstrained aircraft with controlled thrust for constant ground speed. An aircraft with constant thrust constrained onto a sphere will exhibit similar responses to the planar case where the motion discrepancy increases as the sphere radius decreases. This is as a result of the hard limitation caused by the constraint affecting the trajectory and hence velocity and aerodynamic loads of the aircraft. Note that the planar constraint is equivalent to

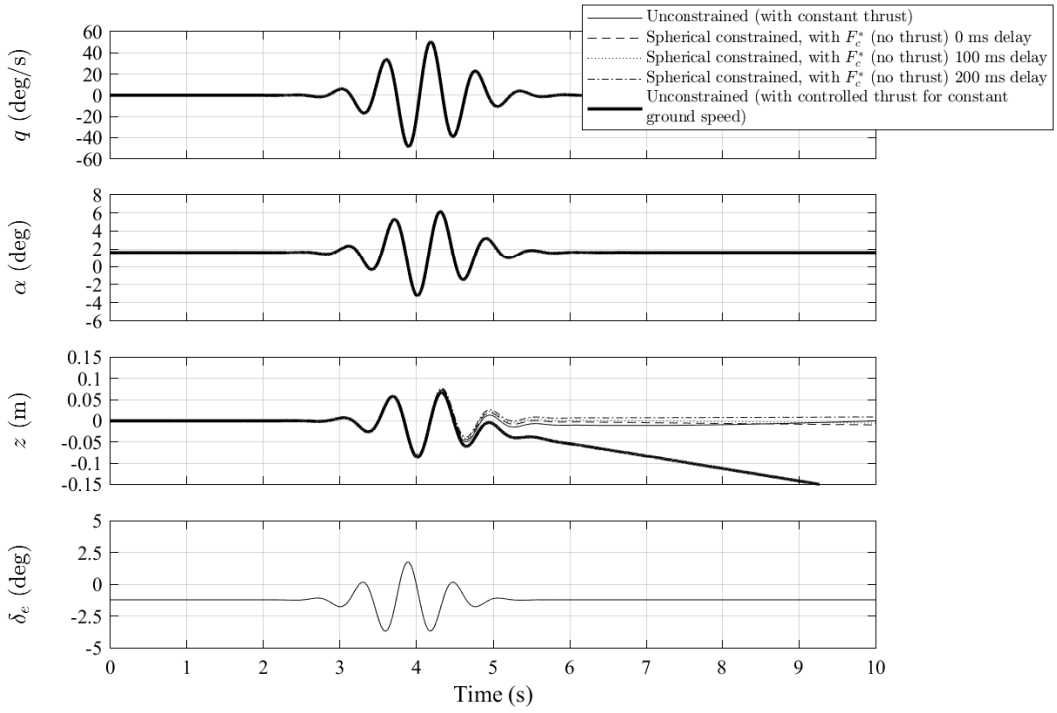

FIGURE 4.19. Short-period response with $\mathbf{F_c^*}$ compensation including transmission delay.

the spherical constraint with an infinite radius. As a result, long term motion such as the full phugoid mode cannot be replicated while physically constrained. The onset of the phugoid mode can still be simulated if the heave motion is available, after which the effects on the response will be dominated by the velocity limitation the constraint places on the aircraft model.

If the aircraft model does not create thrust while spherically constrained a destabilizing moment caused primarily by drag will cause the aircraft responses to diverge around the sphere. This leads to the concept of kinematic compensation ($\mathbf{F_c^*}$) where the objective is to cancel this moment by applying an external tangential force onto the aircraft model. On the manoeuvre rig this can be achieved by its compensator. The derivation of this compensation force and its improvement on the motion of the aircraft model have been presented. The improvement has been quantified using root mean square errors of the motion states as well as changes to the perceived aerodynamic coefficients of the aircraft model using parameter estimation. It was seen that the larger the response translation is, the less effective the compensation becomes. Additionally, the concept of artificial thrust compensation ($\mathbf{F_c^{**}}$) was also presented where an additional tangential force component is used to match the motion of the constrained aircraft without thrust with the motion of an unconstrained aircraft at constant ground speed. Although including artificial thrust compensation does show minor improvement to the initial response of

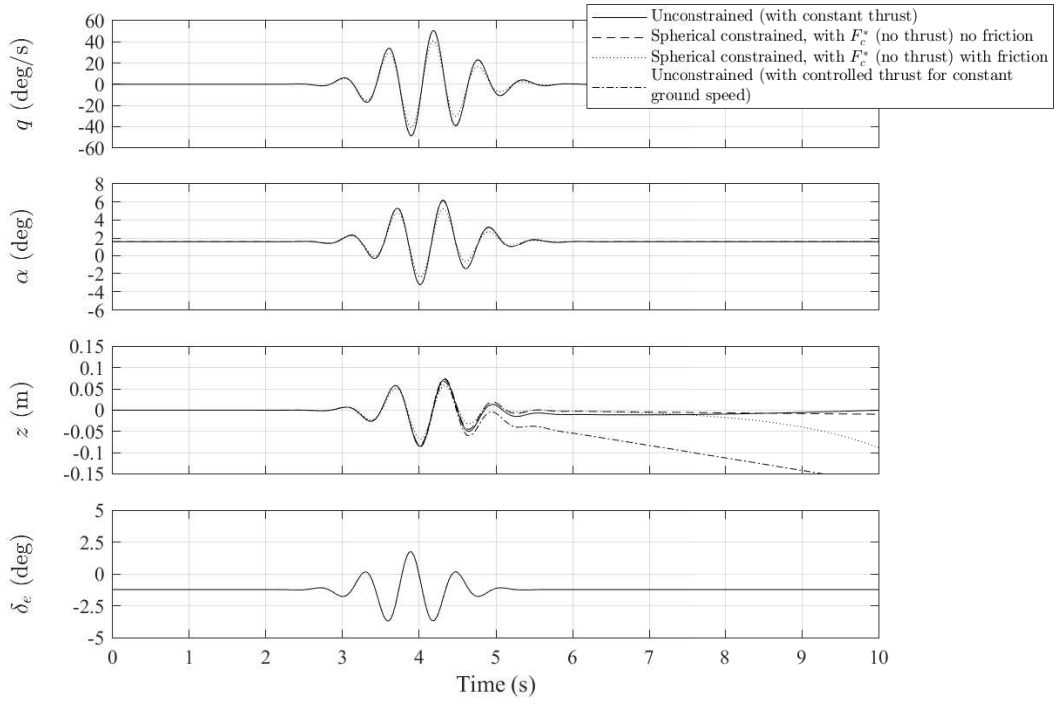

FIGURE 4.20. Effects of friction on the short-period response with kinematic compensation.

the aircraft, the resulting deviating motion will limit practical use. In addition, the deviating motion will further exacerbate the hard limitations of the spherical constraint on the overall response match as mentioned before. Effects of delay when applying the compensation force and aircraft gimbal friction were studied. It was concluded that if the delay is less than 150 ms, then an improvement in response match with the free-flying aircraft will be seen. On the other hand, friction in the aircraft gimbal cannot be directly compensated for and should be reduced as much as possible.

Since responses with kinematic compensation alone show a good match with an aircraft with constant thrust (as is the common case) especially for longer responses, it will be the primary focus for practical implementation. This compensation concept will be explored experimentally in Chapter 7.

CHAPTER 5

LOAD CELL IMPLEMENTATION

5.1 Introduction

In the previous chapter, it was recognized that in order to compensate for the manoeuvre rig kinematic, inertial and aerodynamic effects the measurement of the reaction force between the aircraft model and the manoeuvre rig is required. This can be achieved with a load cell. A load cell will further extend the capabilities of the manoeuvre rig making it possible to perform conventional static and dynamic wind tunnel experiments. This chapter will detail all design aspects and considerations taken for the implementation of the load cell on the manoeuvre rig. It will include defining the requirements for the load cell, the design of the structural modifications of the rig's arm to accommodate the load cell, and software implementation in order to combine with the existing interface. This chapter will also contain preliminary aerodynamic measurements taken for the Hawk model.

5.2 Estimation of load cell requirements

This section contains the methods used to find the requirements for the load cell as well as discussions on the considerations taken when designing the load cell attachment and the choice of the load cell itself. The aerodynamics model developed in the Hypothetical High Incidence Research Model (HHIRM) scaled for a T-tail airliner model is used to estimate the maximum load cases. This T-tail model is currently being planned to be manufactured and tested on the manoeuvre rig and is relatively larger than the current Hawk model, resulting in higher aerodynamic and inertial loads. Dimensional and inertial properties of the T-tail model used in the simulation are shown in Appendix E. The HHIRM was chosen over existing aerodynamic models due to the HHIRM's capability in estimating dynamic lift overshoot, during which the

maximum loads will most likely be observed. An overview of the HHIRM is given in Section 3.8.4. Dynamic lift overshoot can be assumed to be mainly dependent on the pitch rate of the aircraft, angle of attack, and elevator deflection. The maximum lift can be expected to be observed when the aircraft pitch rate and elevator deflection are at their highest. However, the maximum aircraft pitch rate is in turn dependent on the pitch inertia (I_{yy}) of the aircraft model. The highest angle of attack for the aircraft is expected to occur at the largest rotation angle of the aircraft gimbal and when the rig pitch rate is the highest to give maximum aircraft vertical velocity, although the highest lift may occur at an angle of attack value lower than the maximum. The same is true for lateral-directional loads. Rig dynamics will also couple with the aerodynamic loads of the aircraft which may result in an even higher reaction force experienced by the load cell. As a result, a specific maximum force or moment may occur at a combination of rig and aircraft attitudes and rotation rates. A comprehensive list of load cases will be analysed to identify when these maximum loads will occur.

A wind speed of 40 m/s was chosen as the overload range of the load cell with an additional safety factor of 1.5 to take into account impact loads. The working range windspeed was chosen to be 30 m/s for the T-tail airliner model. The current maximum operable wind speed of the manoeuvre rig is 40 m/s which is limited by the current design of the rig's arm (which has a reserve factor of 1.2) [10].

The ideal position of the load cell is on the arm of the manoeuvre rig below the aircraft model. Two possibilities for the position were identified (both vertically below the aircraft model): the first being below the component of the aircraft gimbal providing yaw motion (318.3 mm below the aircraft, lower position) and the second above it (88.3 mm below the aircraft, upper position). Both positions have their advantages and disadvantages. The lower position has the advantage that the load cell's connecting cable can be easily passed through the rig's arm, producing no interference with the aircraft's motion. The disadvantage is that, due to its distance from the aircraft, the load cell must have the capacity to withstand much larger moments. It was found that the moment experienced by the load cell is the driving factor for the choice of product. Load cells meeting these moment requirements are large in size, heavy, and have poor resolution and accuracy, all of which are undesirable. It is beneficial for the load cell to have a low profile to have minimum aerodynamic interference and a low mass to keep the total rig inertia low. Additionally, the part of the gimbal/rig between the aircraft and load cell will contribute to the measured drag, which should preferably be minimised. On the other hand, the upper position will experience much lower moments (about three times less). Hence, the load cell can be small, light weight, and can have better accuracy (9.8 times better) and resolution (4.7 times better). However, the disadvantage of the higher position is that, since the load cell is mounted on the yaw component of the aircraft gimbal, the connection cable will add some stiffness to the aircraft's yaw motion. A strain-relieved cable type was chosen in an attempt to minimise its effect. It was decided that the upper position for the load cell will be chosen based on the significant improvement of accuracy

and resolution compared to the lower position.

The full equations of motion for the manoeuvre rig and aircraft model shown in Section 3.7 will be used here and simulated in Matlab®/Simulink® as described in Section 3.11. The properties of each component simulated are given in Appendix E. The reaction forces and moments that will be experienced by the load cell can be extracted from the ${C_q}^T \boldsymbol{\lambda}$ term in the main combined equations of motion (Equation 3.18). The Jacobian matrix C_q for the manoeuvre rig was expressed in Equation 3.97. From the Jacobian, the portion of the matrix associated with the constraint equations connecting the load cell to the link can be isolated to define the reaction loads as

$$\boldsymbol{Q_E}^{lc}_{reaction} = \begin{bmatrix} -I_3 & 0_{3,4} \\ \widetilde{2(A^{lc}\overline{\boldsymbol{u}}^l)}E^{lc} & I_4 \end{bmatrix}^T \boldsymbol{\lambda}_{21:27} \tag{5.1}$$

The reaction forces and moments (${\boldsymbol{Q_R}}^{lc}$ and ${\overline{\boldsymbol{F}}_{\boldsymbol{\theta}}}^{lc}$ respectively) can now be calculated using Equation 3.29. Note that the forces will need to be transformed onto the load cell body axes. The bar above a symbol represents that the quantity is relative to the body axes.

First, the maximum and minimum possible aerodynamic forces and moments (except rolling moment) that can be produced by the aircraft model is obtained by simulating the aircraft with frequency sweep inputs to the elevator and rudder (0.5 to 3.0 Hz). This will be done with the rig arm fixed, but the aircraft able to rotate about all three axes individually (1 DOF). The maximum and minimum rolling moments were obtained from a step input of $\pm 30^\circ$ to the ailerons. The maximum aerodynamic loads found are shown in Figures 5.1 and 5.2, and Table 5.1 for a wind speed of 40 m/s. Note that some of the motions exceed the physical limits of the aircraft's gimbal. However, these loads will still be considered and used as an additional safety margin.

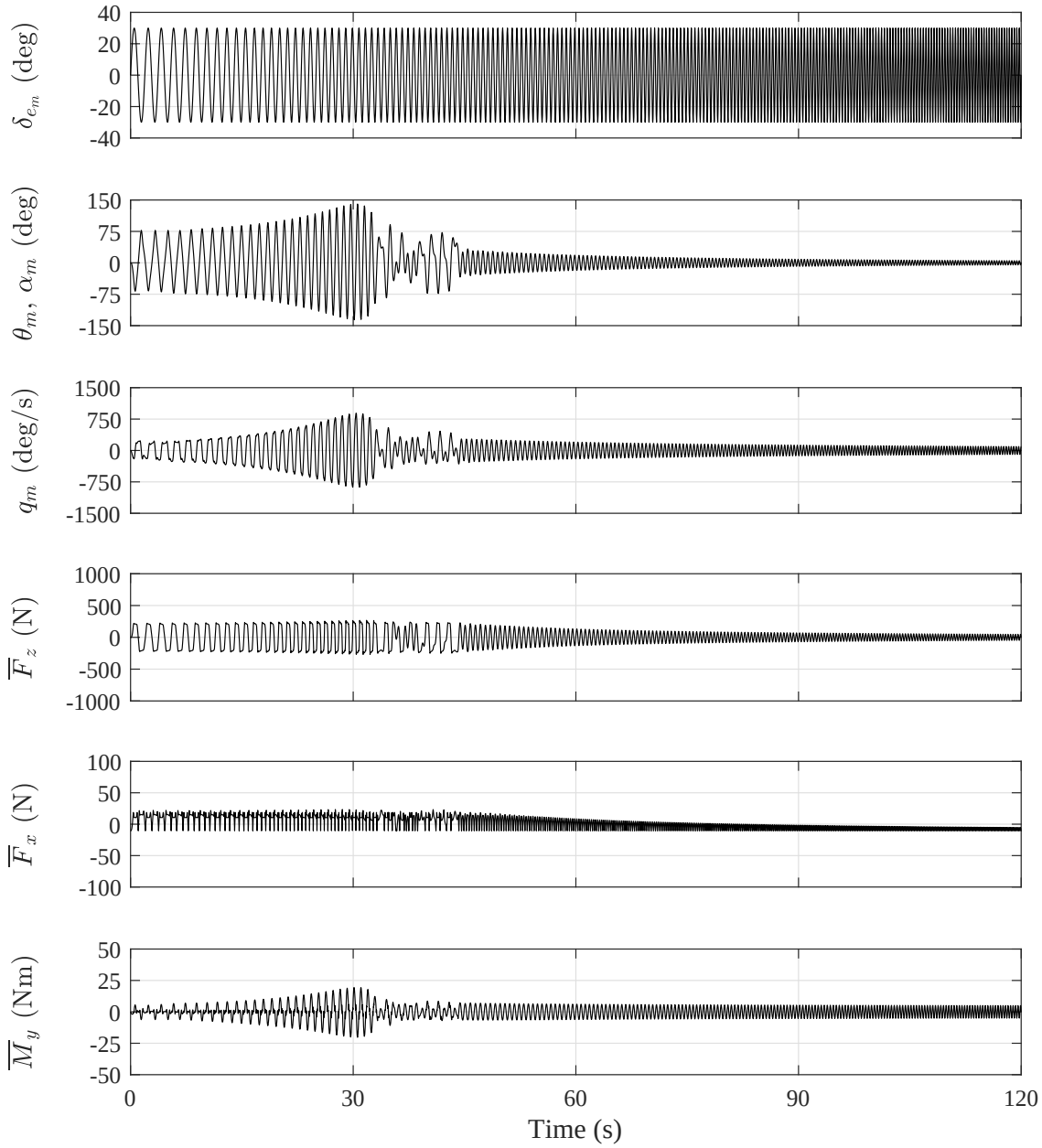

FIGURE 5.1. T-tail model pitch frequency sweep response at 40 m/s wind speed (elevator input of 0.5 to 3.0 Hz).

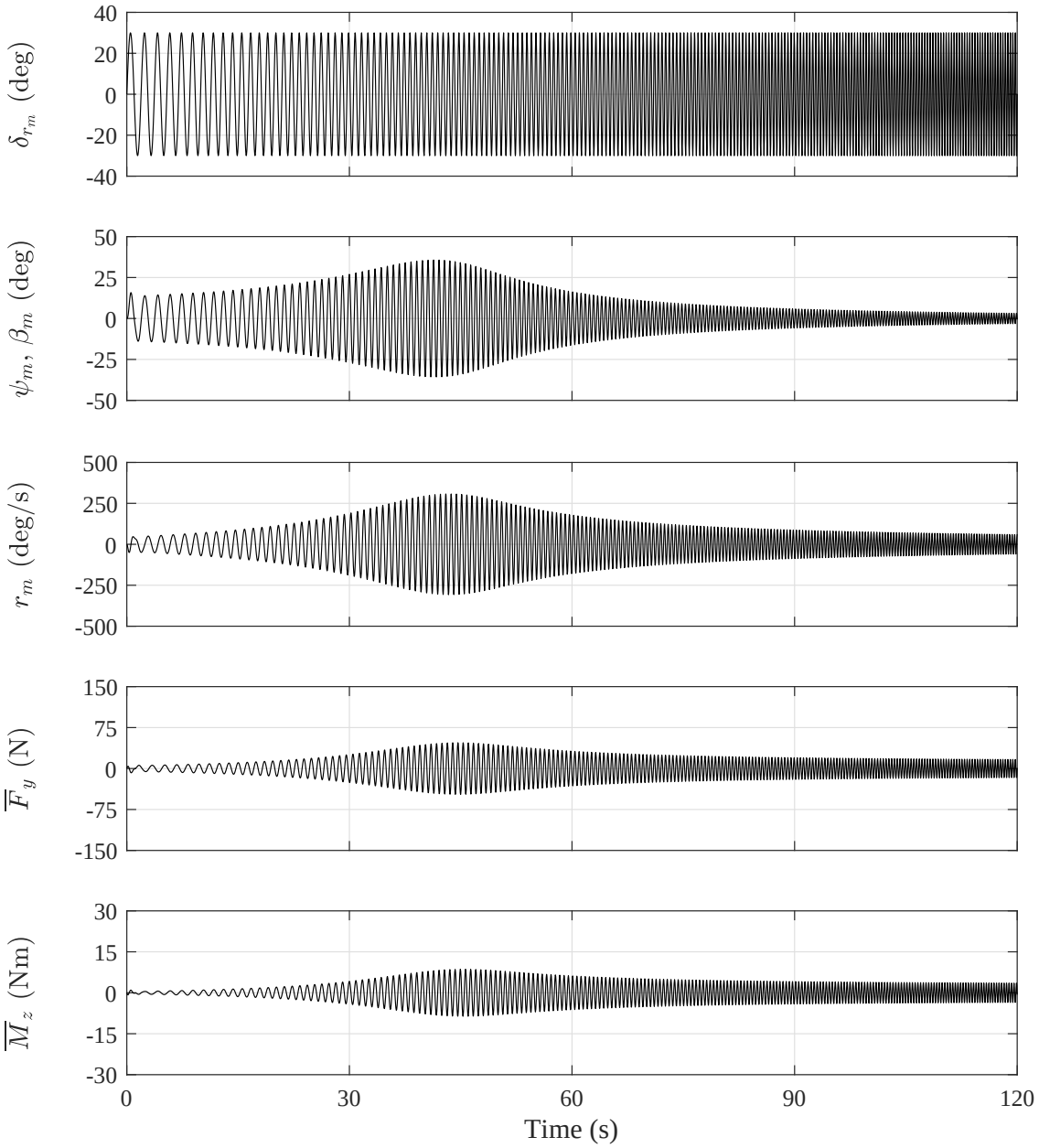

FIGURE 5.2. T-tail model yaw frequency sweep response at 40 m/s wind speed (rudder input of 0.5 to 3.0 Hz).

TABLE 5.1. T-tail model maximum and minimum dynamic loads (wind axes) at 40 m/s wind speed.

	Minimum	Maximum
$\overline{F}_x$ (N)	-10.6	23.5
$\overline{F}_y$ (N)	-47.3	47.3
$\overline{F}_z$ (N)	-268.6	267.9
$\overline{M}_x$ (Nm)	-3.4	3.4
$\overline{M}_y$ (Nm)	-20.3	19.4
$\overline{M}_z$ (Nm)	-8.6	8.6

TABLE 5.2. Aircraft and rig attitudes considered for load cell load simulation (approximate limitations of the manoeuvre rig).

ϕ_a (°)	0 , 90 , 180 , 270
θ_a (°)	-12.5 , 0 , 7
ψ_a (°)	-30 , 0 , 30
ϕ_m (°)	$\phi_a - 40$, ϕ_a , $\phi_a + 40$

Next, these loads are applied directly onto the aircraft's c.g. (with the aircraft fixed to not rotate) at different rig arm positions and the reaction force at the load cell was recorded. This considers the approximate physical limitations of the rig gimbal. Note that an extended version of the rig arm is used here to accommodate the larger T-tail mode. The aircraft and rig attitudes considered are shown in Table 5.2. All attitude angles are given in the inertial axes and follows the conventional rotation sequence (from inertial to body axes: yaw, pitch, roll). Note that only aircraft roll is considered for the aircraft because the maximum/minimum aerodynamic loads covers the possible range of angle of attack and sideslip. All combinations of aerodynamics loads, and aircraft and rig attitudes sum up to a total of 6912 load cases. The maximum and minimum forces and moments applied on the load cell (while the rig is static) found from the load cases are shown in Table 5.3 for both load cell positions. As expected, the magnitudes of the rolling and pitching moments are lower when the load cell is placed closer to the aircraft.

Next, the maximum rotation rates of the rig are found and applied as initial conditions to the maximum/minimum load cases found. This will consider the effect of centrifugal forces on the load cell requirements. The maximum rig pitching and yawing rates were found by setting the initial position of the arm at the gimbal stop position (for each arm DOF) and using maximum compensator and aircraft control surface deflections, along with aircraft attitude to create the maximum moment about the arm gimbal. The maximum rotation velocity achieved as the arm moves to the opposite gimbal stop was recorded. The maximum rolling rate was found by releasing the rig arm from an attitude of $\phi_a = \pm 180^\circ$ (inverted) with maximum compensator control surface deflections for maximum rolling moment and recording the maximum rate observed during one

TABLE 5.3. Maximum and minimum load cell reaction loads (body axes) at 40 m/s wind speed with rig arm fixed.

	Load cell lower position (318.3 mm below aircraft model)		Load cell upper position (88.3 mm below aircraft model)	
	Minimum	Maximum	Minimum	Maximum
$\overline{F}_x$ (N)	-151.7	171.0	-151.7	171.0
$\overline{F}_y$ (N)	-253.2	253.2	-253.2	253.2
$\overline{F}_z$ (N)	-300.7	300.0	-300.7	300.0
$\overline{M}_x$ (Nm)	-88.4	88.4	-30.6	30.6
$\overline{M}_y$ (Nm)	-75.4	67.4	-36.5	33.7
$\overline{M}_z$ (Nm)	-15.6	15.6	-15.6	15.6

revolution. Note that the rig was fixed for pure roll. The maximum rates found are shown in Table 5.4. Note that these extreme cases are unlikely to occur, however they are still considered to cover all possibilities.

TABLE 5.4. Maximum rig arm rotation rates.

p_a ($^\circ/s$)	±944.1
q_a ($^\circ/s$)	±346.4
r_a ($^\circ/s$)	±350.7

Following this, the maximum/minimum load cases were repeated with the rig arm free to move, the maximum rotation rates set as initial conditions, and using maximum compensator control surface defections (about 7,000 new load cases). This will include the centrifugal force and additional loads applied by the compensator. There has been an intention to move the position of the compensator further aft in order to increase its control power, however, this will restrict the rig's usability in the open-jet wind tunnel due to limited working space. At this stage the new position of the compensator has not been decided, however for the purpose of simulating any effect on the load cell, the compensator (c.g.) has been moved from 0.38m to a roughly estimated 0.68m behind the arm's gimbal. The rig arm free loads experienced by the load cell for both lower and upper positions are shown in Table 5.5.

Comparing with Table 5.3 for the rig fixed case, the loads that increased in magnitude are the maximum X, minimum M, maximum N, and minimum N. The increase in magnitude of maximum X and minimum M are a direct cause of the centrifugal force due to the rigs rotation rates. The increase in magnitude of N is due to the yaw moment transferred by the compensator. The reduced magnitudes of the rig free load cell Y and Z reaction forces compared to the rig fixed case forces indicate that the compensator's control power was insufficient to overcome the aircraft's aerodynamic forces simulated (Table 5.1).

The load cell required capacities can now be decided by the maximum magnitudes of loads

TABLE 5.5. Maximum and minimum load cell reaction loads (body axes) at 40 m/s wind speed with the rig free to move.

	Load cell lower position (318.3 mm below aircraft model)		Load cell upper position (88.3 mm below aircraft model)	
	Minimum	Maximum	Minimum	Maximum
$\overline{F}_x$ (N)	41.3	390.1	51.9	381.8
$\overline{F}_y$ (N)	-205.7	205.7	-206.2	206.3
$\overline{F}_z$ (N)	-266.5	244.2	-271.5	235.3
$\overline{M}_x$ (Nm)	-70.7	70.9	-23.0	23.1
$\overline{M}_y$ (Nm)	-147.7	9.1	-66.8	28.0
$\overline{M}_z$ (Nm)	-42.8	42.8	-42.9	42.9

found in Table 5.3 and 5.5. Tables 5.6 and 5.7 show the working and overload ranges for the combined rig arm fixed and free cases for the lower and upper load cell positions respectively. A safety factor of 1.5 is used to take into account impact loads. Due to time constraints, loads at 30 m/s were obtained by multiplying the loads at 40 m/s by 0.56, due to the loads being proportional to V^2. As stated before, the load cell higher position was chosen due to the aforementioned reasons.

TABLE 5.6. Load cell required capacities for the lower position (318.3 mm below aircraft model).

	Working range 30 m/s		Overload range 40 m/s, Safety Factor 1.5	
	Minimum	Maximum	Minimum	Maximum
$\overline{F}_x$ (N)	-85.3	219.4	-227.6	585.1
$\overline{F}_y$ (N)	-142.4	142.4	-379.8	379.8
$\overline{F}_z$ (N)	-169.2	168.8	-451.1	450.1
$\overline{M}_x$ (Nm)	-49.7	49.7	-132.6	132.6
$\overline{M}_y$ (Nm)	-83.1	37.9	-221.5	101.1
$\overline{M}_z$ (Nm)	-24.1	24.1	-64.1	64.1

The resolution required by the load cell was decided by the capability to measure changes in load due to a change in angle of attack and sideslip of 0.5°. The HHIRM aerodynamic model was used scaled to the Hawk as the loads created by it will be lower than that of the larger T-tail model. The aircraft was also constrained to the arm (locked aircraft gimbal), such that the aerodynamic moments are transferred onto the load cell. The rig is fixed at zero attitude angles. A wind speed of 20 m/s was used. The simulated results are shown in Tables 5.8 and 5.9 for angle of attack and sideslip respectively. Therefore the required resolution should be less than about 0.1 N for force measurements and 0.015 Nm for moment measurements. Note that these requirements are sufficient for the compensation concept introduced in Chapter 4, as shown by

TABLE 5.7. Load cell required capacities for the upper position (88.3 mm below aircraft model).

	Working range 30 m/s		Overload range 40 m/s, Safety Factor 1.5	
	Minimum	Maximum	Minimum	Maximum
$\overline{F}_x$ (N)	-85.3	214.8	-227.6	572.8
$\overline{F}_y$ (N)	-142.4	142.4	-379.8	379.8
$\overline{F}_z$ (N)	-169.1	168.7	-451.1	450.0
$\overline{M}_x$ (Nm)	-17.2	17.2	-45.9	45.9
$\overline{M}_y$ (Nm)	-37.6	19.0	-100.2	50.5
$\overline{M}_z$ (Nm)	-24.2	24.2	-64.4	64.4

TABLE 5.8. Load cell required resolution decided by the change in loads due a change in α of 0.5° at a wind speed of 20 m/s (Hawk).

Load cell reaction loads	$\alpha = 0°$	$\alpha = 0.5°$	Change in load
$\overline{F}_x$ (N)	-2.081	-1.977	0.104
$\overline{F}_y$ (N)	0.000	0.000	0.000
$\overline{F}_z$ (N)	23.789	23.165	-0.624
$\overline{M}_x$ (Nm)	0.000	0.000	0.000
$\overline{M}_y$ (Nm)	0.662	0.619	-0.043
$\overline{M}_z$ (Nm)	0.000	0.000	0.000

TABLE 5.9. Load cell required resolution decided by the change in loads due a change in β of 0.5° at a wind speed of 20 m/s (Hawk)

Load cell reaction loads	$\beta = 0°$	$\beta = 0.5°$	Change in load
$\overline{F}_x$ (N)	-2.081	-2.081	0.000
$\overline{F}_y$ (N)	0.000	-0.125	-0.125
$\overline{F}_z$ (N)	23.789	23.789	0.000
$\overline{M}_x$ (Nm)	0.000	-0.042	-0.042
$\overline{M}_y$ (Nm)	0.662	0.662	0.000
$\overline{M}_z$ (Nm)	0.000	0.015	0.015

experimental testing in Chapter 7.

5.3 Selected load cell: Mini45

The load cell chosen was the Mini45 from ATI Industrial Automation (Figure 5.3). This load cell is capable of measuring forces and moments in three axes. The transducer is disc shaped with physical dimensions of 45.0 mm diameter and 15.7 mm thickness. It has a mass of 0.0917 kg. A schematic of the load cell is shown in Appendix H. Its capacity, resolution, and accuracy data (for two selected calibration settings) are shown in Table 5.10. The specifications of the Mini45 satisfy the capacity requirements shown in Table 5.7 except for minimum pitching moment, and minimum and maximum yawing moments; however, the extreme simulated cases that resulted in those loads are unlikely to be encountered. The loads measured during experimentation need to be monitored to avoid loads exceeding the overload ranges in order to avoid damage. The high range calibration offers a larger range but worse resolution and accuracy whereas the low range calibration offers better resolution and accuracy at the cost of range. The low range calibration satisfies resolution requirements shown in Tables 5.8 and 5.9. Note that the accuracy values shown in Table 5.10 are for worst case situations. According to the manufacturer, normally a much better accuracy can be expected, but this is not guaranteed.

One major reason for choosing this load cell is that it is compatible with a wireless transmitter (also provided by the company) and is capable of capturing loads at up to 4000 Hz. Signal conditioning and amplification is also done by the wireless transmitter itself. The load cell exit cable will be passed through the rig arm, entering below the aircraft gimbal and exiting behind the arm gimbal in front of the compensator where the wireless transmitter will be placed. The wireless transmitter was placed here for two reasons: the first being due to insufficient space within the compensator fairing, and the second being the weight of the wireless transmitter (0.27 kg) could be used to statically balance the increase in weight at the aircraft position created by the load cell and attachment components. Note that a light tension on the cable should not affect the measurements; vibrations on the cable may affect measurements but can be filtered. The manufacturer stated resonant frequency of the Mini45 load cell is 5600 Hz for the x and y direction force measurements and for the moment measurement about the z axis, and 5400 Hz for the z axis force measurement and moment measurements about the x and y axes. The wireless transmitter is capable of recording data to a local MicroSD card if required. Both the load cell and wireless transmitter are powered by a removable lithium-polymer battery located in the transmitter.

Once the load cell was acquired, calibration tests were carried out to verify the manufacturer stated specifications. This was performed with the load cell mounted on the rig and using masses with known weights placed directly on the load cell and on the aircraft roll/pitch gimbal. The load cell could be rotated about each axis using the rig's arm gimbal and aircraft yaw mechanism in order to apply a force and moment about each axis. It was found that the measurements were within the load cell specifications, and load measurements were more accurate when an additional static load offset was present, i.e. it was less accurate around zero load. Drift of measured loads

FIGURE 5.3. ATI Mini45 load cell.

was not noticeable but should be investigated. Effect of ambient temperature on measurements should also be assessed. Table 5.11 shows the estimated uncertainly of non-dimensional load coefficients for the Hawk model and given conditions. The loads measured at the position of the load cell need to be transformed onto the aircraft body axes and therefore the uncertainties compound (the link length is the vertical distance between the load cell and aircraft model). These are calculated using the maximum load for each axis for the "low range" calibration which has a better accuracy. Note that the uncertainties of Hawk reference dimensions have not been verified. The physical rig modifications necessary to integrate the load cell is covered in the next section.

TABLE 5.10. Load cell capacities, resolutions and accuracy data.

	Low range (SI-145-5)	High range (SI-580-20)	Overload range (single axis)
$\overline{F}_x$ (Res, Acc) (N)	± 145 (0.0625, ± 1.813)	± 580 (0.25, ± 10.150)	± 5100
$\overline{F}_y$ (Res, Acc) (N)	± 145 (0.0625, ± 1.450)	± 580 (0.25, ± 7.250)	± 5100
$\overline{F}_z$ (Res, Acc) (N)	± 290 (0.0625, ± 2.175)	± 1160 (0.25, ± 11.600)	± 10000
$\overline{M}_x$ (Res, Acc) (Nm)	± 5 (0.00133, ± 0.063)	± 20 (0.00532, ± 0.250)	± 110
$\overline{M}_y$ (Res, Acc) (Nm)	± 5 (0.00133, ± 0.075)	± 20 (0.00532, ± 0.350)	± 110
$\overline{M}_z$ (Res, Acc) (Nm)	± 5 (0.000665, ± 0.063)	± 20 (0.00266, ± 0.200)	± 140

5.4 Rig modifications

This section describes the modifications done to the manoeuvre rig to accommodate the Mini45 load cell. The new designed components are presented including Finite Element Analysis to

TABLE 5.11. Estimated non-dimensional load coefficient uncertainties.

	Value	Absolute uncertainty	Percentage uncertainty
X_m (N)	-145	± 3.263	$\pm 2.25\%$
Y_m (N)	145	± 3.263	$\pm 2.25\%$
Y_m (N)	290	± 2.175	$\pm 0.75\%$
l_m (Nm)	5	± 0.138	$\pm 2.76\%$
m_m (Nm)	5	± 0.138	$\pm 2.76\%$
n_m (Nm)	5	± 0.063	$\pm 1.26\%$
ρ (kg/m^3)	1.225	± 0.001	$\pm 0.08\%$
V (m/s)	30.0	± 0.1	$\pm 0.3\%$
S (m^2)	0.0849	± 0.0001	$\pm 0.1\%$
c (m)	0.142	± 0.001	$\pm 0.7\%$
b (m)	0.594	± 0.001	$\pm 0.2\%$
Link length (m)	0.065	± 0.001	$\pm 2\%$
C_{L_m}	6.196	± 0.100	$\pm 1.62\%$
C_{D_m}	3.098	± 0.097	$\pm 3.12\%$
C_{Y_m}	3.098	± 0.097	$\pm 3.12\%$
C_{l_m}	0.180	± 0.010	$\pm 5.34\%$
C_{m_m}	0.752	± 0.044	$\pm 5.88\%$
C_{n_m}	0.180	± 0.007	$\pm 3.84\%$

ensure strength requirements are met. An additional modification to the aircraft gimbal locking mechanism is also presented.

From the previous section, out of the two investigated possible positions for the load cell the upper position was chosen (88.3 mm below the aircraft model). This positions the load cell below the pitch/roll gimbal and above the yaw mechanism with the load cell mounted on the yaw shaft. After deciding on the load cell, the position of the load cell was moved further up to 65.8 mm below the aircraft gimbal (distance to the upper surface of the load cell where loads are measured, see Figure 5.9). This is beneficial since it reduced the moment arm and thus the magnitude of moments experienced by the load cell. The accompanying load cell wireless transmitter was to be positioned between the compensator and arm gimbal since there is insufficient space within the compensator shroud. Due to lack of space at the location of the load cell, the yaw mechanism needs to be lowered by 36 mm and the yaw shaft length reduced by 19 mm. The modified yaw shaft is shown in Figure 5.4. Two attachment components are also required to attach the bottom side of the load cell to the yaw shaft and the top side of the load cell to the aircraft pitch/roll gimbal. The designed attachments are shown in Figures 5.5 and 5.6. The material used for both attachment components is aluminium 6082 T6. The wiring from the yaw encoder passes through the centre hole of the load cell and the opening in the upper attachment, and connects to the aircraft model. The wire from the load cell passes through the rig arm through an opening below

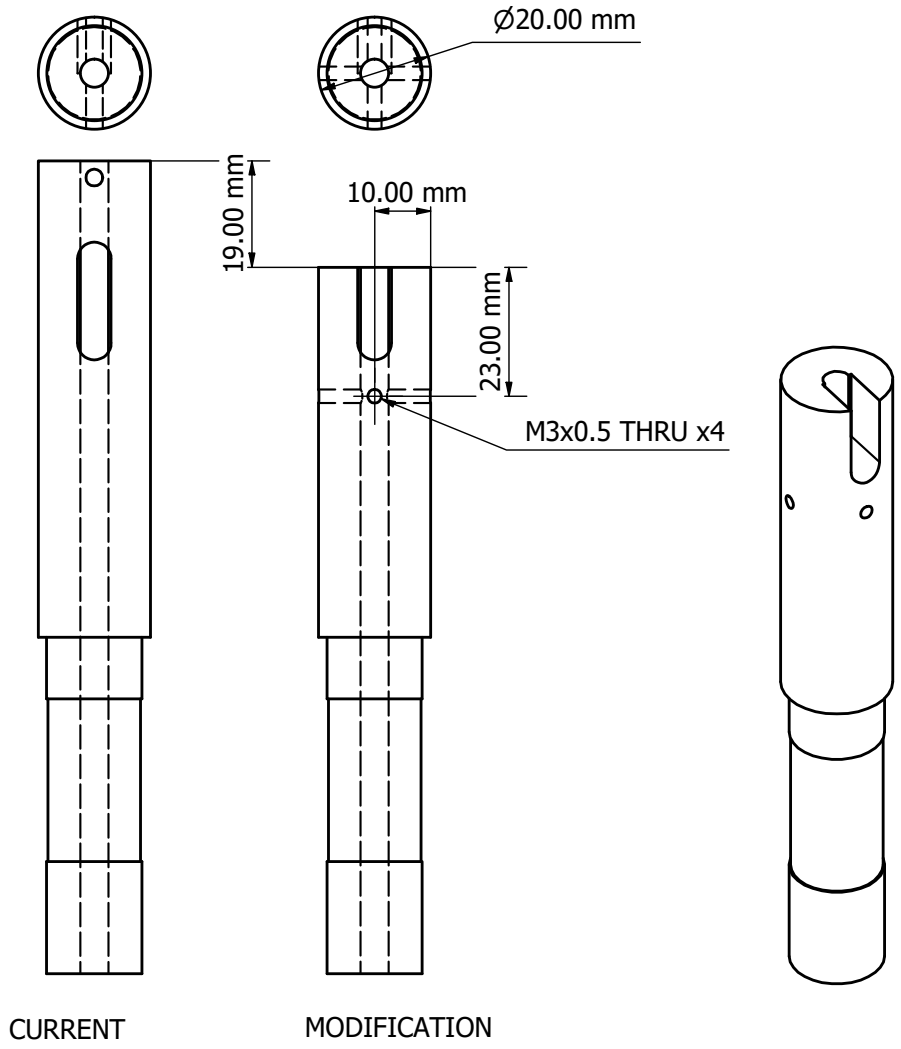

FIGURE 5.4. Modification to the gimbal yaw shaft.

the aircraft yaw mechanism and exits through another hole on the arm behind the arm gimbal where the load cell transmitter is located. These new holes reduce the strength of the arm and therefore these regions need to be reinforced. Figure 5.7 shows a strengthened hole reinforced by welding a steel nut onto the arm. The wireless transmitter itself is held by another construction grade steel attachment welded onto the rig arm, as shown in Figure 5.8. An overview of the original and modified rig is shown in Figure 5.9 and an exploded view of the modified assembly is shown in Figure 5.10.

The new components needed to be checked to ensure they can withstand the loads produced by the aircraft model and rig. This was done through Finite Element Analysis within Autodesk

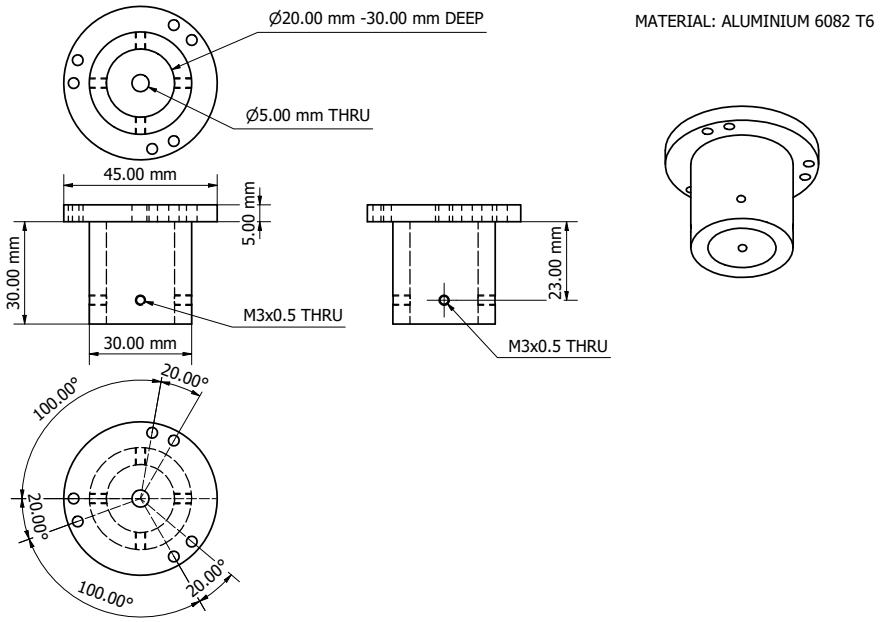

FIGURE 5.5. Load cell lower attachment.

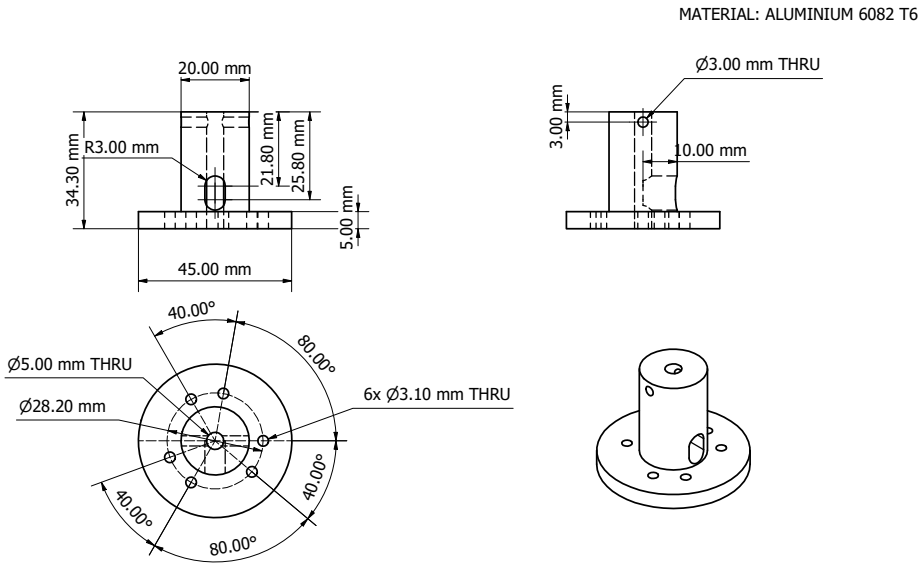

FIGURE 5.6. Load cell upper attachment.

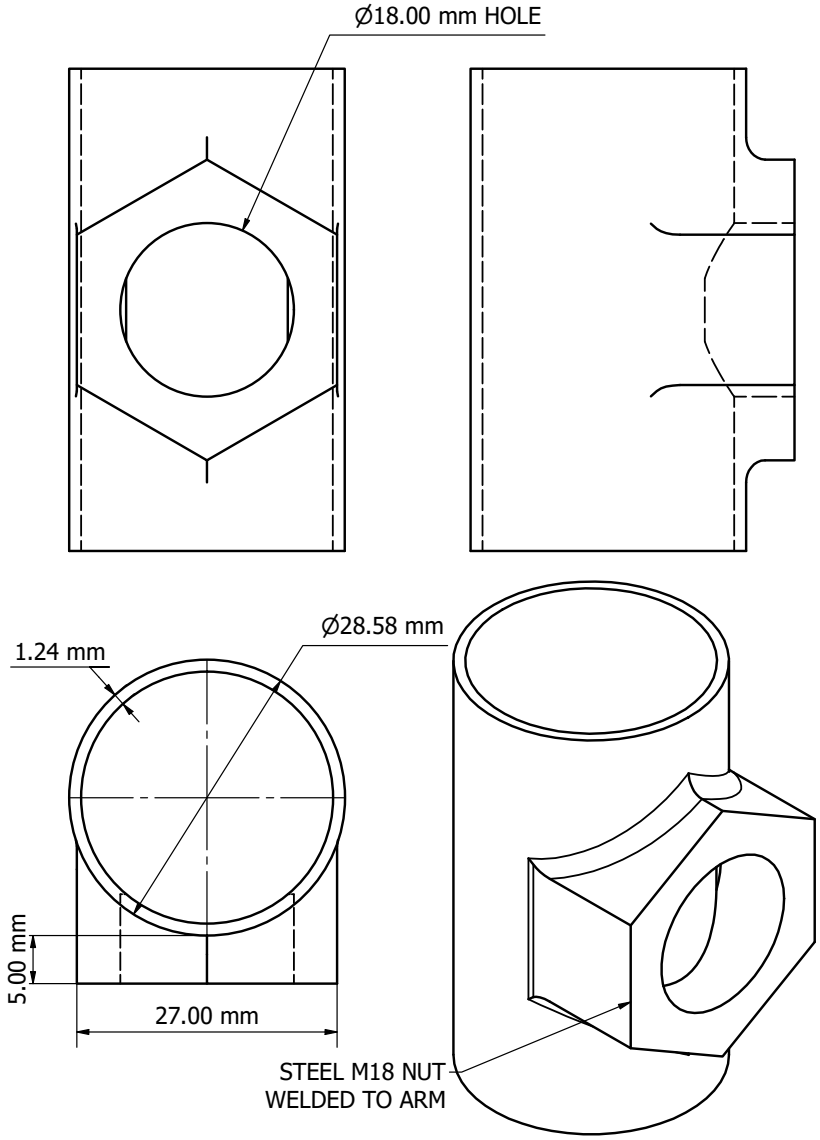

FIGURE 5.7. Rig arm hole reinforcement.

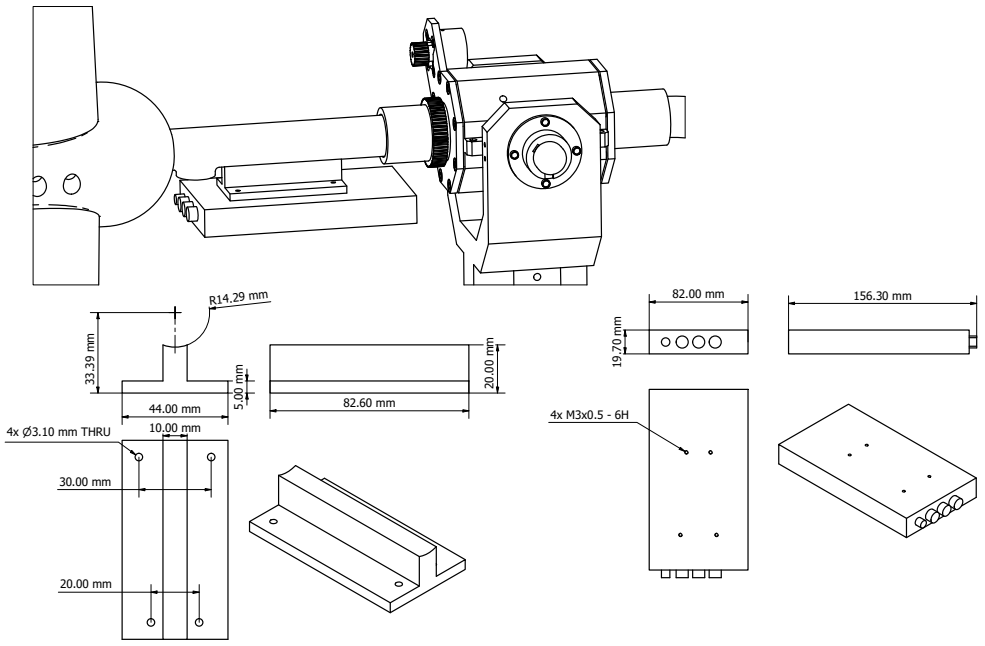

FIGURE 5.8. Load cell wireless transmitter attachment.

Inventor. The maximum/minimum loads found when defining the requirements for the load cell are used here again (overload range loads in Table 5.7). These loads are applied onto each component individually (as static loads) with suitable boundary condition. The Stress Analysis tool within Autodesk Inventor is capable of automatically generating a mesh and checking for convergence of the solution. The resulting maximum stress was recorded and ensured that it was below the maximum tensile strength of the material. Note that the loads used for the stress simulation for each maximum/minimum load are those in the load case in which that particular maximum/minimum load was found. Symmetric load cases were ignored to reduce the total number of simulations to run. The maximum stress found is 332 MPa and occurs on the lower load cell attachment for the minimum pitching moment load case. This is slightly higher than the tensile strength of aluminium 6082 T6 which is 330 MPa. It was decided that it will be acceptable since the likelihood of this load case occurring is very low. The yaw mechanism bearings are also capable of withstanding all loads simulated. Figure 5.11 shows the installed load cell along with its wireless transmitter.

The aircraft roll/pitch gimbal also received an update to its locking mechanism. Previously, the gimbal was locked at a particular attitude by tightening a screw through a slot in both pitch and roll. This made the model prone to sliding especially under load and vibrations while testing due to the locking screw getting loose. In order to make the locking mechanism more secure, the slots in the gimbal are replaced with discrete holes. An overview of the updated gimbal is shown

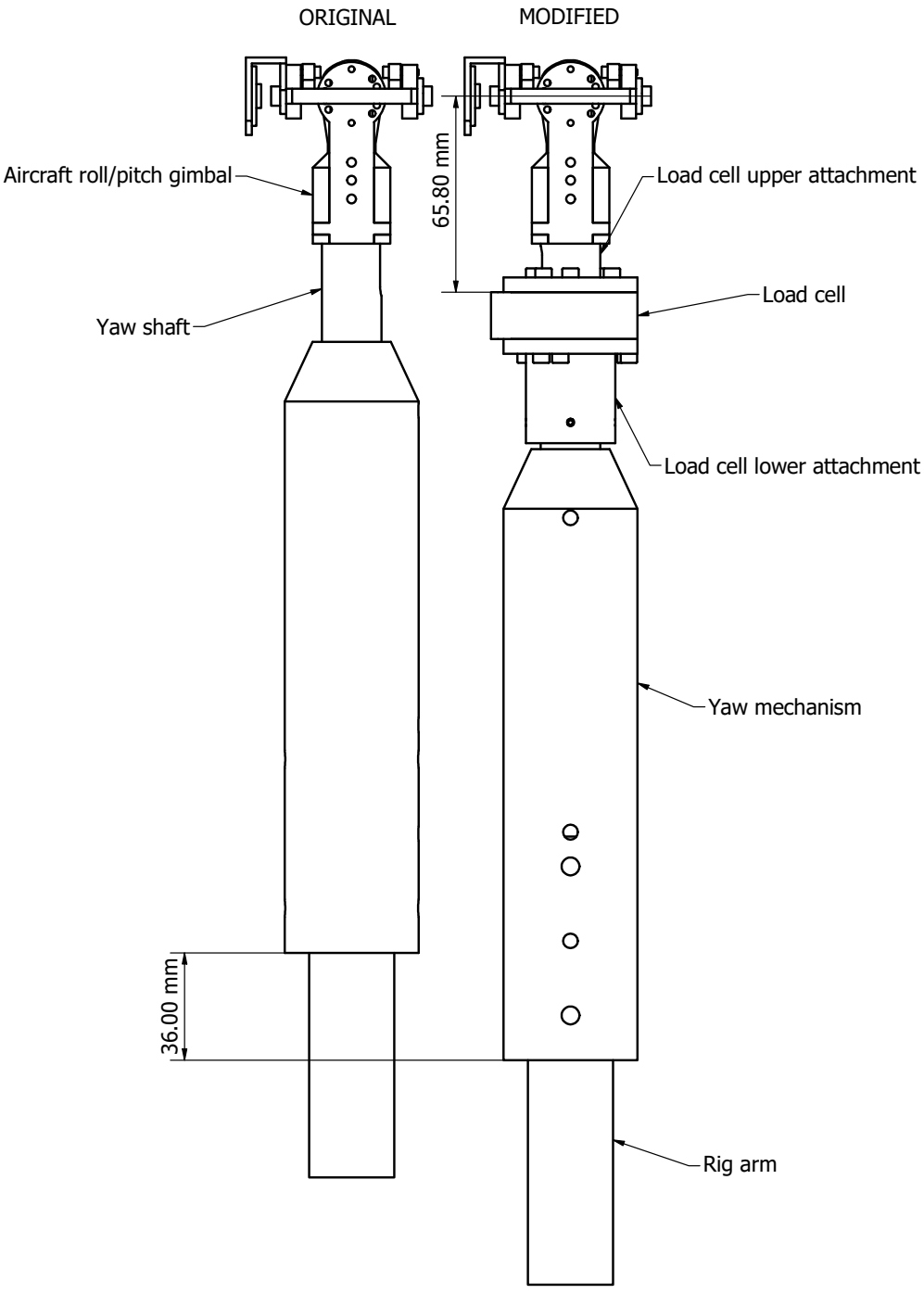

FIGURE 5.9. Overview of rig modifications for load cell installation.

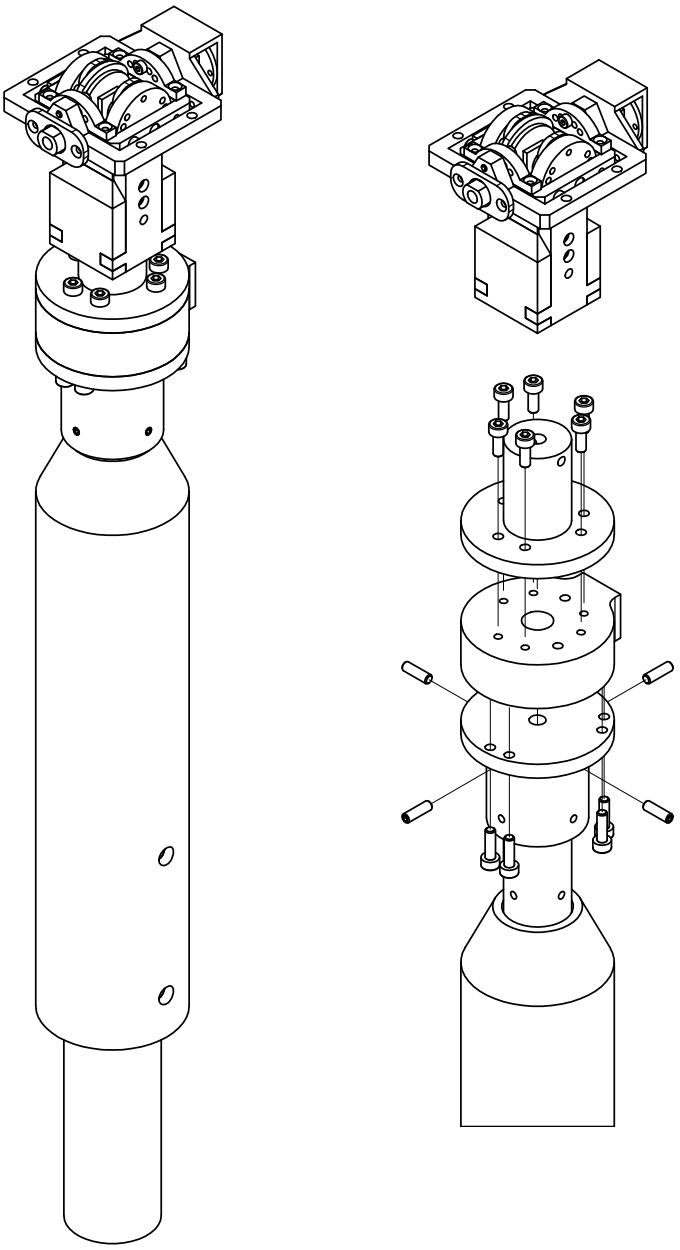

FIGURE 5.10. Exploded view of the modified assembly.

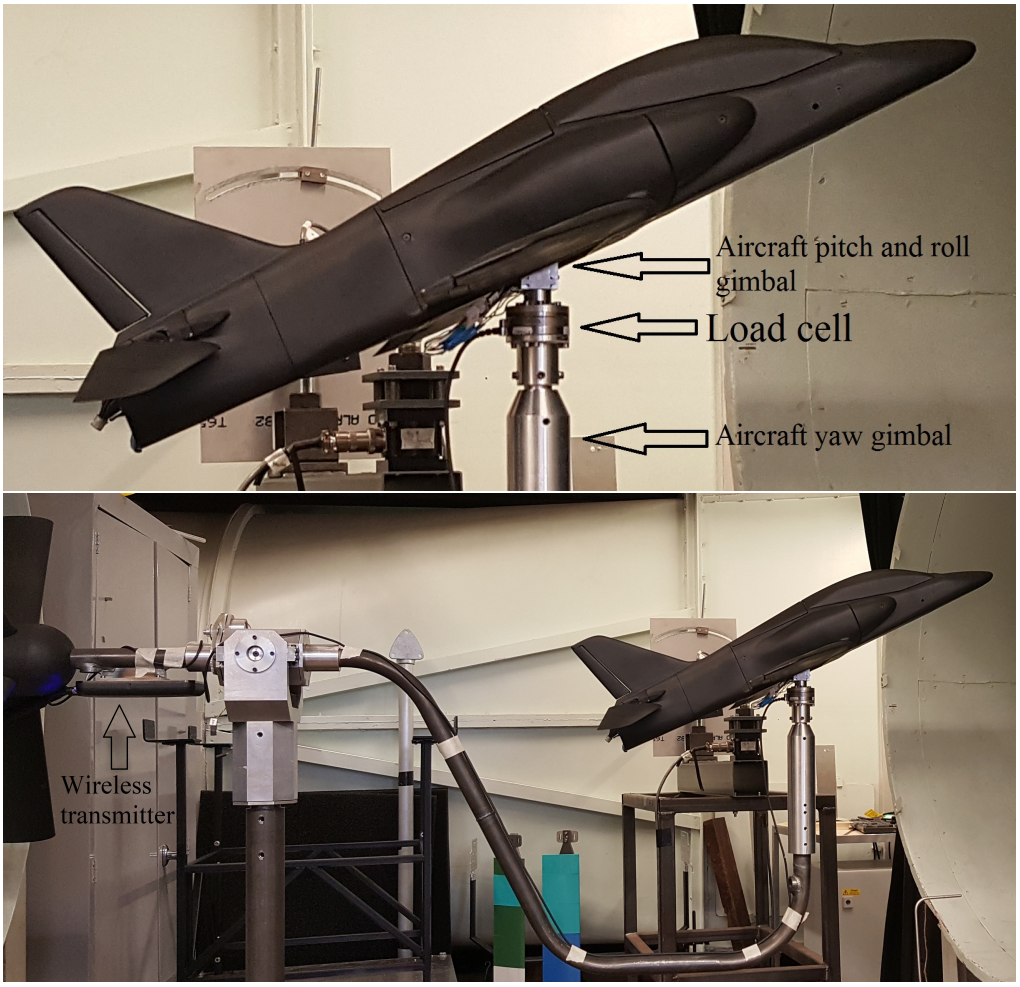

FIGURE 5.11. Load cell system incorporated into the manoeuvre rig.

in Figure 5.12. This allows the aircraft model to be locked in pitch from $-30°$ to $30°$ in steps of $10°$, and in roll from $-40°$ to $40°$ in steps of $20°$. Note that the pitch locking plate has an addition hole at $-40°$ and $40°$ but these are unused due to the physical stops of the gimbal itself.

5.5 Software implementation

This section will describe the steps necessary to integrate the load cell with the current communication system of the manoeuvre rig. Currently the manoeuvre rig's compensator, ground board (which processes rig arm angle measurements), and aircraft model communicate using WiFi. All components connected to the main control station computer via a central network hub. These components are synchronised using Network Time Protocol (NTP) for increased time accuracy [11]. The software carrying out these tasks are written using the programming language Python.

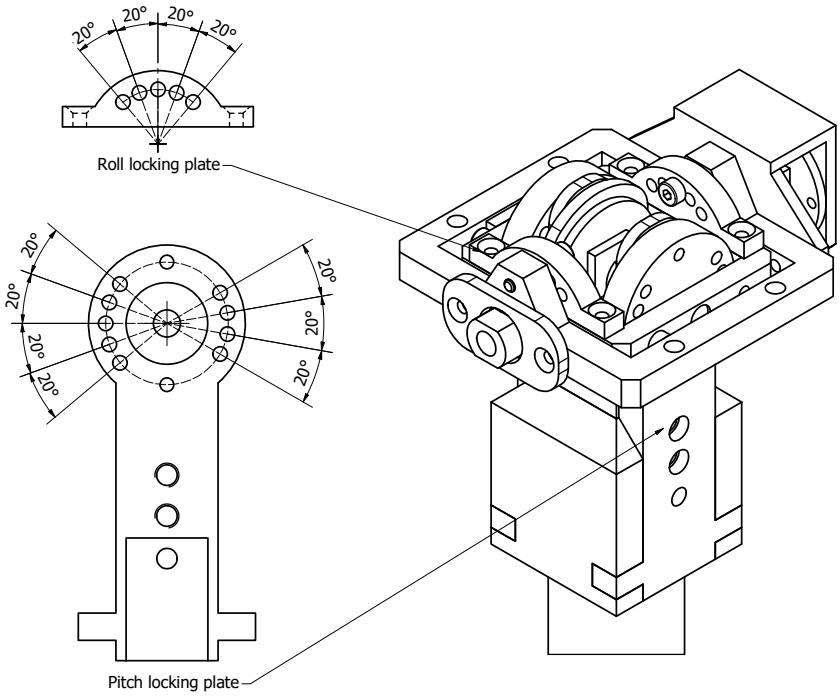

FIGURE 5.12. Updated aircraft model gimbal.

Data received by the main control station was sent to Matlab Simulink using User Datagram Protocol (UDP) packets. The load cell will also need to communicate in a similar manner.

The load cell arrived with software written in Java created by the manufacture which allows it to connect, view and record measurements from a computer using WiFi. This software is also capable of creating and saving profiles containing configuration settings such as calibration, transmission rate, oversampling rate, NTP synchronisation, and filtering. These settings can also be modified from the provided Graphical User Interface (GUI). The code is translated to Python in order to be combined with the existing software. An update to the GUI is also required to carry over all capabilities. Figure 5.13 shows the update GUI containing the previous manoeuvre rig controls and the new load cell controls. The load cell settings are essentially changed using telnet commands remotely. A comprehensive list of commands and more information can be found in its user manual. Note that for all measurements taken when testing no filtering was used from the transmitter directly, filtering was done in Matlab Simulink or in post processing of data. Data is also set to transmit at 244 Hz with an oversampling rate of 1 to match the rate of the current manoeuvre rig system. The main control station computer is set as the NTP server for time synchronisation. Figure 5.14 shows the clock offset and delay for a typical measurement test. Note that the W32Time service in Windows operating system needs to be stopped before the NTP server can be initialized since they both use the same port. Measurements received from the load cell are sent to Matlab Simulink using UDP.

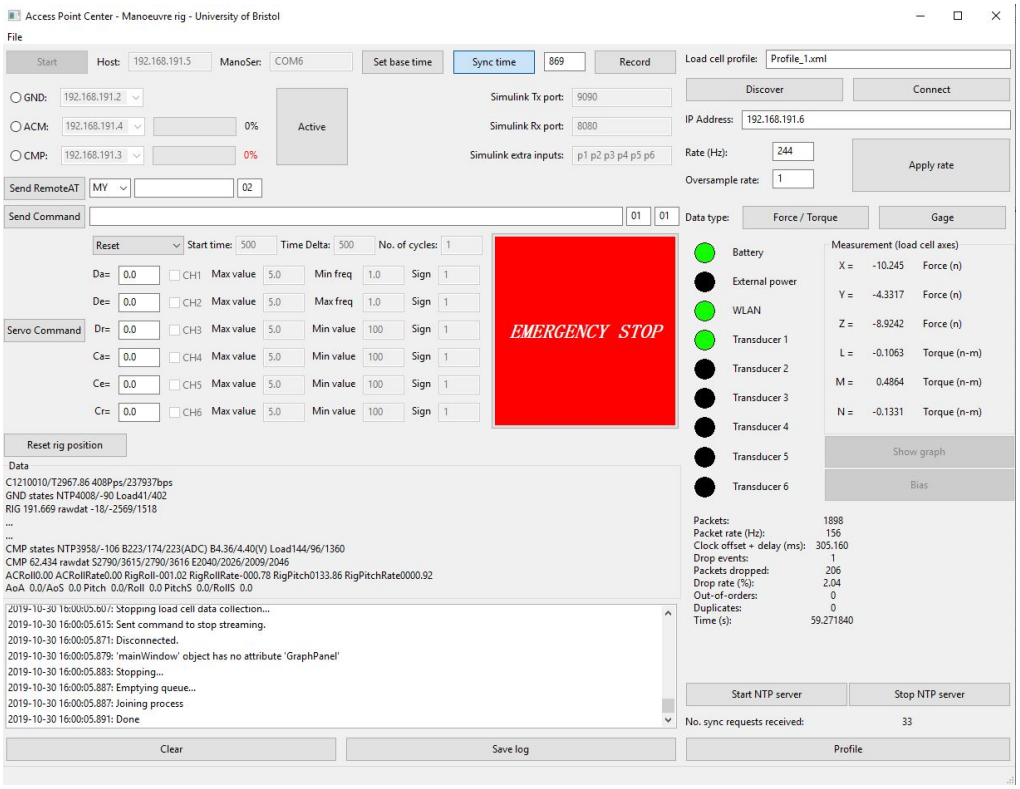

FIGURE 5.13. Updated manoeuvre rig Graphical User Interface.

More information on the manoeuvre rig communication system can be found in [11].

5.6 Rig mass, inertia and gimbal friction estimation

The inertia of the rig including all its components (compensator and arm), rig centre of gravity position and friction properties of the arm gimbal have previously been estimated experimentally with free oscillation experiments [11]. Here, an alternative method is used to estimate these parameters which utilises the load cell. The load cell allows the measurement of all external loads applied through the aircraft gimbal. With this information and along with a model of the rig itself, the inertia values, centre of gravity and friction parameters can be identified. The advantage of this method over the previous free oscillation experiments is that the parameters can be identified much more easily by applying a force to manually move the aircraft gimbal (without the aircraft model mounted), and recording the rig's motion using the arm gimbal encoders and loads with the load cell. This can be carried out while the rig is on its usual support without the need of mounting the entire rig vertically to obtain oscillations due to gravity, as was done previously. This method also allows for the estimation of inertia values even if the rig's centre of gravity is close to the rotation point which will produce no oscillations due to gravity. Note that since different components of the arm gimbal move for each axis, the rig will have different mass

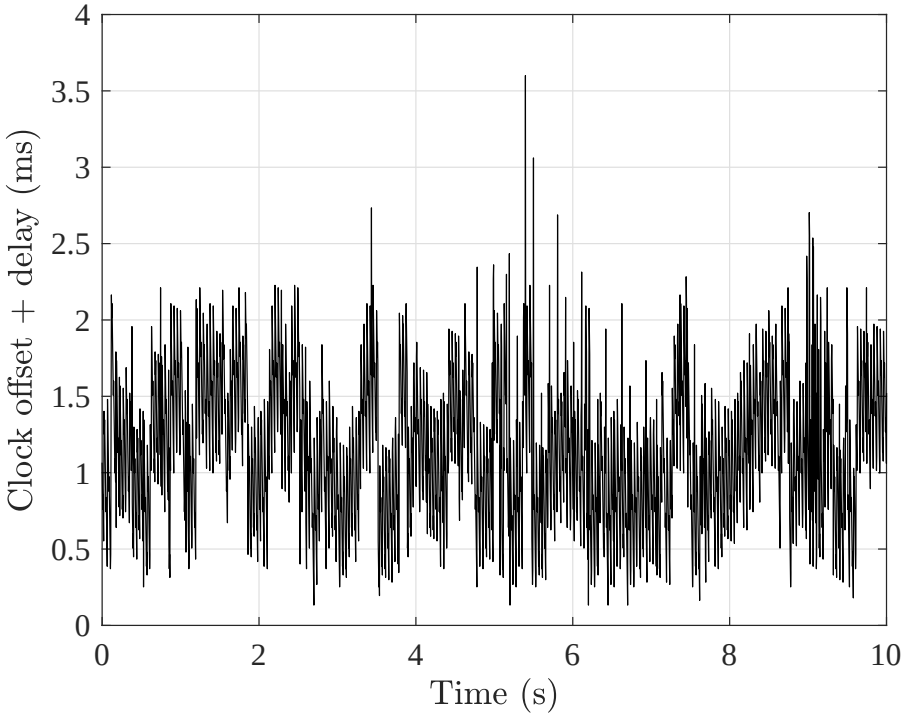

FIGURE 5.14. Load cell typical packet clock offset and delay.

values and centre of gravity locations about each axis of rotation.

The rigid body mathematical model described in Section 3.4 is used here with two modifications. First, the compensator, rig arm, load cell and link are all combined into a single body. Second, a new virtual object is introduced and placed at the exact location of the load cell but with zero mass and inertia. This virtual object is used to apply the forces and moments measured during the test onto the rig model as external loads. The same constraint equations that are used for the load cell in Section 3.4 are used for this virtual body as well. The model for friction shown in Equation 3.119 is used here.

Three tests were conducted for each axis of rotation of the rig. The mathematical model will also need to be constrained in the same way, which can be achieved as follows. To constrain the rig for pitch motion only, no translation in the y direction can be defined for both the rig and virtual bodies (subscript i) which is described mathematically as

$$y_i = 0. \tag{5.2}$$

Following the same procedure as was described in Section 3.6 to caluclate the C_q and $\boldsymbol{Q_C}$

components, the above equation need to be differentiated twice with respect to time:

$$\begin{bmatrix} 1 & 0 & 0 \\ 0 & 0 & 0 \\ 0 & 0 & 0 \end{bmatrix} \ddot{\boldsymbol{R}}_i = \begin{bmatrix} 0 \\ 0 \\ 0 \end{bmatrix} \tag{5.3}$$

which is in the same form as equation 3.15. The same can be repeated for yaw only constraint by defining no translation in the z direction for both the rig and virtual bodies. For the roll only constraint a second virtual object is introduced again with zero mass and inertia placed directly behind the arm gimbal and constrained to the rig in the same way as the first virtual object/load cell, and a constraint for no translation in the y and z directions is defined. The distance the second virtual object is placed behind the arm gimbal does not matter (a distance of 0.5 m is used here). The model used for friction is described by Equation 3.119 and is applied as an external moment acting about each axis.

The mass, centre of gravity locations and moments of inertia of the whole rig as well as the friction parameters are estimated using the parameter estimation tool provided by Matlab Simulink. The optimization technique used here is the nonlinear least squares method and the minimising cost function is the sum squared error.

Figures 5.15, 5.16 and 5.17 show the time histories for the rig roll only, pitch only and yaw only tests respectively. The forces shown are in the inertial axes at the position of the load cell, and the moments are in the rig body axes. A third order low pass Butterworth filter with a cut-off frequency of 20 Hz is used for all load measurements to remove noise. The topics of noise and filtering are discussed in Section 6.2.2. Here, the match between the experimentally measured and simulated responses are good. Table 5.12 shows the estimated rig mass, location of its centre of gravity relative to the arm rotation point, and inertia values for each test. Note that I_{ii} in the table represents the inertia of the rig about each axes at its centre of gravity. $I_{ii} + mr^2$ is the total inertia about the rig's rotation point. Since the rig was tested upright in yaw there was no moment contribution due to weight, therefore the mass, centre of gravity position and moment of inertia about the c.g. cannot be estimated, only the inertia about the arm rotation point is. The estimated rig gimbal friction parameters are shown in Table 3.2. Compared with the inertia of the rig prior to the implementation of the load cell, the total inertia of the rig has increased by 74% in roll, 15% in pitch, and 36% in yaw.

5.7 Summary

This chapter covered the steps taken to define the requirements for the load cell installed on the manoeuvre rig as well as physical modifications and a software update necessary to integrate the load cell with the existing system. The new mass and inertial properties of whole rig, and friction parameters of the arm gimbal were also re-estimated.

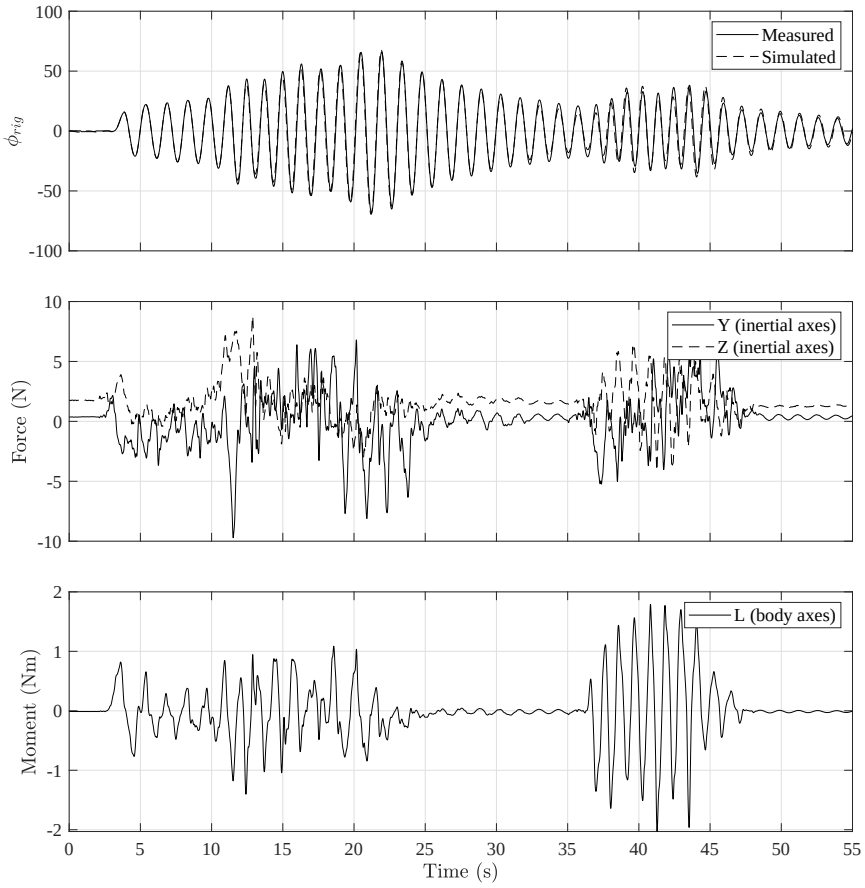

FIGURE 5.15. Rig roll forced oscillation by hand for mass, inertia and friction parameter estimation.

With the addition of the load cell the capabilities of the manoeuvre rig as a testing platform has been extended. It is now possible to perform conventional static and dynamic wind tunnel tests to calculate aerodynamic derivatives from direct load measurements. The rig is also ready to perform inertial and kinematic compensation as discussed in Chapter 4 where the reaction force measurements between the aircraft and the rig will be used for feedback control. Experimental results using the load cell for the Hawk aircraft model are presented in Chapter 6, and inertial and kinematic compensation results are presented in Chapter 7.

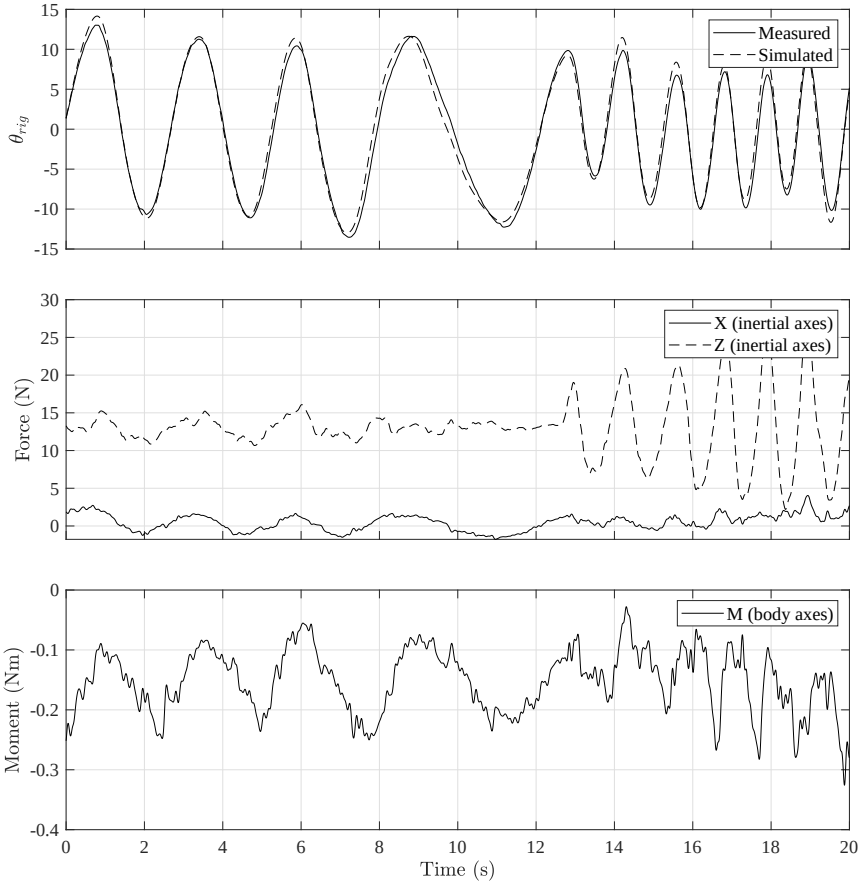

FIGURE 5.16. Rig pitch forced oscillation by hand for mass, inertia and friction parameter estimation.

TABLE 5.12. Estimated properties of the whole updated manoeuvre rig (excluding the aircraft model).

	Mass (kg)	**Centre of gravity** (m)			**Inertia** ($kg.m^2$)			
		x	y	z	I_{xx}	I_{yy}	I_{zz}	$I_{ii}+mr^2$
Roll	13.33	−0.08962	0	0.04017	0.2233	-	-	0.3516
Pitch	12.11	−0.08962	0	0.04101	-	1.832	-	1.950
Yaw	-	-	-	-	-	-	-	2.270

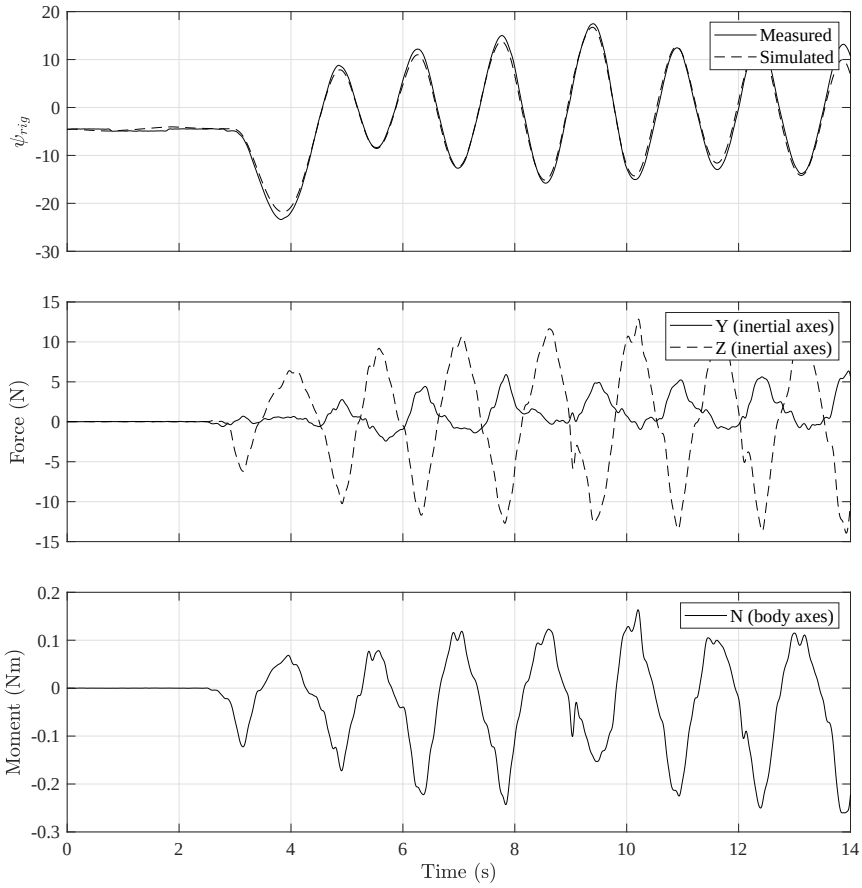

FIGURE 5.17. Rig yaw forced oscillation by hand for mass, inertia and friction parameter estimation.

CHAPTER 6

APPLICATIONS OF THE MANOEUVRE RIG

6.1 Introduction

This chapter presents new use cases for the manoeuvre rig that utilise the newly implemented load cell. First, conventional static test results for the Hawk model are presented in which the longitudinal and lateral-directional static aerodynamic derivatives are measured. This is followed by a longitudinal forced heave oscillation test for the Hawk to estimate its dynamic derivatives. Next, hysteresis observed at stall for the Hawk model is studied which also reveals aerodynamic asymmetry. Finally, a method for creating self-induced model roll and yaw oscillations when the aircraft model is free to only rotate about those axes is derived and demonstrated on the manoeuvre rig.

6.2 Hawk static aerodynamic measurements

This section details the experiments done with the Hawk model using the ATI Mini45 load cell implemented in the manoeuvre rig. The aim of these tests is to collect new experimental results for the Hawk model which can then be compared with previous parameter estimation results as well as to demonstrate the upgraded capability of the manoeuvre rig with the newly implemented load cell.

The low range SI-145-5 (higher sensitivity) calibration was chosen for these measurements (see Table 5.10).

6.2.1 Methodology

Static tests were done to measure the lift, drag, and side forces over a range of angles of attack and sideslip. This was done at wind speeds of $20m/s$ and $30m/s$ in the 7' by 5' closed section wind tunnel. Conventionally, these tests are carried out with the aircraft model locked at specific attitude angles. The current design of the aircraft gimbal on the manoeuvre rig allows the model to be locked in roll between $40°$ and $-40°$ at intervals of $20°$. The pitch angle can be locked between $30°$ and $-30°$ at intervals of $10°$. The model can be locked in yaw at any angle. For all tests carried out, the manoeuvre rig's arm is fully locked in all degrees of freedom in order to hold the model stationary, although significant vibrations were observed at some stages where the model is within the limit cycle region of the Hawk model. Investigation of the self-induced limit cycle oscillation observed on the Hawk model has been reported in Reference [11].

Two methods were used to obtain the static results: the first being conventional static tests in which the aircraft is locked at specific attitudes, and the second being quasi-static tests, where the aircraft is allowed to freely pitch and its pitch angle controlled using the aircraft's elevator, thus allowing the tests to be carried out in a continuous range of angles of attack. The full static cases where the aircraft gimbal was locked in all degrees of freedom were carried out mainly to assess control surface effectiveness of the aileron, elevator and rudder. The aileron effectiveness test was done with the aircraft gimbal locked in all degrees of freedom at zero attitude angles and giving a ramp input. Similarly, elevator effectiveness tests were conducted with the aircraft gimbal locked at pitch angles $-20°$, $-10°$, $0°$, $10°$, $20°$ and $30°$ (yaw and roll angles locked at zero). Finally, the rudder effectiveness was carried out at with the yaw gimbal locked at $-30°$, $-20°$, $-10°$, $0°$, $10°$, $20°$ and $30°$ (roll and pitch angles locked at zero). This was an attempt to observe any effects the Hawk's canopy has on the vertical tailplane and rudder.

For the quasi-static tests, a slow ramp up and ramp down input ($0.167°/s$) is given to the elevator to continuously sweep the aircraft in angle of attack. This is then repeated at sideslip angles of $-30°$, $-20°$, $-10°$, $0°$, $10°$, $20°$ and $30°$. Note that in these free pitch test cases the aircraft is in trim and so no pitching moment can be measured. On the other hand when the aircraft gimbal is fixed in pitch the pitching moment can be measured and also allows for the assessment of elevator effectiveness, albeit at sparse angles of attack. All control surface inputs were given using Matlab Simulink linked with the python software used for wireless communication with the Hawk aircraft. The control surface deflection angles are measured using potentiometers within the servo motors.

Since the load cell is placed below the aircraft ($66mm$ below) the measured loads have to be transformed onto the gimbal pivot. In addition, when installing the load cell it had to be rotated in yaw by $20°$ in order to keep its cable aligned with the rig. The drawing of the load cell is shown in Appendix H. It should be noted that the aerodynamic influence of the portion of the gimbal between the load cell and the aircraft model (link) and the cutout beneath the Hawk is not being assessed in this work and should be investigated in the future. It is expected that the measured

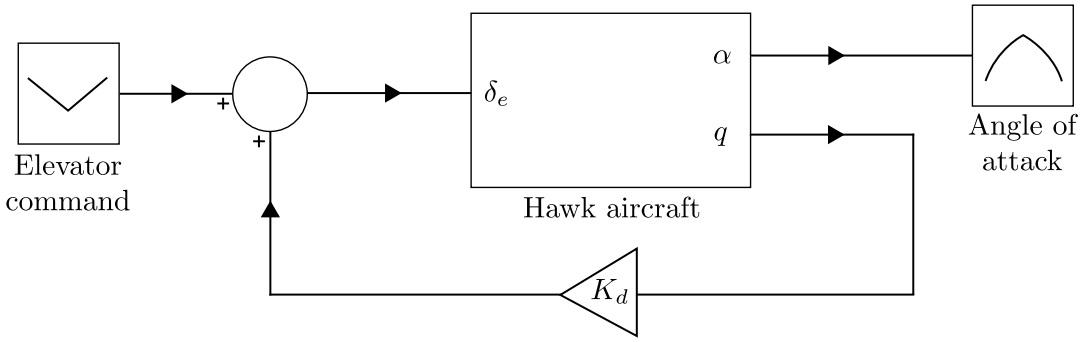

FIGURE 6.1. Feedback control used to suppress the Hawk's limit cycle oscillations.

drag will be an overestimate but the degree to which this occurs is unknown.

Apart from the quasi-steady pitch free test cases where pitching moment cannot be measured, all forces and moments are recorded for all tests. Although it is possible to be carried out, tests with complex roll, pitch and yaw attitudes were not performed due to time constraints. Such tests could be used to construct detailed look-up table type aerodynamic models for the aircraft which can capture nonlinear behaviour and/or asymmetry. The tests that can describe the Hawk's main aerodynamic characteristics are presented here.

The Hawk model being tested exhibits limit cycle behaviour in pitch which affects tests where the pitch degree of freedom is free. In order to suppress these limit cycle oscillations, feedback control was used to hold the aircraft stationary as best as possible throughout the angle of attack sweep. Figure 6.1 shows the simple proportional feedback control used to suppress the oscillations. This proportional control scheme should not affect the location of the equilibria solution, only their solution. The pitch rate of the Hawk (q) is measured by an Inertial Measurement Unit. The gain values used are stated in section 6.2.3. This control was applied onto the Hawk using Matlab Simulink.

6.2.2 Noise and filtering

Before the results are presented, the topic of measured noise needs to be addressed. The observed frequencies of the observed noise are used to determine the cut-off frequency of the low pass filter for a given experiment. Note that when applying the filter while post processing, the data is filtered twice: forwards and backwards in time so that there is zero phase shift. This is done using the "filtfilt" function in Matlab. A Fourier transform of a portion of data is performed to identify the frequency content of the measured load data. This is analysed for a wind speed of 20 m/s and 30 m/s for the same rig setup (performed in the 7' by 5' closed section wind tunnel). In this the aircraft gimbal is fully fixed at 0 deg in roll, pitch, and yaw attitudes. No input was given to any control surface. The load cell was biased with the wind off, the wind speed then increased to 20 m/s and held for about 100 seconds and then increased to 30 m/s and held for another 100

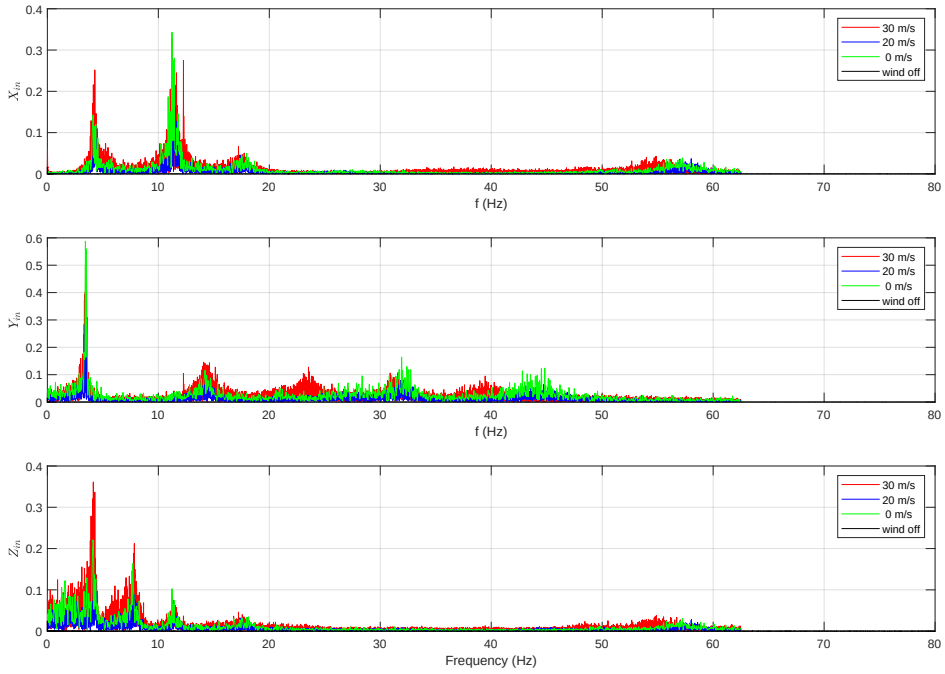

FIGURE 6.2. Frequency spectrum of the measured forces by the load cell.

seconds. Loads here are measured at 125 Hz.

Figures 6.2 and 6.3 shows the frequency spectrum of the unfiltered measured forces and moments respectively. For each load the frequency content is shown for three wind speeds: wind tunnel off, and three wind speeds: 0 m/s, 20 m/s and 30 m/s. Note that the amplitudes for the wind off case are almost zero, which indicates that the 0 m/s frequencies (wind tunnel on) shown by the green lines are due to vibrations caused by the wind tunnel motor possibly exciting a mode of the rig arm. These vibrations are mostly captured by the force measurements with their lowest frequency being about 4 Hz. Natural frequencies of the updated rig are not assessed in this work. Since no assessment of the wind tunnel turbulence has been performed, the appearance of the frequencies peaks at 12.3 Hz and 23.5 Hz at 30 m/s wind speed (red line) cannot be attributed with certainty to either wind tunnel vibrations or air flow turbulence.

For the data processing of static measurements, a low pass filter with a cut-off frequency of below 4 Hz is sufficient to filter out noise caused by tunnel vibrations and turbulence. For dynamic testing, a low pass filter with a cut-off frequency being an order of magnitude higher than the frequency of interest should be sufficient. Filtered static and dynamic test results are presented in the next sections.

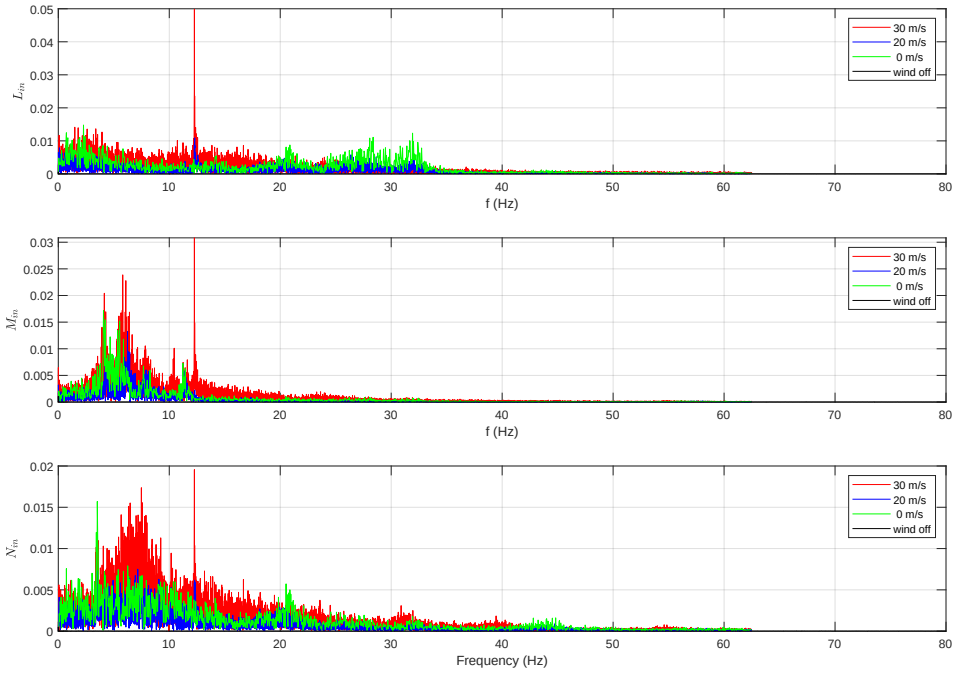

FIGURE 6.3. Frequency spectrum of the measured moments by the load cell.

6.2.3 Results

Figure 6.4 shows an example of filtered load measurement for the rudder ramp test case with the aircraft locked at zero attitude angles. The wind speed for this test is 30 m/s. The filter used here is a third order low pass Butterworth filter with a cut-off frequency of 0.01 Hz. Note that all loads are transformed such that they represent the loads acting through/about the aircraft rotation point. The recorded loads are relative to the loads measured with the wind tunnel off and so these recorded loads are purely aerodynamic. Since these tests are static and the translational velocities of the aircraft model is zero, the angle of attack is equal to the pitch angle and the angle of sideslip is equal to the negative of the yaw angle. Attitude angles are measured using the rig's encoders, and control surface deflections are measured using potentiometers in the actuators.

The first set of tests carried out are the control surface effectiveness tests. The aileron effectiveness is presented in Figure 6.5 showing $C_{l_{\delta_a}}\delta_a$ against δ_a where the gradient equals the aileron coefficient $C_{l_{\delta_a}}$. This test was carried out at zero attitude angle. The gradient is linear around zero aileron deflection where $C_{l_{\delta_a}} = 0.123/rad$. Nonlinearity can be seen past approximately $\pm 10^\circ$ where the gradient decreases indicating a reduction in control effectiveness. Good agreement can be seen between wind speeds of 20 m/s and 30 m/s. The upsweep and downsweep measurements are nearly identical indicating no static hysteresis is present. Reference [11] estimated $C_{l_{\delta_a}} = 0.0840/rad$ using the Equation Error Method and $C_{l_{\delta_a}} = 0.104/rad$ using the

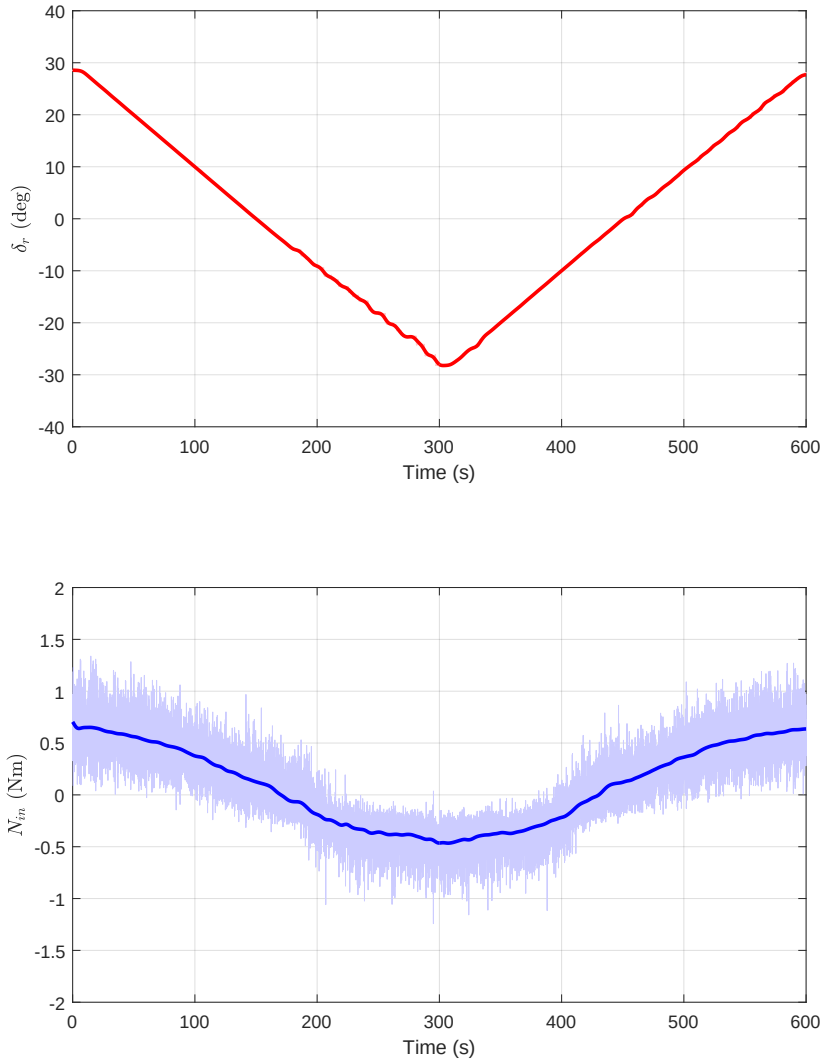

FIGURE 6.4. Static Hawk rudder ramp at zero attitude angles and at a wind speed of 30 m/s. N_{in} here is the yawing moment in the inertial frame of reference.

Output Error Method for the Hawk model which are similar to the value measured here. These values were estimated at $\delta_a = 0°$.

The elevator effectiveness is presented in Figure 6.6 showing $C_{m_{\delta_e}}\delta_e$ against δ_e where the gradient equals the elevator coefficient $C_{m_{\delta_e}}$. Although referred to as elevator, the Hawk model has an all-moving tailplane for pitch control. This test is carried out at a range of pitch angles from $-20°$ to $30°$ except a pitch angle of $20°$. Testing at a pitch angle of $20°$ at 30 m/s is not possible with the aircraft gimbal locked in pitch due to significant vibrations of the rig arm caused by the limit cycle phenomena exhibited by the Hawk model. However, testing at 20 m/s is still possible as the vibrations are not as excessive. The roll and yaw attitude of the aircraft are locked at zero. It can be seen that $C_{m_{\delta_e}}\delta_e$ is roughly linear in the $\pm 5°$ deflection region, however its gradient ($C_{m_{\delta_e}}$) varies significantly with pitch angle. $C_{m_{\delta_e}}$ is highest with a value of $-1.14/rad$ when pitch is zero and decreases as the magnitude of pitch increases. $C_{m_{\delta_e}} = -0.369/rad$ when $\theta = -20°$ and $C_{m_{\delta_e}} = -0.352/rad$ when $\theta = 30°$. This observation can be associated with the wake effect from the main wing reducing the local angle of attack at the tailplane. Significant nonlinearity can be seen at large combined negative deflections and pitch angles as the elevator stalls and loses its effectiveness indicated by the point at which the gradient changes from negative to positive. The stall occurs more gradually at smaller pitch angles. The upsweep and downsweep measurements are nearly identical again indicating that static hysteresis is not present. Results of CFD simulations performed on the Hawk model (see Section 3.8.3 and Appendix C) are also plotted for a pitch angle of zero and elevator deflections of $-20°$, $0°$ and $20°$ on Figure 6.6. The gradient ($C_{m_{\delta_e}} = -0.837/rad$) can be seen to agree with the linear region of the experimental results, although the computational results failed to capture the stall of the elevators. Note that the CFD simulations are not part of this PhD and were obtained from Nanjing University of Aeronautics and Astronautics. Reference [11] estimated $C_{m_{\delta_e}} = -0.886/rad$ using the Equation Error Method and $C_{m_{\delta_e}} = -0.975/rad$ using the Output Error Method for the Hawk model which are similar to the values measured here for $\alpha = 1°$. Reference [11] also concluded that $C_{m_{\delta_e}}$ reduces in magnitude at larger angles of attack which matches the results presented here.

The rudder effectiveness is presented in Figure 6.7 showing $C_{n_{\delta_r}}\delta_r$ against δ_r where the gradient equals the rudder coefficient $C_{n_{\delta_r}}$. This test is carried out at a range of yaw angles from $-30°$ to $30°$. The roll and pitch attitudes of the aircraft are locked at zero. It can be seen that $C_{n_{\delta_r}}\delta_r$ is roughly linear in the $\pm 5°$ deflection region, however its gradient ($C_{n_{\delta_r}}$) decreases as the yaw angle increases in magnitude. This may be caused by the canopy reducing the local angle of sideslip. $C_{n_{\delta_r}} = -0.0556/rad$ at $\psi = 0$ and $C_{n_{\delta_r}} = -0.0290/rad$ at $\psi = \pm 30°$. Nonlinearity can be seen at large deflection angles and can be associated with the gradual stall of the vertical tailplane. The upsweep and downsweep measurements are nearly identical again indicating that static hysteresis is not present. Reference [11] estimated $C_{n_{\delta_r}} = -0.0791/rad$ using the Equation Error Method and $C_{n_{\delta_r}} = -0.0705/rad$ using the Output Error Method for the Hawk model at zero yaw angle which are higher than the measured value here but similar in magnitude.

Note that forces and moments about all axes were recorded during these tests but are not presented here for brevity. The elevator and rudder effectiveness tests were also repeated at 20 m/s and the results were nearly identical. Compared to previous parameter estimation studies covered in reference [11], the load cell allows for direct measurements of loads within a larger range of data points in terms of attitudes and deflection angles, and also without the need of mathematical models such as for aircraft gimbal friction.

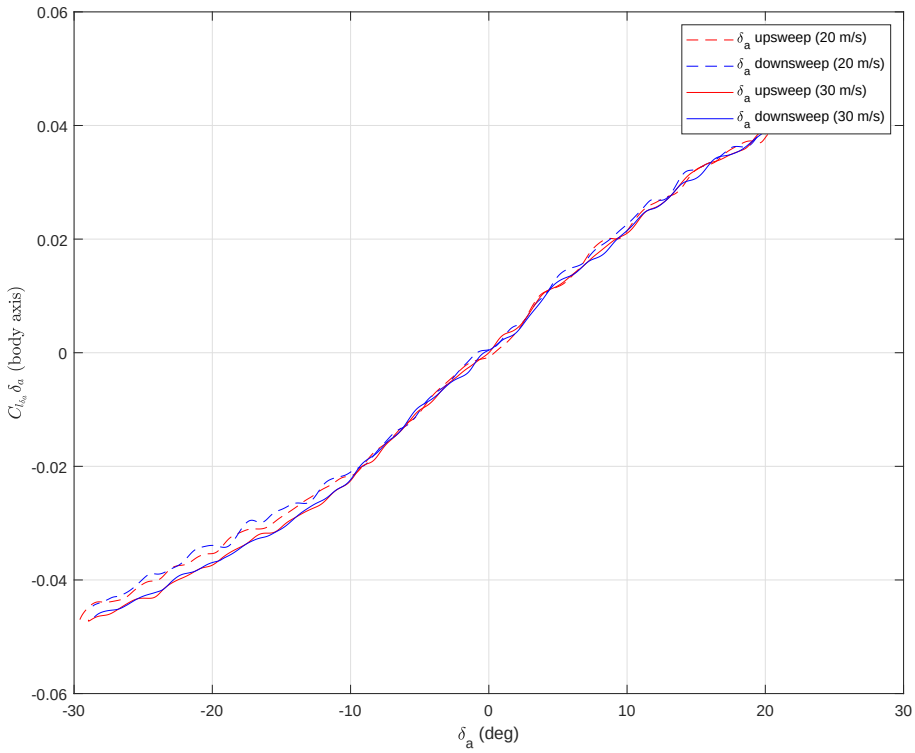

FIGURE 6.5. Static Hawk aileron control effectiveness at wind speeds of 20 m/s and 30 m/s.

Next the measured aerodynamic stiffness is presented. Figure 6.8 shows the pitch stiffness as $C_{m_0} + C_{m_\alpha}\alpha$ against the angle of attack (which is equal to the pitch angle). In this figure the point at which the line crosses the $\alpha = 0$ line is the value of C_{m_0} which is 0.1053 and the gradient of the line is C_{m_α} which is -0.499/rad. The relationship is approximately linear between pitch angles $-20°$ and $+20°$. As previously stated, the moment at 20° pitch angle at 30 m/s could not be measured due to significant rig arm vibration caused to the Hawk model being inside its limit cycle region. For comparison, the results from CFD simulations (see Section 3.8.3 and Appendix C) for the Hawk model are plotted for three angles of attack: $-5°$, 0° and 5°. The gradient ($C_{m_\alpha} = -0.592/rad$) agrees with the experimental results although a clear offset

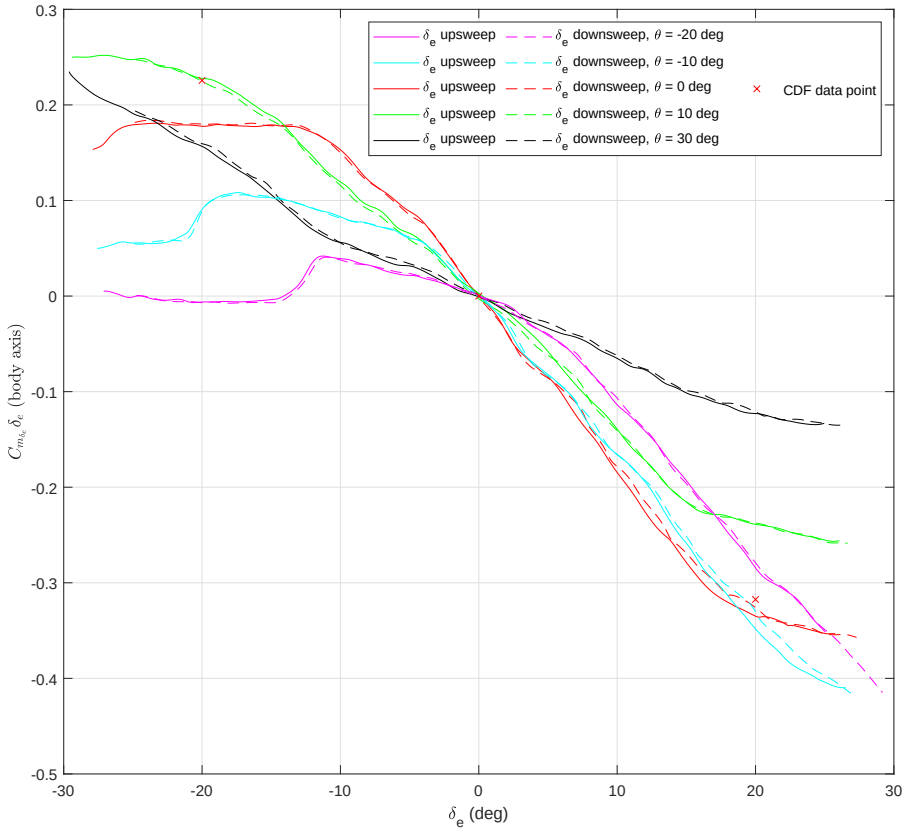

FIGURE 6.6. Static Hawk elevator control effectiveness at a wind speed of 30 m/s.

is present (C_{m_0} = 0.0410). This may be due to different reference body axes used to measure the angle of attack. The reference body axes used for the CFD simulations are unknown. The experimental attitude angles are measured using aircraft gimbal digital encoders. The value of C_{m_0} estimated in Reference [11] varies significantly between -0.458 and 0.174 depending on the initial pitch angle and estimation method. Therefore the parameter estimated value for C_{m_0} is uncertain. The value of C_{m_α} estimated in Reference [11] varies between -0.941/rad and -0.589/rad which also dependant on the initial pitch angle and estimation method, the accuracies of which are unknown.

Figure 6.9 shows the yaw stiffness as $C_{n_0} + C_{n_\beta}\beta$ against the angle of sideslip. In this figure the point at which the line crosses the $\beta = 0$ line is the value of C_{n_0} which is -0.000742 and the gradient of the line is C_{n_β} which is 0.104/rad in the linear region between -10° and $+10^\circ$ angle of sideslip. The values of C_{n_0} estimated in Reference [11] using parameter estimation techniques are -0.0015 using the Equation Error Method and -0.003 using the Output Error Method. The values of C_{n_β} estimated in Reference [11] are 0.158/rad using Equation Error Method and 0.145/rad

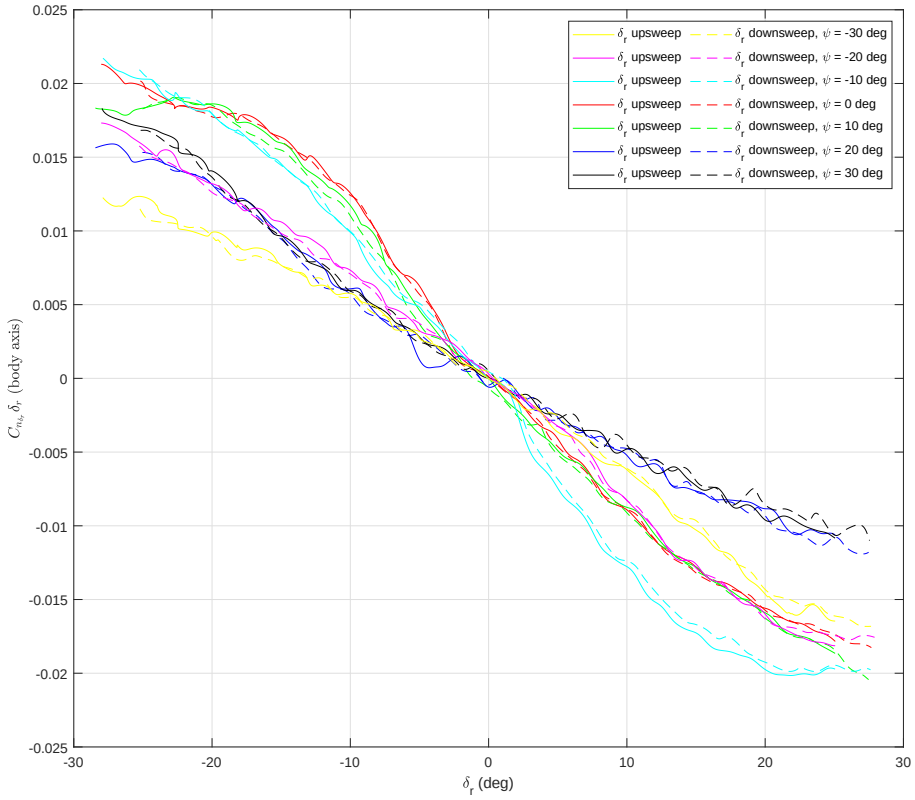

FIGURE 6.7. Static Hawk aileron control effectiveness at a wind speed of 30 m/s.

using Output Error Method. The accuracies of these estimates are unknown.

Figure 6.10 shows the changes in lift, drag, and side force coefficients due to elevator deflection at a wind speed of 30 m/s where the gradient of each curve is the value of elevator derivative $C_{L_{\delta_e}}$, $C_{D_{\delta_e}}$ and $C_{Y_{\delta_e}}$ respectively. Elevator stall is clearly visible in the $C_{L_{\delta_e}}\delta_e$ plots. $C_{D_{\delta_e}}\delta_e$ could not be estimated previously using parameter estimation due to limitations of the mathematical model, but can now be measured using the load cell. Minor asymmetry in side force due to elevator can be seen.

The following are the results of the aforementioned quasi-static tests. A low pass third order Butterworth filter with a cut-off frequency of 1 Hz is used to process the measured data. A gain of 0.15 is used for the feedback of the Hawk's pitch rate to the elevator as depicted on the diagram in Figure 6.1 to suppress its pitch limit cycle. Figure 6.11 shows the lift, drag, and side force coefficients against angle of attack for a range of sideslip angles. Note that forces measured here will contain a component due to elevator deflection since it is used to sweep the aircraft model in pitch. Since the aircraft gimbal is free in pitch for these test cases, the aerodynamic pitching moment cannot be measured but the rolling and yawing moments can still be measured. The force

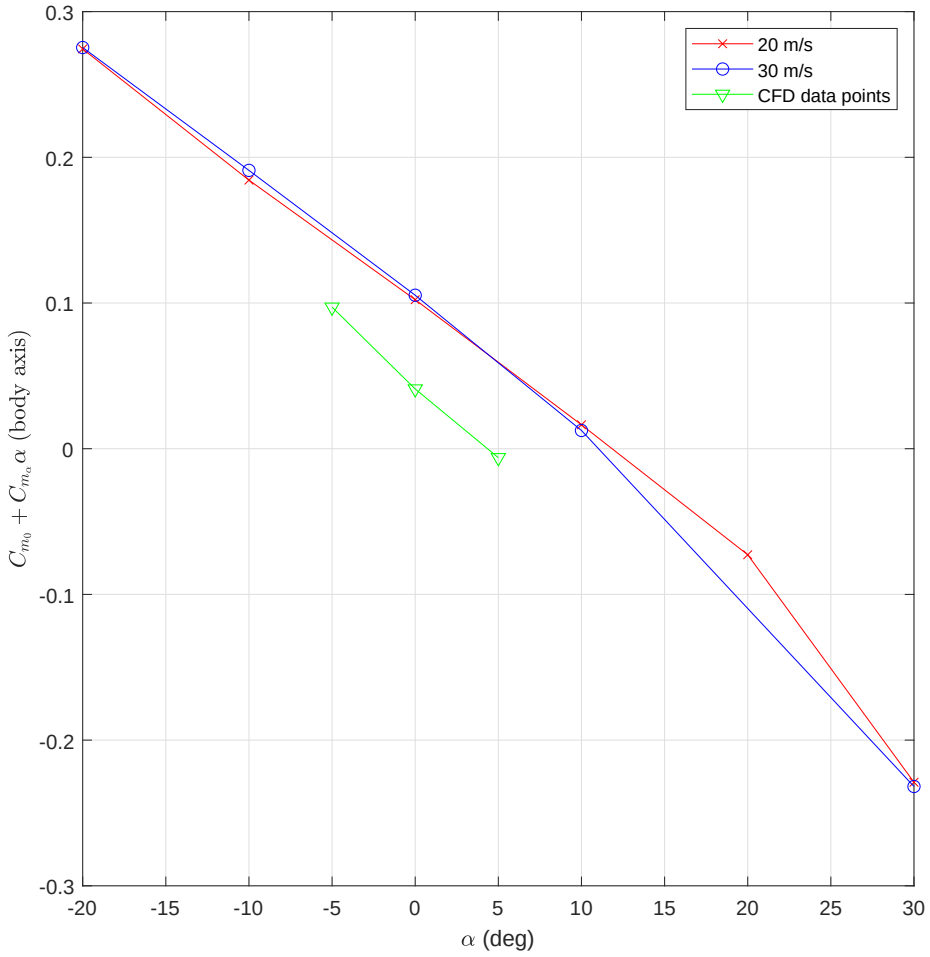

FIGURE 6.8. Static Hawk pitch aerodynamic stiffness measured at wind speeds of 20 m/s and 30 m/s.

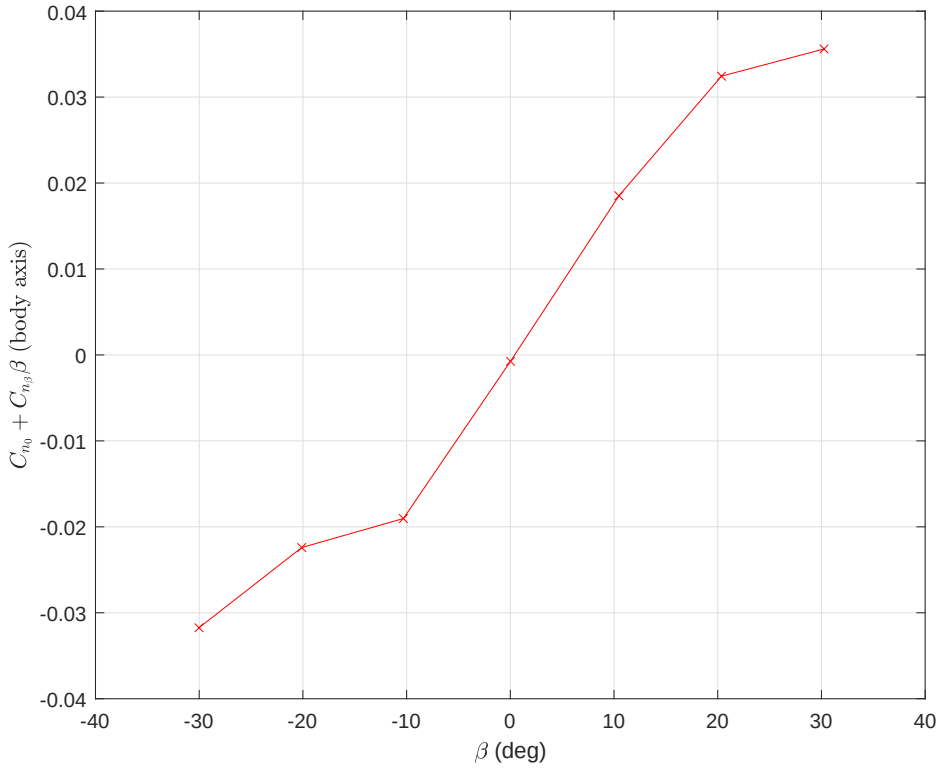

FIGURE 6.9. Static Hawk yaw aerodynamic stiffness measured at a wind speed of 30 m/s.

component due to elevator deflection was measured in the previous static test shown in Figure 6.10 which can be subtracted from these measurements to calculate the sum of bias component and α derivative component. For example, for lift, subtracting $C_{L_{\delta_e}}\delta_e$ from C_L measured in the quasi-static test here will result in $C_L = C_{L_0} + C_{L_\alpha}\alpha$. Then the point at which the curve crosses the $\alpha = 0$ line is the value of C_{L_0} and the gradient is C_{L_α}. Note that the pitch rate is effectively zero because the sweep rate of the elevator is very small ($0.167°/sec$). Figure 6.12 shows the relationship between angle of attack and elevator deflection for the zero sideslip angle test case. From the zero sideslip angle case, $C_{L_0} = -0.104$ and $C_{L_\alpha} = 3.44/rad$ at the linear region around $\alpha = 0$. It can be seen in Figure 6.11 that the abruptness of the stall varies as the magnitude of the angle of sideslip increases. Asymmetry in side force is also observed. This may be associated with a misalignment of the aircraft model with the air flow. The CFD results for the Hawk model for lift and drag at zero angle of sideslip are also plotted on Figure 6.11 for angles of attack of $-5°$, $0°$ and $5°$ (see Section 3.8.3 and Appendix C). The overall trend in lift and drag match the experimental results however a shift in angle of attack is observed. This again may be due to an offset in the reference body axes used in the computational simulation, which is unknown. The CFD results

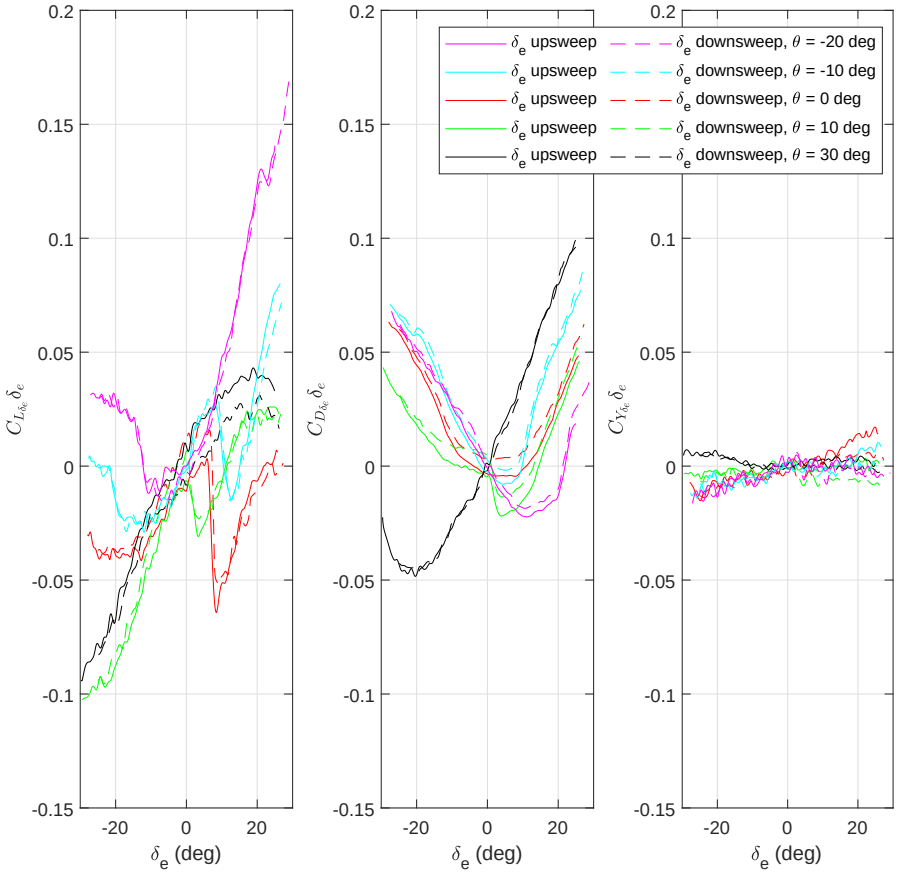

FIGURE 6.10. Static Hawk measured lift, drag and side force coefficient change due to elevator deflection at a wind speed of 30 m/s.

predicted $C_{L_0} = 0.1668$ and $C_{L_\alpha} = 3.36/rad$. The computationally predicted minimum drag of $C_D = 0.0533$ is also a close match with the experimentally measured minimum of $C_D = 0.0607$. C_{L_0} and C_{L_α} as well as drag coefficients could not be identified in previous parameter estimation tests, which demonstrates the advantage of this approach.

During previous testing of the Hawk model conducted in References [11, 52], asymmetry in roll was identified. This was exhibited by a sudden departure in roll (right wing down) as the angle of attack increases, with the aircraft gimbal free in pitch and roll. Physically the geometry of the wings are not symmetric, the left wing is longer than the right. This asymmetry can be observed in the measured rolling moment from the quasi-static pitch sweep test case. Figure 6.13 shows the rolling and yawing moment coefficients for the zero sideslip angle test case. The sudden increase in the rolling moment at an angle of attack of 18.3° indicates the stalling of the right wing followed by the stalling of left wing indicated by the drop in rolling moment at

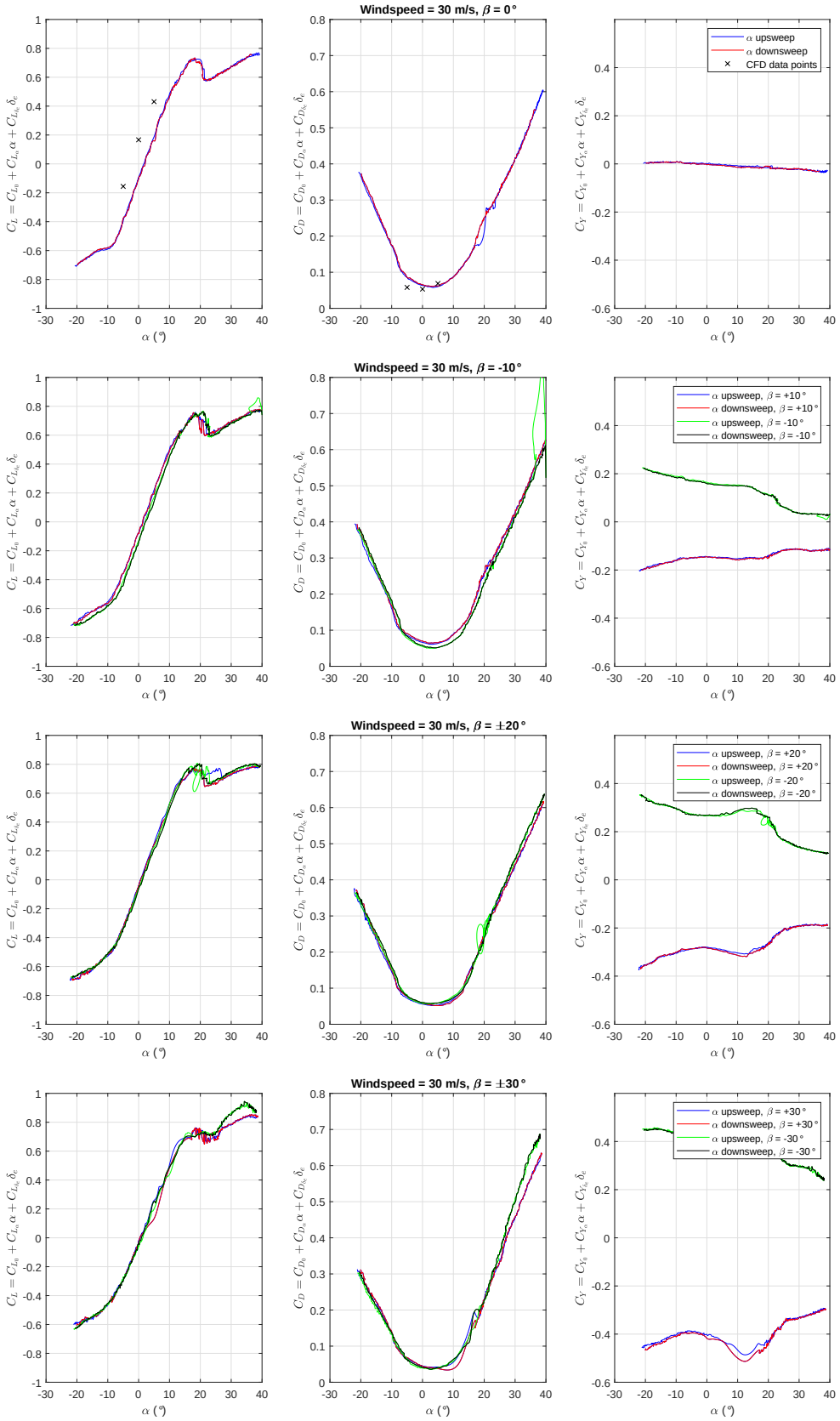

FIGURE 6.11. Quasi-static measured force coefficients at a wind speed of 30 m/s.

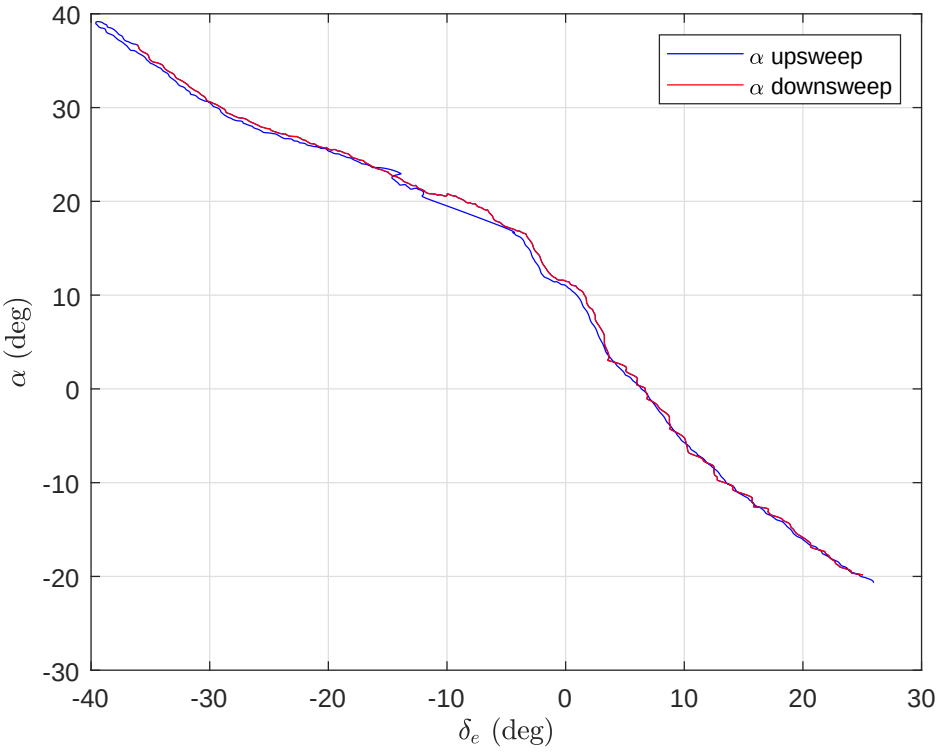

FIGURE 6.12. Change in angle of attack due to elevator deflection at a wind speed of 30 m/s and zero angle of sideslip.

20.7° angle of attack. This is confirmed by the measured yawing moment which shows the same trend and that this is caused by the increase in drag from a stalled wing. Hysteresis is observed here since the right wing flow reattaches at a higher angle of attack while the angle of attack is sweeping down than the angle at which stall occurs while sweeping up. Further investigations of stall hysteresis on the Hawk model are covered in Section 6.4. The asymmetry on the Hawk model was also observed in flow visualisation (China clay testing) experiments done by Hamish Mills [51], which correlate with the findings here.

Table 6.1 summarises the measured static coefficients for the Hawk model estimated in this section along with the CFD predictions and previously identified values using parameter estimation based on the aircraft model motion. Note that these values are at zero attitude and control surface deflection angles where the region is roughly linear.

6.3 Hawk dynamic tests

This section considers the estimation of the dynamic longitudinal aerodynamic coefficients $C_{L_{\dot{\alpha}}}$, C_{L_q}, $C_{m_{\dot{\alpha}}}$ and $C_{m_{\dot{\alpha}}}$. This is accomplished with the manoeuvre rig in 2 degrees of freedom (DOF):

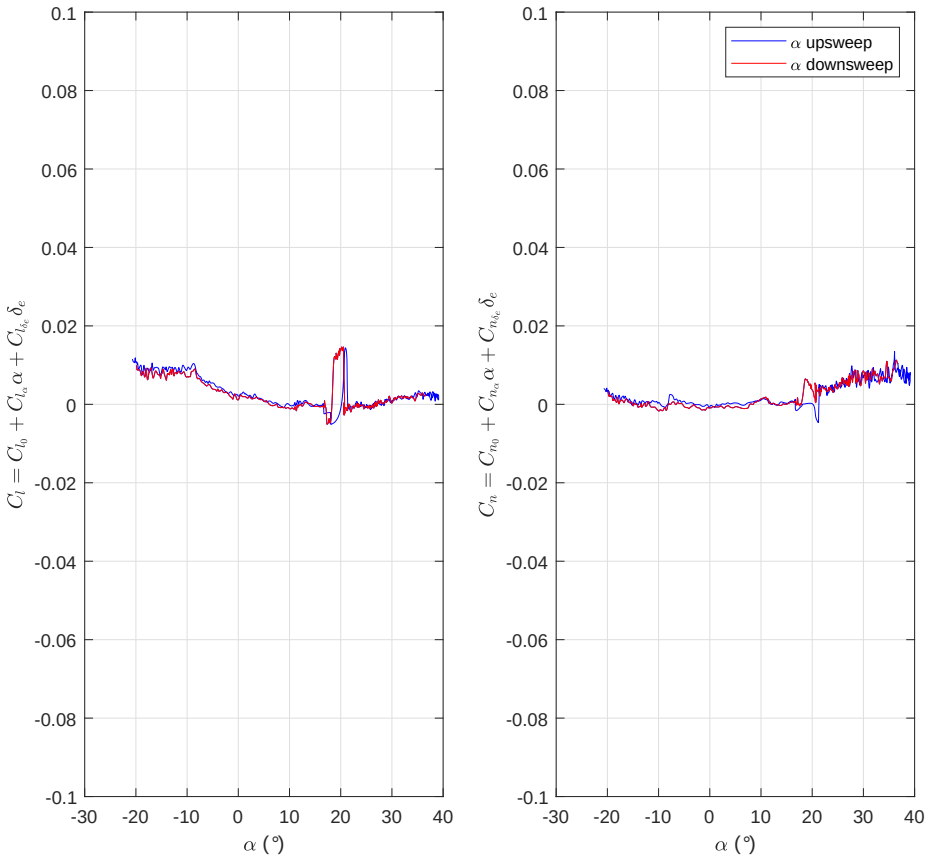

FIGURE 6.13. Hawk roll asymmetry observed in the measured rolling and yawing moment coefficients during the quasi-static pitch sweep test case at a wind speed of 30 m/s and zero angle of sideslip.

aircraft pitch and rig pitch. Rig pitch translates to approximate aircraft heave. Although it is possible to perform dynamic 1-DOF aircraft pitch only tests on the manoeuvre rig (which has been done previously [11]), 1-DOF tests cannot separate $\dot{\alpha}$ and q derivatives due the lack of heave motion causing the angle of attack to be equal to the pitch angle. One of the objectives for the manoeuvre rig has been to obtain pitch and heave motions independently (yaw and sway motions as well).

A lower wind tunnel speed is beneficial to obtain larger changes in angle of attack due to heave, however this reduces the control power available from the compensator. A wind speed of 20 m/s is used for the following 2-DOF dynamic tests. The measured states are rig pitch angle, rig pitch rate, aircraft pitch angle, aircraft pitch rate, aircraft and compensator elevator deflections, and all loads recorded by the load cell. Attitude angles are measured using the rig's encoders, aircraft rotation rates are measured using it's on-board Inertial Measurement Unit, and control

TABLE 6.1. Summary of the experimentally measured, computationally predicted and parameter estimated static Hawk aerodynamic coefficients (at zero attitude and control surface deflection angles).

Coefficient	Measured	CFD	Estimated	
			Equation Error Method	Output Error Method
$C_{l_{\delta_a}}$ (/rad)	0.123	-	0.0840	0.104
$C_{m_{\delta_e}}$ (/rad)	-1.14	-0.837	-0.886	-0.975
$C_{n_{\delta_r}}$ (/rad)	-0.0556	-	-0.0791	-0.0705
C_{m_0} (/rad)	0.1053	0.0410	0.0782	0.0745
C_{m_α} (/rad)	-0.499	-0.592	-0.6716	-0.6984
C_{n_0} (/rad)	-0.000742	-	-0.0015	-0.003
C_{n_β} (/rad)	0.104	-	0.158	0.145
C_{L_0} (/rad)	-0.104	0.167	-	-
C_{L_α} (/rad)	3.44	3.36	-	-
$C_{D_{min}}$ (/rad)	0.0607	0.0533	-	-

surface deflections are measured using potentiometers. The angle of attack and its rate are then calculated using their conventional definitions.

Since the manoeuvre rig was updated with the implementation of the load cell, the change in inertia and mass distribution altered the dynamics of the rig and Hawk model such that a self-induced oscillation was created in aircraft heave. As a result, active feedback is required to stabilise the system. Damping in the form of aircraft or rig pitch rate feedback is sufficient to stop this oscillation. However, a self-induced oscillation can be beneficial for parameter estimation since no external forcing is required. The following study attempts to characterise this self-induced oscillation in terms of the Hawk's pitch angle and angle of attack and their respective rates, as well as their difference in phase as the Hawk pitch rate feedback gain is varied. The controller used is:

$$\delta_{e_a} = \delta_{e_c} + k_q q_a \tag{6.1}$$

where δ_{e_a} is the aircraft elevator input, δ_{e_c} is the commanded deflection, k_q is the pitch rate gain, and q_a is the aircraft pitch rate. Figure 6.14 shows the testing procedure: the Hawk pitch rate feedback gain is changed in small steps and the resulting motion is recorded. No other input or feedback is used. All measured data is processed using a third order Butterworth filter with a cut-off frequency of 20 Hz. The critical gain at which the oscillations begin was found to be $k_q = 0.05$.

Figure 6.15 shows the variation in the amplitudes and frequency of the angle of attack and pitch angle, as well as the phase shift between the two as a function of the pitch rate feedback gain. Note that the calculation of the phase shift was automated using a cross-correlation function to estimate the lag between the two signals. As a result, the accuracy of the estimated phase shift decreases as the amplitude of one or both of the signals become small. The frequency and phase

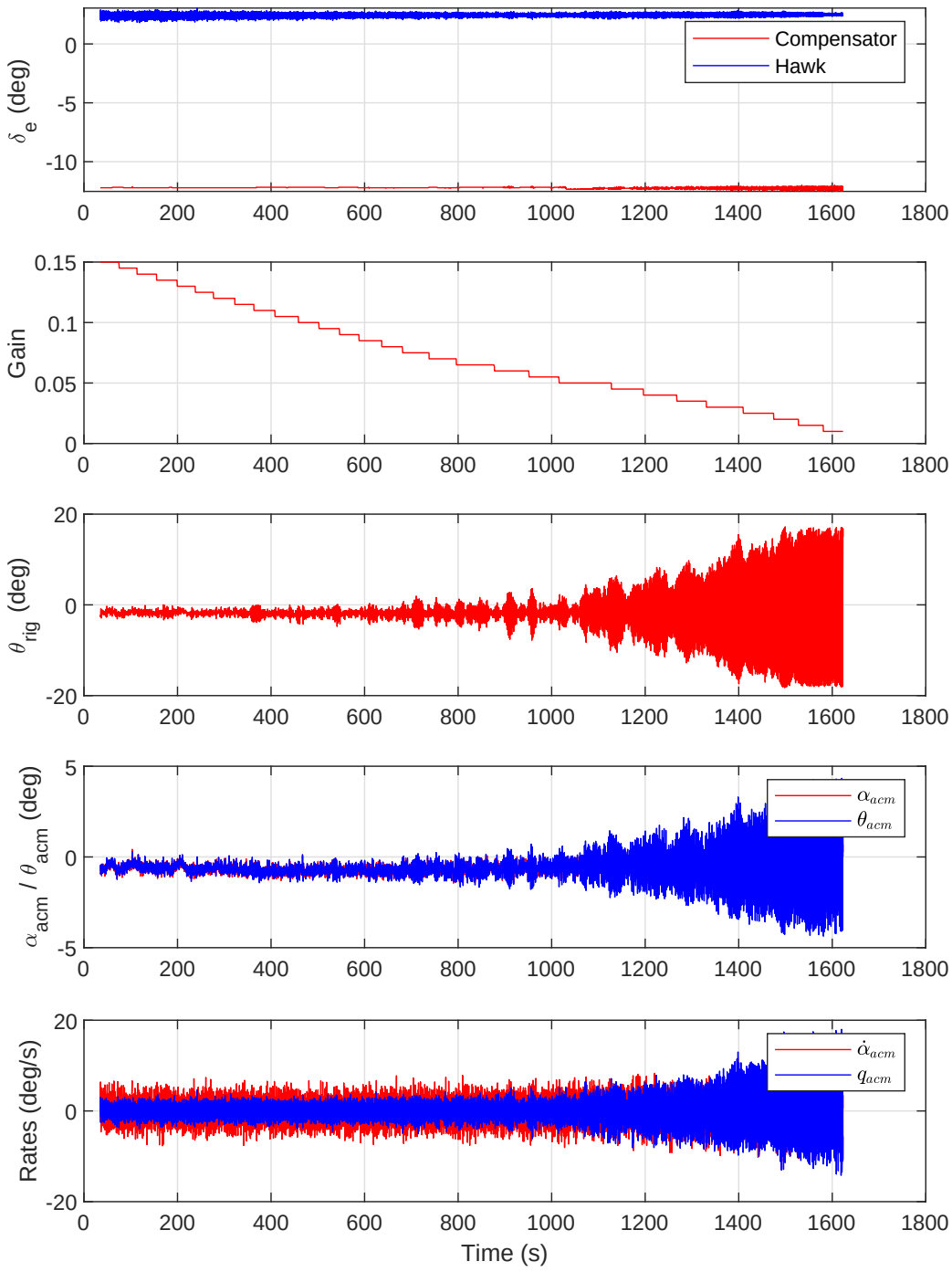

FIGURE 6.14. Self-induced oscillation in aircraft heave as the aircraft pitch rate feedback gain is reduced.

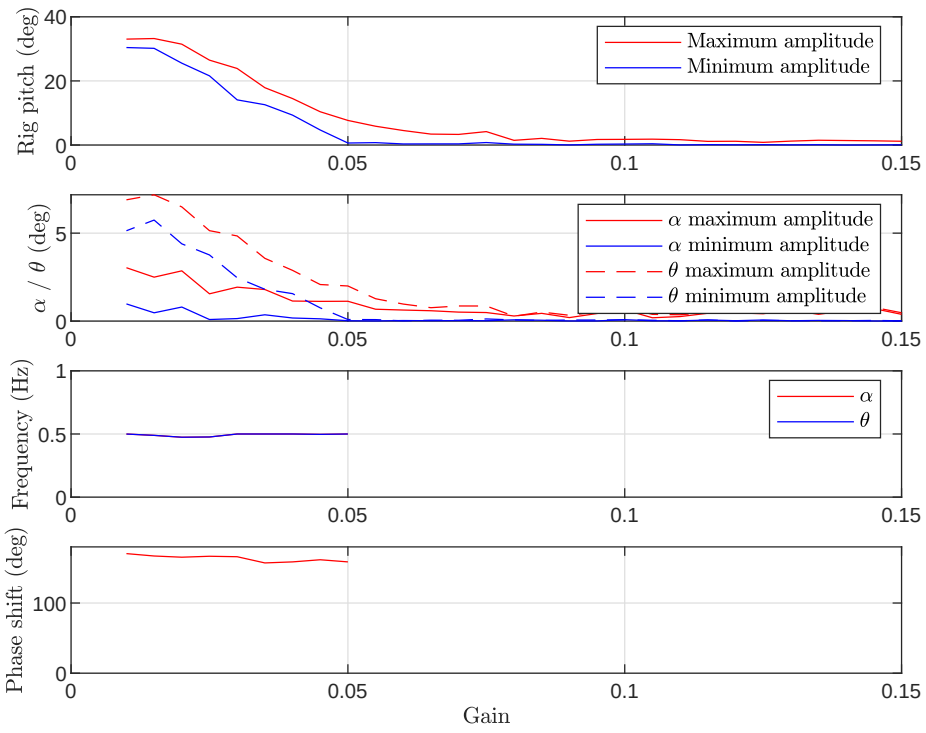

FIGURE 6.15. Amplitude, frequency and phase difference variation of the angle of attack and pitch angle as a function of pitch rate feedback gain (k_q).

shift remains nearly constant at values of 0.5 Hz and 166° respectively while in the oscillation region where the gain is less than 0.05. Figure 6.16 shows the same parameters but for the rate of change of angle of attack and pitch rate which show the same trend. The aerodynamic stiffness in heave can be manipulated using the rig's compensator to change the characteristics of the oscillation to benefit parameter estimation purposes.

Next, the heave motion is driven by a frequency sweep (from 0 to 1.2 Hz) input to the rig compensator elevator. The aircraft pitch rate feedback gain is fixed at $k_q = 0.15$. The time history of the main states are shown in Figure 6.17. All measured data is processed using a third order Butterworth filter with a cut-off frequency of 20 Hz.

Figure 6.18 shows the variation in amplitude, frequency, and difference in phase of the angle of attack and pitch angle. The estimation of the frequency and phase shift is performed for a 30 second moving window which is swept across time. The frequency of angle of attack and pitch rate match the frequency of the compensator elevator input. The resonant frequency producing the largest oscillation is about 0.5 Hz where the difference in phase is about 100°. Note that the phase shift cannot be measured accurately in the regions where the amplitude of oscillations are too small.

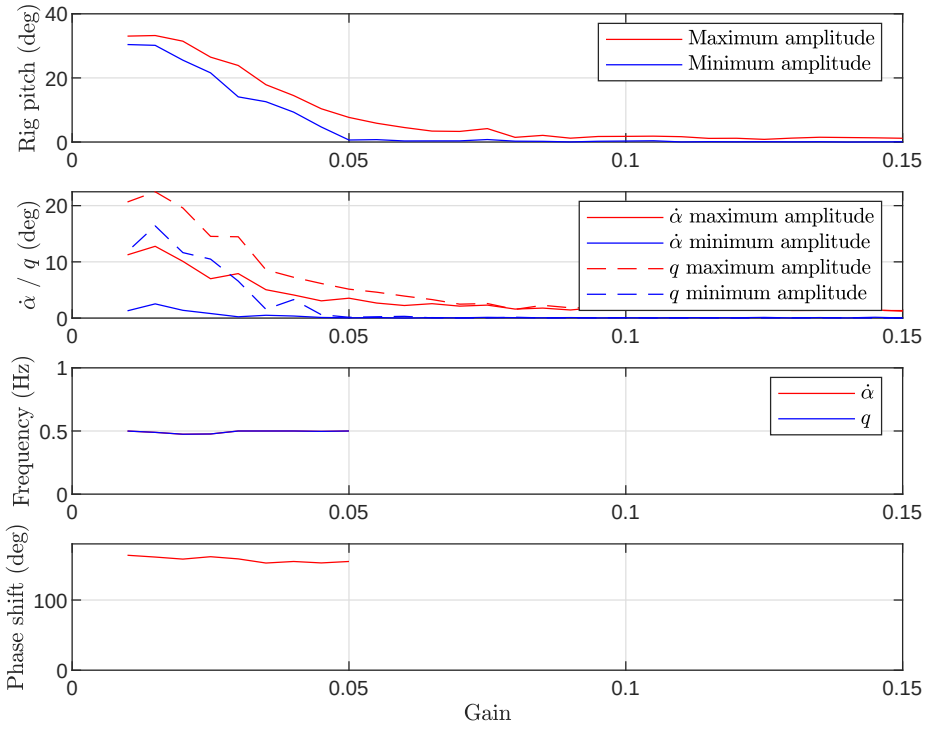

FIGURE 6.16. Amplitude, frequency and phase difference variation of the rate of change of angle of attack and pitch rate as a function of pitch rate feedback gain (k_q).

Figure 6.19 shows the variation in amplitude, frequency, and difference in phase of the rate of change of angle of attack and pitch rate. Again, the frequency of angle of attack and pitch rate match the frequency of the compensator elevator input. Step changes in phase are observed where the phase shift is approximately 92° between input frequencies of 0.4 Hz and 0.65 Hz. As mentioned before, the phase shift cannot be measured accurately in the regions where the amplitude of oscillations are too small. For parameter estimation purposes, a phase shift of 90° is ideal to separate the dependence of those states on the total aerodynamic loads.

To estimate the dynamic derivatives, a 10 second portion of the previous test in which the phase difference is approximately 90° is used. The nonlinear mathematical model described in Section 3.4 is used here for the aircraft model and an additional virtual object to represent the point of rotation. The virtual object is constrained using the spherical constraint described in Section 3.6.5.2, and the aircraft model is constrained to the virtual object using the relative position and attitude fixed constraints described in Sections 3.6.1 and 3.6.2 respectively. The distance offset between the virtual object and the aircraft body represents the offset of the centre of gravity of the aircraft body from the rotation point (gimbal centre). The rig itself is not not modelled; it is represented by the reaction forces measured during the test which are applied

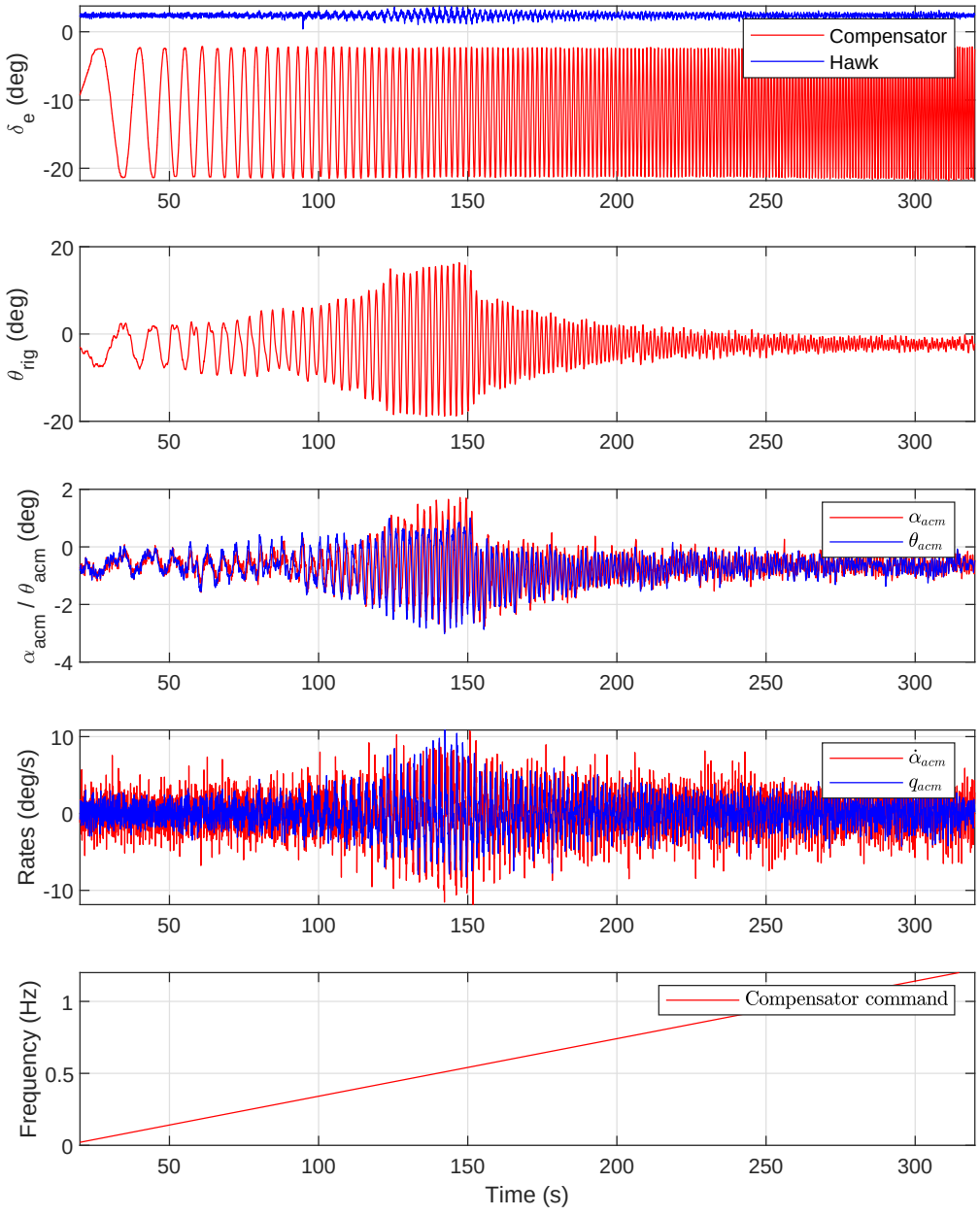

FIGURE 6.17. Hawk longitudinal 2-DOF aircraft pitch and rig pitch forced oscillation test for the estimation of dynamic derivatives.

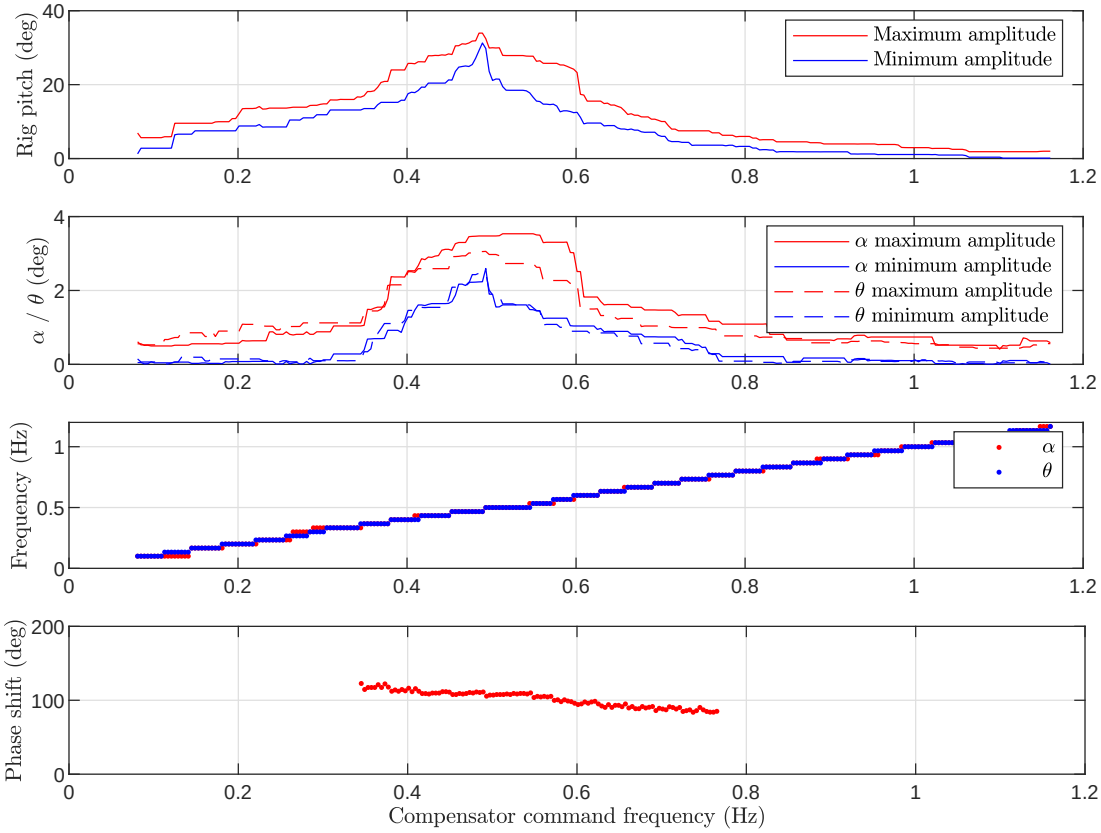

FIGURE 6.18. Amplitude, frequency and phase difference variation of the angle of attack and pitch angle as a function of compensator elevator input frequency.

onto the rotation point. The external forces applied onto the rotation point are the lift, drag, and rig reaction forces. The external moments applied onto the rotation point are pitching moment and friction. Friction and rig reaction forces are measured by the load cell. Lift,drag and pitching moment are modelled as follows:

$$L = \frac{1}{2}\rho V^2 S(C_{L_0}(\alpha) + C_{L_\alpha}(\alpha)\alpha + C_{L_{\dot{\alpha}}}\frac{c\dot{\alpha}}{2V} + C_{L_q}\frac{cq}{2V} + C_{L_{\delta_e}}(\alpha,\delta_e)\delta_e) \quad (6.2)$$

$$D = C_{D_0}(\alpha) + C_{D_\alpha}(\alpha)\alpha \quad (6.3)$$

$$m = \frac{1}{2}\rho V^2 S(C_{m_0}(\alpha) + C_{m_\alpha}(\alpha)\alpha + C_{m_{\dot{\alpha}}}\frac{c\dot{\alpha}}{2V} + C_{m_q}\frac{cq}{2V} + C_{m_{\delta_e}}(\alpha,\delta_e)\delta_e) \quad (6.4)$$

$$(6.5)$$

where the static components measured previously are used here in the form of lookup tables. Note that these aerodynamic loads act in the wind axes and need to be transformed into the

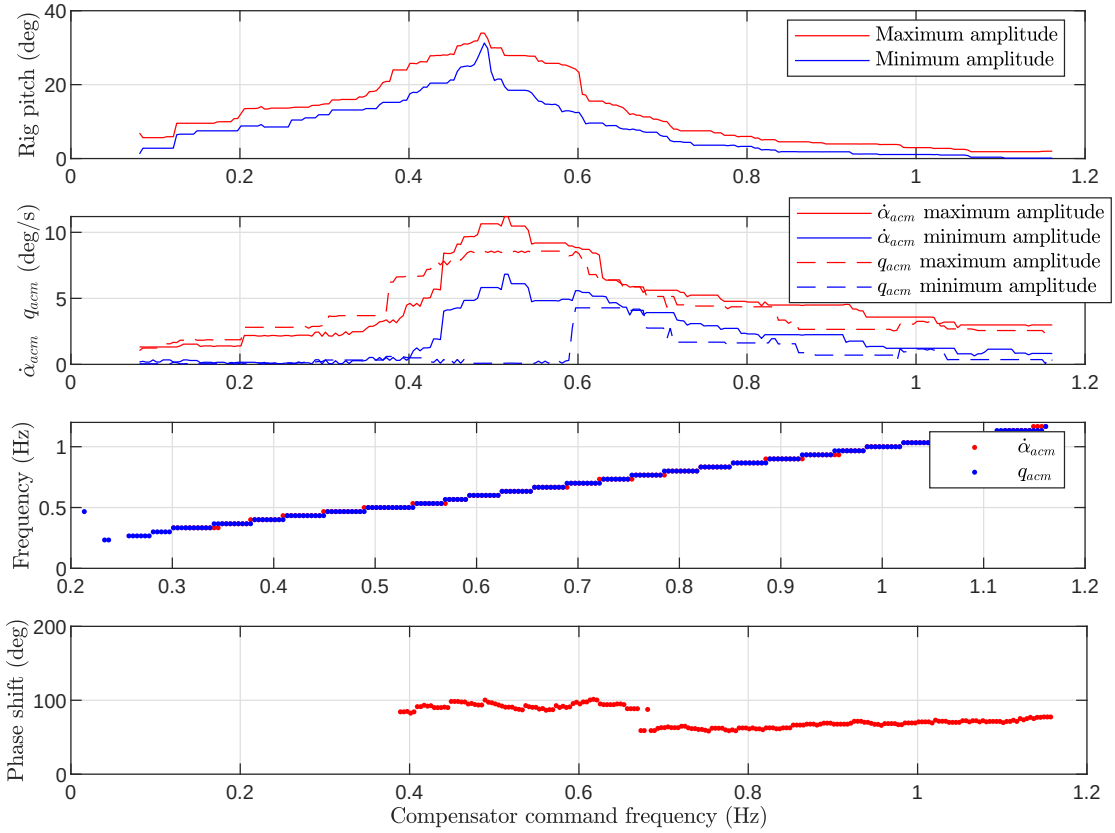

FIGURE 6.19. Amplitude, frequency and phase difference variation of the rate of change angle of attack and pitch rate as a function of compensator elevator input frequency.

inertial/body axes before applying them into the equations of motion.

Since the aircraft gimbal is free to rotate in pitch, the aerodynamic pitching moment cannot be measured directly. However, friction can now be measured directly as a reaction moment and so a friction model is no longer needed. Figure 6.20 shows the friction measured during the experiment run with a comparison along with the model previously defined in Equation 3.119. Some hysteresis type behaviour can be observed in the measured data. The model is a good representation of friction since the gradient of the relationship between friction and gimbal pitch rate is a close match.

The values are identified using the parameter estimation tool provided in Matlab Simulink. The optimization technique used here is the nonlinear least squares method and the minimising cost function is the sum squared error. The objective was to minimise the error in aircraft pitch angle and rig pitch angle. Figure 6.21 shows the measured and simulated responses, and Table

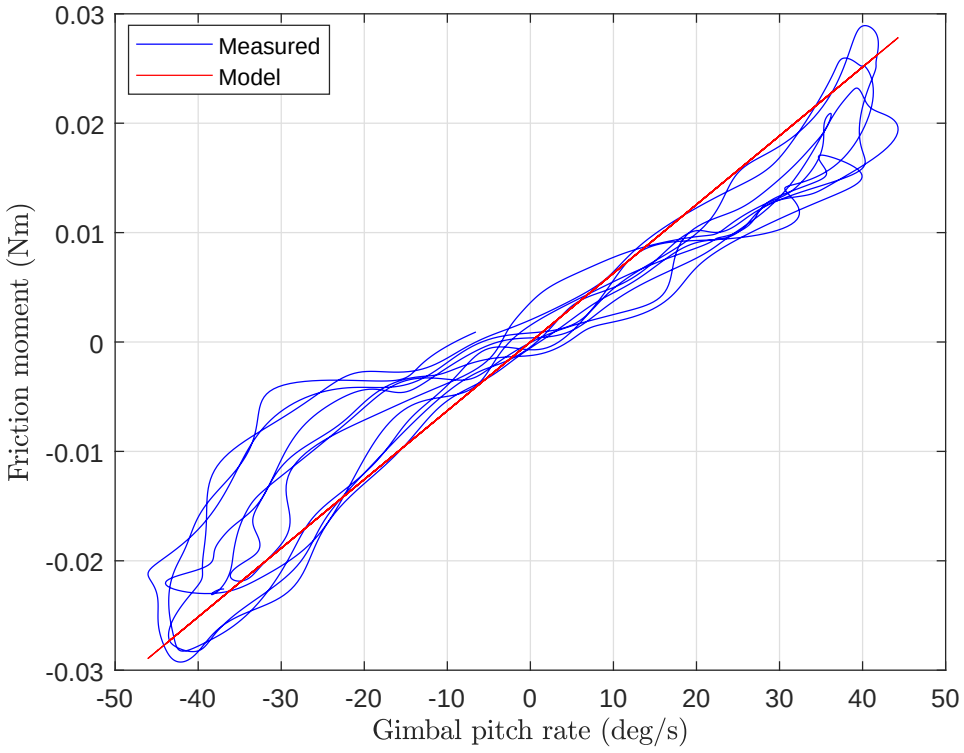

FIGURE 6.20. Comparison between measured friction and friction modelled by Equation 3.119.

6.2 shows the identified parameters. A good match can be seen between the simulation model and the measured states.

Note that the effect of the wires attaching the gimbal encoders to the Hawk have not been modelled. It would be beneficial to characterise and model its effects in the future to further improve the accuracy of the identified derivatives. These tests demonstrate the ability of the rig to facilitate separation of translation and rotational dynamic derivatives and can be repeated in the future in the lateral-directional sense to estimate the rolling and yawing dynamic derivatives.

6.4 Investigation of Hawk Stall Hysteresis

The section covers the investigation of stall hysteresis observed on the Hawk aircraft model. Past testing of the Hawk model on the manoeuvre rig in a 1-DOF configuration (aircraft pitch only) and 2-DOF configuration (rig pitch and aircraft pitch DOFs) have revealed static hysteresis in the stall region of the aircraft model. These past tests were carried out prior to the implementation of the load cell. In the 2-DOF configuration, the lift created by the aircraft model was estimated using its relationship with the rig pitch angle. This is possibly due to the aerodynamic balance

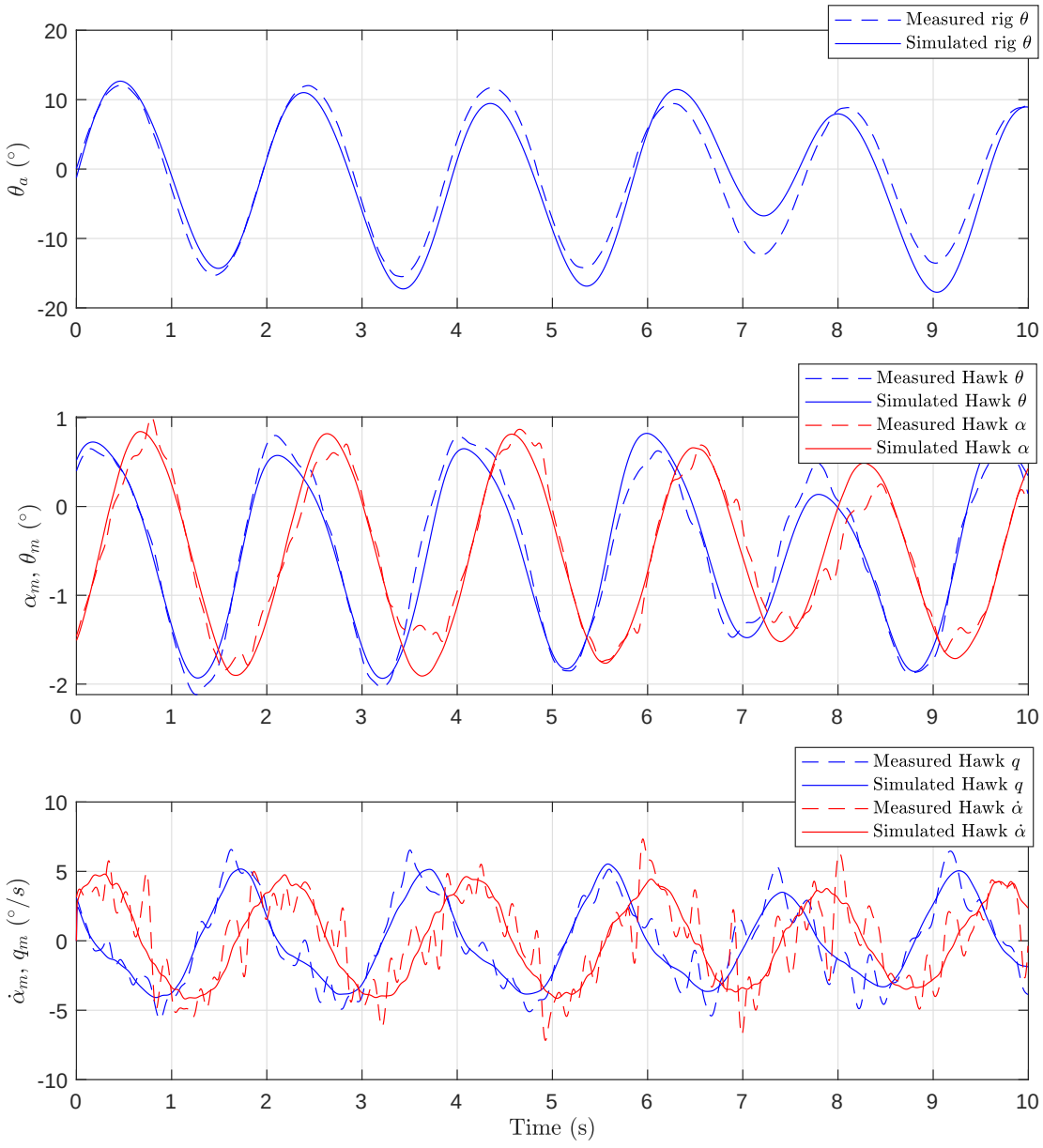

FIGURE 6.21. Comparison between measured and simulated 2-DOF Hawk pitch and rig pitch test for parameter estimation.

TABLE 6.2. Estimated Hawk dynamic aerodynamic derivatives and centre of gravity location relative to the aircraft rotation point (body axes).

Parameter	**Estimated value**
$C_{L_{\dot{\alpha}}}$	1.44×10^{-7}
C_{L_q}	12.1
$C_{m_{\dot{\alpha}}}$	-0.00145
C_{m_q}	-8.93
$x_{c.g.}$ (m)	-0.00857
$z_{c.g.}$ (m)	-0.00565

of lift between the compensator and the aircraft model. An increase in lift of the aircraft model translates to a higher equilibrium rig arm pitch angle and a decrease in lift will result in the opposite. Therefore stall is visually represented as a sudden drop of the rig pitch angle and a sudden increase in rig pitch angle as the flow reattaches. Results of these tests are published in Reference [52].

The study carried out here extends the findings of the previous tests. This includes attempting to further understand the flow mechanics causing hysteresis with the aid of the newly implemented load cell. The same test procedure as previous tests is repeated in the same DOFs. A slow ramp up and ramp down input to the aircraft elevator ($\dot{\delta}_e = \pm 0.2°/s$) is used to pitch nose-up and nose-down through stall. This is done with the rig in the 1-DOF configuration: aircraft pitch only, and then in 2-DOFs: aircraft pitch and rig pitch. The wind speed at which these tests are carried out is 30 m/s. Feedback control is used to suppress the limit cycle oscillation of the Hawk model, and also to counter unwanted oscillations of the rig arm caused by turbulence. The controller used will be defined later for each set of experiments.

Several factors in testing conditions have changed since the tests reported in Reference [52] and some of the previous conditions are unknown. First, the inertia and mass distribution of the manoeuvre rig have changed due to the implementation of the load cell. This changes the elevator deflection required for static balance for a given rig pitch angle and aircraft pitch angle. The increase in rig pitch inertia will affect the dynamics of the rig; this is evident since the updated manoeuvre rig and Hawk system now exhibits self-induced oscillations in aircraft heave without the use of control. This was investigated in Section 6.3. Second, the 7' by 5' closed section wind tunnel had new fan blades installed. Its effect on the air flow quality is unknown. And lastly, the atmospheric conditions of the previous tests and how they may affect the behaviour of the flow mechanics are unknown.

The aircraft controller defined in Reference [52] is used mainly to suppress the Hawk's limit cycle oscillations (LCO). Upon using the exact same controller for the testing here, it was found that its effectiveness in suppressing the LCO has decreased. This could be caused by wear in the

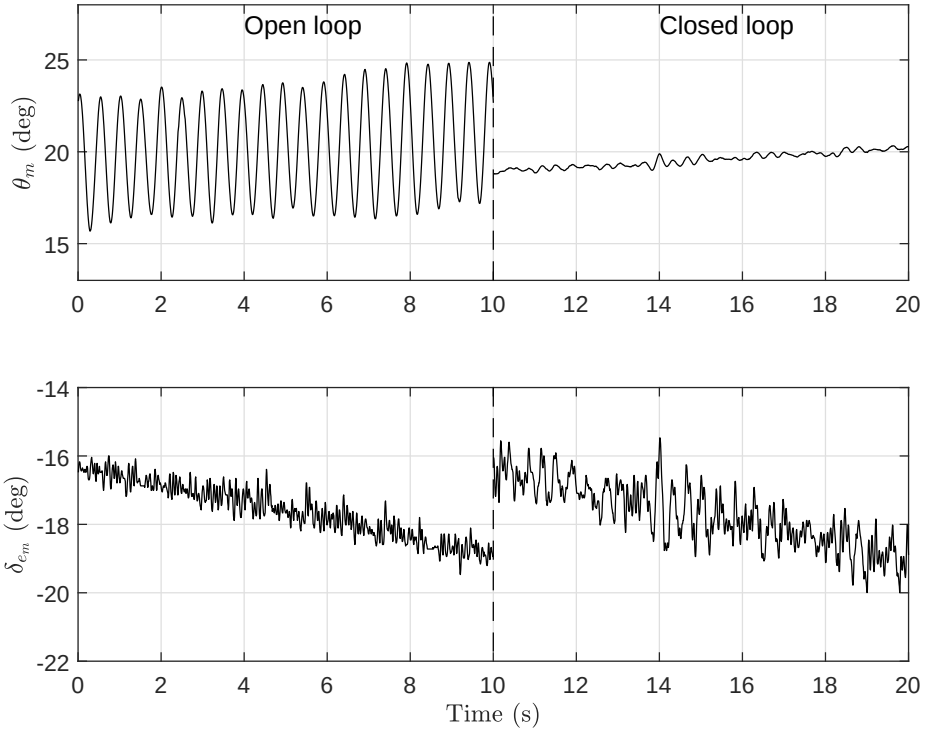

FIGURE 6.22. Limit cycle oscillation suppression on the Hawk model using the controller defined in Equation 6.6 with $K_{q_m} = 0.15$.

Hawk's servo actuators affecting their responsiveness. A new aircraft controller was created by manual tuning to achieve similar LCO suppression and is expressed by:

$$\delta_{em} = \delta_{em_d} + K_{q_m} q_m \tag{6.6}$$

where δ_{em} is the aircraft model elevator input, δ_{em_d} is the elevator demand (ramp) and K_{q_m} is the feedback gain for the aircraft model pitch rate q_m. The gain used for the following 1-DOF and 2-DOF experiments is $K_{q_m} = 0.15$. Figure 6.22 shows the effectiveness of the controller during the ramp elevator inputs when the Hawk is within the LCO region. The measured elevator deflection demonstrates that the controller is able to suppress the LCO with little elevator oscillations. Note that the Hawk's control surfaces have an added high frequency "dither" implemented in order to overcome static friction for improved actuation control. The frequency of this shaking is assumed to be high enough such that it will not affect the Hawk's dynamics.

The same type of controller is used on the rig's compensator to mitigate oscillations caused due to wind tunnel turbulence:

$$\delta_{ec} = \delta_{ec_0} + K_{q_a} q_a \tag{6.7}$$

where δ_{e_c} is the compensator elevator input, $\delta_{e_{c0}}$ is the constant elevator deflection for static equilibrium of the rig and K_{q_a} is the feedback gain for the rig arm pitch rate q_a. The gain used for the following 2-DOF experiments is $K_{q_a} = 0.1$.

Figure 6.23 shows the measured lift, rolling, and yawing moments for both the 1-DOF (aircraft pitch) and 2-DOF (aircraft pitch and rig pitch) cases for three repeats of the aircraft elevator slow ramp up and ramp down while within the region of stall. A third order Butterworth filter with a cut-off frequency of 0.3 Hz is used to process the measured loads. Clear hysteresis can be observed on both DOF cases, however the extent to which it occurs varies between the two. First, the maximum lift reached is higher on the 2-DOF case occurring at the highest angle of attack of 15.5° where as the maximum lift for the 1-DOF case occurs at an angle of attack of 13.8°. All of the tests showing hysteresis follow this higher branch while slowly pitching up. Increasing the angle of attack beyond this point causes the aircraft to drop to an intermediate equilibrium point after which full stall is reached. Two regions of hysteresis are clearly visible before and after this intermediate equilibrium point. In the 2-DOF case, lift continues to increase slightly within the intermediate equilibrium region before dropping again, whereas stall in the 1-DOF case appears to be more gradual. In the 1-DOF case, the intermediate equilibrium spans a larger range of angle of attack where complete stall occurs at a higher angle of 17°. The 2-DOF hysteretic behaviour observed resembles that of which is presented in Reference [52]. Both 1-DOF and 2-DOF cases follow nearly the same path as the aircraft model pitches back down and the air flow reattaches.

Studying the measured rolling moments in Figure 6.23, one can identify that the intermediate equilibrium is caused due to asymmetric stall of the Hawk's wings. The overall increase in rolling moment during stall indicates that the right wing stalls first before the left. This asymmetry was identified in previous tests in Reference [52] through 4-DOF tests, where the DOFs were aircraft roll, aircraft pitch, aircraft yaw, and rig pitch. Repeating the same ramp inputs to the aircraft elevators caused it to suddenly depart in roll at stall (right wing down). Hysteresis is observed on each individual wing. In the 1-DOF case, as the pitch increases gradual stall of the right wing occurs at a highest angle of attack of about 13° - 14° followed by a sudden stall of the left wing at a highest angle of attack of 17°. This is confirmed by the measured yawing moments created by the increase in drag due to stall. Pitching back down, the reattachment of the left wing occurs first albeit delayed at a lowest angle of attack 15.7°. This delay in reattachment of the left wing is the cause of the second hysteresis loop in lift past the intermediate equilibrium point. Similarly, a delay in the reattachment on the right wing which occurs at a lowest angle of attack of about 13° is the reason for the first hysteresis loop in lift. The intermediate branch in lift spans a larger range of angle of attack that for the 2-DOF case due to the larger gap between the angles at which stall and reattachment occur on both wings. Studying the measured rolling moments for the 2-DOF case, the right wing stalls at a highest angle of attack of 15.5° which corresponds to the highest peak in lift followed soon by the stall of the left wing soon after at a highest angle of attack of 15.9°. The smaller gap between the points at which each wing stalls

results in a smaller intermediate equilibrium region. The flow in the 2-DOF case reattaches on each wing much sooner at a higher angle of attack and closer together compared to the 1-DOF case, again causing the intermediate stage to be smaller. These observations are reflected in the yawing moment as well.

In summary, having the Hawk model free to heave via the freedom in rig pitch has shown delays to flow separation to occur at a higher angle of attack on the right wing, and advance flow separation on the left wing to occur at a lower angle of attack. As a result, the hysteretic behaviour of the air flow alters between the 1-DOF and 2-DOF cases. The general patterns of the observed hysteresis behaviour are highlighted on the schematic shown in Figure 6.24.

The reasons as to why the number of DOFs affects the behaviour of the air flow at stall is still unclear. One possibility is that in the 1-DOF case with the arm rigidly locked in pitch, vibrations can pass through the arm and onto the aircraft model leading to alterations in the flow mechanics. By testing the model in 2-DOFs including aircraft heave, the model experiences significantly less vibrations as it is effectively "floating". In this case, the model behaviour is more representative of actual free-flight, which is an advantage the manoeuvre rig has over other multi-DOF dynamic test rigs. Also note that the results shown here have low repeatability and a large number of test runs are required to capture the hysteresis effect since no hysteresis is observed on most runs. This is evidence that the flow mechanics are very fragile and sensitive to testing conditions which further compounds onto the reasoning that rig vibrations could be affecting the flow structure. It was not possible to identify exactly which conditions the hysteresis is affected by.

6.5 Investigation of 2DOF Roll and Yaw Oscillation

This section describes a concept of generating a self-sustained oscillation when an aircraft model is configured in two degrees of freedom (DOF): aircraft roll and aircraft yaw on the manoeuvre rig [71]. This is made possible by the combined effects of the aircraft's aerodynamics and the mechanics of the aircraft gimbal. This type of oscillation is akin to the lateral-directional mode Dutch roll. A self-sustained oscillation has benefits in terms of parameter estimation since no additional external forces or moments are required to drive the motion, hence do not need to be modelled.

First the concept is explained by deriving the equations of motion. This is followed by an experimental demonstration of the 2-DOF roll and yaw oscillations. The work here does not cover parameter estimation itself, although it can be attempted in the future.

This particular self-induced oscillation is only made possible when a 3-DOF aircraft gimbal is locked in pitch. Note that the order of rotation of the gimbal is important and should follow the western convention of axes rotation sequence where the sequence from inertial to body axes is yaw, pitch, roll. Throughout the derivation here, the following angles will be assumed to be small: roll angle, yaw angle, angle of sideslip ($\phi, \psi, \beta << 1$). When resolving the aerodynamic moments

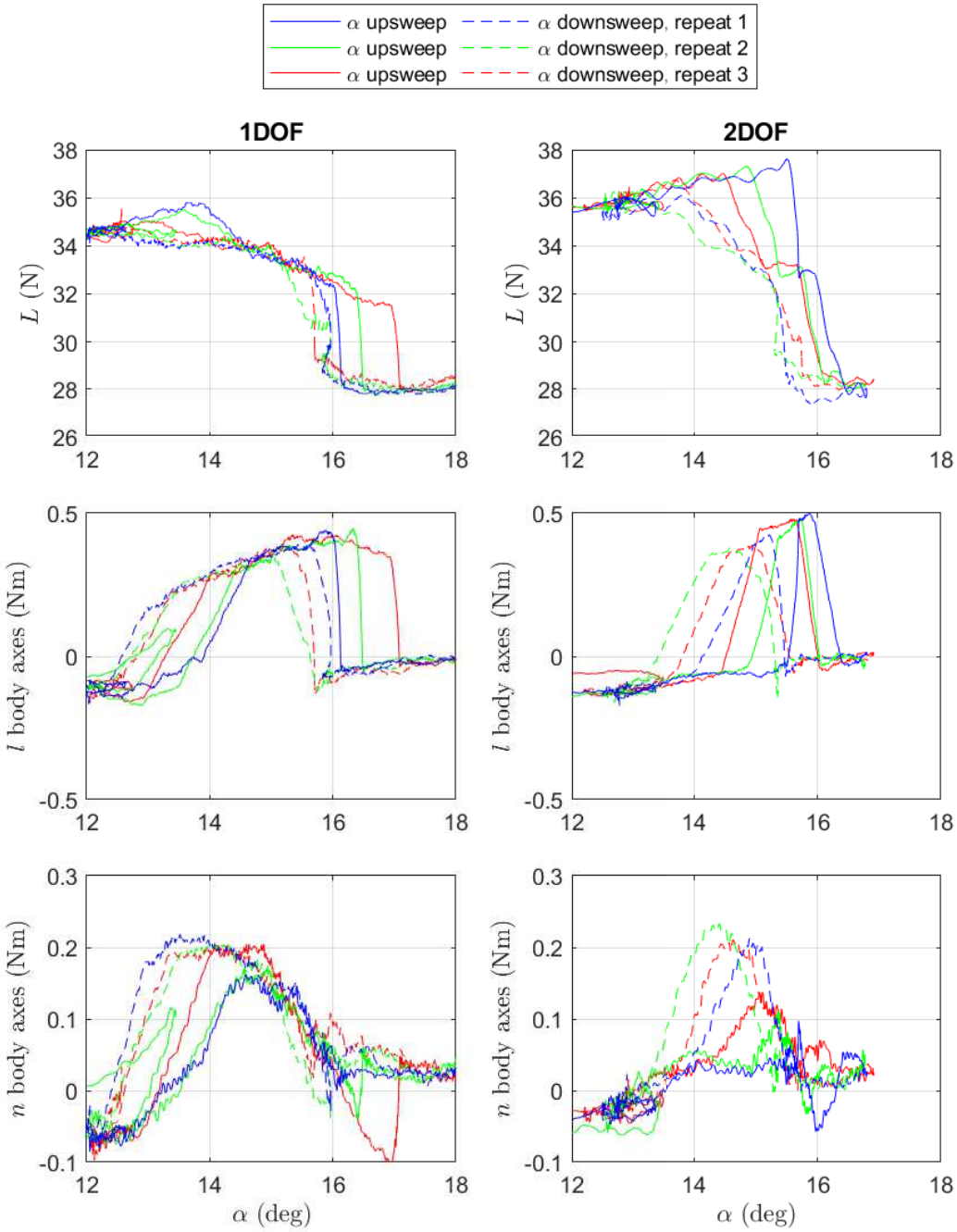

FIGURE 6.23. Stall hysteresis observed on the Hawk aircraft model.

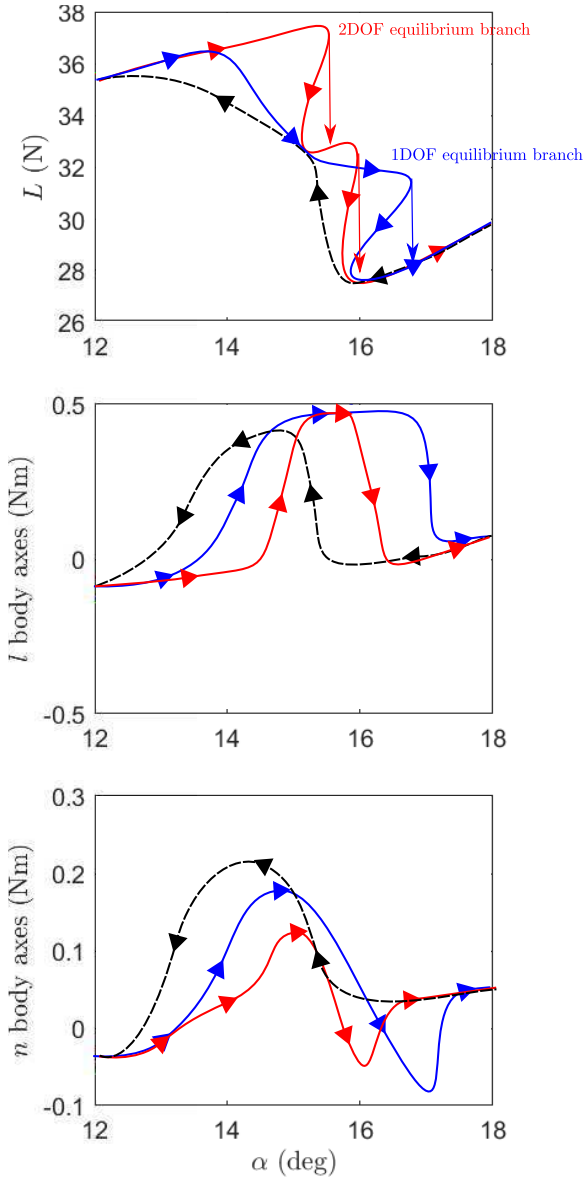

FIGURE 6.24. Schematic of the stall hysteresis observed on the Hawk aircraft model.

from the aircraft model's body axes on the pitch rotation axis, one can derive the reaction moment caused by the locked hinge in the aircraft's body axes which will be equal and opposite to the aerodynamic moment. This reaction moment is defined as:

$$L_r = 0 \tag{6.8}$$

$$M_r = -M + N\phi \tag{6.9}$$

$$N_r = -M\phi \tag{6.10}$$

where L_r, M_r and N_r are the rolling, pitching and yawing reaction moments respectively created by the gimbal in the aircraft body axes, L, M and N rolling, pitching and yawing aerodynamic moments also in the aircraft body axes, and ϕ is the aircraft model roll angle. Note that yawing reaction moment N_r is a function of pitching moment M and roll angle ϕ. The body axes velocities can be derived to be:

$$V_x = V_0 \cos\theta_0 \tag{6.11}$$

$$V_y = -V_0\psi + V_0\phi\sin\theta_0 \tag{6.12}$$

$$V_z = V_0 \sin\theta_0 \tag{6.13}$$

where V_0 is the wind tunnel velocity, and θ_0 is the pitch setting angle. Using the above velocities, one can derive the definition for the angle of attack and sideslip as:

$$\alpha = \theta_0 \tag{6.14}$$

$$\beta = -\psi + \phi\sin\theta_0 \tag{6.15}$$

Therefore, $\dot{\alpha} = 0$. The rate of change of the angle of sideslip can be defined in terms of the body axes rotation rates as:

$$\dot{\beta} = r\cos\theta_0 - p\sin\theta_0 \tag{6.16}$$

The rotational roll and yaw accelerations in the aircraft body axes can be defined as:

$$\dot{p} = \overline{M}_l^{\beta}\beta + (\overline{M}_l^{p} - \overline{M}_l^{\dot{\beta}}\sin\theta_0)p + (\overline{M}_l^{r} + \overline{M}_l^{\dot{\beta}}\cos\theta_0)r + \overline{M}_l^{\delta_a}\delta_a + \overline{M}_l^{\delta_r}\delta_r \tag{6.17}$$

$$\dot{r} = \overline{M}_n^{\beta}\beta + (\overline{M}_n^{p} + \overline{M}_n^{\dot{\beta}}\sin\theta_0)p + (\overline{M}_n^{r} + \overline{M}_n^{\dot{\beta}}\cos\theta_0)r + \overline{M}_n^{\delta_a}\delta_a + \overline{M}_n^{\delta_r}\delta_r - \overline{M}_n^{*}\phi \tag{6.18}$$

where $\dot{p}$ and $\dot{r}$ are the roll and yaw accelerations respectively, and the terms with a bar are defined as:

$$\overline{M}_l^{\beta} = \frac{\overline{q}SbC_{l_\beta}}{I_{xx}}, \overline{M}_n^{\beta} = \frac{\overline{q}SbC_{n_\beta}}{I_{zz}} \tag{6.19}$$

$$\overline{M}_l^{p} = \frac{\overline{q}SbcC_{l_p}}{2VI_{xx}}, \overline{M}_n^{p} = \frac{\overline{q}SbcC_{n_p}}{2VI_{zz}} \tag{6.20}$$

$$\overline{M}_l^{r} = \frac{\overline{q}SbcC_{l_r}}{2VI_{xx}}, \overline{M}_n^{r} = \frac{\overline{q}SbcC_{n_r}}{2VI_{zz}} \tag{6.21}$$

$$\overline{M}_l^{\dot{\beta}} = \frac{\overline{q}SbcC_{l_{\dot{\beta}}}}{2VI_{xx}}, \overline{M}_n^{\dot{\beta}} = \frac{\overline{q}SbcC_{n_{\dot{\beta}}}}{2VI_{zz}} \tag{6.22}$$

$$\overline{M}_l^{\delta_a} = \frac{\overline{q}SbC_{l_{\delta_a}}}{I_{xx}}, \overline{M}_n^{\delta_a} = \frac{\overline{q}SbC_{n_{\delta_a}}}{I_{zz}} \tag{6.23}$$

$$\overline{M}_l^{\delta_r} = \frac{\overline{q}SbC_{l_{\delta_r}}}{I_{xx}}, \overline{M}_n^{\delta_r} = \frac{\overline{q}SbC_{n_{\delta_r}}}{I_{zz}} \tag{6.24}$$

$$\overline{M}_n^{*} = \frac{\overline{q}Sb(C_{m_a}\theta_0 + C_{m_{\delta_e}}\delta_e)}{I_{zz}} \tag{6.25}$$

Here, $\overline{M}_n^{*}\phi$ is the yawing reaction moment created due to the gimbal's restriction in pitch. Note that if the aircraft model is balanced in pitch ($\overline{M}_n^{*} = 0$), there will be no reaction yawing moment. The above system of equations can be written in the state space form as

$$\begin{bmatrix} \dot{\beta} \\ \dot{p} \\ \dot{r} \\ \dot{\phi} \end{bmatrix} = \begin{bmatrix} 0 & -\sin\theta_0 & \cos\theta_0 & 0 \\ \overline{M}_l^{\beta} & (\overline{M}_l^{p} - \overline{M}_l^{\dot{\beta}}\sin\theta_0) & (\overline{M}_l^{r} + \overline{M}_l^{\dot{\beta}}\cos\theta_0) & 0 \\ \overline{M}_n^{\beta} & (\overline{M}_n^{p} + \overline{M}_n^{\dot{\beta}}\sin\theta_0) & (\overline{M}_n^{r} + \overline{M}_n^{\dot{\beta}}\cos\theta_0) & -\overline{M}_n^{*} \\ 0 & 1 & 0 & 0 \end{bmatrix} \begin{bmatrix} \beta \\ p \\ r \\ \phi \end{bmatrix} + \begin{bmatrix} 0 & 0 \\ \overline{M}_l^{\delta_a} & \overline{M}_l^{\delta_r} \\ \overline{M}_n^{\delta_a} & \overline{M}_n^{\delta_r} \\ 0 & 0 \end{bmatrix} \begin{bmatrix} \delta_a \\ \delta_r \end{bmatrix} \tag{6.26}$$

The eigenvalues can now be found by solving the characteristic equation:

$$det \begin{bmatrix} \lambda & \sin\theta_0 & -\cos\theta_0 & 0 \\ -\overline{M}_l^{\beta} & \lambda - (\overline{M}_l^{p} - \overline{M}_l^{\dot{\beta}}\sin\theta_0) & -(\overline{M}_l^{r} + \overline{M}_l^{\dot{\beta}}\cos\theta_0) & 0 \\ -\overline{M}_n^{\beta} & -(\overline{M}_n^{p} + \overline{M}_n^{\dot{\beta}}\sin\theta_0) & \lambda - (\overline{M}_n^{r} + \overline{M}_n^{\dot{\beta}}\cos\theta_0) & \overline{M}_m^{*} \\ 0 & -1 & 0 & \lambda \end{bmatrix} = 0 \tag{6.27}$$

The spiral root (near zero) can be approximated by making the assumption that λ is small:

$$\lambda_0 = \frac{\overline{M}_m^{*}\overline{M}_n^{\beta}\cos\theta_0}{A} \tag{6.28}$$

where A is

$$\begin{aligned} A = (-\overline{M}_n^{*} + \overline{M}_n^{\beta}\sin\theta_0)(\overline{M}_l^{r} + \overline{M}_l^{\dot{\beta}}\cos\theta_0) - (\overline{M}_n^{r} + \overline{M}_l^{\dot{\beta}}\cos\theta_0)\overline{M}_l^{\beta}\sin\theta_0 \\ - (\overline{M}_n^{p} + \overline{M}_n^{\dot{\beta}}\sin\theta_0)\overline{M}_l^{\beta}\cos\theta_0 + (\overline{M}_l^{p} + \overline{M}_l^{\dot{\beta}}\sin\theta_0)\overline{M}_n^{\beta}\cos\theta_0 \end{aligned} \tag{6.29}$$

The sign of λ_0 and hence the stability of the spiral mode depends primarily on the sign of the term $\overline{M}_n^*$ which depends on the pitching moment of the aircraft model as a function of the pitch stability, pitch setting angle and elevator deflection. If the aircraft model has lateral stability ($\overline{M}_n^\beta < 0$), and the total pitching moment of the aircraft model is less than 0, the sign of λ_0 will become positive and an instability will arise. This instability of the spiral mode leads to the model rotating in yaw, which then couples to roll. This is the basis for the self-induced oscillation in roll and yaw.

Next, a demonstration of this oscillation is presented using the Hawk model on the manoeuvre rig. Figure 6.25 shows a time history of the model in 2-DOFs only (roll and yaw) where only the elevator deflection is varied and the motion observed. This test aims to find the critical elevator deflection at which the oscillation is triggered. This was found in the opposite manner, i.e. by finding the elevator deflection at which oscillations decay. This was because of friction resisting the onset of the oscillation. A pulse input to the elevator and rudder was imposed at time 497 seconds to force the onset and overcome friction. The time at which the elevator deflection changes are marked by the vertical red dashed lines across all plots. An elevator deflection of more than 8.5° is required for the Hawk to sustain this oscillation. With the implementation of the load cell, we are now able to directly measure the pitching moment to validate this concept. It can be seen that the oscillations are sustained when the pitching moment of above -0.35 Nm. The offset in the pitching moment below zero required for the oscillation is also due to friction. The frequency of oscillation is 0.82 Hz. A lower elevator deflection will cause oscillations to decay.

In summary, a negative pitching moment created by an aircraft free to rotate in only roll and yaw will produce self-induced oscillation in roll and yaw. Such self-induced oscillations are useful for parameter estimation purposes since no additional forcing is required to drive its motion. The properties of the motion may be altered by attaching springs in the yaw axis, for example. Parameter estimation is beyond the scope of the work done here and can be attempted in the future. Other than the research in Reference [71], this work is believed to be unique.

6.6 Summary

This chapter has covered several new applications for the manoeuvre rig which make use of its load cell. Static and dynamic aerodynamic derivatives have been measured and re-estimated which show good agreement with previous parameter estimation studies. The load cell improves the capability of the manoeuvre rig since it can now measure forces and moments directly which reveals nonlinearity of derivatives. This could not be achieved previously using parameter estimation alone since linearised aerodynamic models about equilibrium were used. Previous linear models were also unable to truly differentiate between lift and drag of the aircraft through parameter estimation. This is because the mathematical model used in parameter estimation techniques considers only a single moment about the arm gimbal contributed by both lift and

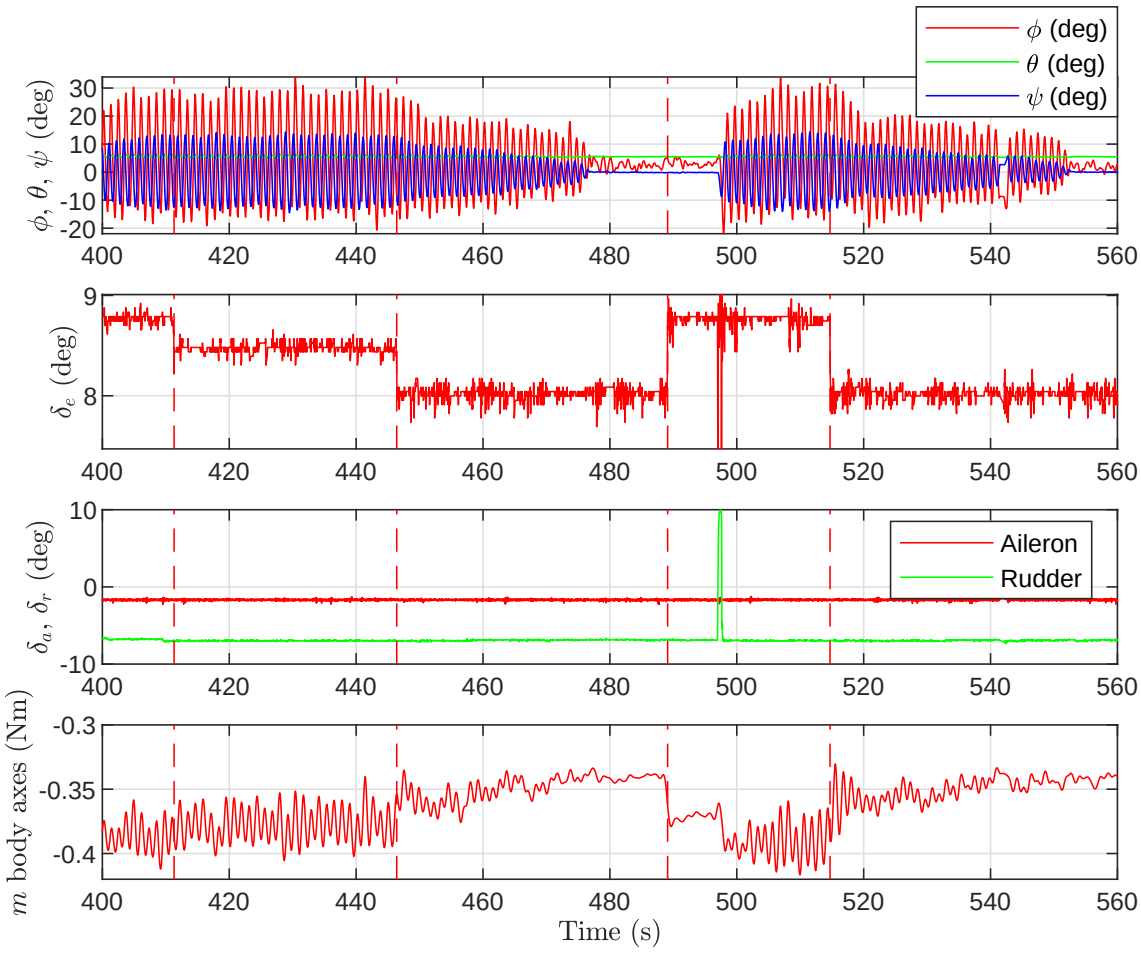

FIGURE 6.25. Self-induced oscillations in aircraft model roll and yaw on the manoeuvre rig.

drag of the aircraft. The alternative had been to either estimate the lift induced component of drag (using the quadratic relationship with lift) which was still an underestimate of the total drag [10], or to assume the moment contribution of drag (about the arm gimbal) is negligible compared to the lift component for small heave motions. As a result, the linear lift model of the aircraft obtained via parameter estimation will indirectly include the effects of drag (or components of it) if the rig pitch angle is large enough for drag to contribute a significant moment, which can overestimate or underestimate the lift produced by the model (depending on the sign of rig pitch angle).

The load cell can also directly measure friction in roll and pitch for the aircraft gimbal. The rig's capability in estimating dynamic derivatives for the Hawk model using forced oscillations created by the compensator has also been presented. It is possible to create multi-dimensional

lookup tables to accurately capture the aerodynamics of the Hawk but is beyond the scope of this work.

The study of the Hawk's stall hysteresis has revealed lateral asymmetry where each wing has separate stall angles. The right wing of the Hawk stalls before the left. Characteristics of the hysteresis were seen to be dependant on the number of DOFs the rig is configured in: in 1 DOF aircraft pitch only, or 2DOFs aircraft pitch and rig pitch. Releasing the rig pitch DOF reduces the gap between the stall angles of the two wings, and increases the maximum lift. The cause of these changes are still unclear and needs further investigation, although it is evident that the flow structure responsible for the hysteresis is very fragile.

Finally, a method for creating self-induced roll and yaw oscillations in the aircraft model was demonstrated on the manoeuvre rig. The oscillation is mainly driven by a component of the pitching moment about the yaw axis created due to the aircraft gimbal being locked in pitch. Such oscillations are useful for parameter estimation purposes of aerodynamic derivatives since the motion is driven by the aircraft's aerodynamics alone without the need for external forcing.

The next chapter experimentally investigates the practical implications of the inertial and kinematic compensation concept presented in Chapter 4.

CHAPTER 7

RIG INERTIAL, AERODYNAMIC AND KINEMATIC COMPENSATION

7.1 Introduction

In Chapter 4, a kinematic compensation concept was derived to improve the match in aircraft response between a free-flying aircraft model and that which is constrained spherically, such as on the manoeuvre rig. This was achieved by applying a calculated tangential force onto the aircraft model, F_c^*, to compensate for the rig's inertial, aerodynamic and kinematic effects. The effect of thrust can also be recreated artificially for the initial part of the response using the tangential force F_c^{**}. The calculation of both these compensatory forces required the measurement of the tangential and radial reaction forces. These forces can now be measured with the implemented load cell.

This chapter presents the experimental investigations conducted on the practical implementation of inertial, aerodynamic and kinematic compensation on the manoeuvre rig with the Hawk model. Where possible, comparisons with computational simulations are made. The experiments are divided into two parts. The first being rig inertial and aerodynamic compensation, where the objective is to cancel inertial and aerodynamic effects that the rig applies on the aircraft model. These effects are essentially in the form of tangential reaction forces acting as an additional external load on the aircraft model. In the ideal case, the aircraft's motion will resemble that of responses simulated in Chapter 4 where the rig is not present (zero tangential force) and the motion is only affected by the kinematic spherical constraint.

The second part of the experiment is to additionally implement kinematic compensation derived in Chapter 4 where the objective is to demand a reaction force (F_c^*) onto the aircraft model using active feedback on the manoeuvre rig which requires reaction force measurements from the load cell. Since the improvement in response due to artificial thrust is small (F_c^{**}

compensation), only kinematic compensation is investigated using a practical approach.

The work done in this chapter focuses on the longitudinal motion only. The concepts of compensation can be equally applied in the lateral-directional sense as well and should be a future objective.

7.2 Rig inertial and aerodynamic compensation

7.2.1 Preliminary experimental results

Preliminary experiments were carried out in an attempt to cancel out inertial and aerodynamic effects of the rig on the aircraft (in the longitudinal sense) using a simple multi-proportional controller. A linear model of the longitudinal dynamics of the system was derived in Section 3.2 in conventional state space form, where $\dot{\boldsymbol{x}} = A\boldsymbol{x} + B\boldsymbol{u}$ and $\boldsymbol{y} = C\boldsymbol{x} + D\boldsymbol{u}$, and is shown in Equations 3.8 and 3.9. The properties of the rig and aircraft used in this model were obtained previously using parameter estimation techniques [46, 53]. These tests were carried out prior to the implementation of the load cell.

An overview of the controller used is shown in Figure 7.1. The values for the proportional gains were derived from the linearised model of the system and are shown in Equations (7.1-7.3). Note that vertical acceleration feedback (n_z) is possible due to the Inertial Measurement Unit (IMU) installed within the Hawk model.

$$K_{\theta_r} = \frac{C_{L_{\alpha_c}}}{C_{L_{\delta_{e_c}}}} + \frac{m_r g z_{c.g._r}}{\bar{q} S_c x_{c.g._c} C_{L_{\delta_{e_c}}}} \tag{7.1}$$

$$K_{q_r} = \frac{C_{L_{q_c}}}{C_{L_{\delta_{e_c}}}} \frac{\bar{c}_c}{2V} \tag{7.2}$$

$$K_{n_z} = \frac{I_{yy_r}}{\bar{q} S_c x_{c.g._c} C_{L_{\delta_{e_c}}}} \frac{g}{x_{c.g._a}} \tag{7.3}$$

Comparisons between the linear simulation and experimental responses for a wavelet input to the Hawk's elevators are shown in Figure 7.2. An acceptable match can be seen, where the difference in the responses compared to the computational simulation are caused mainly due to wind tunnel turbulence as well as extreme response sensitivity to initial conditions, which is mostly visible for the aircraft heave motion (created by the rig arm motion θ_r). The differences between the experimental responses are due to the same reasons. The 'noise' visible before and after the aircraft elevator wavelet input represents feedback used to try to hold the aircraft and rig at the initial conditions.

Although a good match, there is still uncertainty as to whether the controller used was effective in truly negating the inertial and aerodynamic influences of the rig since there is no guarantee on the accuracy of the parameter estimated mathematical model of the rig, and hence also for the controller. In order to measure this influence, the reaction force between

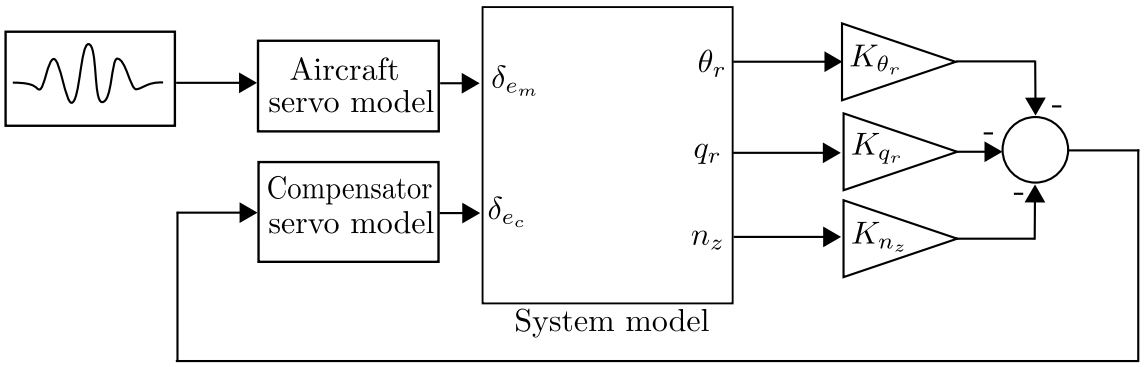

FIGURE 7.1. Preliminary feedback controller for rig inertia and aerodynamic compensation.

the rig arm and aircraft model needs to be measured, which leads to the primary reason for the implementation of a load cell for the purpose of physical/virtual flight simulation. Note that the divergent behaviour that should occur as a result of rig inertia and aerodynamic compensation does not appear here as simulated in Section 4.3.2. This is an indication that a simple linear controller based on parameter estimated values may be insufficient for rig inertial and aerodynamic compensation. One reason is because drag isn't truly represented within the model. The simulations performed in Section 4.3.2 have shown that drag does indeed have a significant impact on the aircraft's response and causes the motion to become unstable if the aircraft model does not produce its own thrust, as is the case for the Hawk model, when simulating near free-flying responses.

7.2.2 Experimental results using the load cell

Now with the load cell installed on the rig, its measurements can be used to measure the reaction loads between the aircraft and rig. This section will outline the attempts to control the reaction forces using simple proportional, derivative, and integral control. The gains to be used are explored experimentally and chosen based on observed behaviour of responses. Advanced control techniques are not explored here due to time constraints and should be a future objective.

The objective of the control law here is to counter the reaction force measured by the load cell using the manoeuvre rig's compensator elevator deflections. Matlab Simulink is used for near real-time control, and for ease of creating and rapid modification of the control law during testing. The tests here are carried out at a wind tunnel speed of 30 m/s. The controller used for the following experiments is as follows:

$$\delta_{e_c} = \delta_{e_{c_0}} + K_P R_e + K_D s R_e + K_I \frac{1}{s} R_e \tag{7.4}$$

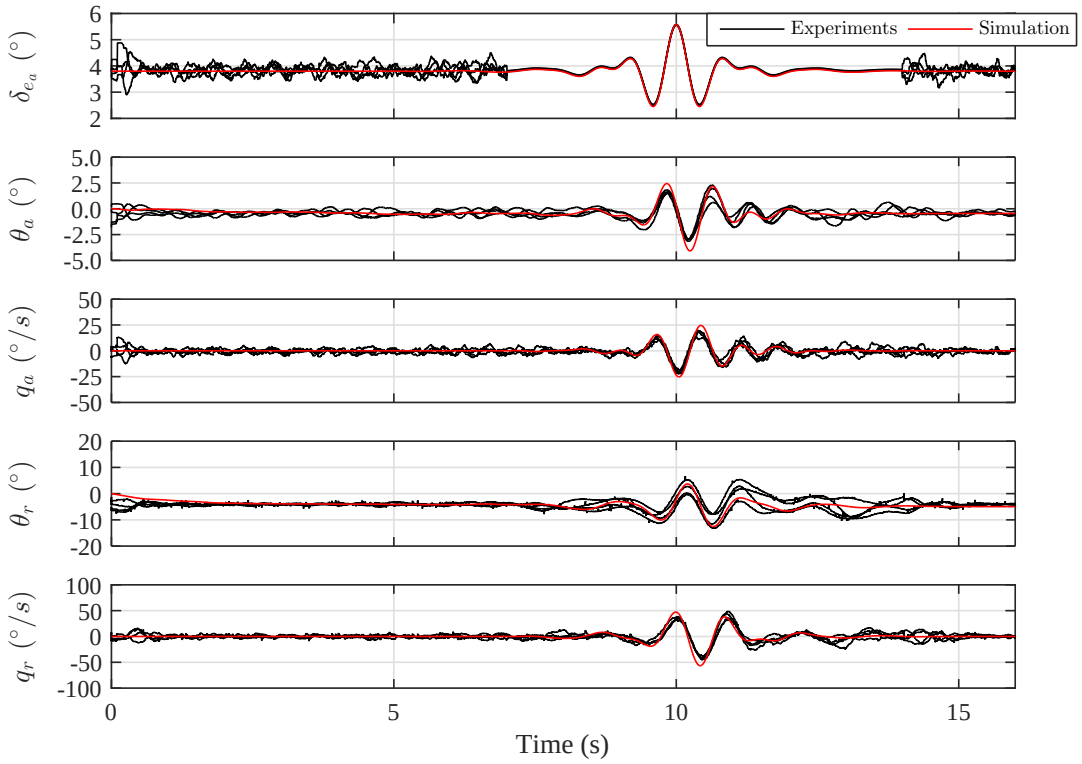

FIGURE 7.2. Preliminary experimental and computational simulation comparison for rig inertial and aerodynamic compensation.

where δ_{e_c} is the compensator elevator input, $\delta_{e_{c_0}}$ is the compensator elevator setting angle for equilibrium, R_e is the error in tangential reaction force and is defined as:

$$R_e = R_d - R \tag{7.5}$$

where R_d is the demanded tangential reaction force and R is the measured reaction force. K_P, K_D and K_I are the proportional, derivative, and integral gains respectively. As the objective here is to negate the tangential reaction force created by inertial and aerodynamic rig effects, the demanded reaction force is $R_d = 0$. When compensating for kinematic effects of the rig as well (total compensation), $R_d = F_c^*$. Kinematic compensation is covered in Section 7.3.

First, the response of the Hawk model to a filtered doublet elevator input is studied. The doublet is passed through a second order low pass Butterworth filter with a cut-off frequency of 0.8 Hz which is equal to the frequency of the short-period mode. This will approximately excite the Hawk's short-period mode. A regular doublet is not used here because it would be the worse case for the controller as it will perform poorly to sharp changes in reaction force. The recorded measurements are filtered using a second order low pass Butterworth filter with a cut-off frequency of 10 Hz. The effect of cut-off frequency on the performance of the controller is

investigated later on.

To combat perturbations in motion due to turbulence, all tests are repeated multiple times (6-10 times) and the average response is calculated. A large set of repeat tests would be ideal, but the experiments were limited due to time constraints. These perturbations make it difficult to compare with simulated responses especially since the motion is sensitive to initial conditions. Figure 7.3 shows the open loop responses of the Hawk where the response is affected by rig's inertial and aerodynamic stiffness created by the compensator, evident by the measured tangential reaction force R (which is the measured Z force in the rig's body axes frame of reference). The other presented states are the aircraft model elevator deflection δ_{e_m}, aircraft model angle of attack α_m, compensator elevator deflection δ_{e_c}, and rig pitch angle θ_{rig}. Note that the open loop response is between 9 and 13 seconds; feedback is used for the rest of the time to stabilise the rig in order to keep initial conditions identical between runs. This is done by adding damping through rig pitch rate feedback to the compensator elevator and aircraft pitch rate feedback to the aircraft elevator. Some differences in initial conditions caused due to wind tunnel turbulence are still present. The thick red line represents the average response of all repeated tests. Note that for all the following tests, the controller used is activated at 9 seconds, and disabled at 13 seconds.

Figure 7.4 shows the effect of now adding proportional reaction force feedback to the compensator elevator for gains ranging from $K_P = 1$ to $K_P = 5$ (P controller). The controller used is shown in Equation 7.4. Note that $K_D = 0$ and $K_I = 0$, and the demanded reaction force is $R_d = 0$. The responses shown for each gain are averages of multiple responses. The cut-off frequency of the second order low pass Butterworth filter used to process the measurements here is 10 Hz. With regards to the magnitude of the measured tangential reaction force, a gain of $K_P = 5$ gives the smallest, however oscillations begin to arise indicating that this gain to too high for the total lag and delays present in the system (100 milliseconds compensator actuation lag and 4 milliseconds data transmission delays, and filtering lag). The magnitude of the tangential force R is still too large and requires better compensation. Next, the effect of filter cut-off frequency on control effectiveness is investigated.

Figure 7.5 shows the responses for the same damped doublet input for a range of filter cut-off frequencies from 10 Hz to 16 Hz. The filter used is a second order low pass Butterworth filter. A proportional gain of $K_P = 5$ only is used here. Again, the presented responses are averages over multiple repeat tests. It is difficult to notice much difference in the recorded reaction force. Small oscillations can be seen past the 9 second mark, although they are within the amplitude of perturbations caused by turbulence. All cut-off frequencies show similar levels of oscillation in compensator elevator, which indicates the gain used is close to making the system unstable. Figure 7.6 shows the delays caused by the second order low pass Butterworth filter as a function of frequency. Increasing the cut-off frequency by $2Hz$ increases the maximum delay by approximately 5 to 9 milliseconds. Figure 7.7 shows the frequency content of the measured reaction force found by performing Fast Fourier Transform. The highest frequency peak occurs at

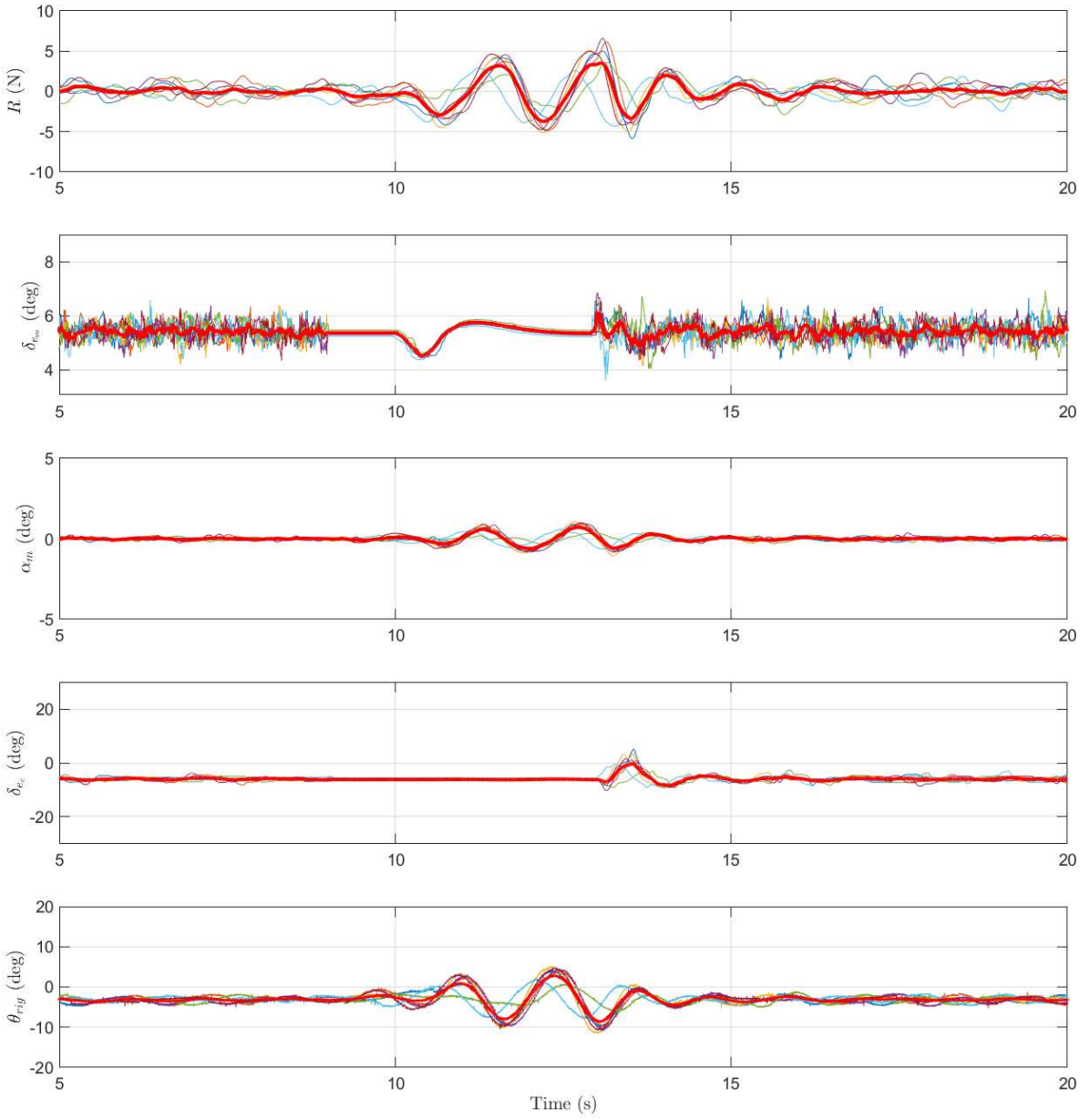

FIGURE 7.3. Open loop aircraft response to a damped doublet elevator input.

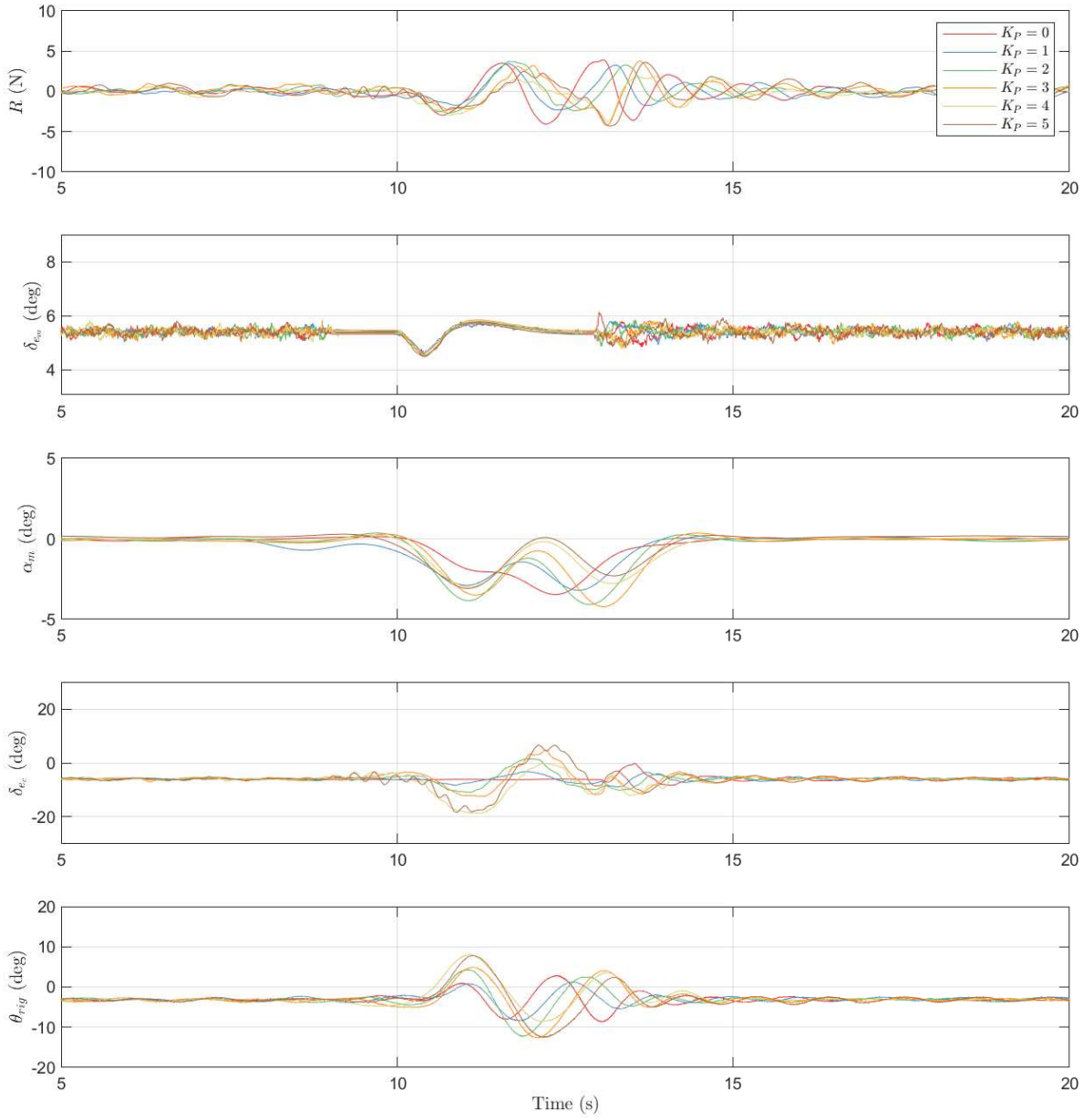

FIGURE 7.4. Aircraft response to a damped doublet elevator input with proportional feedback for rig inertial and aerodynamic compensation.

16.5Hz. Therefore, a cut-off frequency of 16Hz was decided to be sufficient in removing most of the noise in the following tests while reducing filter phase lag.

Next, derivative feedback is added with the proportional gain kept constant at $K_P = 5$ (PD controller). No integral control is used yet. Figure 7.8 shows the responses with the proportional and derivative controller for a range of derivative gains from $K_D = 0.1$ to $K_D = 0.3$. From the measured reaction force, oscillations are observed at $K_D = 0.3$ as well as in the compensator elevator input indicating the gain is too high. $K_D = 0.1$ seems to give the best response where the reaction force stays the closest to zero for a longer period of the input. Compared with the previous proportional only controller, the reaction force matches the demand more closely.

For kinematic compensation (studied in Section 7.3), it is important for the controller to be able to track a demand in reaction force (F_c^*). Integral control should be beneficial in achieving this and reduce error in reaction force over a longer time period. A proportional and integral (PI) feedback controller is studied next with the aim of satisfying this requirement. The proportional gain is kept constant at $K_P = 5$ and the integral gain is varied between $K_I = 4$ and $K_I = 12$. No derivative control is used here. Figure 7.9 shows the responses to the same damped doublet aircraft input. At first glance, it appears the effectiveness of the PI controller is worse than the previous controllers investigated. All responses with integral control appear to drift downwards soon after the initial stabilising control is switched off and the PI controller activated at 9 seconds, as seen on the rig pitch time history plots. However, between 9 and 10.5 seconds, the reaction force is held near zero despite this drift, after which the error in reaction force increases. The stabilising control is reactivated and the rig controller disabled at 13 seconds. Recalling simulations investigating the effects of kinematic constraints discussed Section 4.3.2, divergence was also observed and is primarily caused by drag creating a destabilising moment about the arm gimbal. This divergence is amplified when the aircraft model does not create thrust, as is the case with the Hawk model being tested here. Therefore, this divergent behaviour is to be expected. In the simulated responses where the inertial and aerodynamic loads on the rig were ideally compensated for (perfectly zero tangential reaction force), the aircraft would swing continuously around the spherical constraint. Note in this experiment, the rig arm hitting the physical stop is not apparent in the figure shown since the responses are an average of multiple runs. Depending on the initial rig pitch angle being positive or negative, the aircraft will continue to diverge in that direction. Examples of individual runs where the rig arm strikes the physical stops can be seen later in Figures 7.14 and 7.15.

One way of circumventing the effects of lag and improving overall response is by including a pre-designed feedforward compensator elevator signal for a given aircraft elevator input. The following tests study the response of the Hawk model to a periodic aircraft elevator input signal: a sine wave input of frequency 0.8 Hz (equal to the short-period frequency of the model) and 4° amplitude. Additional aircraft pitch rate feedback is used for stability since the manoeuvre rig and Hawk together are unstable without any control. The controller used for stability is shown

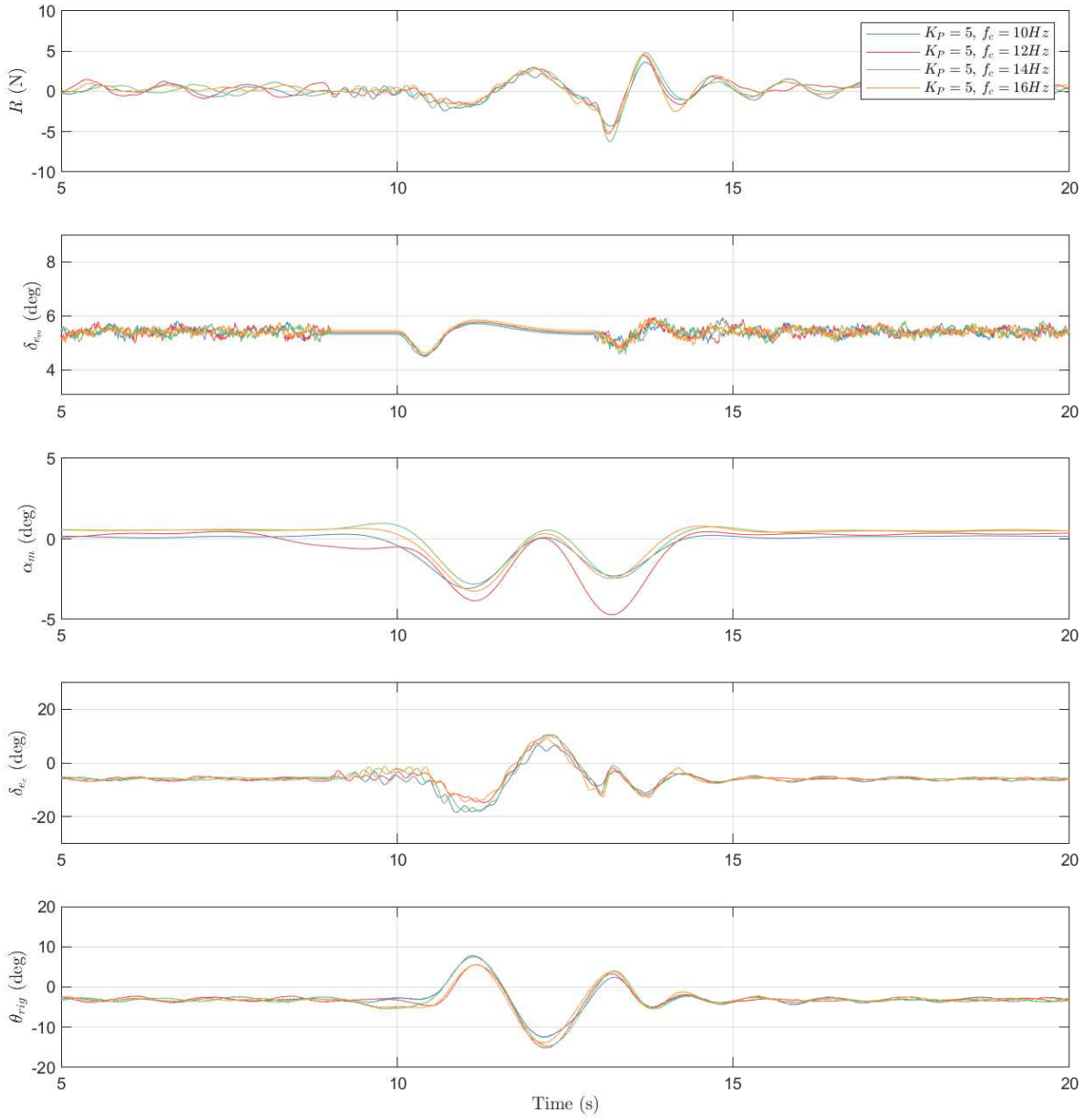

FIGURE 7.5. Effect of second on low pass Butterworth filter cut-off frequency on compensation response.

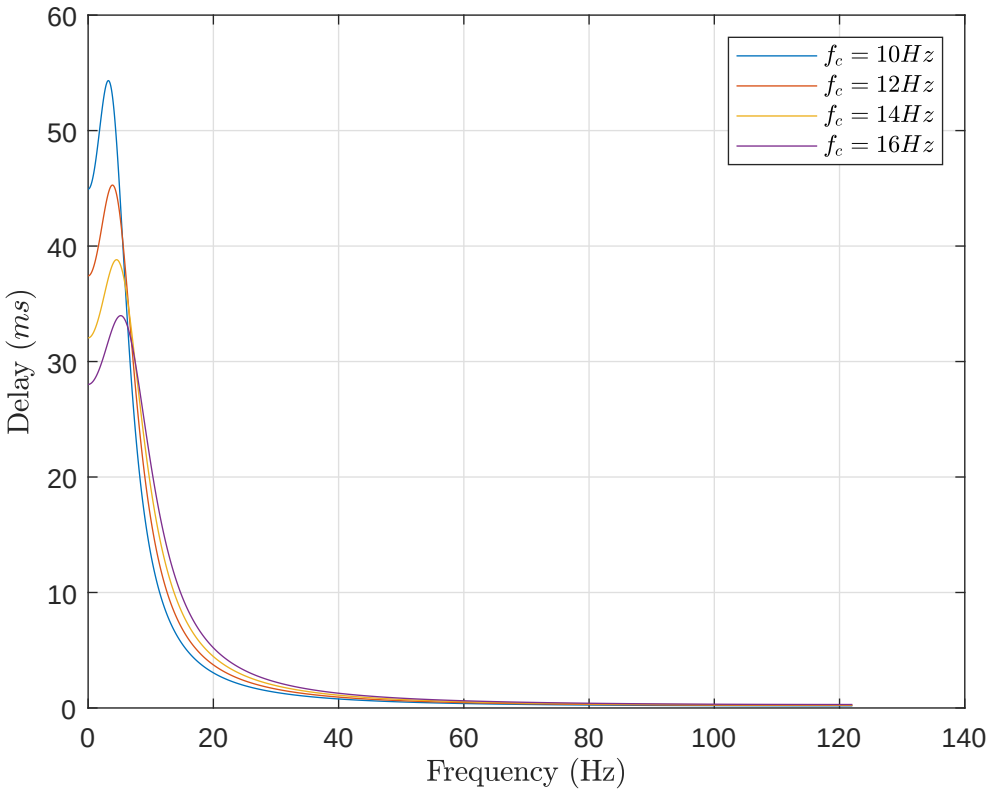

FIGURE 7.6. Delay caused by a second order low pass Butterworth filter.

in Equation 6.6 where $K_{q_m} = 0.15$. A feedforward signal is the same as the aircraft elevator but multiplied by a gain K_{FF}. A diagram of the controller is shown in Figure 7.10. First, the required feedforward gain is found experimentally by searching for the gain at which the lowest tangential reaction force is observed. Figure 7.11 shows a total of eight separate tests where the responses for a range of compensator feedforward gains ranging from $K_{FF} = -0.5$ to $K_{FF} = -3.5$ are studied. From these tests, it can be seen that a feedforward gain of $K_{FF} = -2$ produces the lowest reaction force amplitude. Figure 7.12 shows the resulting variation in the amplitude of the aircraft's angle of attack, which increase as the amplitude of the feedforward signal increases. This indicates that the reaction force between the rig and aircraft model does affect its aerodynamic response.

Next, PI and PID controllers are included in addition to the feedforward signal and any improvements observed. These were tuned based on the Ziegler-Nichols technique where

$$K_P = 0.45K_u \tag{7.6}$$

$$K_I = \frac{0.54K_u}{T_u} \tag{7.7}$$

for the PI controller and

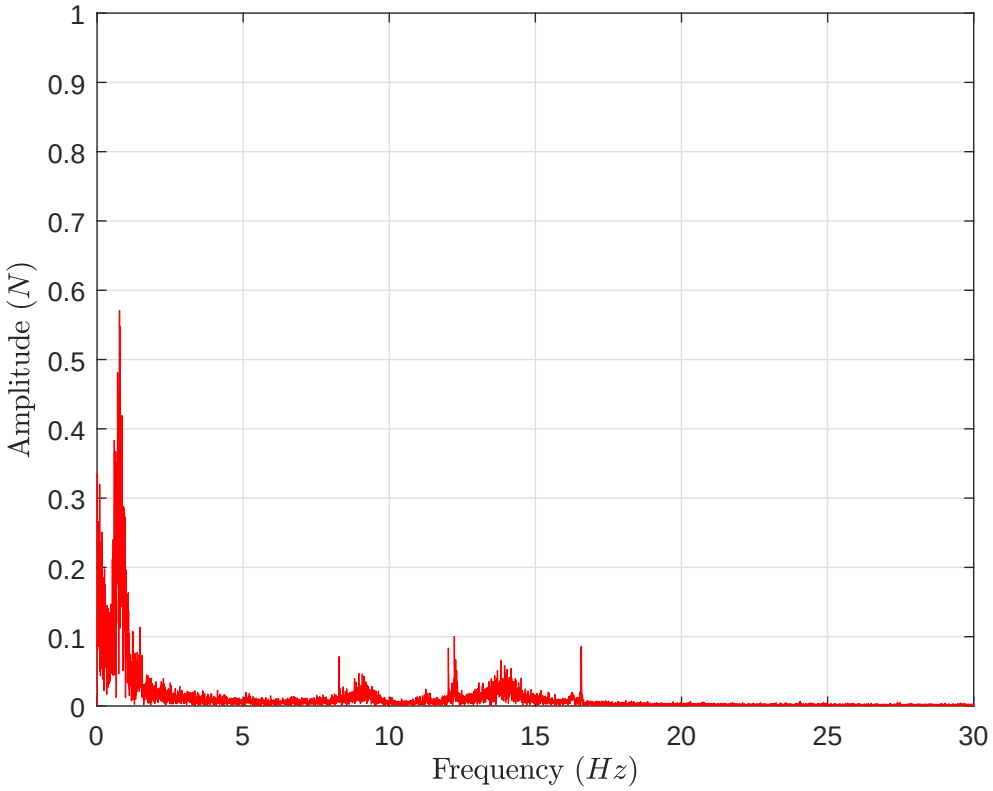

FIGURE 7.7. Frequency content of the measured tangential reaction force (R).

$$K_P = 0.6K_u \tag{7.8}$$

$$K_I = \frac{1.2K_u}{T_u} \tag{7.9}$$

$$K_D = \frac{3K_uT_u}{40} \tag{7.10}$$

for the PID controller, where K_u is the ultimate gain at which stable oscillations are observed, and T_u is the period of those oscillations. Figure 7.13 shows the process of finding the ultimate gain where the proportional gain is varied. No derivative or integral feedback are used for these tests. The parameters found were $K_u = 2.5$ which is the gain at which oscillations are first noticed, and the period is $T_u = 0.26$ seconds. Therefore, the gains for the PI or PID controllers can be calculated, and are shown in Table 7.1.

The responses with feedforward and the Ziegler-Nichols tuned PI/PID feedback controllers for the sine wave aircraft elevator input are shown in Figure 7.14. Multiple runs are shown for each tested controller, and the thick red line is the averaged response of those tests. Note that the feedforward signal is present throughout all experiments. The feedback controllers are

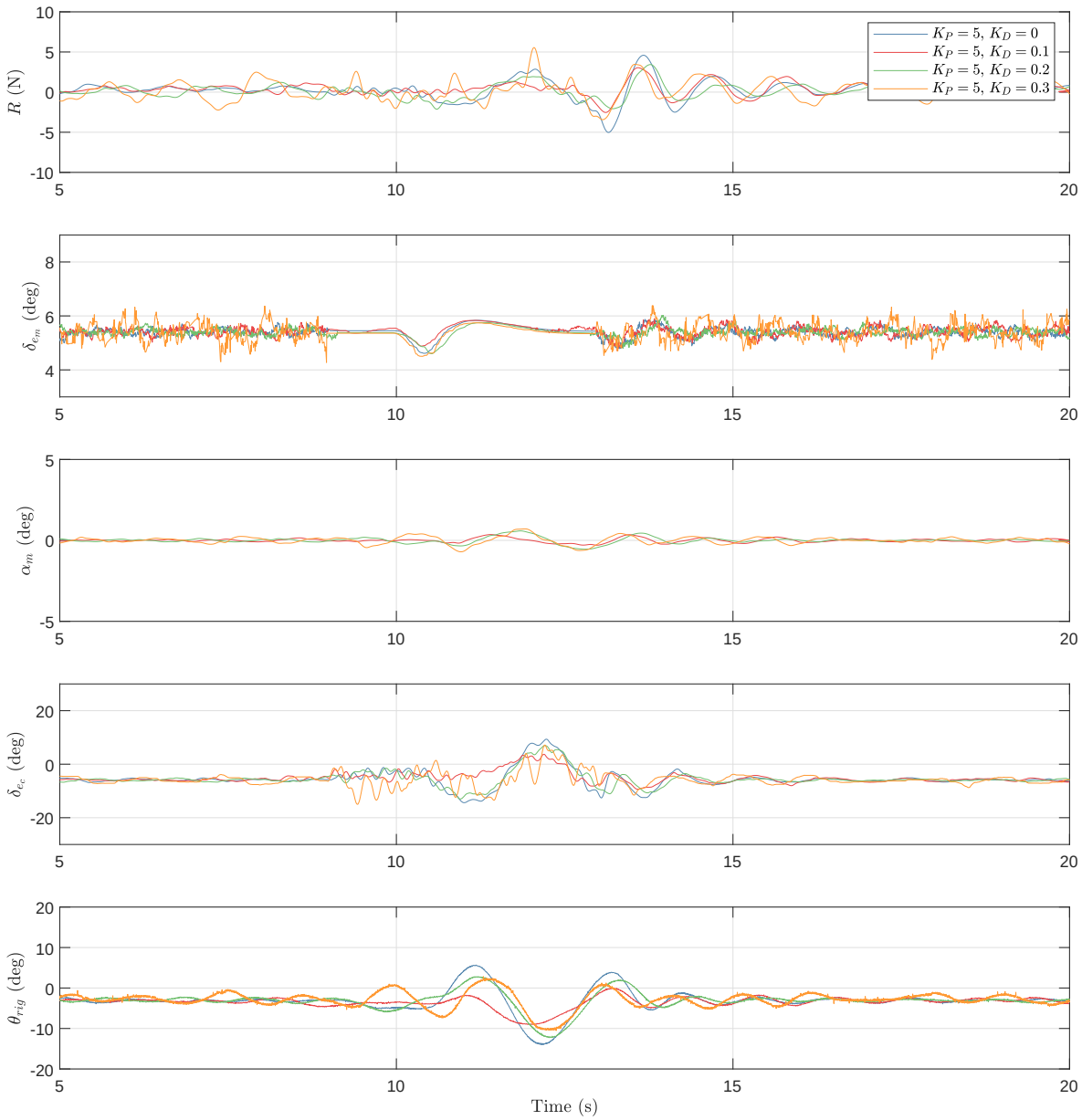

FIGURE 7.8. Aircraft response to a damped doublet elevator input with proportional and derivative feedback for rig inertial and aerodynamic compensation.

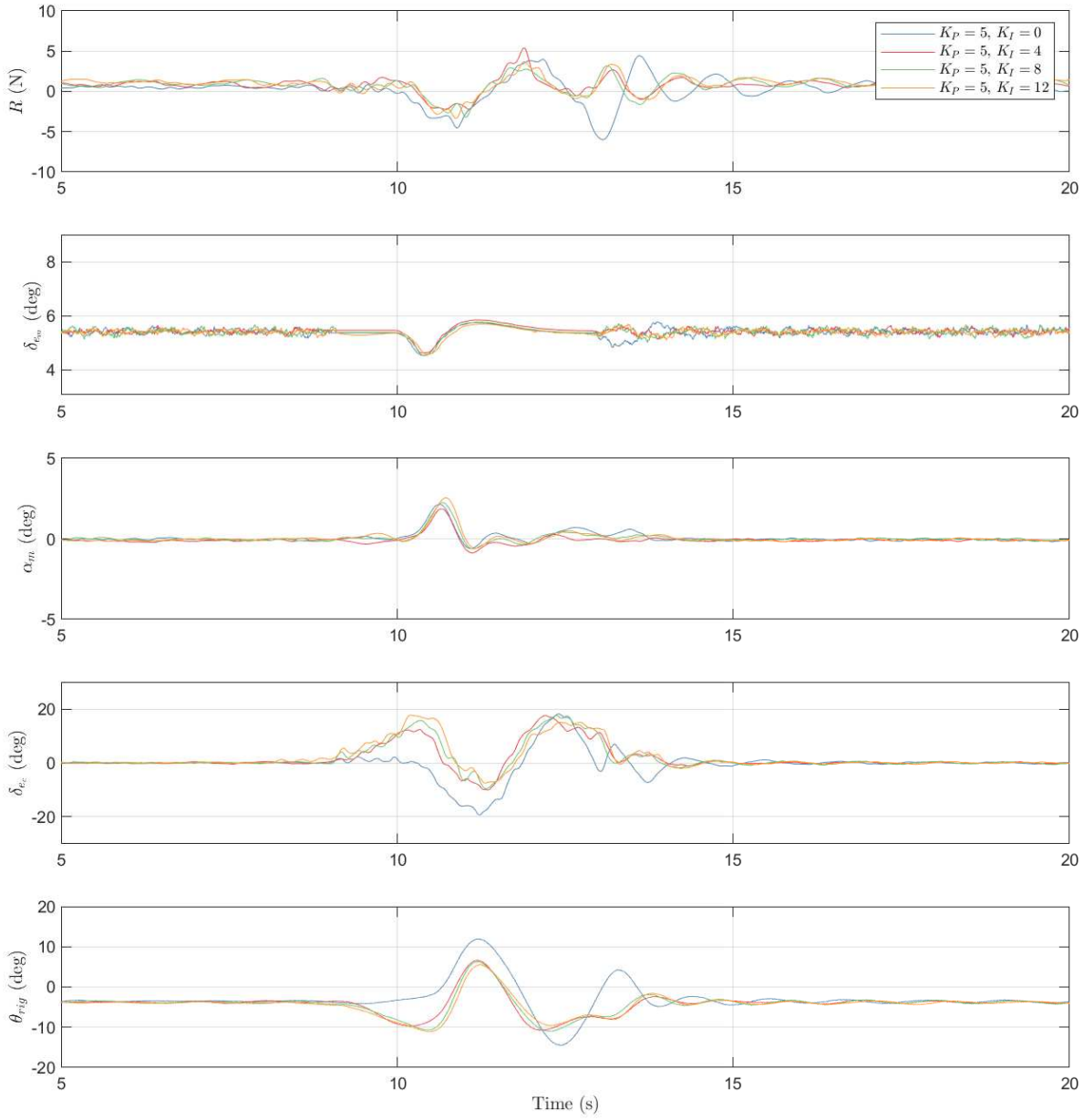

FIGURE 7.9. Aircraft response to a damped doublet elevator input with proportional and integral feedback for rig inertial and aerodynamic compensation.

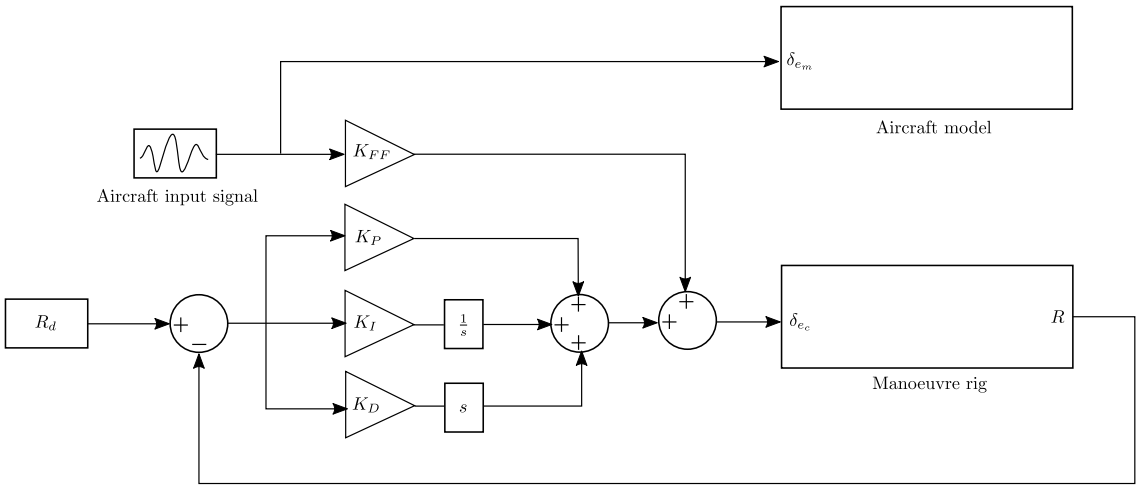

FIGURE 7.10. The feedforward and feedback controller used for rig compensation.

TABLE 7.1. Gains calculated using the Ziegler-Nichols method.

	PI controller	**PID controller**
K_P	1.125	1.500
K_I	5.192	11.54
K_D	-	0.04875

only enabled at 9 seconds and then disabled at 14 seconds for the PI controllers tests, and at 13 seconds for the PID controller tests.

With regards to the controllers, ability to reach the demanded reaction force (the demand being $R_d = 0$ in this case), both PI and PID perform well up to the point at which the rig arm hits the physical stops, indicated by the spike in reaction force. Similar to the PI-only controller tested earlier, drift in heave is observed until the arm hits the gimbal stops. As explained previously, this is to be expected due to the destabilising moment created by drag. Kinematic compensation (attempted in Section 7.3) counters this moment to an extent, preventing significant divergence in heave.

The PID controller with feedforward is tested with the damped doublet aircraft elevator input, and the responses are shown in Figure 7.15. The PID gains used are shown in Table 7.1, and the feedforward gain is $K_{FF} = -4$. Again, multiple runs of the same test were carried out and the thick red line is the averaged response. The behaviour as before is observed: the controller is effective at maintaining a zero reaction force on average despite of the aircraft's drift in heave, which is expected. Differences in initial conditions due to turbulence between test runs cause the aircraft response in heave to differ significantly. The destabilising moment due to drag is the cause since the sign of this moment is the same sign as the rig pitch angle (relative to equilibrium): if the aircraft has a slight positive or negative rig pitch angle initially (at 9 seconds,

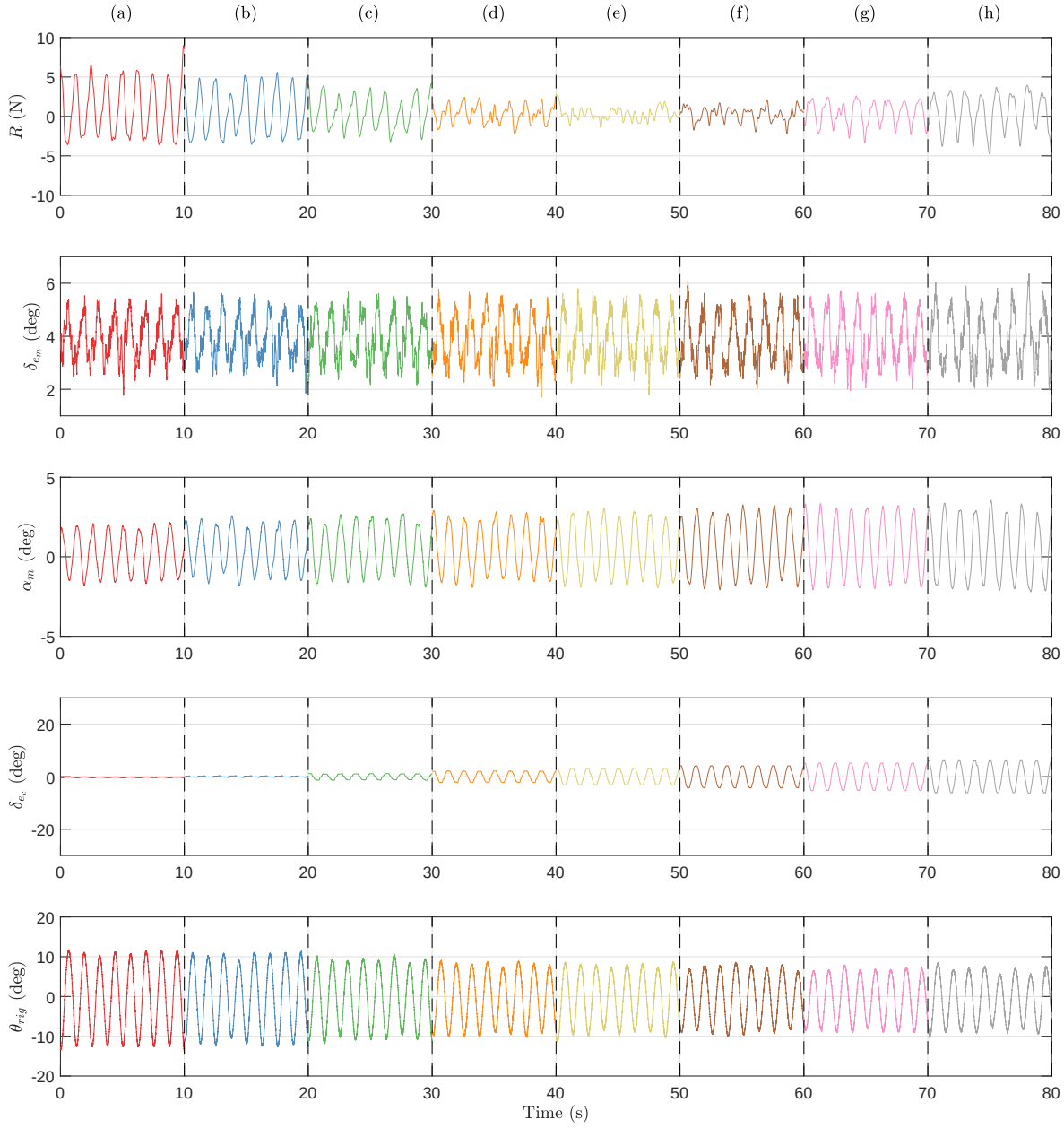

FIGURE 7.11. Tangential reaction force responses to sine wave aircraft elevator input with rig feedforward compensation gains K_{FF} of (a) 0, (b) −0.5, (c) −1, (d) −1.5, (e) −2, (f) −2.5, (g) 3, and (h) −3.5.

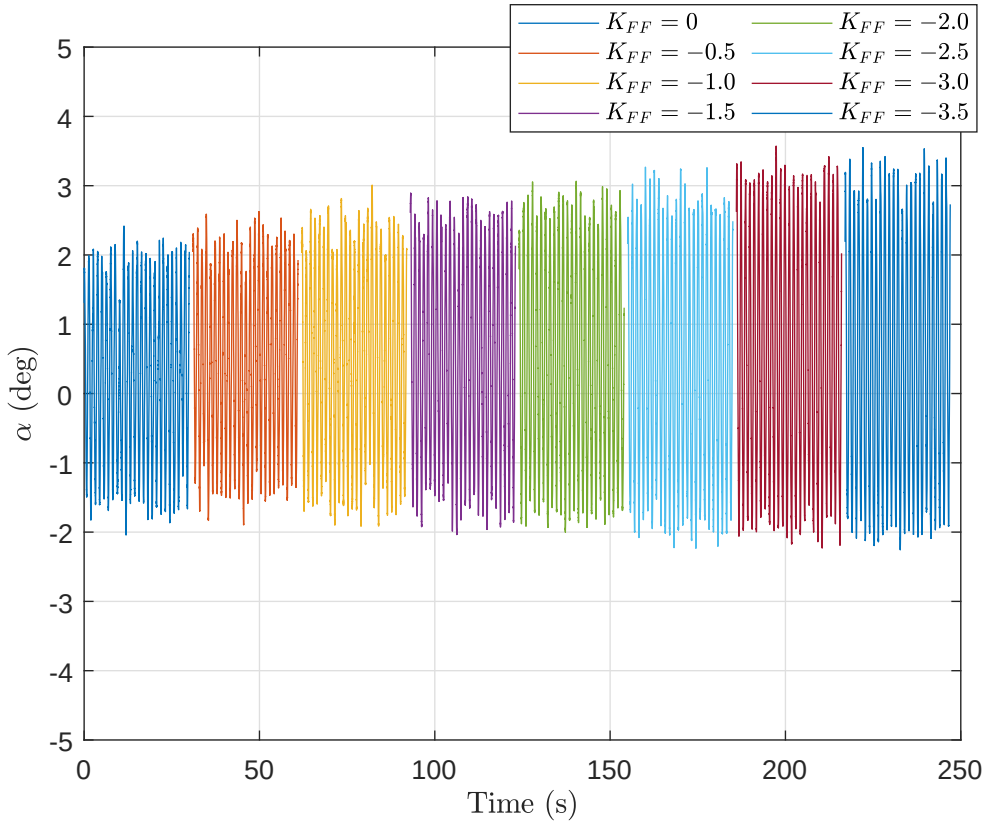

FIGURE 7.12. Change in the amplitude of aircraft's angle of attack due to compensator feedforward amplitude.

when the rig stabilising control is switched off and compensation control is activated), then the aircraft model will continue to diverge in that same direction. This behaviour is observed in simulations as well.

Next, the PID feedback and feedforward controller will be used to test the kinematic compensation concept presented in Chapter 4.

7.3 Kinematic compensation

In this section, the kinematic compensation concept presented in Section 4.3.3 is tested using the PID feedback and feedforward control developed in Section 7.2. Two variations of the kinematic compensation concept were developed. The first being compensation of the kinematic constraint of the rig only ($\mathbf{F}_\mathbf{c}^*$), and the second including added artificial thrust ($\mathbf{F}_\mathbf{c}^{**}$). Through simulations it was observed that there was very little improvement to the aircraft response when also including artificial thrust over kinematic compensation alone. It is highly unlikely to see such minor differences practically especially due to the presence of turbulence causing larger perturbations.

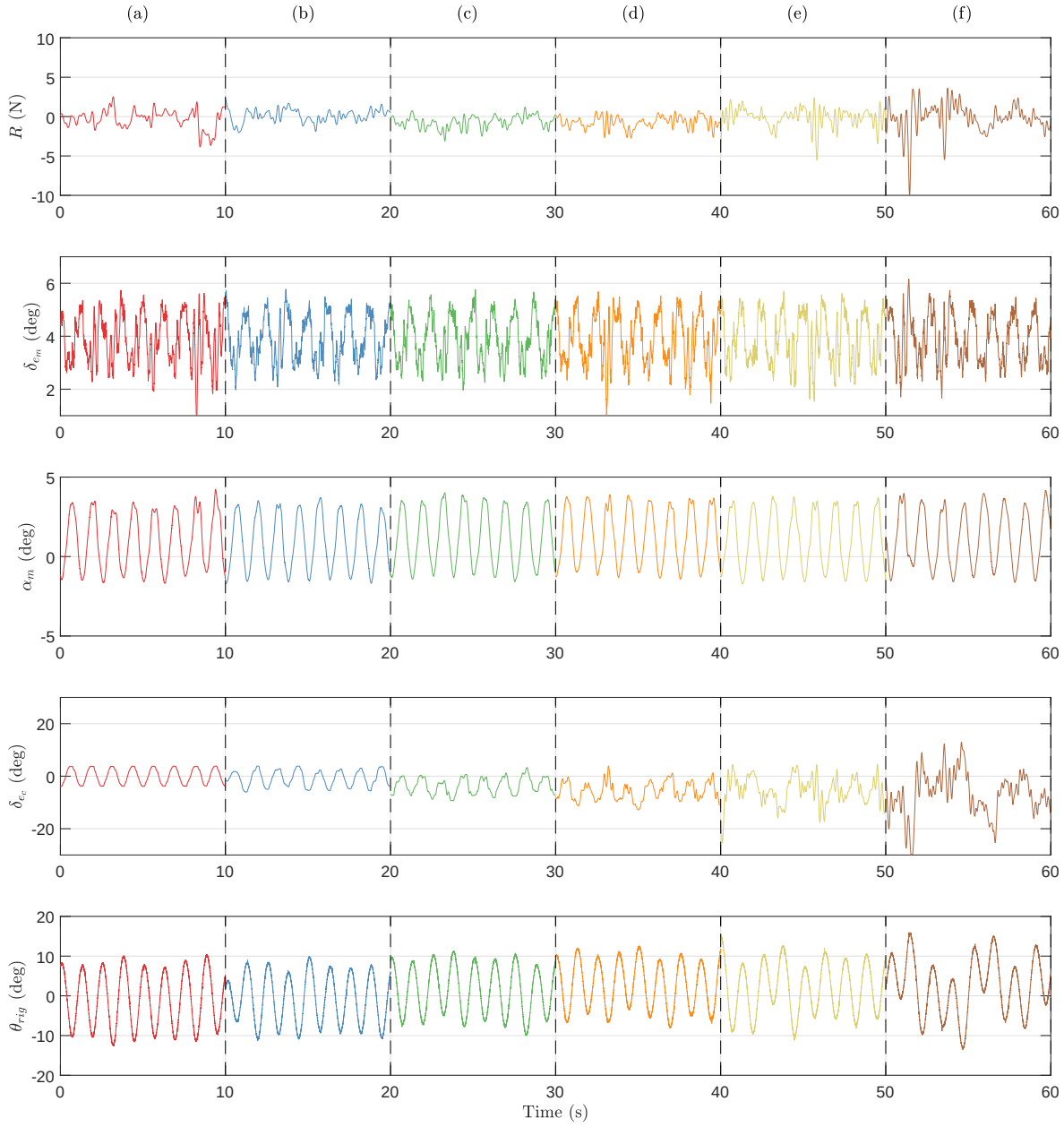

FIGURE 7.13. Responses to aircraft elevator sine wave input with rig compensation controller having feedforward and feedback proportional gains K_P of (a) 0, (b) 1, (c) 2, (d) 3, (e) 4, and (f) 5.

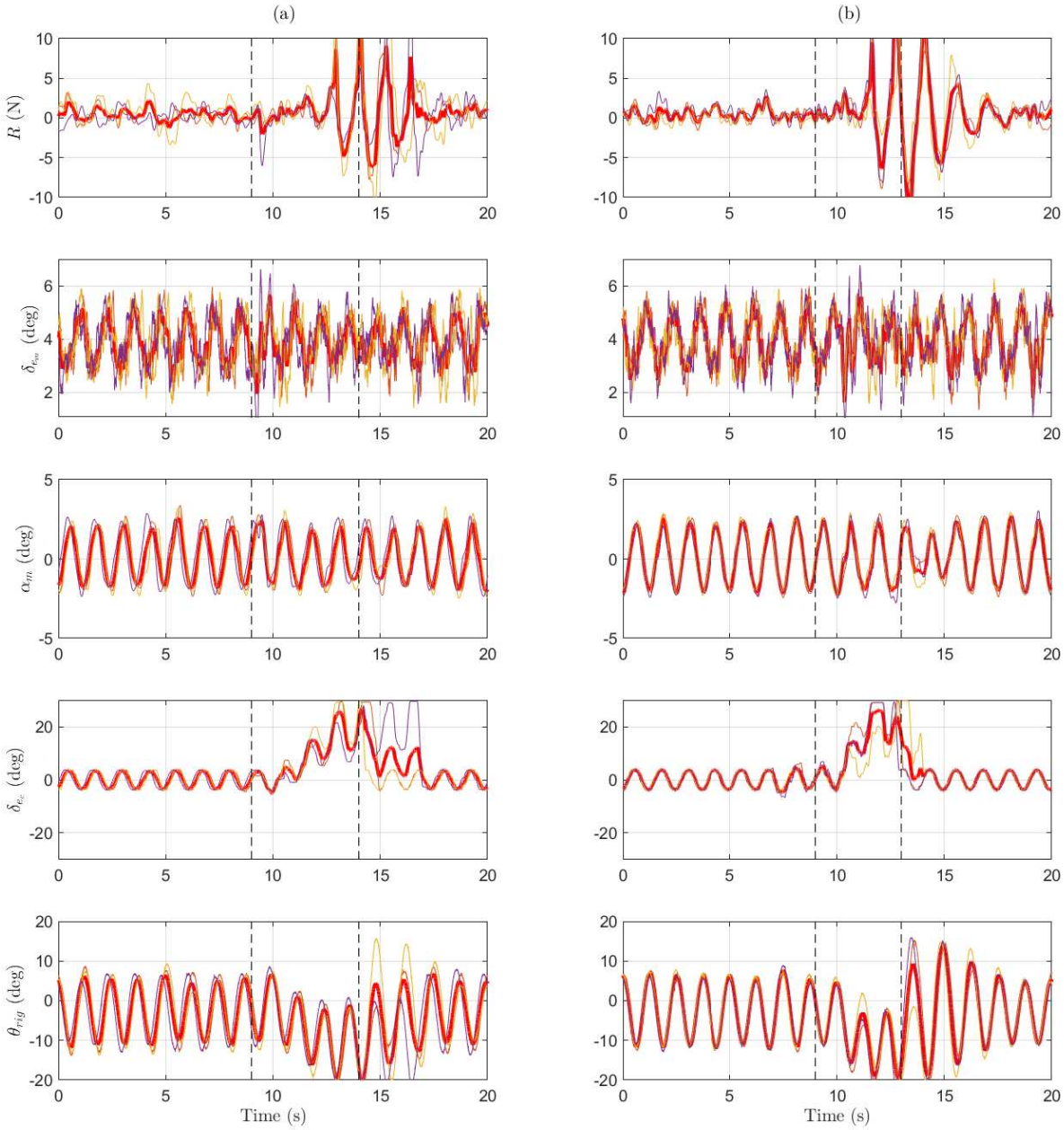

FIGURE 7.14. Responses to aircraft elevator sine wave input with rig compensation controller having feedforward and (a) PI feedback, and (b) PID feedback.

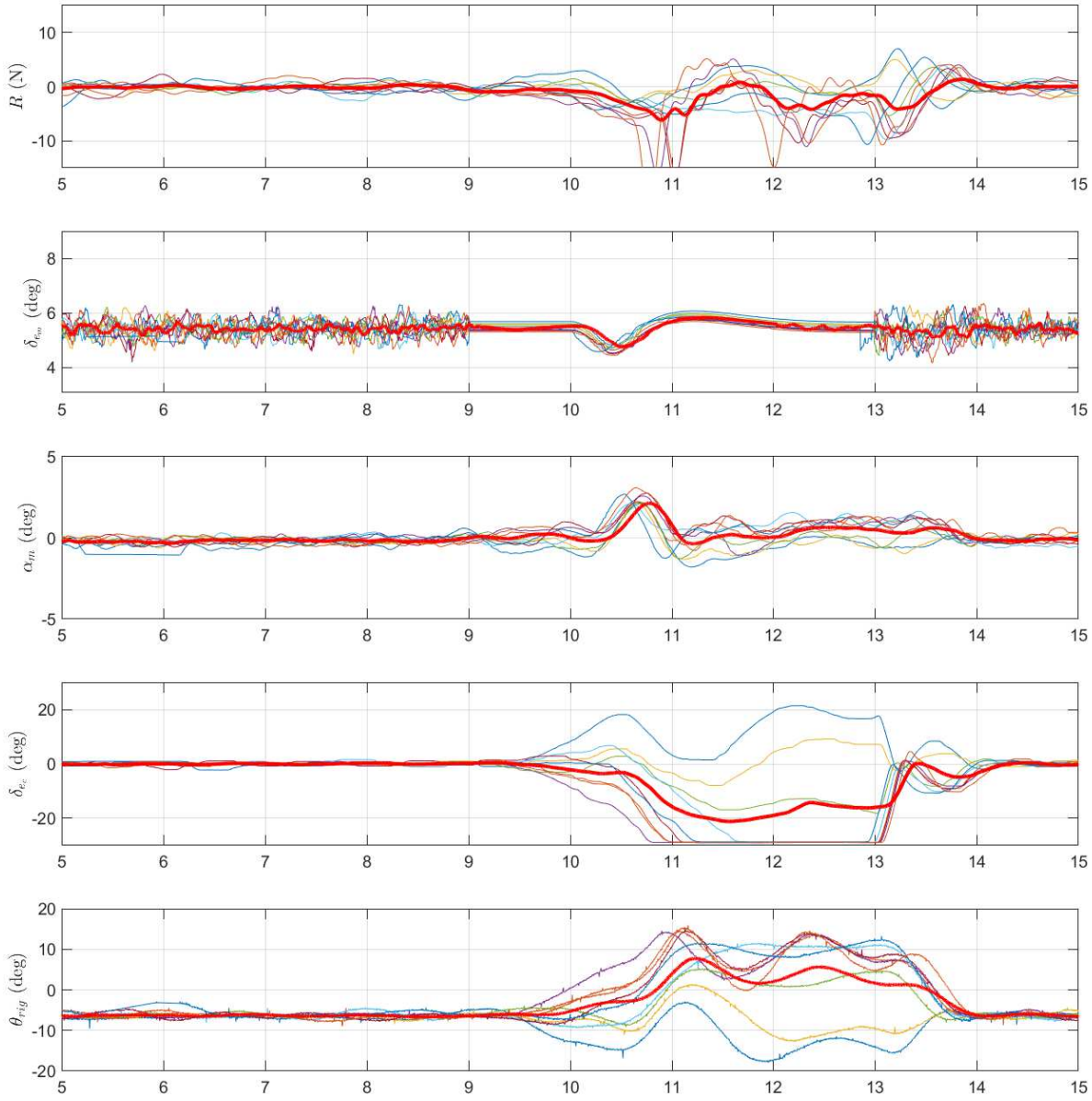

FIGURE 7.15. Responses to aircraft elevator damped doublet input with feedforward and feedback control for rig inertia and aerodynamic compensation (zero reaction force demand).

Therefore, in the experiments to follow, only pure kinematic compensation is focused on. Note that when the required tangential reaction force is applied, inertial and aerodynamic effects of the rig are compensated for implicitly. The success of this concept depends largely on how well the rig can apply the desired tangential reaction force onto the aircraft model.

$\mathbf{F_c^*}$ defined by Equation 4.58 is the demand in reaction force required for kinematic compensation. Therefore, R_d can be defined as:

$$R_d = \mathbf{F_c^*} \cdot \left(A_{rig} \begin{bmatrix} 0 & 0 & 0 \end{bmatrix}^T \right) \tag{7.11}$$

which is essentially $\mathbf{F_c^*}$ transformed into the tangential z direction. A_{rig} is the transformation matrix for the rig. Following the derivation in Section 4.3.3, the required measurements for the calculation are: attitude angles of the rig (measured by arm gimbal encoders), attitude angles of the aircraft model (aircraft model encoders), accelerations of the aircraft model (measured by an Inertial Measurement Unit), and the radial reaction force (measured by the load cell). All measurements are filtered using a second order low pass Butterworth filter with a cut-off frequency of 16 Hz. The calculation of $\mathbf{F_c^*}$ is done in real time within Matlab Simulink.

Figure 7.16 shows multiple repeats of the same test where a filtered doublet input is given to the Hawk model elevators. Kinematic compensation is only active between 9 and 13 seconds, and rig stabilising control active for the remainder of the time in order to prevent perturbations of the system caused by turbulence, and keep initial conditions at 9 seconds as consistent as possible. The red thick line shows the averaged response across all runs. The plots in order from top to bottom show: the demanded reaction force, the error between the demanded and measured reaction force, Hawk elevator input, Hawk angle of attack, compensator elevator response, and the rig pitch angle.

Studying the demanded the reaction forces, the maximum demand recorded is just below 2 N and the average is just below 1 N. These are in the same magnitude as the variations in reaction force caused due to turbulence, however, averaging numerous runs of the same test can be used to distinguish between response due to turbulence and compensation. The magnitude of the demanded reaction force almost follows the trend of the rig pitch angle angle. This can again be thought of as the compensation controller working to counter the moment created by drag about the arm gimbal rotation point, which is proportional to the rig pitch angle. The reaction force error histories shown in the second plot show that a significant error still develops for the aircraft input used. Ideally the error should remain at zero. This indicates the compensation controller still needs improving. A possible way of improving the controller to better maintain an error closer to zero could be to improve the pre-designed feedforward signal; investigating the addition of a lead component to the feedforward signal to take into account slower compensation elevator actuation speed, deflection of the rig arm delaying the transfer of the reaction force from the compensator to the aircraft model, and using the aircraft translation/rig pitch response to determine the feedforward signal rather than aircraft elevator input signal. Another option is

designing a phase lead-lag compensator to tailor the system's frequency response; however, the implications of using it, such as potential amplification of noise, needs to be investigated. These ideas are not explored here due to time constraints, but should be studied in the future.

Compensator control power is also an issue since it can be seen to saturate at about 11.5 seconds on average. Again, the required control power is dependant on the magnitude of the moment due to drag about the arm rotation point, which in turn is dependant on the heave translation distance of the aircraft model and the magnitude of drag itself. A smaller translation in heave means the moment arm is shorter and there a smaller drag moment. This indicates a limitation on the magnitude of translation in the manoeuvre that can be performed on the rig. The magnitude of drag is dependant on the aerodynamics of the aircraft model being tested. A lower drag implies a lower compensator control power requirement or a larger range of manoeuvre translations that can be performed on the rig. Increasing the control power of the compensator will be beneficial for all the compensation covered by this concept (rig inertia, aerodynamics, and kinematic constraint) which may be achieved by moving the rig's compensator further aft, but would increase the total inertia of the rig. This trade-off needs to be further investigated in the future.

Despite the error in reaction force, several indications can be observed showing that the compensation is effective. Two aspects of the response confirm that the destabilising moment due to drag has been cancelled to at least some extent. The first main observation is that not a single test run hit the gimbal stops: the aircraft models tends to settle at a new rig pitch angle of about 12° once the input is complete. The second is that there is much higher repeatability in the translation response as seen by the rig pitch time histories; the destabilising drag moment present without kinematic compensation causes the translation response of the aircraft model to be extremely sensitive to its initial conditions. In those cases, the direction of divergence is highly dependant on the sign the rig pitch angle relative to the equilibrium point, as seen in Figure 7.15.

In order to validate the response to kinematic compensation, the same aircraft input used here is applied on the simulated Hawk aircraft model and its response is shown in Figure 7.17. In this simulation, ideal kinematic compensation is assumed where the exact desired tangential force $\mathbf{F}_\mathbf{c}^*$ is applied, i.e. zero reaction force error. Very similar behaviour with both the physical and simulated Hawk models can be seen: the demand in reaction force is similar both in terms of shape, and the simulated translation response also settles at a higher position. The magnitude of the demanded reaction force is large since the translation of the model is also larger in comparison to the experiment. Note that the compensation technique assumes the centre of gravity (c.g) of the aircraft model is located at the rotation point through which the tangential reaction force acts. Therefore, aircraft pitching moments created as a result of a c.g offset cannot be compensated for. This is true for all moments including gimbal friction.

It is still uncertain as to whether the motion response of the Hawk model is comparable to its actual free-flight response. Comparing with computational simulations alone does not truly

indicate that an improvement in the match with free-flight has been achieved, due to errors in identified parameters and modelling, for example. In the ideal case, one would compare the response of the aircraft model on the manoeuvre rig with actual free-flight responses of the same aircraft. This should be a goal carrying on to further validate the effectiveness of the kinematic compensation concept.

7.4 Summary

This chapter studies the experimental application of kinematic compensation using a practical approach. The compensation technique is largely dependant on the ability of the rig in controlling the reaction being applied onto the aircraft model. The objective of the controllers designed here was to apply a demanded tangential reaction force on the aircraft model. A demand of zero tangential reaction force is used for the compensation of the rig's inertial and aerodynamic effects, and a demand of $\mathbf{F}_\mathbf{c}^*$ reaction force also includes kinematic compensation. Sensitivity of the aircraft's response to initial conditions combined with random perturbations created by turbulence made it difficult to assess the effectiveness of a given controller. Therefore comparisons were made of averaged responses of numerous runs of the same tests in order to mitigate these random variations. More than 20 runs per test may be sufficient.

Several feedback controllers were tested: P, PI, PD, and PID. A combination of feedforward and a feedback PID controller tuned using the Ziegler-Nichols method was shown to be the best out of the controllers tested in terms of demanding the required tangential reaction force. The design of the final controller still needs further iterating for better reaction force control. Tailored feedforward signals may be required for specific aircraft inputs and responses to achieve the best results.

Despite non-ideal reaction force control, improvements to the aircraft response were observed mainly as a result of the disappearance of the divergence caused by drag, which is the main objective of the kinematic compensation concept derived in this work. Compensation also drastically improved repeatability of tests especially in terms of translation response. This was validated using computational simulations.

Limitations in compensation were identified and suggestions for improvement presented. Limited rig compensation control power implied a limitation to the overall magnitude of the translation response of the aircraft model. For the damped doublet input tested here on the Hawk model, the compensator elevator saturated when the aircraft translated a distance of about 0.215 m. Increasing the control power of the compensator will benefit compensation. This may be achieved by moving the rig's compensator further aft along the rig arm. It is also important for the model's c.g. position to match the gimbal/rotation point to prevent additional pitching moments created due to a c.g offset. Friction in the aircraft gimbal also cannot be compensated for. The effectiveness of the compensation concept in experimentally improving the match of the

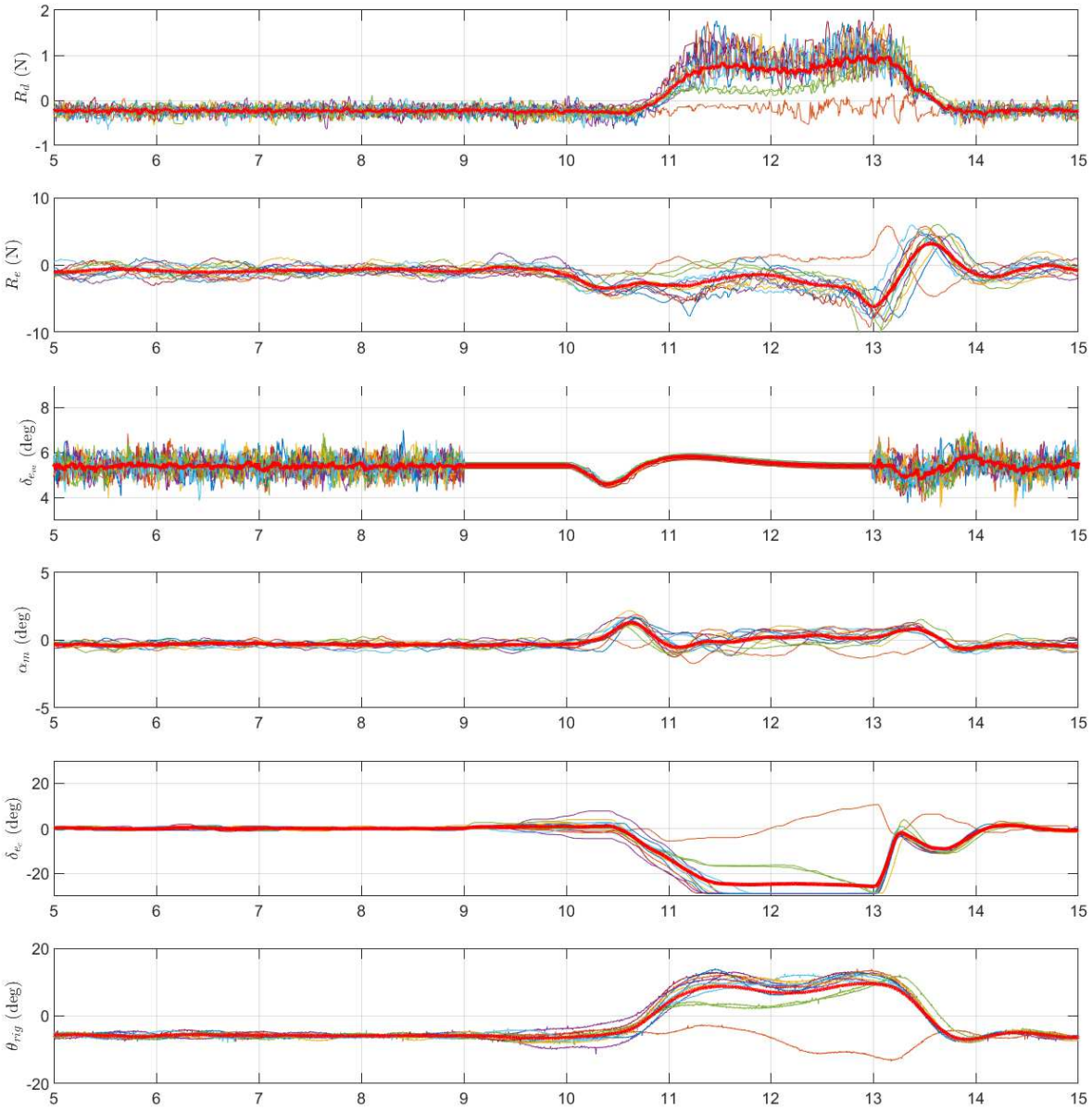

FIGURE 7.16. Kinematic compensation by demanding a tangential reaction force of $\mathbf{F}_\mathbf{c}^*$.

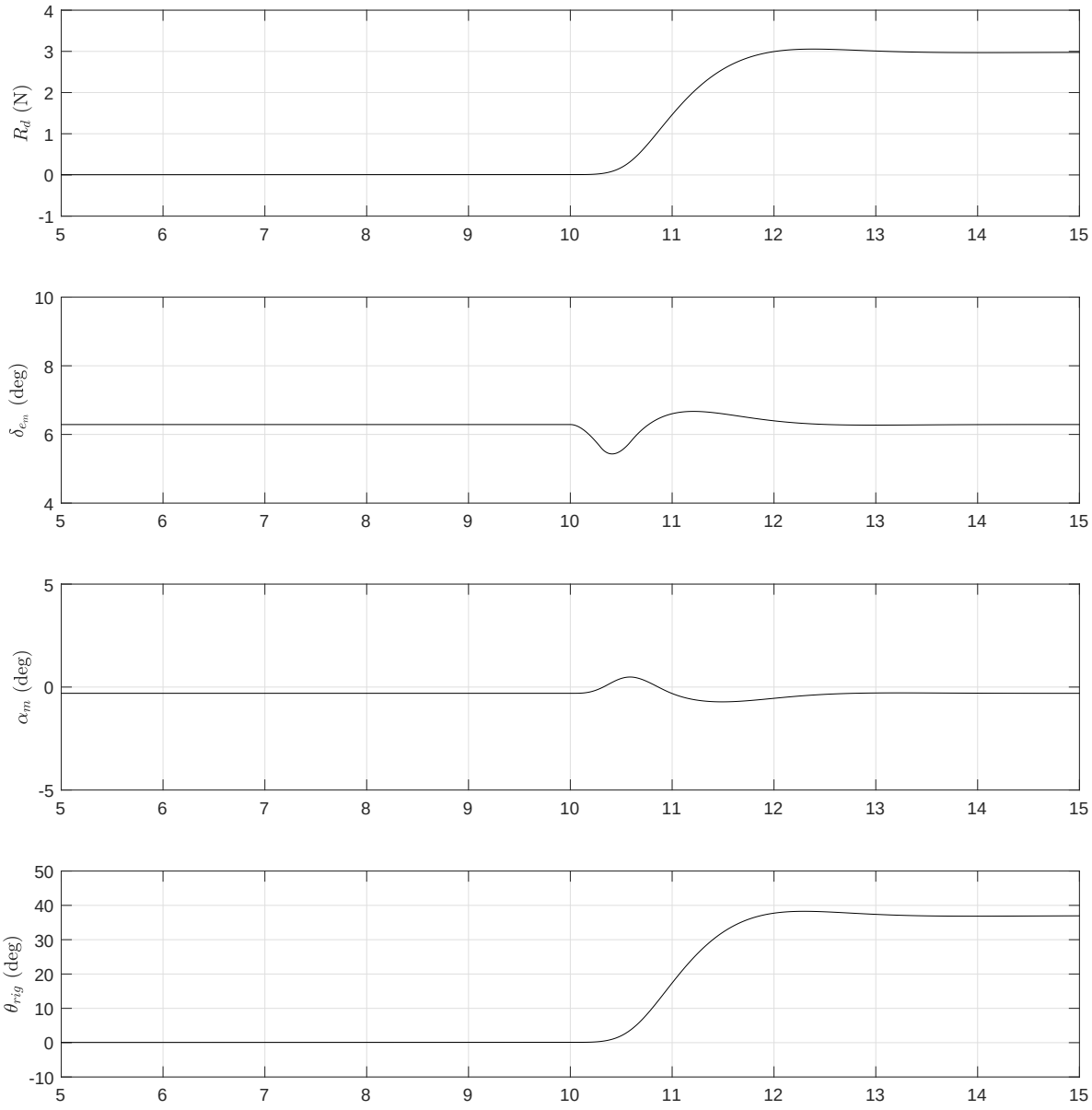

FIGURE 7.17. Simulated ideal kinematic compensation for the Hawk model.

responses in the tests carried out here with free-flying responses could not be truly assessed. This can only be achieved by having a second identical free-flying aircraft performing the same manoeuvre in order to gauge the viability of using the manoeuvre rig for physical free-flight simulation, which can be a future goal.

The compensation concept has only been applied in the longitudinal sense so far. This concept can be extended to lateral-directional and combined multi-DOF motions in the future, with the objective of achieving good physical simulation of either specified or arbitrary manoeuvres in multiple degrees of freedom.

CHAPTER 8

CONCLUSION AND FURTHER WORK

8.1 Introduction

This chapter will summarise the primary findings of the work carried out here. Progress has been made with regards to the novel concept of rig compensation for achieving true free-flying responses of an aircraft model on the manoeuvre rig. This has been achieved through both computational simulation and experimental demonstration. New applications of the manoeuvre rig, such as performing conventional type tests and investigation of stall hysteresis, were demonstrated, which was made possible with the implementation of a load cell. This work has been successful in extending the overall capability of the manoeuvre rig as a wind tunnel testing platform for subscale aircraft models.

Suggestions for each topic will now be given with respect to further improvements and the directions in which this work should be carried forward.

8.2 Mathematical modelling of the manoeuvre rig

The mathematical model developed in Chapter 3 has been instrumental throughout the work carried out here. It is a full nonlinear model of the manoeuvre rig and aircraft system and can model motion in any number of DOFs that are of interest. The constraint equations allow the rig or aircraft model to be locked similar to the physical rig. These constraint equations can be easily enabled or disabled within the Matlab/Simulink environment, making the simulation process very streamlined during the investigative studies.

The full model was used for the estimation of load cell requirements by simulating the rig at extreme test cases. This work is presented in Chapter 5. The equations allow for the extraction of the reaction forces experienced by the load cell, which has been very useful for this purpose.

The method also allows for the creation of imaginary constraints such as the planar and spherical constraints. These constraints were used in Chapter 4 to study their effects on longitudinal and lateral-directional responses of the aircraft model.

Aerodynamic load measurements taken from static and dynamic wind tunnel tests on the manoeuvre rig can be introduced into the equations of motion as external loads. The aerodynamics modelled as multidimensional lookup tables can accurately represent the nonlinearities observed on the Hawk model. The models for gimbal friction and servo actuators have also shown good representation of actual responses.

A possible extension for the modelling technique would be to model body deformations. This can be especially useful for the rig arm since elastic deformation can delay the transfer of loads from the compensator at the rear of the manoeuvre rig to the front where the aircraft model resides. Taking rig arm deformations into account when designing the controller for rig inertial, aerodynamic and kinematic compensation may improve reaction force control. The derivation of the kinematic of deformable bodies can be found in Reference [63].

8.3 Kinematic rig effects

The investigations conducted on effects of kinematic constrains on the motion of an aircraft model were presented in Chapter 4. The following are the generalised findings from the simulations performed

1. The response of a planar constrained aircraft matches the response of a free-flying aircraft at constant ground speed.

2. The difference between the response of a planar constrained aircraft with that of free-flying aircraft with constant thrust is caused due to the restriction in forward velocity.

3. Long period responses such as the phugoid mode cannot be replicated while constrained due to limitations in possible variations to aircraft velocity. This is true for both planar and spherical constraints.

4. The larger the radius of the spherical constraint, the closer the responses are to free-flight responses.

5. The spherical constraint applied an added effect where the total aircraft force in the forward direction affects model translation. This is due to the force creating a moment about the sphere centre. As a result, if the aircraft model does not create thrust, the magnitude of the force is much larger and dominated by drag. This leads to divergent behaviour of the aircraft model.

6. The kinematic compensation concept presented can be used to prevent the divergent translation of the model by countering the destabilising moment created by drag. This can

be achieved by applying a tangential reaction force onto the aircraft model. This concept requires the measurement of the radial reaction force. The concept improves the response of the spherically constrained aircraft to match that of the free-flying aircraft.

7. The improvement to the constrained aircraft responses were reflected in the estimated perceived aerodynamic derivatives.

8. The kinematic compensation concept only improves the translation response of the aircraft model. Responses with mainly rotational motion, such as the roll subsidence mode, are unaffected by compensation.

9. The smaller the translation of the aircraft model while spherically constrained (with compensation) the closer the match in response with a free-flying aircraft model will be. This is again due to the inherent limitation to aircraft velocity caused by the constraint.

10. An additional concept for artificially applying the vertical component on thrust was presented. This showed improvement to the match in initial conditions required for trim. However, the improvement to the transient responses were minor.

11. Friction within the arm gimbal can be compensated for, however, friction in the aircraft gimbal cannot be. Therefore it is important to have low aircraft gimbal friction in order for the response to better match with free-flight. Moments created as a result of an aircraft c.g. position offset from its rotation point also cannot be compensated for. It is important to keep this offset as small as possible.

8.4 Load cell implementation and application

The process of defining requirements for the load cell, choosing a load cell, and its physical and software integration with the current manoeuvre rig system was presented in Chapter 5. The implementation of the Mini45 load cell has been successful. The total inertia of the rig has increased by 74% in roll, 15% in pitch, and 36% in yaw.

The new inertial and mass distribution properties of the rig has caused a new self-induced coupled oscillation in heave with the Hawk model. This was studied in Chapter 6. Use of the load cell for conventional wind tunnel testing of the Hawk model was also demonstrated in Chapter 6. Good agreement with most of the previously estimated stability derivatives were seen. Comparisons could not be made for drag, since it cannot be estimated via parameter estimation techniques as it cannot be mathematically modelled; both lift and drag create a moment about the rig arm gimbal. However, drag can now be measured directly using the load cell. The 2-DOF forced oscillation dynamic tests have been presented for aircraft pitch and heave. This can easily be repeated aircraft yaw and rig yaw, as well as in roll to identify the lateral-directional damping derivatives.

Additional applications of the manoeuvre rig using the load cell were also explored. The first related to the investigation of stall hysteresis observed on the Hawk model. Characteristics of the hysteresis were seen to be dependant on the number of DOFs the rig is configured in: in 1-DOF aircraft pitch only, or 2-DOFs aircraft pitch and rig pitch. Releasing the rig pitch DOF reduces the gap between the stall angles of the two wings, and increases the maximum lift. The cause behind these changes are still unclear and needs further investigation, although it is evident that the flow structure responsible for the hysteresis is very fragile.

Secondly, a method to create self-induced oscillations in 2-DOF aircraft model roll and yaw was derived. The stability of this oscillation depends on the order of aircraft gimbal rotation, and the total pitching moment of the aircraft model. The oscillation only appears as a result of the aircraft gimbal being locked in pitch. This was demonstrated experimentally, however their responses were not used for parameter estimation. The identification of the lateral-directional aerodynamic derivatives can be a future task to perform.

The magnitude of the current measurements of the Hawk model's drag is overestimated due to the presence of the link attaching the load cell to the aircraft model (portion of the aircraft gimbal) being in contact with the wind tunnel airflow. The measurement of the extra drag caused by this link cannot be taken simply by running tests without the aircraft model. This is because a portion of the aircraft gimbal resides within the aircraft, which would now also be in direct contact with the airflow if the aircraft was not present. A possible solution is as follows: since the cover on top of the Hawk is removable, a new support mount can be created that will hold the aircraft model from above, with the rig inverted in roll by 180°. The aircraft will not be attached to or be in contact to its gimbal, it is merely held in place from the second support. This will prevent the aerodynamic loads of the aircraft from being transferred onto the load cell. Therefore, the measured loads from the load cell are caused by the link only, which can be subtracted from the total drag to calculate the drag created by the aircraft only. A diagram of this process is shown in Figure 8.1.

Another issue is the aerodynamic interference caused by the link and the cut-out beneath the Hawk model. This can be measured as follows. The aircraft model would be mounted up-side-down on the manoeuvre rig with the rig itself rotated by 180° in roll. The second support can hold a dummy aircraft gimbal which is not attached to or in contact with the aircraft. Two tests can be carried out: first with the Hawk cut-out open with the dummy gimbal positioned inside, and a second where the dummy gimbal is removed and the cut-out covered. The difference in measured loads will be caused by the aerodynamic interference. A diagram of this process is shown in Figure 8.1.

Drift in load cell measurements were not noticeable during the tests carried out, but should be investigated. If drift is present, they can be taken into account during testing. Effect of ambient temperature on measurements should also be considered, since the temperature within the wind tunnel rises when it is in use. The natural frequencies of the updated rig arm also need to be

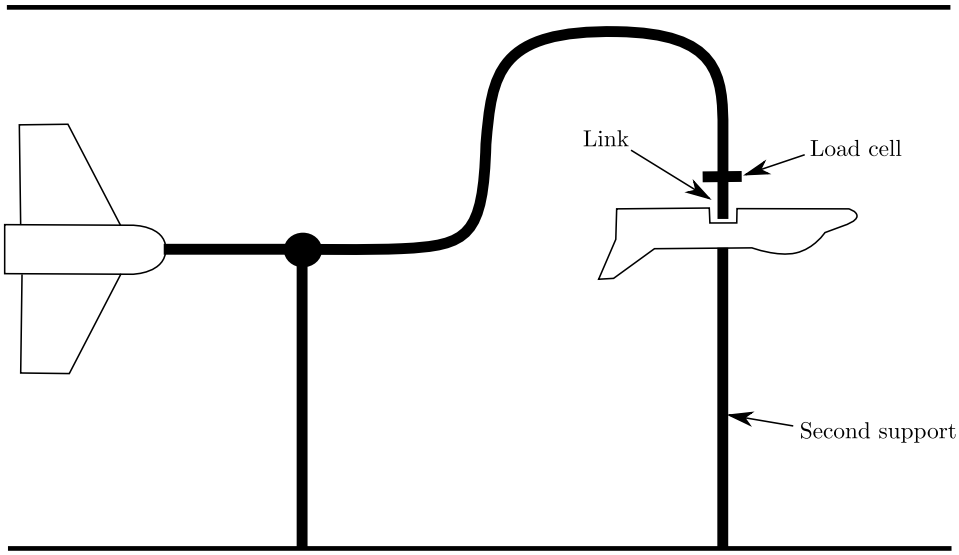

FIGURE 8.1. Possible method to measure drag created by the link connecting the load cell to the aircraft model.

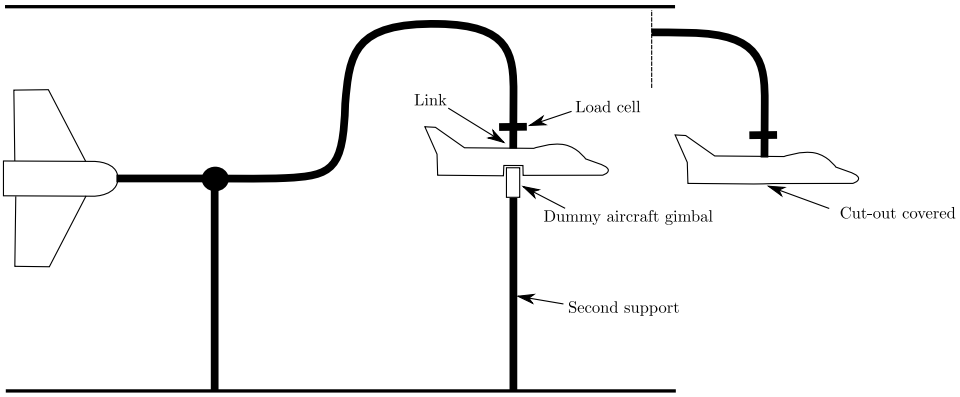

FIGURE 8.2. Possible method to measure aerodynamic interference caused by the link and aircraft cut-out.

re-estimated in order to avoid tests from exciting those modes.

8.5 Experimental compensation

Experimental application of rig inertial, aerodynamic, and kinematic compensation was demonstrated in Chapter 7. The main findings are summarised as follows:

1. The ability of the rig in precisely controlling the tangential reaction applied on the aircraft model is crucial for the success of the compensation concept.

2. Demanding a zero tangential force, i.e. compensating the rig's inertial and aerodynamic effects only, produced responses that match the observations of simulations performed in Chapter 4: the motion diverges in translation due to the unstable moment about the arm's gimbal created by drag.

3. Demanding a tangential force of $\mathbf{F}_{\mathbf{c}}^{*}$, i.e. compensating for rig's inertial, aerodynamic and kinematic effects, was successful at negating the divergent behaviour. This observation matches behaviour seen in simulations performed in Chapter 4.

4. Aircraft responses are sensitive to initial conditions, especially if kinematic compensation is not used where small perturbations caused due to turbulence can result in large differences in the translation response.

5. PID feedback and feedforward control performed decently in controlling the tangential reaction force, although improvements are still required.

Overall, the work done here has made significant progress towards mitigating effects of the rig, thus making the aircraft's motion more representative of free-flight. More work still needs to be done with regards to improving the rig's capability for reaction force control. This can be achieved in several ways: the first is to further iterate the design of the controller, and the second is to increase the control power of the rig's aerodynamic compensator. Using feedforward control showed good potential even with the presence of lag. The feedforward signal can be tailored to the specific manoeuvre to be performed.

Other control techniques can also be explored such as Linear Quadratic Regulator (LQR). A linear model of the rig has been derived in Section 3.2. This model would need to be extended to have the reaction force between the aircraft model and rig as a measured output, as it is done on the full 3D nonlinear model, with which a controller can be created. The optimum controller gains can be easily obtained in Matlab using the "$lqr()$" function. However, the cost function for LQR control needs to be investigated with regards to which states are prioritised and the available controllability of the system in order to best control the reaction force. The resulting controller can then be applied onto the nonlinear model and evaluated, and then tested on the actual manoeuvre rig.

Increasing the control power of the compensator will be beneficial to all compensation covered by this concept (rig inertia, aerodynamics, and kinematic constraint) which may be achieved by moving the rig's compensator further aft, but would increase the inertia of the system. This trade-off needs to be further investigated in the future. Reference [11] has suggested several more possible ways to increase the control power of the compensator, which are still relevant for this work. To summarise those suggestions:

1. Increase the span and/or surface area of the compensator wings.

2. Using separate inboard and outboard control surface for each wing. Inboard surfaces can be used for trim, while the outboard can be used for control purposes.

3. Faster control surface actuators.

Another avenue of interest is the possibility of using the reaction force control to change the perceived mass of the aircraft by demanding a reaction force opposite to its weight. This may prove to be especially useful in meeting dynamic scaling requirements (such as Froude number similitude) since the mass of the aircraft does not have to be hard requirement when designing the physical model.

The compensation concept has only been applied in the longitudinal sense so far. The next logical direction is to extend this concept to lateral-directional and combined multi-DOF motions in the future. Note that for multi-DOF manoeuvres, the demanded reaction force vector may not lie in-line with the attitudes of the rig. Therefore, the controller used will need to take into account the rig's attitudes when commanding the compensator control surface to ensure the applied reaction force is in the right direction. Rig roll compensation, such as the studies done in Referece [11], to make the rig follow the aircraft in roll will play a vital role.

It may be very beneficial to directly measure the reaction forces created by the compensator to identify the magnitudes of the forces and any nonlinearities present. This will prove useful in creating models that could be used for advanced control laws. One possible way that this could be done is by creating a supplementary rig that can hold the manoeuvre rig by the aircraft gimbal at different stationary attitudes. This supplementary rig could be mounted from the ceiling for example. Static wind tunnel test can now be conducted to measure the reaction forces for a range of rig roll, pitch, and yaw angles.

There is still uncertainty as to how close the responses performed are to true free-flight. The only way to truly identify the differences is to compare the responses between the wind tunnel aircraft model and another identical free-flying model. This should be a future goal.

8.6 Other work

8.6.1 Manoeuvre rig operation safety

It is important to perform manoeuvres, especially multi-DOF, in a safe and controlled manner within the wind tunnel. If manoeuvres resulting in aircraft model loss-of-control are performed, the rig and aircraft should be able to recover ideally before the rig hits the physical stops or before being stopped by the safety tethers. In case the aircraft and rig produce unpredictable or violent motion, the rig should have the capability of returning to a full stop within a reasonable time limit. Since communication with all components of the manoeuvre rig system are done through WiFi, a drop in the connection can lead to unstable behaviour. The following suggested algorithm can be implemented to ensure fast recover of the rig. During a connection interruption, the rig

and aircraft model can be programmed to apply maximum control surface deflections on both the rig's compensator and aircraft model. This ensures that an aerodynamic moment is applied on the rig, holding it at the arm stops, thus preventing oscillations. The rig position to be held must coincide with the natural resting position of the rig (with the wind tunnel off); this will indicate the direction of the control surface command to be applied. The wind speed must then be reduced or turned off, and the connection re-established remotely.

All components, including the ground station board transmit data to the control station wirelessly. The reason for this was to keep the programme architecture consistent between all components. The data acquisition method for the rig attitude can be changed from wireless to wired. This will ensure a more secure connection. Information on the rig's attitude (through a wired connection) and the ability to send commands to the rig's compensator can be used to implement autonomous control to enhance the stability of the rig. The software and hardware interface will need to be modified to accommodate this change.

Another suggestion is to implement an Inertial Measurement Unit for the compensator as well, similar to the Hawk model. Direct measurements of the rig's accelerations and rotation rates will be useful for many applications such as dynamic testing and kinematic compensation, for example.

8.6.2 Update to electronics

The current electronic boards used for the manoeuvre rig have been worn from several years of use. These boards still act as prototypes and an update is required with better options for secure attachment of cables. More suggestions made in Reference [11] still hold true, and are summarised below:

1. Replace the rig arm gimbal potentiometers for digital encoders to improve measurements of the rig's attitude angles.

2. Implement air flow sensors for the aircraft model in order to measure angle of attack and sideslip directly.

3. Upgrading on-board electronic boards from 16-bit to 32-bit for improved versatility in programming.

REFERENCES

[1] Pilmoor, M., Crowther, W., and Wood, N., "Development of a dynamic wind tunnel model for demonstration of flow control maneuver effectors," *3rd AIAA Flow Control Conference*, 2006, pp. 1383–1391.

[2] Papageorgiou, G. and Glover, K., "Two-degree-of-freedom control of an actively controlled wind-tunnel model," *Journal of Guidance, Control, and Dynamics*, Vol. 25, No. 3, 2002, pp. 510–516.

[3] Gatto, A. and Lowenberg, M., "Evaluation of a three degree of freedom test rig for stability derivative estimation," *Journal of aircraft*, Vol. 43, No. 6, 2006, pp. 1747–1761.

[4] Carnduff, S., Erbsloeh, S., Cooke, A., and Cook, M., "Characterizing stability and control of subscale aircraft from wind-tunnel dynamic motion," *Journal of Aircraft*, Vol. 46, No. 1, 2009, pp. 137–147.

[5] Jordan, T. L., Foster, J. V., Bailey, R. M., and Belcastro, C. M., "AirSTAR: A UAV platform for flight dynamics and control system testing," *25th AIAA Aerodynamic Measurement Technology and Ground Testing Conference, AIAA 2006-3307*, 2006.

[6] Owens, B., Brandon, J., Croom, M., Fremaux, M., Heim, G., and Vicroy, D., "Overview of Dynamic Test Techniques for Flight Dynamics Research at NASA LaRC," *25th AIAA Aerodynamic Measurement Technology and Ground Testing Conference*, No. AIAA 2006-3146, Fluid Dynamics and Co-located Conferences, 2006, doi:10.2514/6.2006-3146.

[7] Bergmann, A., Huebner, A., and Loeser, T., *Experimental and numerical research on the aerodynamics of unsteady moving aircraft*, Vol. 44, Elsevier, 2008, pp. 121–137, doi: 10.1016/j.paerosci.2007.10.006.

[8] Lutze, F. H. and Fan, Y., "Unsteady Aerodynamic Testing Using the Dynamic Plunge Pitch and Roll Model Mount," Department of Aerospace and Ocean Engineering, Virginia Polytechnic Institute and State University, NASA Grant NAG-1-1737, 1999, Document ID: 20000013325.

[9] Muse, J. A., Kutay, A., and Calise, A. J., "Novel force control traverse for simulating UAV flight in wind tunnel," *Proceedings of AIAA Atmospheric Flight Mechanics Confer-*

ence and Exhibit, Honolulu, Hawaii, AIAA-2008-6714, , No. AIAA 2008-6714, 2008, doi:10.2514/6.2008-6714, doi:10.2514/6.2008-6714.

[10] Pattinson, J., *Development and Evaluation of a Wind Tunnel Manoeuvre Rig*, Ph.D. thesis, Department of Aerospace Engineering, University of Bristol, 2010.

[11] Araujo-Estrada, S. A., *Control of a Wind Tunnel Manoeuvre-Rig to Physically Simulate Free-Flight Motion of an Aircraft Model*, Ph.D. thesis, University of Bristol, Department of Aerospace Engineering, Bristol, England, 2016.

[12] Blake, W. B., "A study of the rotary balance technique for predicting pitch damping," *Flight Simulation and Technologies*, Guidance, Navigation, and Control and Co-located Conferences, American Institute of Aeronautics and Astronautics, Aug. 1993.

[13] Kalviste, J., "Use of rotary balance and forced oscillation test data in a six degrees of freedom simulation," *Proceedings of the AIAA 9th Atmospheric Flight Mechanics Conference, AIAA-82-1364*, 1982.

[14] Malcolm, G. N., Kramer, B. R., and Suhrez, C. J., "US/UK rotarybalance test comparisons with a generic fighter model," *Proceedings of the 32nd Aerospace Sciences Meeting & Exhibit, AIAA 94-0196*, 1994.

[15] Ericsson, L., Beyers, M., Ericsson, L., and Beyers, M., "Wind tunnel aerodynamics in rotary tests of combat aircraft models," *35th Aerospace Sciences Meeting and Exhibit*, Aerospace Sciences Meetings, American Institute of Aeronautics and Astronautics, Jan. 1997.

[16] Hoe, G., Owens, D. B., and Denham, C., "Forced Oscillation Wind Tunnel Testing for FASER Flight Research Aircraft," *AIAA Atmospheric Flight Mechanics Conference*, Guidance, Navigation, and Control and Co-located Conferences, American Institute of Aeronautics and Astronautics, Aug. 2012, pp. –.

[17] Kilgore, R. A. and Averett, B. T., "A forced-oscillation method for dynamic-stability testing," *Journal of Aircraft, vol. 5, no. 1, pp. 304-305*, 1964.

[18] Burt, G. E., "A forced-oscillation test mechanism for measuring dynamic-stability derivatives in roll," *Proceedings of the 12th AIAA Aerospace Sciences Meeting, AIAA-74-86*, 1974.

[19] Tang, D. and Dowell, E. H., "Effects of a Free-to-Roll Fuselage on Wing Flutter: Theory and Experiment," *AIAA Journal*, Vol. 52, No. 12, Oct. 2014, pp. 2625–2632.

[20] Morris, R., "Utilization of a free oscillation wind tunnel model in conjunction with an analog computer to determine the dynamic stability derivatives," *2nd Aerodynamic Testing Conference*, Aerodynamic Testing Conference, American Institute of Aeronautics and Astronautics, Sept. 1966.

[21] Murri, D. G., Nguyen, L. T., and Grafton, S. B., "Wind-tunnel free-flight investigation of a model of a forward-swept-wing fighter configuration," Tech. rep., National Aeronautics and Space Administration NASA TP-2230, NASA, 1984.

[22] Huang, M. and Wang, Z.-w., "A Review of Wind Tunnel Based Virtual Flight Testing Techniques for Evaluation of Flight Control Systems," *International Journal of Aerospace Engineering*, Vol. 2015, 2015.

[23] Wolowicz, C. H., Brown Jr, J., and Gilbert, W. P., "Similitude requirements and scaling relationships as applied to model testing," *NASA TP-1435*, 1979.

[24] Kyle, H., *An investigation into the use of a pendulum support rig for aerodynamic modelling*, Ph.D. thesis, University of Bristol, Bristol, England, UK. Department of Aerospace Engineering., 2004.

[25] Gatto, A., "Application of a pendulum support test rig for aircraft stability derivative estimation," *Journal of Aircraft*, Vol. 46, No. 3, 2009, pp. 927–934.

[26] Lowenberg, M. and Kyle, H., "Derivation of unsteady aerodynamic models from wind tunnel multi-axis test rigs," *Proceedings of The International Council of the Aeronautical Sciences*, Vol. 3, No. 2, 2002.

[27] Kyle, H., Lowenberg, M. H., and Greenwell, D., "Comparative evaluation of unsteady aerodynamic modelling approaches," *AIAA Atmospheric Flight Mechanics Conference and Exhibit, Providence, Rhode Island. AIAA*, 2004, doi: 10.2514/6.2004-5272.

[28] Loeser, T. and Bergmann, A., *Development of the Dynamic Wind Tunnel Testing Capabilities at DNW-NWB*, 2003.

[29] Jackson, E. B. and Buttrill, C. W., "Control Laws for a Wind Tunnel Free-Flight Study of a Blended-Wing-Body Aircraf," *National Aeronautics and Space Administration (NASA)*, 2006.

[30] Lineberry, D., "AirSTAR: For the Sake of Pilots and Passengers," *NASA Langley Research Center*, 2017 [https://www.nasa.gov/larc/airstar-for-the-sake-of-pilots-and-passengers].

[31] Loeser, T. and Bergmann, A., "Capabilities of Deployment Tests at DNW-NWB," 2006.

[32] Rein, M., Hohler, G., Schutte, A., Bergmann, A., and Loser, T., "Ground-Based Simulation of Complex Maneuvers of a Delta-Wing Aircraft," *Journal of Aircraft*, Vol. 45, No. 1, 2008, pp. 286–291.

[33] Veazey, D., "Current AEDC Weapons Separation Testing and Analysis to Support Flight Testing," *USAF Developmental Test and Evaluation Summit*, 2004.

[34] Manning, T. E., Ratliff, C. L., and Marquart, E. J., "Bridging the gap between ground and flight tests: virtual flight testing (VFT)," *Proceedings of the 1st AIAA Aircraft Engineering, Technology, AIAA-95-3875*, 1995.

[35] Liu, F., Wang, L., and Tan, X., "Digital virtual flight testing and evaluation method for flight characteristics airworthiness compliance of civil aircraft based on HQRM," *Chinese Journal of Aeronautics, vol. 28, no. 1, pp. 112-120*, 2015.

[36] Ratliff, C. L. and Marquart, E. J., "An assessment of a potential test technique: virtual flight testing (VFT)," *Proceedings of the AIAA Flight Simulation Technologies Conference, AIAA-95-3415*, 1995.

[37] Magill, J. C., Cataldi, P., Morency, J. R., Hammer, D. X., Burgess, R., and Jeter, E., "Demonstration of a Wire Suspension for Wind-Tunnel Virtual Flight Testing," *Journal of Spacecraft and Rockets, Vol. 46, No. 3*, 2009.

[38] Gebert, G., Kelly, J., Lopez, J., and Evers, J., "Virtual flight testing in a ground test facility," *Proceedings of the 18th AIAA Applied Aerodynamics Conference, AIAA 2000-4019*, 2000.

[39] Linliang, G., Minghong, Z., Bowen, N., Peng, K., and Chengwen, Z., "Initial virtual flight test for a dynamically similar aircraft model with control augmentation system," *Chinese Journal of Aeronautics, Volume 30, Issue 2, pp. 602-610*, 2017, doi:10.1016/j.cja.2016.12.034.

[40] Bacic, M. and MacDiarmid, M., "Hardware-in-the-loop simulation of aerodynamic objects," *Proceedings of the AIAA Modeling and Simulation Technologies Conference and Exhibit, AIAA 2007-6465, Hilton Head, SC, USA*, August 2007.

[41] Boria, F., Stanford, B., Bowman, S., and Ifju, P., "Evolutionary optimization of a morphing wing with wind-tunnel hardware in the loop," 2009.

[42] Chandramohan, R., Muse, J., and Calise, A., "Modeling of a 3-DOF Dynamic Wind Tunnel Traverse," *Proceedings of AIAA Modeling and Simulation Technologies Conference, Toronto, Ontario, Canada, AIAA-2010-7790*, 2010, doi:10.2514/6.2010-7790.

[43] Muse, J., Kutay, A., Brzozowski, D., Culp, J., Calise, A., and Glezer, A., "Dynamic Flight Maneuvering Using Trapped Vorticity Flow Control," *Proceedings of the 46th AIAA Aerospace Sciences Meeting and Exhibit, Reno, Nevada*, 2008, doi: 10.2514/6.2008-522.

[44] Muse, J., Tchieu, A., Kutay, A., Chandramohan, R., Calise, A., and Leonard, A., "Vortex Model Based Adaptive Flight Control Using Synthetic Jets," *Proceedings of AIAA Guidance, Navigation, and Control Conference, Chicago, Illinois, AIAA 2009-5761*, 2009, doi:10.2514/6.2009-5761.

[45] Jee, S., Mejia, O. D. L., Moser, R. D., Muse, J. A., Kutay, A. T., and Calise, A. J., "Simulation of Rapidly Maneuvering Airfoils with Synthetic Jet Actuators," *AIAA Journal Vol. 51, No. 8*, 2013, doi:10.2514/1.J052080.

[46] Pattinson, J., Lowenberg, M., and Goman, M., "A multi-degree-of-freedom rig for the wind tunnel determination of dynamic data," *AIAA Atmospheric Flight Mechanics Conference*, No. AIAA 2009-5727, 2009, doi:10.2514/6.2009-5727.

[47] Araujo-Estrada, S. A., Lowenberg, M. H., Neild, S., and Goman, M., "Evaluation of Aircraft Model Upset Behaviour Using Wind Tunnel Manoeuvre Rig," *AIAA Atmospheric Flight Mechanics Conference*, No. AIAA 2015-0750, 2015, doi:10.2514/6.2015-0750.

[48] Peyada, N., Ghosh, A., and Go, T., "Mathematical modelling, simulation, and estimation of aircraft parameters using five degree-of-freedom dynamic test rig," *Proceedings of the Institution of Mechanical Engineers, Part G: Journal of Aerospace Engineering*, Vol. 226, No. 1, 2011, pp. 55–63, doi: 10.1177/0954410011407265.

[49] Pattinson, J., Lowenberg, M., and Goman, M., "Characterisation of wind tunnel observed, large-amplitude pitch limit-cycles," *AIAA Atmospheric Flight Mechanics Conference*, No. AIAA 2011-6526, 2011, doi:10.2514/6.2011-6526.

[50] Pattinson, J., Lowenberg, M. H., and Goman, M. G., "Investigation of Poststall Pitch Oscillations of an Aircraft Wind-Tunnel Model," *Journal of Aircraft*, Vol. 50, No. 6, 2013, pp. 1843–1855.

[51] Mills, H., "Nonlinear Flow Visualisation," Individual exploratory project report, University of Bristol, 2017.

[52] Gong, Z., Araujo-Estrada, S., Lowenberg, M. H., Neild, S. A., and Goman, M. G., "Experimental Investigation of Aerodynamic Hysteresis Using a Five-Degree-of-Freedom Wind-Tunnel Maneuver Rig," *Journal of Aircraft*, Vol. 56, No. 3, 2019, pp. 1029–1039.

[53] Pattinson, J., Lowenberg, M. H., and Goman, M. G., "Multi-Degree-of-Freedom Wind-Tunnel Maneuver Rig for Dynamic Simulation and Aerodynamic Model Identification," *Journal of Aircraft*, Vol. 50, No. 2, 2013, pp. 551–566, doi:10.2514/1.c031924.

[54] Araujo-Estrada, S. A., Gong, Z., Lowenberg, M. H., Neild, S., and Goman, M., "Wind Tunnel Manoeuvre Rig: A Multi-DOF Test Platform for Model Aircraft," *54th AIAA Aerospace Sciences Meeting*, No. AIAA 2016-2119, 2016, doi:10.2514/6.2016-2119.

[55] Gainer, T. G. and Hoffman, S., "Summary of transformation equations and equations of motion used in free flight and wind tunnel data reduction and analysis," Tech. Rep. NASA-SP-3070, NASA Langley Research Center; Hampton, VA, United States, 1972.

[56] Fraser-Mitchell, H., "The HAWK Story," *Journal of Aeronautical History*, , No. 2013/01, 2013.

[57] Wilborn, J. E. and Foster, J. V., "Defining commercial transport loss-of-control: A quantitative approach," *AIAA Atmospheric Flight Mechanics Conference and Exhibit*, 2004, pp. AIAA–2004–4811.

[58] Chambers, J. R. and Stough III, H. P., "Summary of NASA stall/spin research for general aviation configurations," *AIAA General Aviation Technology Conference, AIAA 86-2597*, 1986.

[59] Abramov, N., Goman, M., Khrabrov, A., Kolesnikov, E., Fucke, L., Soemarwoto, B., and Smaili, H., "Pushing Ahead - SUPRA Airplane Model for Upset Recovery," *Proceedings of AIAA Modeling and Simulation Technologies Conference, Minneapolis, Minnesota*, 2012, doi: 10.2514/6.2012-4631.

[60] Groen, E., Ledegang, W., Field, J., Smaili, H., Roza, M., Fucke, L., Nooij, S., Goman, M., Mayrhofer, M., Zaichik, L., Grigoryev, M., and Biryukov, V., "SUPRA - Enhanced Upset Recovery Simulation," *Proceedings of AIAA Modeling and Simulation Technologies Conference, Minneapolis, Minnesota*, 2012, doi:10.2514/6.2012-4630.

[61] Magill, J. C., McManus, K. R., Miller, M. G., and Allen, M. G., "A high bandwidth air bearing balance for dynamic wind tunnel testing," *Proceedings of the 22nd Atmospheric Flight MechanicsConference, AIAA-97-3648, New Orleans, La, USA*, 1997.

[62] Gebert, G., Kelly, J., Lopez, J., and Evers, J., "Wind tunnel based virtual flight testing," *Proceedings of the 38th Aerospace Sciences Meeting & Exhibit, AIAA 2000-46669*, 2000.

[63] Shabana, A. A., *Dynamics of Multibody Systems*, Cambridge University Press, ISBN 0-521-85011-8, 3rd ed., 2005, doi:10.1017/CBO9780511610523.

[64] Cook, M., *Flight Dynamics Principles: A Linear Systems Approach to Aircraft Stability and Control*, Elsevier, ISBN 9780080982427, 3rd ed., 2013, doi:10.1016/c2010-0-65889-5.

[65] Goman, M., Khramtsovsky, A., and Usoltev, S., "High incidence aerodynamics model for hypothetical aircraft," *Central Aerohydrodynamic Institute (TsAGI), Contract Report to Flight Systems Department, Defence Research Agency, Bedford*, 1995, Contract No. ASF/2454/E.

[66] Nelson, R. C., *Flight Stability and Automatic Control*, McGraw-Hill, 1989.

[67] Banneheka Navaratna, P., Lowenberg, M., and Neild, S., "Minimally-constrained flight simulation in a wind tunnel," *Journal of Aircraft*, 2019, doi:10.2514/1.C035199.

[68] Navaratna, P. D. B., Lowenberg, M. H., Neild, S., and Zhang, X., "Physical simulation of free-flight in captive wind tunnel tests," *Applied Aerodynamics Conference*, Royal Aeronautical Society, Bristol, 2016.

[69] Scordamaglia, V., "Trajectory and Attitude Plot Version 3 for MATLAB 6.5.1 (R13SP1)," https://uk.mathworks.com/matlabcentral/fileexchange/5656-trajectory-and-attitude-plot-version-3, date accessed: 15-05-2016.

[70] Jategaonkar, R. V., *Flight Vehicle System Identification: A Time-domain Methodology*, Progress in Astronautics and Aeronautics, American Institute of Aeronautics and Astronautics, ISBN 9781563478369, 2006, doi:10.2514/4.102783.

[71] Goman, M. G., Usoltsev, S. P., and Khrabrov, A. N., "Dynamics of an airplane model in a wind tunnel with roll and yaw mobility," *TsAGI Scientific Notes, No. 3-4*, 1995.

[72] Henderson, D. M., "Euler angles, quaternions, and transformation matrices for space shuttle analysis," Tech. Rep. NASA-CR-151435, National Aeronautics and Space Administration, United States, 1977.

APPENDIX A

QUATERNION TRANSFORMATION MATRICES

The transformation matrix (A^i) for a body i adheres to the following Euler angle rotation sequence: the first rotation is ψ^i about the z axis, the second rotation is θ^i about the resulting y axis and the third rotation is ϕ^i about the resulting x axis. The equations for alternative rotation sequences can be found in Reference [72].

$$\begin{aligned}
{\theta_{q0}}^i &= +\sin(\frac{\psi^i}{2})\sin(\frac{\theta^i}{2})\sin(\frac{\phi^i}{2})+\cos(\frac{\psi^i}{2})\cos(\frac{\theta^i}{2})\cos(\frac{\phi^i}{2}) \\
{\theta_{q1}}^i &= -\sin(\frac{\psi^i}{2})\sin(\frac{\theta^i}{2})\cos(\frac{\phi^i}{2})+\sin(\frac{\phi^i}{2})\cos(\frac{\psi^i}{2})\cos(\frac{\theta^i}{2}) \\
{\theta_{q2}}^i &= +\sin(\frac{\psi^i}{2})\sin(\frac{\phi^i}{2})\cos(\frac{\theta^i}{2})+\sin(\frac{\theta^i}{2})\cos(\frac{\psi^i}{2})\cos(\frac{\phi^i}{2}) \\
{\theta_{q3}}^i &= +\sin(\frac{\psi^i}{2})\cos(\frac{\theta^i}{2})\cos(\frac{\phi^i}{2})-\sin(\frac{\theta^i}{2})\sin(\frac{\phi^i}{2})\cos(\frac{\psi^i}{2})
\end{aligned} \tag{A.1}$$

$$E^i = \begin{bmatrix} -{\theta_{q1}}^i & {\theta_{q0}}^i & -{\theta_{q3}}^i & {\theta_{q2}}^i \\ -{\theta_{q2}}^i & {\theta_{q3}}^i & {\theta_{q0}}^i & -{\theta_{q1}}^i \\ -{\theta_{q3}}^i & -{\theta_{q2}}^i & {\theta_{q1}}^i & {\theta_{q0}}^i \end{bmatrix}, \overline{E}^i = \begin{bmatrix} -{\theta_{q1}}^i & {\theta_{q0}}^i & {\theta_{q3}}^i & -{\theta_{q2}}^i \\ -{\theta_{q2}}^i & -{\theta_{q3}}^i & {\theta_{q0}}^i & {\theta_{q1}}^i \\ -{\theta_{q3}}^i & {\theta_{q2}}^i & -{\theta_{q1}}^i & {\theta_{q0}}^i \end{bmatrix} \tag{A.2}$$

$$A^i = E^i {\overline{E}^i}^T, G^i = 2E^i, \overline{G}^i = 2\overline{E}^i \tag{A.3}$$

APPENDIX B

SUBSCALE A-4D AIRCRAFT MODEL PROPERTIES

Table B.1 presents the reference dimensions, mass and inertia of the subscale model aircraft used in the computational simulation: 6.31% scale model of a A-4D aircraft [66]. Table B.2 shows the list of the aerodynamic derivatives and their values. Table B.3 compares the A-4D aerodynamic coefficients with the Hawk's experimentally measured coefficients (in the linear region).

TABLE B.1. A-4D model aircraft reference dimensions, mass and inertia properties.

Property	**Symbol**	**Value**
Wing area	S	0.0961 m^2
Mean aerodynamic chord	c	0.208 m
Span	b	0.529 m
Mass	m	2.00 kg
Inertia	I_{xx}	0.0109 kg m^2
	I_{yy}	0.0350 kg m^2
	I_{zz}	0.0395 kg m^2
	I_{xy}	0.00 kg m^2
	I_{xz}	0.00180 kg m^2
	I_{yz}	0.00 kg m^2

TABLE B.2. A-4D aircraft non-dimensional aerodynamic stability derivatives at Mach 0.4.

Derivative	**Value**
C_{L_0}	0.28
C_{L_α}	3.5
$C_{L_{\dot{\alpha}}}$	0.72
$C_{L_{\delta_e}}$	0.36
C_{D_0}	0.030
C_{D_α}	0.30
C_{Y_β}	-0.98
$C_{Y_{\delta_r}}$	0.17
C_{l_β}	-0.12
C_{l_p}	-0.26
C_{l_r}	0.14
$C_{l_{\delta_a}}$	0.080
$C_{l_{\delta_r}}$	0.11
C_{m_α}	-0.38
$C_{m_{\dot{\alpha}}}$	-1.1
C_{m_q}	-3.6
$C_{m_{\delta_e}}$	-0.50
C_{n_β}	0.25
C_{n_p}	0.022
C_{n_r}	-0.35
$C_{n_{\delta_a}}$	0.060
$C_{n_{\delta_r}}$	-0.030

TABLE B.3. Comparison between the A-4D aerodynamic coefficients and Hawk model's experimentally measured values.

Derivative	**A-4D**	**Hawk**
C_{L_0}	0.28	-0.104
C_{L_α}	3.5	3.44
$C_{L_{\dot{\alpha}}}$	0.72	1.44×10^{-7}
C_{L_q}	-	12.1
C_{D_0}	0.030	0.0607
$C_{l_{\delta_a}}$	0.080	0.123
C_{m_0}	-	0.1053
C_{m_α}	-0.38	-0.499
$C_{m_{\dot{\alpha}}}$	-1.1	-0.00145
C_{m_q}	-3.6	-8.93
$C_{m_{\delta_e}}$	-0.50	-1.14
C_{n_0}	-	-0.000742
C_{n_β}	0.25	0.104
$C_{n_{\delta_r}}$	-0.030	-0.0556

APPENDIX C

HAWK CFD DATA

The following is the data obtained using CFD from Nanjing University of Aeronautics & Astronautics for the BAe Hawk model:

TABLE C.1. Aerodynamic data for the BAe Hawk model.

α (°)	δ_e (°)	C_L	C_D	C_m
-5	-20	-0.3387	0.1174	0.2917
0	-20	-0.0339	0.0946	0.2666
5	-20	0.1962	0.1016	0.2167
-5	0	-0.2395	0.05835	0.09716
0	0	0.0944	0.04895	0.04101
5	0	0.4238	0.06673	-0.006148
-5	20	-0.0269	0.0779	-0.2605
0	20	0.2754	0.0890	-0.2764
5	20	0.4537	0.1194	-0.2821

TABLE C.2. Hawk aerodynamic derivatives for Equations 3.114-3.116 by performing a surface fit on data points given in Table C.1.

i	C_{L_i}	C_{D_i}	C_{m_i}
0	0.1155	0.04953	0.04463
α	3.800	0.04801	-0.5919
δ_e	0.4429	-0.008018	-0.7775
$\alpha\delta_e$	-0.4456	0.4703	0.4383
$\alpha\alpha$	-8.894	3.339	-0.2455
$\delta_e\delta_e$	-0.08645	0.6890	-0.8427
$\alpha\delta_e\delta_e$	-21.94	0.6306	7.760
$\alpha\alpha\delta_e$	-13.90	-2.962	9.875
$\alpha\alpha\alpha$	0.004824	0.00006094	-0.0007513
$\delta_e\delta_e\delta_e$	0.008993	-0.0001628	-0.01579
q	-1.828	-	-3.528
$\dot{w}$	-1.342	-	-2.604

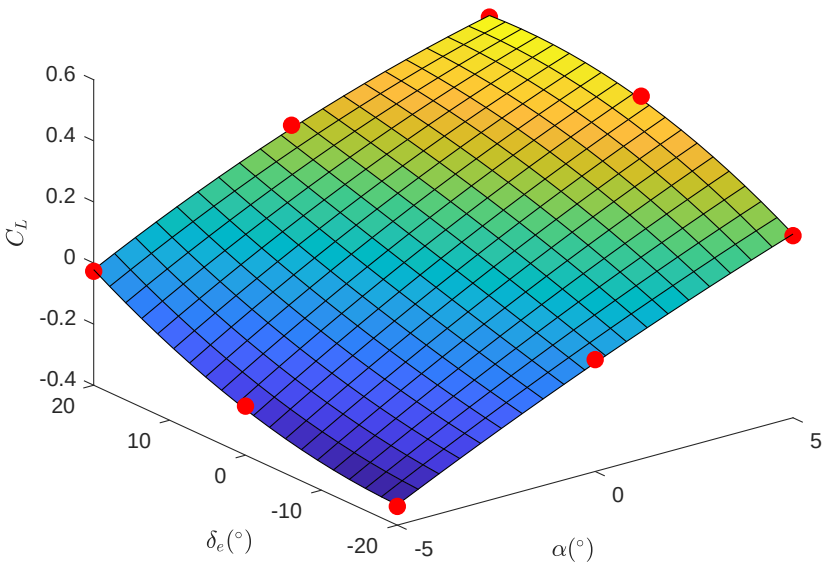

FIGURE C.1. Surface plot for the Hawk model lift.

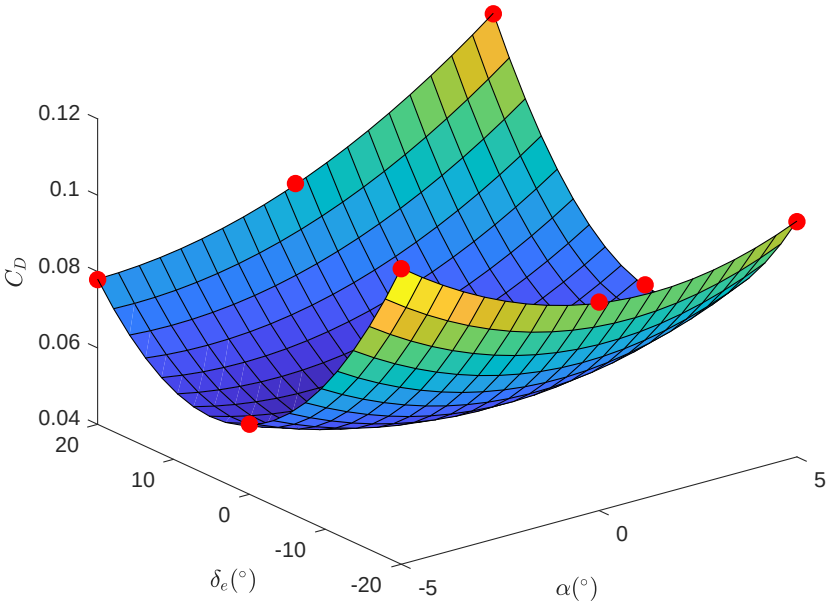

FIGURE C.2. Surface plot for the Hawk model drag.

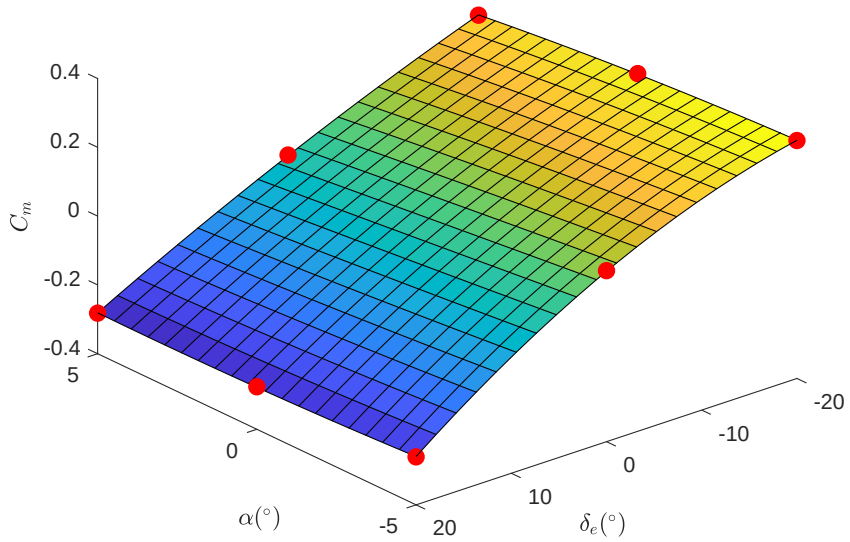

FIGURE C.3. Surface plot for the Hawk model pitching moment.

APPENDIX D

COMPENSATOR AND HAWK CONTROL SURFACE MODEL PARAMETERS

Table D.1 shows the estimated parameters for the control surface models for the manoeuvre rig's compensator and Hawk as shown in Figure 3.11. The estimation was carried out using Simulink's in-built parameter estimation tool. This tool was set to use the nonlinear least squares optimisation method with the Trust-Region-Reflective algorithm. The responses of the control surfaces and its simulated responses are presented in Figures D.1 and D.2 for the compensator and Hawk respectively. The model can be used for all control surfaces of the compensator and the Hawk model. Note that the parameters presented here were estimated at the time when the compensator servos were updated. As a result, the performance of the previous compensator servos (HS-645MG) would have degraded at this point due to wear compared to new servos. All experiments using the compensator presented in this work use the new MX-355WP servos.

TABLE D.1. Estimated parameters for the control surface actuation model shown in Figure 3.11.

	K_1	K_2	**Saturation 1**[1]	**Saturation 2**[2]
Previous compensator servo (HS-645MG)	5.865	18.08	±1.597	±0.6981
Updated compensator servo (MX-355WP)	13.24	21.80	±3.574	±0.6981
Hawk servo (HS-65MG)	11.40	40.39	±8.067	±0.6981

[1]Saturation 1 represents voltage saturation

[2]Saturation 2 represents control surface deflection limit of ±40°

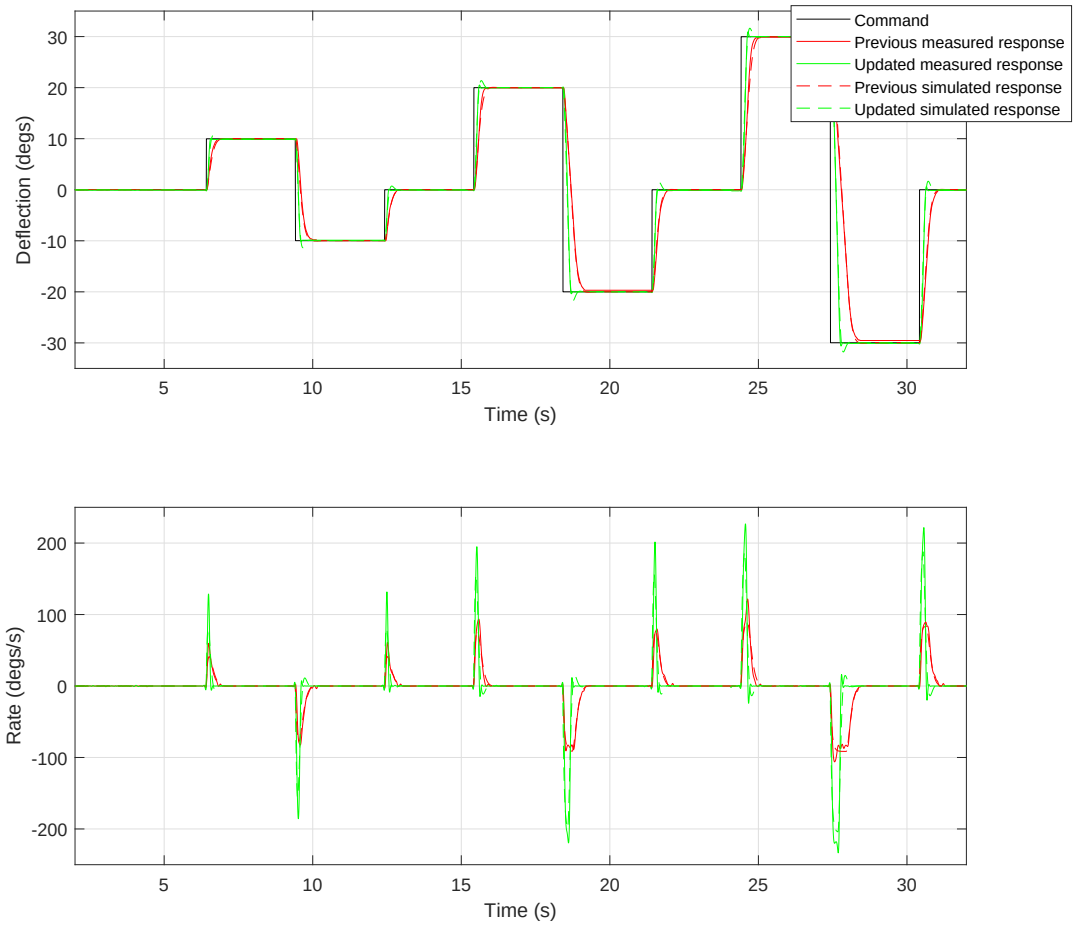

FIGURE D.1. Compensator control surface actuation responses.

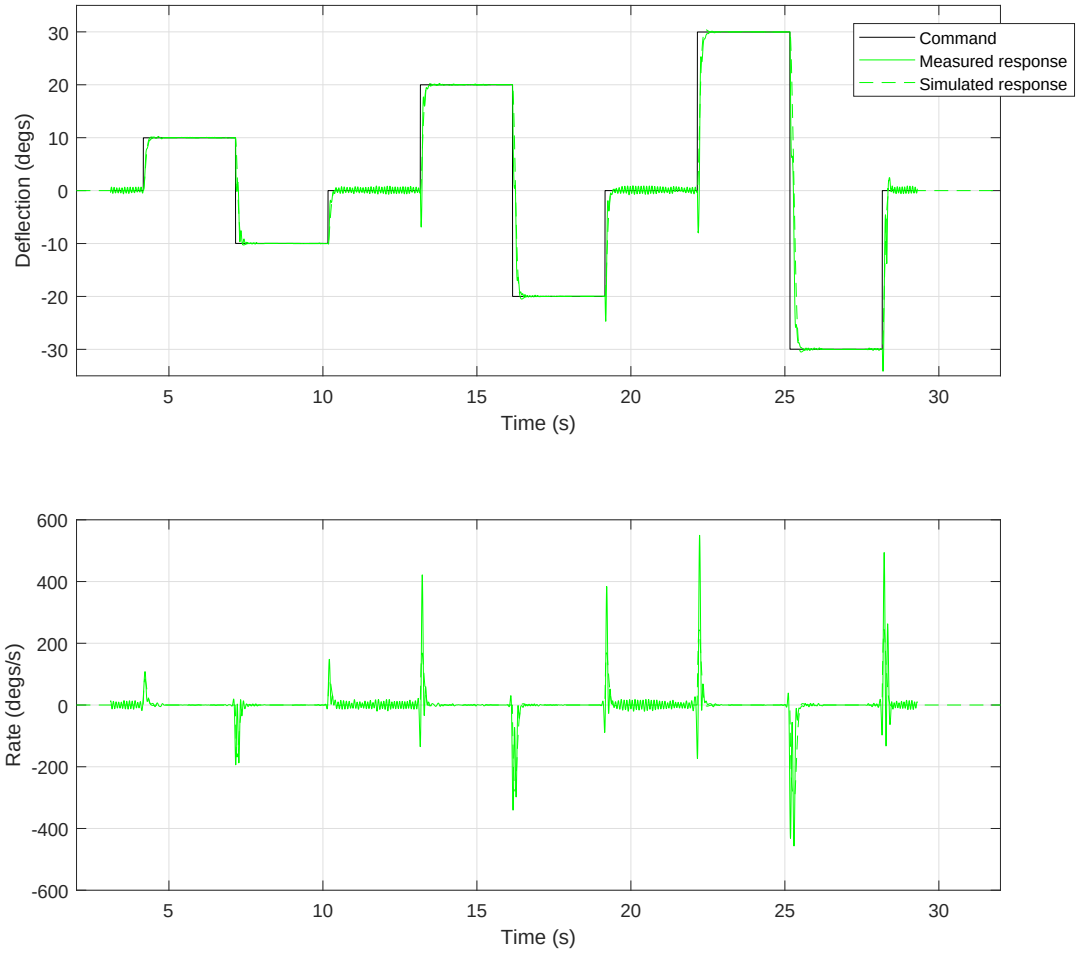

FIGURE D.2. Hawk control surface actuation responses.

APPENDIX E

MANOEUVRE RIG BODY PROPERTIES

Table E.1 shows the mass and inertia values used for each body in the computational simulation of the manoeuvre rig. $\bar{\boldsymbol{u}}$ is the centre of gravity position/rotation point of each component relative to the rig arm rotation point. Figure E.1 shows a schematic for the different load cell positions and their respective arm dimensions. Note that the inertia values for the rig arm, load cell, and link were approximated by simplifying these components as cylinders/tubes in Autodesk Inventor with uniform density. Their density values were set to match the actual component weights.

TABLE E.1. Manoeuvre rig body properties used for simulation.

											$\bar{\boldsymbol{u}}$		
	Mass (kg)	I_{xx} $(kg.m^2)$	I_{yy} $(kg.m^2)$	I_{zz} $(kg.m^2)$	I_{xy} $(kg.m^2)$	I_{xz} $(kg.m^2)$	I_{yz} $(kg.m^2)$	S (m^2)	c (m)	b (m)	x (m)	y (m)	z (m)
Hawk model	1.970	0.008083	0.03800	0.06121	0.000	0.000	0.000	0.0849	0.143	0.594	0.8000 [8]	0.000	0.000
A-4D model	2.000	0.01090	0.03500	0.03950	0.000	0.001800	0.000	0.0961	0.208	0.529	0.8000 [8]	0.000	0.000
T-tail airliner model [1]	2.500	0.02280	0.1610	0.1810	0.000	0.000	0.000	0.108	0.142	0.897	0.8000 [8]	0.000	0.000
Load cell (lower position) [2]	0.1000	0.00004260	0.00004260	0.00001790	0.000	0.000	0.000	-	-	-	0.8000 [8]	0.000	0.3183
Load cell (upper position) [2]	0.1000	0.00004260	0.00004260	0.00001790	0.000	0.000	0.000	-	-	-	0.8000 [8]	0.000	0.08830
Rig arm (original, without load cell) [2,3]	3.647	0.09145	0.7938	0.6688	0.000	0.000	0.000	-	-	-	0.2615	0.000	0.1090
Rig arm (original, modified for lower load cell position) [2,4]	2.897	0.1130	0.6250	0.5130	0.000	0.000	0.000	-	-	-	0.1290	0.000	0.1780
Rig arm (original, modified for upper load cell position) [2,4]	3.270	0.1160	0.7760	0.6610	0.000	0.000	0.000	-	-	-	0.2050	0.000	0.1850
Rig arm (extended, modified for lower load cell position) [2,4,5]	3.237	0.1350	0.7680	0.6330	0.000	0.000	0.000	-	-	-	0.1690	0.000	0.2190
Rig arm (extended, modified for upper load cell position) [2,4,5]	3.609	0.1370	0.9730	0.8370	0.000	0.000	0.000	-	-	-	0.250	0.000	0.220
Link (lower load cell position) [2]	0.4550	0.003000	0.003000	0.000	0.000	0.000	0.000	-	-	-	0.8000 [8]	0.000	0.1460
Link (upper load cell position) [2]	0.08200	0.000	0.000	0.000	0.000	0.000	0.000	-	-	-	0.8000 [8]	0.000	0.03100
Compensator (current) [6]	3.912	0.06524	0.04421	0.04423	0.000	0.000	0.000	0.125	0.181	0.700	-0.3800	0.000	0.000
Compensator (extended) [7]	3.912	0.06524	0.04421	0.04423	0.000	0.000	0.000	0.125	0.181	0.700	-0.6800	0.000	0.000

[1] The properties for the T-tail airliner model were estimated using Autodesk Inventor at it's current design stage.
[2] The properties were estimated using Autodesk Inventor.
[3] These are the original arm properties prior to the load cell installation modifications.
[4] These are the estimated arm properties after load cell modification installation.
[5] This is the an elongated version of the arm designed to accommodate the future T-tail airliner model.
[6] This is the current compensator placed at it's original position along the rig arm.
[7] This is the compensator positioned further aft of the rig arm in order to increase its effectiveness and performance.
[8] The x position is $0.95m$ for the extended rig arm.

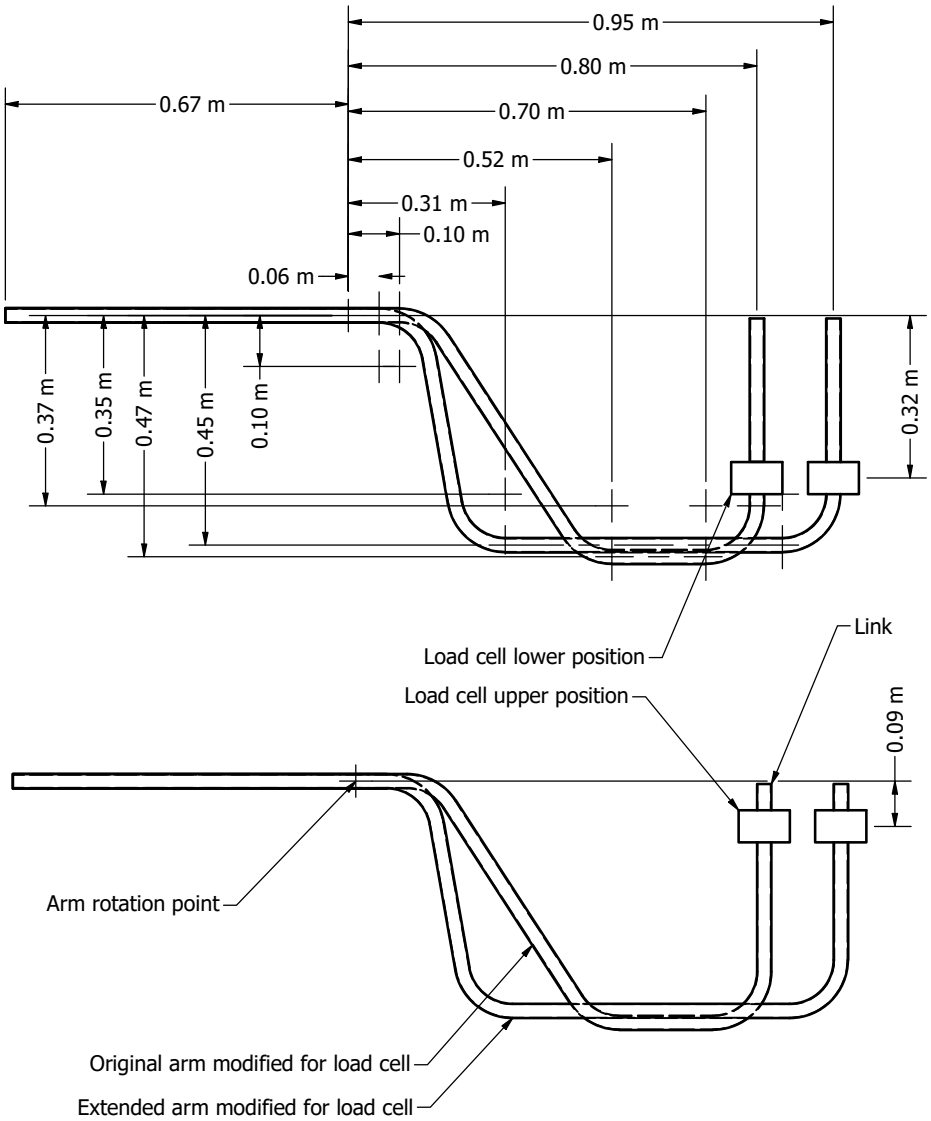

FIGURE E.1. Drawing of the different load cell positions considered for the manoeuvre rig.

APPENDIX F

RIG COMPENSATOR AERODYNAMIC COEFFICIENTS

Tables F.1, F.2 and F.3 shows the aerodynamic coefficients found for the manoeuvre rig's compensator using parameter estimation techniques done in Reference [11].

TABLE F.1. Rig compensator pitching moment parameters (at $\theta_c = 0$) [11].

Parameter	**Estimated**	
	Equation Error Method	Output Error Method
$C_{L_{\alpha_c}}$	2.1814	2.1567
$C_{L_{q_c}}$	15.3215	16.0339
$C_{L_{\delta_{e_c}}}$	5.9743	5.9095

TABLE F.2. Rig compensator yawing moment parameters [11].

Parameter	**Estimated**	
	Equation Error Method	Output Error Method
$C_{Y_{\beta_c}}$	1.9258	1.9408
$C_{Y_{r_c}}$	-4.0494	-4.0642
$C_{Y_{\delta_{r_c}}}$	5.9652	6.2074

TABLE F.3. Rig compensator rolling moment parameters [11].

Parameter	**Estimated**
$C_{l_c 0}$	1.007×10^{-2}
$C_{l_{\phi_{c1}}}$	0.498×10^{-3}
$C_{l_{\phi_{c2}}}$	1.171×10^{-2}
$C_{l_{\phi_{c3}}}$	-1.109×10^{-3}
$C_{l_{\phi_{c4}}}$	-8.052×10^{-3}
$C_{l_{\phi_{c5}}}$	0
$C_{l_{\phi_{c6}}}$	0
$C_{l_{\phi_{c7}}}$	0
$C_{l_{\phi_{c8}}}$	0
k	1.702
$C_{l_{\delta a_{c11}}}$	-5.47×10^{-2}
$C_{l_{\delta a_{c12}}}$	1.95
$C_{l_{\delta a_{c13}}}$	-5.60×10^{-3}
$C_{l_{\delta a_{c14}}}$	-1.70×10^{-3}
$C_{l_{\delta a_{c21}}}$	-6.19×10^{-2}
$C_{l_{\delta a_{c22}}}$	1.23
$C_{l_{\delta a_{c23}}}$	2.15×10^{-2}
$C_{l_{\delta a_{c24}}}$	-4.30×10^{-3}
$C_{l_{\delta a_{c31}}}$	-4.84×10^{-2}
$C_{l_{\delta a_{c32}}}$	1.47
$C_{l_{\delta a_{c33}}}$	2.99×10^{-2}
$C_{l_{\delta a_{c34}}}$	-9.30×10^{-3}
$C_{l_{\delta a_{c41}}}$	-4.29×10^{-2}
$C_{l_{\delta a_{c42}}}$	1.55
$C_{l_{\delta a_{c43}}}$	3.40×10^{-3}
$C_{l_{\delta a_{c44}}}$	3.80×10^{-3}
$C_{l_{p_c}}$	-0.45

APPENDIX G

ALGEBRAIC LOOPS

Algebraic loops can occur in Matlab Simulink simulations when the input of a function or model is directly dependant on the output. As a result the output cannot be solved within a given time step. Enclosing a model in a subsystem block (whose input is again directly dependant on the output) will also cause an algebraic loop even though the enclosed model is not a direct feedthrough. For example, the Simulink model shown in Figure 3.12 can be simplified as:

$$\ddot{q} = f\left(q, \dot{q}, Q_R^m, F_\theta^m, Q_R^c, F_\theta^c\right) \tag{G.1}$$

When introducing the kinematic compensation concept presented in Section 4.3.3, $\ddot{q}$ will also be a function of F_c^* where

$$\ddot{q} = f\left(q, \dot{q}, Q_R^m, F_\theta^m, Q_R^c, F_\theta^c, F_c^*\right) \tag{G.2}$$

$$F_c^* = g\left(q, \dot{q}, \ddot{q}, Q_R^m, F_\theta^m, Q_R^c, F_\theta^c\right) \tag{G.3}$$

which creates an algebraic loop. Simulink will attempt to solve the algebraic loop by iterating within the current time step. However, this increases simulation time and may not solve all cases, for example if the function is not smooth. Adding an initial condition block to the input of the function can help this iteration solution to converge onto the correct solution. This was the solution adopted for the example above by placing an initial condition block for F_c^* input to function f.

Another method to overcome this issue is to add a step delay to the function output thus making the current solution dependant on the solution of the previous time step. If the time step is small enough this would not significantly affect the overall model behaviour.

APPENDIX H

MINI45 DRAWING

The following is the drawing for the Mini45 load cell and its wireless transmitter installed on the manoeuvre rig.

H.1 Drawing of the ATI Mini45 load cell

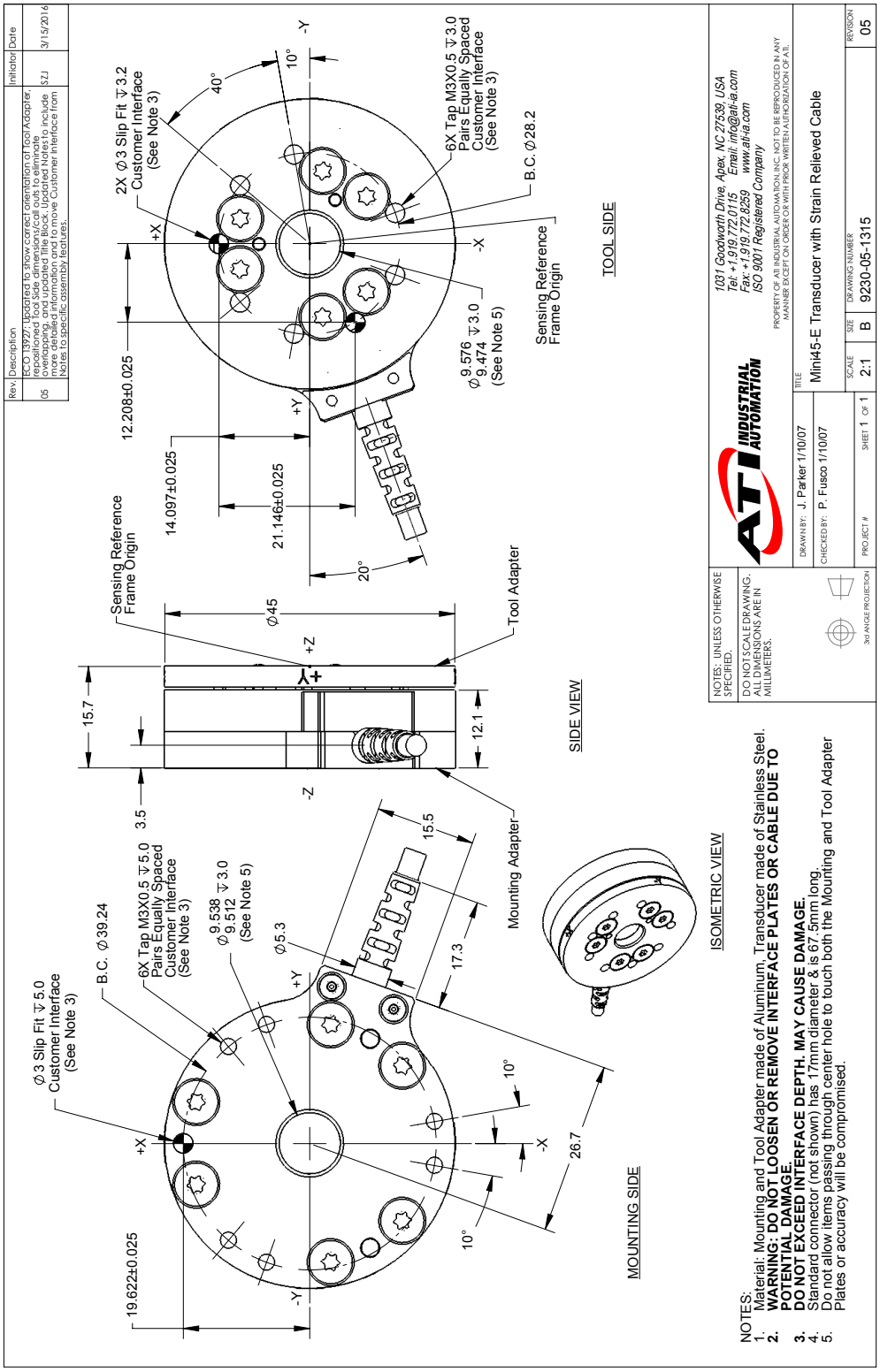

H.2 Drawing of the load cell wireless transmitter